Weak Lensing by Galaxy Clusters: from Pixels to Cosmology

Daniel Grün

Weak Lensing by Galaxy Clusters: from Pixels to Cosmology

Daniel Grün

Dissertation der Fakultät für Physik
Dissertation of the Faculty of Physics

der Ludwig-Maximilians-Universität München
at the Ludwig Maximilian University of Munich

für den Grad des
for the degree of

Doctor rerum naturalium

vorgelegt von Daniel Grün
presented by

aus Filderstadt
from

München, 11. März 2015

1st Evaluator: Prof. Dr. Ralf Bender
2nd Evaluator: Prof. Dr. Jochen Weller

Tag der mündlichen Prüfung: 8. Mai 2015

Zusammenfassung

Der Ursprung und die Entwicklung unseres Universums zeigt sich gleichermaßen in der Raumzeit selbst wie in den Strukturen, die in ihr entstehen. Galaxienhaufen sind das Ergebnis hierarchischer Strukturbildung. Sie sind die massivsten Objekte, die sich im heutigen Universum bilden konnten. Aufgrund dieser Eigenschaft ist ihre Anzahl und Struktur hochgradig abhängig von der Zusammensetzung und Evolution des Universums.

Die Messung der Anzahldichte von Galaxienhaufen beruht auf Katalogen, die nach einer beobachtbaren Größe ausgewählt werden. Die Anwendung einer Massen-Observablen-Relation (MOR) erlaubt es, die beobachtete Anzahl als Funktion der Observablen und der Rotverschiebung mit Vorhersagen zu vergleichen und so kosmologische Parameter zu bestimmen.

Man kann jedoch zu Recht behaupten, dass diese Messungen noch nicht präzise im Prozentbereich sind. Hauptgrund hierfür ist das unvollständige Verständnis der MOR. Ihre Normalisierung, die Skalierung der Observablen mit Masse und Rotverschiebung und die Größe und Korrelation von intrinsischen Streuungen muss bekannt sein, um Anzahldichten korrekt interpretieren zu können. Die Massenbestimmung von Galaxienhaufen durch die differenzielle Lichtablenkung in ihrem Gravitationsfeld, i.e. durch den so genannten schwachen Gravitationslinseneffekt (weak lensing), kann erheblich hierzu beitragen.

In dieser Arbeit werden neue Methoden und Ergebnisse solcher Untersuchungen vorgestellt. Zu ersteren gehören, als Teil der Datenaufbereitung, (i) die Korrektur von CCD-Bildern für nichtlineare Effekte durch die elektrischen Felder der angesammelten Ladungen (Kapitel 2, Gruen et al. 2015a) und (ii) eine Methode zur Maskierung von Artefakten in überlappenden Aufnahmen eines Himmelsbereichs durch Vergleich mit dem Median-Bild (Kapitel 3, Gruen et al. 2014a). Schließlich ist (iii) eine Methode zur Selektion von Hintergrundgalaxien, basierend auf deren Farbe und scheinbarer Magnitude, die eine neue Korrektur für die Kontamination durch Mitglieder des Galaxienhaufens einschließt, im Abschnitt 5.3.1 beschrieben.

Die wissenschaftlichen Hauptergebnisse sind die folgenden. (i) Für den Hubble Frontier Field-Haufen RXC J2248.7–4431 bestimmen wir Masse und Konzentration mittels weak lensing und bestätigen die durch Röntgen- und Sunyaev-Zel'dovich-Beobachtungen (SZ) vorhergesagte große Masse. Die Untersuchung von Haufengalaxien zeigt die Abhängigkeit von Morphologie und Leuchtkraft sowie Umgebung (Kapitel 4, Gruen et al. 2013). (ii) Unsere Massenbestimmung für 12 Galaxienhaufen ist konsistent mit Röntgenmassen, die unter Annahme hydrostatischen Gleichgewichts des heißen Gases gemacht wurden. Wir bestätigen die MOR, die für die Signifikanz der Detektion mit dem South Pole Telescope bestimmt wurde. Wir finden jedoch Diskrepanzen zur *Planck* SZ MOR. Unsere Vermutung ist, dass diese mit einer flacheren Steigung der MOR oder einem größen-, rotverschiebungs- oder rauschabhängigen Problem in der Signalextraktion zusammenhängt (Kapitel 5, Gruen et al. 2014b). (iii) Schließlich zeigen wir, durch die Verbindung von Simulationen und theoretischer Modellierung, dass die Variation von Dichteprofilen bei fester Masse signifikant zur Ungenauigkeit von Massenbestimmungen von Galaxienhaufen mittels weak lensing beiträgt. Ein Modell für diese Variationen, wie das hier entwickelte, ist daher wichtig für die genaue Bestimmung der MOR, wie sie für kommende Untersuchungen nötig sein wird (Kapitel 6, Gruen et al. 2015b).

Abstract

The story of the origin and evolution of our Universe is told, equivalently, by space-time itself and by the structures that grow inside of it. Clusters of galaxies are the frontier of bottom-up structure formation. They are the most massive objects to have collapsed at the present epoch. By that virtue, their abundance and structural parameters are highly sensitive to the composition and evolution of the Universe.

The most common probe of cluster cosmology, abundance, uses samples of clusters selected by some observable. Applying a mass-observable relation (MOR), cosmological parameters can be constrained by comparing the sample to predicted cluster abundances as a function of observable and redshift.

Arguably, however, cluster probes have not yet entered the era of per cent level precision cosmology. The primary reason for this is our imperfect understanding of the MORs. The overall normalization, the slope of mass vs. observable, the redshift evolution, and the degree and correlation of intrinsic scatters of observables at fixed mass have to be constrained for interpreting abundances correctly. Mass measurement of clusters by means of the differential deflection of light from background sources in their gravitational field, i.e. weak lensing, is a powerful approach for achieving this.

This thesis presents new methods for and scientific results of weak lensing measurements of clusters of galaxies. The former include, on the data reduction side, (i) the correction of CCD images for non-linear effects due to the electric fields of accumulated charges (Chapter 2, Gruen et al. 2015a) and (ii) a method for masking artifact features in sets of overlapping images of the sky by comparison to the median image (Chapter 3, Gruen et al. 2014a). Also, (iii) I develop a method for the selection of background galaxy samples based on their color and apparent magnitude that includes a new correction for contamination with cluster member galaxies (Section 5.3.1).

The main scientific results are the following. (i) For the Hubble Frontier Field cluster RXC J2248.7–4431 our lensing analysis constrains mass and concentration of the cluster halo and we confirm the large mass predicted by X-ray and Sunyaev-Zel'dovich (SZ) observations. The study of cluster members shows the relation of galaxy morphology to luminosity and environment (Chapter 4, Gruen et al. 2013). (ii) Our lensing mass measurements for 12 clusters are consistent with X-ray masses derived under the assumption of hydrostatic equilibrium of the intra-cluster gas. We confirm the MORs derived by the South Pole Telescope collaboration for the detection significance of the cluster SZ signal in their survey. We find discrepancies, however, with the *Planck* SZ MOR. We hypothesize that these are related either to a shallower slope of the MOR or a size, redshift or noise dependent bias in SZ signal extraction (Chapter 5, Gruen et al. 2014b). (iii) Finally, using a combination of simulations and theoretical models for the variation of cluster profiles at fixed mass, we find that the latter is a significant contribution to the uncertainty of cluster lensing mass measurements. A cosmic variance model, such as the one we develop, is necessary for MOR constraints to be accurate at the level required for future surveys (Chapter 6, Gruen et al. 2015b).

Contents

Zusammenfassung **vii**

Abstract **ix**

Contents **xi**

1 Introduction **1**
1.1 The onset: Homogeneous universe . . . 3
1.1.1 General Relativity . . . 3
1.1.2 Metric and expansion of a homogeneous universe . . . 4
1.2 The rise: Structures in the universe . . . 9
1.2.1 Linear growth of structures . . . 9
1.2.2 Collapse of structures . . . 12
1.2.3 Clusters of galaxies . . . 15
1.2.4 Gravitational lensing . . . 19
1.3 The finale: Observing the Universe . . . 26
1.4 Closing the loop: Cosmological constraints . . . 31

2 Charge-induced pixel shifts in DECam **35**
2.1 Introduction . . . 36
2.2 Brighter/fatter effect in DECam . . . 37
2.3 Model . . . 39
2.3.1 A priori symmetries . . . 40
2.3.2 Flat field covariances . . . 40
2.3.3 Assumed model symmetries . . . 45
2.3.4 Fitting of coefficients . . . 47
2.4 Effects on galaxy shape measurement . . . 48
2.5 Correction on pixel-level basis . . . 51
2.6 Summary . . . 52

3 Image artifact removal through clipped stacking **57**
3.1 Introduction . . . 58
3.2 Method . . . 60
3.2.1 Spatial filtering of outliers . . . 61

3.3 Properties of the stack . . . 65
3.3.1 Noise . . . 67
3.3.2 Point spread function . . . 67
3.4 Application to astronomical images . . . 69
3.4.1 Simulations . . . 69
3.4.2 Example images . . . 71
3.5 Download and application . . . 72
3.5.1 Implementation . . . 72
3.5.2 Practical use . . . 74
3.6 Summary . . . 75

4 Weak lensing analysis of RXC J2248.7–4431 77
4.1 Introduction . . . 78
4.2 Observations and data reduction . . . 79
4.3 Previous work on RXC J2248.7–4431 . . . 81
4.4 Photometric analysis . . . 82
4.4.1 Photometric redshifts . . . 82
4.4.2 Cluster member SEDs . . . 83
4.4.3 Mass from richness and luminosity . . . 85
4.5 Weak lensing measurement . . . 86
4.5.1 Model of the point spread function . . . 86
4.5.2 Shape Measurement . . . 88
4.5.3 Noise bias calibration . . . 89
4.6 Weak Lensing Analysis . . . 91
4.6.1 Introduction . . . 91
4.6.2 Tangential alignment . . . 92
4.6.3 Significance map . . . 92
4.6.4 Mass density map . . . 93
4.6.5 NFW model . . . 93
4.7 On the hypothesis of a recent merger in RXC J2248.7–4431 . . . 96
4.7.1 Galaxy number density . . . 97
4.7.2 Galaxy SEDs . . . 97
4.7.3 Centroid offsets . . . 97
4.7.4 Discrepancy between lensing and other mass estimates . . . 99
4.7.5 Influence of neighbouring structures on lensing mass . . . 99
4.8 Secondary cluster at $z \approx 0.6$ . . . 100
4.9 Conclusions . . . 100

5 Weak lensing analysis of SZ-selected clusters from SPT and Planck 103
5.1 Introduction . . . 104
5.1.1 Calibration of the SZ mass-observable relation . . . 105
5.2 Sample and data . . . 106
5.2.1 Data reduction and photometry . . . 107
5.3 Background selection . . . 109
5.3.1 β from limited photometric information . . . 109
5.4 Weak lensing analysis . . . 119
5.4.1 Model of the point spread function . . . 120

5.4.2 Shape measurement . . . 121
5.4.3 Correction of shape measurement bias . . . 122
5.4.4 Mass mapping . . . 123
5.4.5 Mass measurement . . . 124
5.5 Sunyaev-Zel'dovich catalogues . . . 126
5.5.1 South Pole Telescope . . . 127
5.5.2 *Planck* . . . 127
5.6 Individual cluster analysis . . . 131
5.6.1 SPT-CL J0509–5342 . . . 132
5.6.2 SPT-CL J0551–5709 . . . 135
5.6.3 SPT-CL J2332–5358 . . . 138
5.6.4 SPT-CL J2355–5056 . . . 140
5.6.5 PLCKESZ G287.0+32.9 . . . 143
5.6.6 PLCKESZ G292.5+22.0 . . . 145
5.6.7 MACS J0416.1–2403 . . . 148
5.6.8 SPT-CL J2248–4431 . . . 151
5.6.9 PSZ1 G168.02–59.95 . . . 152
5.6.10 PSZ1 G230.73+27.70 . . . 154
5.6.11 PSZ1 G099.84+58.45 . . . 156
5.6.12 PSZ1 G099.48+55.62 . . . 159
5.7 Combined analysis . . . 161
5.7.1 Comparison of X-ray and weak lensing mass estimates . . . 161
5.7.2 Comparison of SZ signal and mass . . . 164
5.7.3 Hypothesis tests . . . 167
5.7.4 Planck redshift dependence . . . 168
5.7.5 Centring and shear . . . 170
5.8 Conclusions . . . 171

6 Cosmic variance of cluster weak lensing 177
6.1 Introduction . . . 178
6.2 Simulations . . . 180
6.3 Model definition . . . 181
6.3.1 Mean profile . . . 181
6.3.2 Components of profile covariance . . . 183
6.3.3 Covariance estimation . . . 189
6.4 Determination of covariance model parameters . . . 190
6.4.1 Results . . . 191
6.4.2 Redshift dependence . . . 191
6.5 Effect on weak lensing cluster surveys . . . 192
6.5.1 Mass confidence intervals . . . 193
6.5.2 Mass-observable relations . . . 197
6.6 Conclusions . . . 198

7 Summary 201
7.1 Systematic improvements for lensing measurements . . . 201
7.2 Lensing calibration of cluster MORs . . . 202
7.3 Alternative structure probes . . . 203

Bibliography **205**

Curriculum Vitæ **231**

Publications **233**

Acknowledgements **235**

Chapter 1

Introduction

It seems a bit of a stretch: both to proclaim that William Blake's famous line should in any way be an augury of observational cosmology; and to actually connect the origin and structure of the Universe as a whole with the microscopic processes in the silicon of a detector *to*, quite literally, *see a world in a grain of sand*. Yet beauty, as Blake might have agreed, lies in the fact that there indeed exists a thread of cause, and of reason, between these seemingly disparate physical regimes. The story of the Universe, if that may ever be done, must be told as one.

In this thesis, I intend to follow that thread along part of its way. The combined purpose of the five projects described herein is to enable us to learn about the Universe from observations of clusters of galaxies. Clusters are the final stage of structure formation. They have accumulated and virialized matter on scales of Megaparsecs and several 10^{14} solar masses ($M_\odot$). How many of these largest structures get to form in a given volume most sensitively depends on small variations in the mean value, composition, and spatial variation of the matter density, and cosmic expansion. Clusters lie at an intersection of the two potentially most important unresolved questions of cosmology. Their mass content is dominated by *dark matter*, a pressureless component of the Universe that interacts almost exclusively by means of gravitation and outweighs ordinary (baryonic) matter by a factor of five. Their formation and evolution is strongly influenced by the interplay of matter and *dark energy*, the dominant component of the energy density at the present epoch that causes the acceleration of the expansion of the Universe. For this reason, the research field of cluster cosmology has developed from the idea of using these objects as cosmological probes.

The main scientific results of this thesis, presented in Chapters 4, 5, and 6, are directly related to that goal. These projects all center on using the distortion of background galaxy images due to differential gravitational deflection of their light by the foreground matter of clusters (weak gravitational lensing). The measurement of this effect, however, sensitively relies on proper treatment of observational data. Two novel methods for this purpose are therefore developed and described in Chapters 2 and 3.

In Chapter 2 (Gruen et al., 2015a), I characterize the self-interaction of charges in the CCD detectors of the Dark Energy Camera (DECam). Charges that accumulate in pixels in a CCD change the electric fields that newly generated photoelectrons encounter. This means that the response of the camera to the illumination of the sky is not, as one might hope, independent between pairs of pixels and linear in the count level. Two artifacts that arise

from this are (1) the correlation of Poisson noise between pairs of pixels and (2) the spreading of charges around bright stars. I use a model of charge dependent shifts of pixel borders to describe both in the DECam CCDs and show that the effect can be reversed during data processing to recover images largely free from the named artifacts.

Chapter 3 (Gruen et al., 2014a) implements a method of removing unwanted features in astronomical images, such as cosmic ray and satellite tracks or diffuse secondary images of bright stars. The method is based on comparing single images of the sky to the median of a large number of frames and masking regions of increased outlier density. One important point is the comparative robustness towards variation in image quality, i.e. different blurring of images taken under different observational conditions.

I describe a detailed analysis of one particularly interesting cluster of galaxies, RXC J2248.7–4431, in Chapter 4 (Gruen et al., 2013). The X-ray radiation emitted by hot gas in the halo of RXC J2248.7–4431 is among the brightest of all clusters in the Universe, indicating that the system is a very massive object. This and the fact that numerous strong lensing features of multiply-imaged background galaxies are observed have led to the selection of the cluster as part of two deep surveys with the Hubble Space Telescope. Using the MPG/ESO 2.2m Telescope, we have taken deep wide-field images of the cluster in six filter bands. I use this data to study the colors and the spatial distribution of cluster member galaxies, particularly in view of indications for a recent merger from X-ray observations. By analyzing the gravitational distortion of background galaxies due to weak lensing, I constrain the cluster mass as $M_{200m} = 33.1^{+9.6}_{-6.8} \times 10^{14} h_{72}^{-1} M_\odot$ at a concentration of $c_{200m} = 2.6^{+1.5}_{-1.0}$.

Clusters of galaxies like RXC J2248.7-4431 are interesting research subjects in their own right. Yet their cosmological potential is exploited best when large samples are considered. This is most commonly done by selecting clusters based on either their galaxy population detected in large photometric surveys or on signatures of the hot intra-cluster gas. The latter consist of (1) X-ray bremsstrahlung or (2) a distortion of the spectrum of cosmic microwave photons traversing the hot gas due to inverse Compton scattering, the Sunyaev-Zel'dovich (SZ) effect. For comparing observed samples to theoretical predictions as a function of cosmological parameters, these observables have to be related to cluster mass. One promising way of doing this is by calibrating a mass-observable relation (MOR) with weak lensing measurements of a subsample of the selected clusters.

The latter is what is done in Chapter 5 (Gruen et al., 2014b), where I present the weak lensing analysis of a sample of 12 clusters of galaxies selected for their signature in SZ surveys. To this end, I develop an improved method for background selection and determination of geometric lensing scaling factors from multi-band photometry in the vicinity of clusters. I then compare the weak lensing mass estimate with public X-ray and SZ observations. The lensing measurements are consistent with X-ray masses derived under the assumption of hydrostatic equilibrium of the hot cluster gas with no significant mean bias or mass dependent bias and an intrinsic scatter of less than 20%. The ratio of X-ray gas mass to lensing mass is constrained as $f_{\mathrm{gas},500c} = 0.128^{+0.029}_{-0.023}$, in consistency with literature values. I calibrate the South Pole Telescope significance-mass relation and find consistency with previous results based on survey simulations or X-ray based calibrations. The comparison of weak lensing mass and Planck SZ measurements, however, shows significant discrepancies. The deviations from the fiducial MOR calibrated by the Planck collaboration with X-ray observations of a subset of clusters strongly correlate with cluster mass and redshift. This could be explained either by a significantly shallower than expected slope of SZ observable versus mass and a corresponding problem in the previous X-ray based mass calibration, or a size, redshift or

noise dependent bias in SZ signal extraction.

Weak lensing calibration of MORs depends on also knowing the uncertainty of lensing mass measurements. This is particularly important when the intrinsic scatter of other observables at fixed mass should be determined with lensing. Chapter 6 (Gruen et al., 2015b) focuses on one reason for scatter in lensing mass measurements that had previously been mostly neglected: intrinsic variations of the projected density profiles of clusters of galaxies at fixed mass. I present a semi-analytical model to account for this effect, based on a combination of variations in halo concentration, ellipticity, and orientation, and the presence of correlated haloes. The model is calibrated with simulations to match the empirical cosmic variance of cluster profiles at $M_{200m} \approx 10^{14} \ldots 10^{15} h^{-1} M_\odot$ in the redshift range $z = 0.25 \ldots 0.5$. If intrinsic profile variations are ignored, uncertainties in lensing mass measurements are significantly underestimated (with ≈ 20 per cent uncertainty from cosmic variance alone at $M_{200m} \approx 10^{15} h^{-1} M_\odot$ and $z = 0.25$). The model can be used to provide correct mass likelihoods. Neglecting intrinsic profile variations leads to biases in the MOR constrained with weak lensing, both for intrinsic scatter and overall scale (the latter at the 15 per cent level). These biases are in excess of the statistical errors of upcoming surveys and can be avoided if the cosmic variance of cluster profiles is accounted for.

Each of the five substantial chapters is intended to be self-contained in the sense that all formalism and notation used is introduced and/or referenced explicitly. A brief introduction, including a description of the contributions of the respective co-authors, is given at the beginning of each chapter. In the remaining sections of this first chapter, I introduce some concepts that are relevant for the projects described subsequently. As a guiding principle, I use the connecting threat of photons traversing the Universe.

1.1 The onset: Homogeneous universe

Not how the world is, is the mystical, as a positivist would put it, *but that it is* (Wittgenstein, 1922, 6.44). We do not unambiguously know why and how we got to a Universe filled with a hot plasma of photons and particles, although abductive reasoning has it that it was through an inflationary phase of exponential expansion. *What can be said* is connected to the longest story a photon could tell us today. Although it relates to what happened before that, this story begins when the Universe had roughly one part in a billion of its present volume – and therefore had a billion times its present matter density. At this point of *re-combination*, the Universe had cooled down enough for protons and electrons to form Hydrogen atoms. Photons could then travel through space freely enough to be detected today, mostly without any further scattering in between, constituting the *cosmic microwave background* (CMB). We will follow one such photon on its way from the last scattering through the aging Universe.

1.1.1 General Relativity

The path our photon follows is a *null geodesic*, i.e. its space-time coordinates $(x^0 = t, x^{1,2,3})$ fulfill

$$\mathrm{d}s^2 = c^2 \mathrm{d}\tau^2 = \sum_{i,j=0}^{3} g_{ij} \mathrm{d}x^i \mathrm{d}x^j = 0 \,, \tag{1.1}$$

where the metric tensor g_{ij} defines the line element $\mathrm{d}s$ and the differential proper time $\mathrm{d}\tau$ measured by a co-moving clock.[1] The metric tensor is related to the content of the universe, according to General Relativity (GR), by means of Einstein's field equations (Einstein, 1915),

$$R_{ij} - \frac{1}{2} g_{ij} R - \Lambda g_{ij} = \frac{8\pi G}{c^4} T_{ij} \ , \tag{1.2}$$

where G is Newton's constant, c is the speed of light and Λ is, for the time being, an arbitrary constant. The left-hand side of Eqn. 1.2 is a short-hand notation of a differential expression of g_{ij}. It uses the Ricci tensor R_{ij}, defined as (cf. Peebles, 1993, Eqn. 8.82)

$$R_{ij} = \frac{\partial(\Gamma^k_{ij})}{\partial x^k} - \frac{\partial(\Gamma^k_{ik})}{\partial x^j} + \Gamma^k_{nk}\Gamma^n_{ij} - \Gamma^k_{jn}\Gamma^n_{ik} \tag{1.3}$$

from the Christoffel symbols (cf. Peebles, 1993, Eqn. 8.57)

$$\Gamma_{kij} = g_{kl}\Gamma^l_{ij} = \frac{1}{2}\left(\frac{\partial g_{ki}}{\partial x^j} + \frac{\partial g_{ki}}{\partial x^i} - \frac{\partial g_{ij}}{\partial x^k}\right) \ . \tag{1.4}$$

The scalar curvature R is constructed from the Ricci tensor as (cf. Peebles, 1993, Eqn. 8.83)

$$R = g^{ij} R_{ij} \ , \tag{1.5}$$

with the inverse metric tensor g^{ij} defined such that

$$g^{ij} g_{jk} = \begin{cases} 1 & i = k \\ 0 & i \neq k \end{cases} \ . \tag{1.6}$$

The right-hand side of Eqn. 1.2 is the stress-energy tensor T. For an ideal fluid of energy density ρ and pressure p that moves through space-time with four-velocity $u^i = \frac{\mathrm{d}x^i}{\mathrm{d}\tau}$ (cf. Peebles, 1993, 10.49),

$$T^{ij} = \left(\rho + \frac{p}{c^2}\right) u^i u^j - g^{ij} p \ . \tag{1.7}$$

1.1.2 Metric and expansion of a homogeneous universe

To see the world as our photon finds it, let us consider the metric on very large scales. Here, assuming the *cosmological principle*, we can take space-time to be isotropic and homogeneous. Friedmann (1922), Lemaître (1933), Robertson (1935), and Walker (1937) showed independently that the most general line element in concordance with this principle can be written as (cf. Peebles, 1993, Eqn. 5.9)

$$\mathrm{d}s^2 = c^2 \mathrm{d}t^2 - a^2(t) \left[\mathrm{d}r^2 + f_K^2(r)(\mathrm{d}\theta^2 + \sin^2\theta \mathrm{d}\phi^2)\right] \ . \tag{1.8}$$

The three dimensional space described by the spherical coordinate system (r, θ, ϕ) is Euclidean, closed with positive curvature, or open with negative curvature, with the function

$$f_K(r) = \begin{cases} r, & K = 0 \\ 1/K \sin(Kr), & K > 0 \\ 1/|K| \sinh(|K|r), & K < 0 \end{cases} \ . \tag{1.9}$$

[1] In the following, we will imply summation over indices appearing twice as in Eqn. 1.1 according to the Einstein summation convention.

We have defined K such that for curved spaces the radius of curvature is $|K|^{-1}$.

The dimensionless scale factor $a(t)$ allows for homogeneous expansion or contraction of that space over time. Changes in a correspond to a re-scaling of the physical distances between objects in the universe. The metric of the actual Universe is a solution to Einstein's equations 1.2. Friedmann (1922, 1924) was the first to derive the time dependence of $a(t)$, for which we give a brief derivation here, following Peebles (1993, p. 63, p. 75).

Consider a fluid, described at a point by its pressure p, (energy) density ρ, and velocity. By a suitable Lorentz transformation, we can find a local coordinate frame at that point with a Minkowski metric

$$g_{ij} = \begin{bmatrix} c^2 & 0 & 0 & 0 \\ 0 & -1 & 0 & 0 \\ 0 & 0 & -1 & 0 \\ 0 & 0 & 0 & -1 \end{bmatrix} , \tag{1.10}$$

in which the fluid is instantaneously at rest, i.e. $u = (1, 0, 0, 0)$. Its stress energy tensor is then diagonal with $(T_{00}, T_{11/22/33}) = (\rho, p)$.

For a moment, set $\Lambda = 0$ and consider Eqn. 1.2 as an analog of the Poisson equation of Newtonian gravitation,

$$\boldsymbol{\nabla}^2 \Phi = -\boldsymbol{\nabla} \cdot \boldsymbol{g} = 4\pi G \rho \, , \tag{1.11}$$

where $\boldsymbol{g}$ is the gravitational acceleration of a test particle and Φ is the gravitational potential. For a general fluid in general relativity, both its rest mass and the energy contained in its pressure gravitate and appear on the right-hand side of Einstein's equations (cf. Eqn. 1.7). This replaces the source of the gravitational field ρ by an effective gravitating density

$$\rho_g = \rho + \frac{3p}{c^2} \, . \tag{1.12}$$

The gravitational acceleration on a surface of a sphere of radius R is

$$\ddot{R} = -\frac{GM_g}{R^2} = -\frac{4}{3}\pi G \left(\rho + \frac{3p}{c^2} \right) R \, . \tag{1.13}$$

Here the source of gravitation, i.e. the enclosed effective mass of the sphere M_g, has again been expressed by the effective gravitating density of Eqn. 1.12 times the volume. If this acceleration corresponds to the expansion of a universe that is homogeneous and isotropic, then a physical distance between two points $R(t)$ will scale as $R(t) = R_0 a(t)$. Division by R_0 yields the *acceleration equation* of cosmic expansion (cf. Peebles, 1993, Eqn. 5.15),

$$\frac{\ddot{a}}{a} = -\frac{4}{3}\pi G \left(\rho + \frac{3p}{c^2} \right) \, . \tag{1.14}$$

Now, consider a sphere of volume $V = \frac{4}{3}\pi R^3$, filled by our homogeneous fluid. The energy inside the sphere, based on the rest energy of the fluid, is

$$U = Mc^2 = \rho V c^2 \, . \tag{1.15}$$

The change in energy when the sphere expands by $\mathrm{d}V$ is given either by the differential of the above equation or the work done by the pressure, thus

$$\mathrm{d}U = (\rho \, \mathrm{d}V + V \, \mathrm{d}\rho) c^2 = p \, \mathrm{d}V \, . \tag{1.16}$$

Dividing by dt and using $\dot{V} = 4\pi R^2 \dot{R}$, we find the *energy equation* (cf. Peebles, 1993, Eqn. 5.16)

$$\dot{\rho} = -3\left(\rho + \frac{p}{c^2}\right)\frac{\dot{a}}{a} \ . \tag{1.17}$$

Assume that the fluid has an equation of state of the form

$$p = w\rho c^2 \tag{1.18}$$

to re-write Eqn. 1.17 as

$$\dot{\rho} = -3\rho\,(1+w)\,\frac{\dot{a}}{a} \ , \tag{1.19}$$

which is solved by

$$\rho(t) = \rho_0 a^{-3(1+w)}(t) \ . \tag{1.20}$$

We see that normal matter (pressureless, i.e. $w = 0$) is diluted as a^{-3} as expected. The energy density of fluids with considerable pressure ($w > 0$), such as relativistic particles, is diluted by the expansion more strongly. This is due to the loss of momentum, which is a significant contribution to the total energy.

The equation of state 1.18 can be used to eliminate p from the acceleration equation 1.14 to yield

$$\frac{\ddot{a}}{a} = -\frac{4}{3}\pi G\rho(1+3w) \ , \tag{1.21}$$

which shows that all fluids with $w < -\frac{1}{3}$ accelerate the expansion (and all with larger pressure decelerate it).

We multiply both sides of Eqn. 1.21 by $2a\dot{a}$ and apply Eqn. 1.20 to express the time dependence of ρ by means of a,

$$2\dot{a}\ddot{a} = -\frac{8}{3}\pi G\rho_0(1+3w)\frac{\dot{a}}{a^{2+3w}} \ . \tag{1.22}$$

Noting that

$$2\dot{a}\ddot{a} = \frac{\mathrm{d}}{\mathrm{d}t}\left(\dot{a}^2\right) \quad \text{and} \quad (1+3w)\frac{\dot{a}}{a^{2+3w}} = -\frac{\mathrm{d}}{\mathrm{d}t}\left[a^{-(1+3w)}\right] \ , \tag{1.23}$$

we integrate Eqn. 1.22 over time to find the *Friedmann equation*

$$H^2 := \left(\frac{\dot{a}}{a}\right)^2 = \frac{8}{3}\pi G\rho - \frac{K|K|c^2}{a^2} \ , \tag{1.24}$$

with an integration constant $\frac{K|K|c^2}{a^2}$ that corresponds to a curvature of space-time as described by Eqns. 1.8 and 1.9 (as could be seen by deriving Eqn. 1.24 from inserting Eqn. 1.8 into Eqns. 1.2).

The derivation of Eqns. 1.14 and 1.24 was done for a single fluid and $\Lambda = 0$. Since the Einstein equations 1.2 are linear in the stress-energy tensor, the effects of multiple components, such as non-relativistic matter ($w = 0$) and radiation or ultra-relativistic matter ($w = 1/3$), are simply linearly combined. Likewise, a non-zero cosmological constant term Λg_{ij} in the metric of Eqn. 1.10, if brought to the right-hand side, represents a fluid with negative pressure ($w = -1$), which can be treated in the same way.[2] A more general dark energy component with negative pressure but $w \neq -1$ is also imaginable.

[2] This is a good example of Poincaré's concept of conventionalism, i.e. the inter-relation and arbitrariness of conventions in the laws of physics and geometry (Poincaré, 1905).

We can rewrite the matter density ρ_m, radiation density ρ_r, cosmological constant Λ, and curvature in terms of the critical density that fulfills Eqn. 1.24 for $K = 0$ and $\Lambda = 0$ at the present value H_0 of H,

$$\rho_\mathrm{c} = \frac{3H_0^2}{8\pi G} \,. \tag{1.25}$$

With the ratios

$$\Omega_\mathrm{m} = \frac{\rho_\mathrm{m}}{\rho_\mathrm{c}} \qquad \Omega_\mathrm{r} = \frac{\rho_\mathrm{r}}{\rho_\mathrm{c}} \tag{1.26}$$

$$\Omega_\Lambda = \frac{\Lambda c^2}{8\pi G \rho_\mathrm{c}} \tag{1.27}$$

and

$$\Omega_\mathrm{k} = 1 - \Omega_\mathrm{m} - \Omega_\mathrm{r} - \Omega_\Lambda \tag{1.28}$$

we can write the Friedmann equation 1.24 in the form

$$H^2(t) = H_0^2 \left(\Omega_{r,0} a^{-4}(t) + \Omega_{m,0} a^{-3}(t) + \Omega_{k,0} a^{-2}(t) + \Omega_{\Lambda,0}\right) =: H_0^2 E^2(a) \,. \tag{1.29}$$

The subscript 0 denotes values at the present epoch ($a_0 := 1$). It is useful to define a dimensionless parameter

$$h = H_0 / \left[100\mathrm{kms}^{-1}\mathrm{Mpc}^{-1}\right] \tag{1.30}$$

or, more generally, $h_X = H_0 / \left[X\mathrm{kms}^{-1}\mathrm{Mpc}^{-1}\right]$, in order to express the propagation of our uncertainty about the value of H_0 into numerical values for other cosmological measurements (cf. Croton, 2013).

It is instructive to imagine what happens to our photon, or pairs of photons, as the Universe evolves. The expansion of space (i.e. an increase in a) causes a proportional expansion of the photon wavelength. Equivalently, the momentum and energy of the photon decrease as a^{-1}. This, in addition to dilution of photons with a^{-3}, leads to an evolution of energy density with a^{-4} (i.e. $w = 1/3$ for ultra-relativistic fluids in Eqn. 1.20). If our photons were drawn from a thermal (Planck) distribution at temperature T, the combined effect of wavelength change and dilution is equivalent to a change in temperature as $T \propto a^{-1}$.

Redshift and distance

The story of our photon implies different notions of *distance* between two points A and B in the expanding universe. From the time t_A, $a_A = a(t_A)$ our photon is emitted at or passes a point A with wavelength λ_A until it reaches B at time t_B, $a_B = a(t_B)$, the scale factor of the universe changes. Correspondingly, the wavelength change of the photon defines a *(cosmological) redshift* z_{AB},

$$z_{AB} = \frac{\lambda_B}{\lambda_A} - 1 = \frac{a_B}{a_A} - 1 \,. \tag{1.31}$$

For observation at the present epoch, $a_B = a_0 = 1$, $t_B = t_0$ and $1 + z_A = 1/a_A$.

We can define the *comoving distance* χ, i.e. the distance between us and a point A in the static (r, θ, ϕ) coordinate system of Eqn. 1.8, by considering the proper length of the differential photon path ($c\,\mathrm{d}t$) re-scaled by $a(t)$. Since

$$\mathrm{d}t = \frac{\mathrm{d}t}{\mathrm{d}a}\mathrm{d}a = \frac{\mathrm{d}a}{Ha} = -\frac{a\mathrm{d}z}{H(z)} \,, \tag{1.32}$$

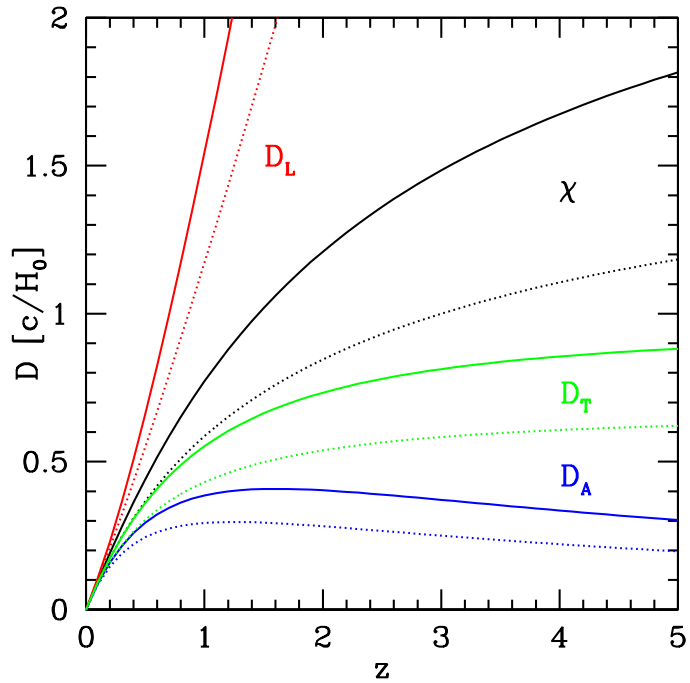

Figure 1.1: Comoving distance (black, Eqn. 1.33), angular diameter distance (blue, Eqn. 1.35), luminosity distance (red, Eqn. 1.37), and look-back distance (green, Eqn. 1.39) for an Einstein-de Sitter (dotted line) and realistic ($\Omega_{m,0} = 0.3$, $\Omega_{\Lambda,0} = 0.7$, solid line) universe.

we can integrate the differential as (cf. Hogg, 1999, Eqn. 15)

$$\chi(z_A, z_B) = \int_{\chi(z_A)}^{\chi(z_B)} \mathrm{d}\chi = \int_{t_B}^{t_A} \frac{c\,\mathrm{d}t}{a(t)} = \frac{c}{H_0} \int_{z_A}^{z_B} \frac{\mathrm{d}z'}{E(z')} \,. \tag{1.33}$$

For a flat universe ($\Omega_k = 0$), $\chi(z) := \chi(0, z)$ also relates the differential angle $\mathrm{d}\theta$ between two photons emitted at the same redshift towards an observer at $z = 0$ to the (transverse) comoving distance between their origins. We see from Eqns. 1.8 and 1.9 that the circumference of a redshift shell is modified by f_K in the non-flat case. Consequently, the transverse comoving distance is (cf. Hogg, 1999, Eqn. 16)

$$\chi_T(z) = f_K[\chi(z)] \,. \tag{1.34}$$

Re-scaling χ_T by the scale factor, we find the *angular diameter distance* that relates $\mathrm{d}\theta$ to the physical distance $\mathrm{d}\eta$ between the origin of the two photons at the time of their emission,

$$D_A = a\chi_T = \frac{\mathrm{d}\eta}{\mathrm{d}\theta} \,. \tag{1.35}$$

In a flat universe (i.e., when $\chi_T = \chi$), this is also interpretable as the proper distance between source and receiver at the time of emission.

We define the *luminosity distance* D_L as the radius of a shell in static Euclidean space on which the flux F received from an object of given luminosity L (both defined bolometrically) would be the same as observed in the expanding universe,

$$L = 4\pi F D_L^2 \,. \tag{1.36}$$

Due to the reduction of an object's solid angle by D_A^{-2} and the dilution of photon energy density by a^{-4},

$$D_L = a^{-2} D_A = (1+z)^2 D_A \ . \tag{1.37}$$

For the purpose of completeness, we define the *look-back time* or equivalently, look-back distance D_T physically traveled by the photon. In a small time interval $\mathrm{d}t$ the physical photon path is, using Eqn. 1.32,

$$\mathrm{d}D_T = c\mathrm{d}t = -\frac{c\,\mathrm{d}z}{(1+z)H(z)} \ . \tag{1.38}$$

Thus

$$D_T(z) = \frac{c}{H_0} \int_0^z \frac{\mathrm{d}z'}{(1+z')E(z')} \ . \tag{1.39}$$

Figure 1.1 shows these definitions of distances plotted as a function of redshift for a flat matter only (Einstein-de Sitter) case and a likely set of parameters for our actual Universe. Notably, the angular diameter distance decreases at large redshift. This can be understood by considering the lower physical circumference of the observed shell of an expanding universe. The rapid increase of the luminosity distance makes observations of objects at large redshift extremely difficult.

1.2 The rise: Structures in the universe

Minute initial perturbations of the homogeneous density were amplified to build the large structures that we find in the world today. It almost seems, to paraphrase what Chekhov lets his Misail Poloznev confess, *that nothing ever passes without trace.* The force that this is due to, in the realm of cosmology, is gravity.

Structures in the Universe are the subject of the main scientific projects of this thesis, described in Chapters 4, 5, and 6. The primary method applied there, cluster weak lensing, uses photons that are generated in stars of background galaxies. The distortion of their paths due to intervening large structures along the line of sight allows us to learn about the properties of the latter. In this section, I describe the basic principles of the rise of structures, the properties of clusters of galaxies as the end product of this process, and the deflection of photon paths in the gravitational field.

1.2.1 Linear growth of structures

When our photon started out, the Universe was not entirely homogeneous. Rather, small relative differences in density and temperature of the order 10^{-5} existed. Consider such a density perturbation, described in terms of the density contrast δ

$$\delta(\boldsymbol{\chi}) = \frac{\rho(\boldsymbol{\chi})}{\langle\rho\rangle} - 1 \ , \tag{1.40}$$

where $\boldsymbol{\chi}$ is a parametrization of the comoving coordinate system (r, θ, ϕ) of Eqn. 1.8. Equivalently, we could write the δ field in terms of its Fourier representation (cf. Coles & Lucchin, 2002, Eqn. 13.2.3)

$$\delta_{\boldsymbol{k}} = \frac{1}{V} \int_V \delta(\boldsymbol{\chi}) \exp(-i\boldsymbol{k}\cdot\boldsymbol{\chi})\, \mathrm{d}^3\boldsymbol{\chi} \ . \tag{1.41}$$

For an infinite space, this is problematic, which is why we used a large finite volume V instead to arrive at the same conclusions. The expectation value of $\delta_{\boldsymbol{k}}$ is zero for any such volume and vector $\boldsymbol{k}$. But there will be a variance in $|\delta_{\boldsymbol{k}}|$ between the different realizations, which defines the *power spectrum*

$$P(k) = \langle |\delta_{\boldsymbol{k}}|^2 \rangle_{|\boldsymbol{k}|=k} \ . \tag{1.42}$$

If δ is a Gaussian random field, as it appears to be the case in our Universe (e.g. Planck Collaboration et al., 2015a), then different Fourier modes are chosen independently from a Gaussian distribution. The power spectrum then contains the full information about the field.

This information can be equivalently expressed as a *two-point correlation function* of density contrast,

$$\xi(r) = \langle \langle \delta(\boldsymbol{x}) \delta(\boldsymbol{x} + \boldsymbol{r}) \rangle_{\boldsymbol{x}} \rangle_{|\boldsymbol{r}|=r} = \frac{V}{(2\pi)^3} \int P(k) e^{-i\boldsymbol{k}\cdot\boldsymbol{r}} \mathrm{d}^3\boldsymbol{k} \ . \tag{1.43}$$

The average in the above expression is meant to be taken over all locations $\boldsymbol{x}$ and all vectors $\boldsymbol{r}$ with length r.

The power spectrum (cf. Fig. 1.2) had some primordial shape, which was modified as radiation and other relativistic species smeared out small-scale modes that entered the horizon. This order of events is expressed by the ansatz

$$P(k, z = 0) = T^2(k) A \, k^{n_s} \ , \tag{1.44}$$

where the primordial spectrum is assumed to be a power-law with amplitude A and scalar spectral index n_s. The amplitude is often alternatively expressed in terms of σ_8, the variance of the matter field when averaged over a sphere of $8h^{-1}$ Mpc radius. A value of n_s close to unity is predicted by inflationary models (e.g. Mukhanov & Chibisov, 1981). It corresponds to a scale-invariant spectrum of fluctuations of the gravitational potential Φ due to the rapid expansion of fluctuations to all observable scales.[3]

The *transfer function* $T(k)$ describes the effect of the early photon-baryon plasma on density fluctuations and is modeled, e.g., by Eisenstein & Hu (1998). For scales of the order of (or larger than) the horizon at matter-radiation equality no damping occurs, and thus $T(k) \to 1$. For large k and a pressureless matter component, $T(k) \propto k^{-2}$ (cf. Mo et al., 2010, their Section 4.3). In addition, the transfer function contains features from sound waves that oscillated in the plasma.

What happens to the density fluctuation over time after radiation is subdominant and the universe can be described as a pressureless fluid of matter? Combining conservation of energy (i.e., mass) as δ varies in time and follows convergent or divergent flows (the continuity equation), conservation of momentum in the flowing density field (the Euler equation, assuming no pressure), and the gravitational potential introduced by the matter density (via the Poisson equation) in an expanding universe, one can derive the time evolution of δ as (cf. Peebles, 1993, Eqns. 5.94-5.111)

$$\frac{\partial^2 \delta}{\delta t^2} + 2 \frac{\dot{a}}{a} \frac{\partial \delta}{\partial t} = 4\pi G \langle \rho \rangle \delta \ . \tag{1.45}$$

As a second-order differential equation, this has two linearly independent solutions. One of these describes the decay, the other the growth of structures in time. If we look back

[3] Scale invariance means $k^3 P_\Phi$ =const. Since the Poisson equation in Fourier space implies $\delta \propto k^2 \Phi$, the power spectra relate as $P \propto k^4 P_\Phi \propto k$.

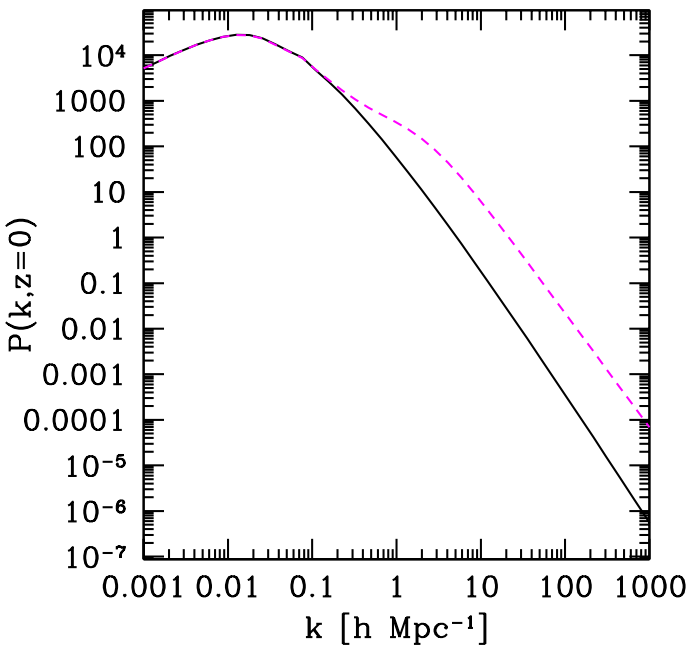

Figure 1.2: Matter power spectrum at $z = 0$. Black: linear power spectrum with (Eisenstein & Hu, 1998) transfer function; magenta/dashed: non-linear power spectrum from fitting formula of Smith et al. (2003).

(or forward) to a time where decaying structures had already virtually disappeared, we can ignore the decaying mode and write only the growing one as

$$\delta(\boldsymbol{\chi}, t) = D(t)\, \delta(\boldsymbol{\chi}, t_0) \ , \tag{1.46}$$

where t_0 is the present time and the *growth factor* D is normalized to $D(t_0) = 1$. The growth factor is calculated as a function of redshift as (e.g. Hamilton, 2001)

$$D(z) = \frac{5}{2}\, \Omega_{\mathrm{m}}\, E(z) \int_z^{\infty} \frac{1+z'}{E^3(z')}\, \mathrm{d}z' \ . \tag{1.47}$$

Note that since this linear growth influences δ independent of position, it also grows all Fourier modes δ_k equivalently, such that

$$P(k, z) = D^2(z)\, P(k, 0) \ . \tag{1.48}$$

As we shall see below, the linear approximation greatly underestimates the growth of structures on scales small enough to collapse. The actual matter power spectrum is therefore a modification of this corrected for non-linear evolution, given e.g. by the fitting formula of Smith et al. (2003). Figure 1.2 shows the linear and non-linear power spectrum for comparison. It can be seen that the k^{n_s} primordial trend is suppressed by the transfer function at scales smaller than ≈ 100 Mpc. At scales smaller than ≈ 5 Mpc, non-linear evolution begins to be significant. This is where we have to consider the effect of collapsed structures.

1.2.2 Collapse of structures

Things get more interesting as the above approximation for $\delta \ll 1$ ceases to be valid and dense structures form. When baryons fall into these collapsed structures, they get to form stellar systems or are bound in the form of gas. This is where the optical photons and the signatures of hot gas, which we'll be observing, come from. The following section therefore gives an overview of the process.

A simple but useful model for this process is to consider a sphere in an initial state i. Let all properties of this sphere be denoted by a $\sim$ superscript. Inside the sphere, assume that we find a constant overdensity $\tilde{\delta}_i$ relative to an Einstein-de Sitter ($\Omega_\mathrm{m} = \Omega_{m,i} = 1$) background universe that expands, initially, with H_i from a scale factor of $a_i = \tilde{a}_i$.

The Friedmann equation in the Einstein-de Sitter case is straightforwardly integrated to find (cf., e.g., Coles & Lucchin, 2002, Section 2.2)

$$a(t) = a_i \left(\frac{t}{t_i}\right)^{2/3} , \tag{1.49}$$

where $H_i = H(t_i) = \frac{\dot{a}}{a}\big|_{t=t_i}$ requires $t_i = \frac{2}{3H_i}$. Conservation of mass, $\rho a^3 = \text{const.}$ implies $\rho t^2 = \text{const.}$, thus we find

$$\rho(t) = \frac{\rho_{c,i} t_i^2}{t^2} = \frac{3H_i^2}{8\pi G}\frac{4}{9H_i^2}\frac{1}{t^2} = \frac{1}{6\pi G t^2} . \tag{1.50}$$

The perturbed sphere, since it is above the critical density, evolves like a closed universe of its own, with $\tilde{\Omega}_{m,i} = 1 + \tilde{\delta} > 1$. The Friedmann equation describing the expansion in terms of its scale factor $\tilde{a}$ becomes (cf. Coles & Lucchin, 2002, Eqn. 14.1.4)

$$\left(\frac{\dot{\tilde{a}}}{a_i}\right)^2 = H_i^2 \left[(1+\tilde{\delta}_i)\frac{a_i}{\tilde{a}} - \tilde{\delta}_i\right] , \tag{1.51}$$

where we have multiplied both sides by $(\tilde{a}/a_i)^2$. Since the metric of the overdense sphere is closed, $\tilde{a}$ reaches some maximum scale at time t_m before its radius starts to decrease. At that point, $\dot{\tilde{a}} = 0$, such that

$$\tilde{a}(t_m) = \frac{1+\tilde{\delta}_i}{\tilde{\delta}_i}\, a_i \tag{1.52}$$

and, since $\tilde{\rho}(t_i) = (1+\tilde{\delta}_i)\rho_\mathrm{c}(t_i)$,

$$\tilde{\rho}(t_m) = \rho_\mathrm{c}(t_i)\frac{\tilde{\delta}_i^3}{(1+\tilde{\delta}_i)^2} . \tag{1.53}$$

From the cycloid solution to the Friedmann equation in a closed, matter-dominated universe, one can find the time of turn-around as (cf. Coles & Lucchin, 2002, Section 2.4.2 and Eqn. 14.1.6)

$$t_m = \sqrt{\frac{3\pi}{32\, G\, \tilde{\rho}(t_m)}} . \tag{1.54}$$

The overdensity of the sphere at turn-around is given by inserting Eqn. 1.54 into 1.50 as

$$\tilde{\delta}_m = \frac{\tilde{\rho}(t_m)}{\rho(t_m)} - 1 = \left(\frac{3\pi}{4}\right)^2 - 1 \approx 4.6 . \tag{1.55}$$

As the sphere begins to shrink, its density increases until virial equilibrium is reached. The energy at turn-around is purely potential. For a homogeneous sphere of turn-around radius $\tilde{R}_m$,

$$\tilde{E}_m = -\frac{3}{5}\frac{G\tilde{M}^2}{\tilde{R}_m} \ . \tag{1.56}$$

This has to be equal to the total energy in the virial state, given by means of the virial theorem as half the potential energy of the smaller sphere or virial radius $\tilde{R}_{\rm vir}$,

$$\tilde{E}_v = -\frac{1}{2}\frac{3}{5}\frac{G\tilde{M}^2}{\tilde{R}_{\rm vir}} \ . \tag{1.57}$$

This implies $\tilde{R}_{\rm vir} = \frac{1}{2}\tilde{R}_m$, $\tilde{\rho}(t_{\rm vir}) = 8\tilde{\rho}(t_m)$. Assuming $t_{\rm vir} \approx 2t_m$ and continued matter domination of the background universe (i.e., $\rho(t) \propto t^{-2}$ according to Eqn. 1.50),

$$\delta_{\rm vir} = \frac{\tilde{\rho}(2t_m)}{\rho(2t_m)} - 1 = 2^2 \times 8 \times (\tilde{\delta}_m + 1) - 1 \approx 178 \ . \tag{1.58}$$

In a matter dominated universe, virialization thus occurs at matter overdensities of approximately 200. For this reason it is common to give properties of haloes in terms of the sphere inside which the overdensity relative to the mean matter density is 200, e.g. as the mass M_{200m} inside that sphere of radius r_{200m}.

The linear approximation is strongly violated in this regime: extrapolating linear growth to $t_{\rm vir}$ yields an overdensity of (cf., e.g. Peebles, 1993, Eqns. 25.42-25.45)

$$\delta_{\rm vir,lin} = \frac{3}{20}\,(12\pi)^{2/3} \approx 1.686 \tag{1.59}$$

rather than 178. However, we can use this value to approximate the *halo mass function*, i.e. the number density of structures of given mass that have virialized in the universe, by calculating the abundance of matter found in regions of $\delta > \delta_{\rm vir,lin}$ according to linear evolution (Press & Schechter, 1974).

Consider, for this, a version δ_{W_R} of the (linearly evolved) matter field at the present epoch smoothed by a spherical top-hat filter of comoving radius R,

$$W_R(r) = \begin{cases} \frac{3}{4\pi R^3} & r \leq R \\ 0 & r > R \end{cases} \ , \tag{1.60}$$

as (Mo et al., 2010, Eqn. 7.42),

$$\delta_{W_R}(\boldsymbol{x}) = \int \delta_{\rm lin}(\boldsymbol{x}')W_R(|\boldsymbol{x}' - \boldsymbol{x}|)\ \mathrm{d}^3\boldsymbol{x}' \ . \tag{1.61}$$

The field $\delta_{W_R}(\boldsymbol{x})$ is a Gaussian random field, inheriting this property from $\delta_{\rm lin}$. Consequently, the probability of finding a value $\delta_{W_R} > \delta_{\rm vir,lin}$ is given by the Gaussian error function (Mo et al., 2010, Eqn. 7.43)

$$\mathrm{Prob}(\delta_{W_R} > \delta_{\rm vir,lin}) = \frac{1}{2}\,\mathrm{erfc}\left(\frac{\delta_{\rm vir,lin}}{\sqrt{2}\sigma(R)}\right) \ . \tag{1.62}$$

Here, we have used the variance $\sigma(R)$ of the field when smoothed with W_R, calculated from the (linear) power spectrum as

$$\sigma^2(R) = \frac{1}{2\pi^2}\int_0^\infty P(k)|\tilde{W}_R(k)|^2 k^2 \mathrm{d}k \ , \tag{1.63}$$

with the Fourier transform $\tilde{W}_R(k)$ of the filter function W_R.

δ_{W_R} corresponds to the linear overdensity inside a sphere large enough to contain a mass $M = \frac{4}{3}\pi\rho_\mathrm{c}\Omega_\mathrm{m}R^3$. Assuming that the fraction of matter virialized in haloes of mass M or larger is given by Eqn. 1.62 at the corresponding $R(M)$, we can write the halo mass function as (cf. Mo et al., 2010, Eqn. 7.45)

$$\frac{\mathrm{d}^2N}{\mathrm{d}V\,\mathrm{d}M} = 2\frac{\rho_\mathrm{m}}{M}\frac{\mathrm{dProb}(\delta_{W(R)} > \delta_\mathrm{vir,lin})}{\mathrm{d}\sigma}\left|\frac{\mathrm{d}\sigma}{\mathrm{d}M}\right| = \sqrt{\frac{2}{\pi}}\frac{\rho_\mathrm{c}\Omega_\mathrm{m}}{M^2}\frac{\delta_\mathrm{vir,lin}}{\sigma}\exp\left(-\frac{\delta^2_\mathrm{vir,lin}}{2\sigma^2}\right)\left|\frac{\mathrm{d}\ln\sigma}{\mathrm{d}\ln M}\right| \ . \tag{1.64}$$

This includes a factor of 2 to ensure that, in the limit of $M \to 0$, the sum of all haloes contains all matter in the universe.

Since the work of Press & Schechter (1974), refined versions of mass functions have been developed (e.g. Sheth & Tormen, 1999). The most common way of constructing accurate mass functions at present is based on identifying and counting haloes in numerical cosmological simulations and deriving a fitting formula for $\frac{\mathrm{d}^2N}{\mathrm{d}V\,\mathrm{d}M}$ as a function of mass and redshift or, equivalently, peak height $\nu := \delta_\mathrm{vir,lin}/\sigma[R(M), z]$ and cosmology (Tinker et al., 2008).

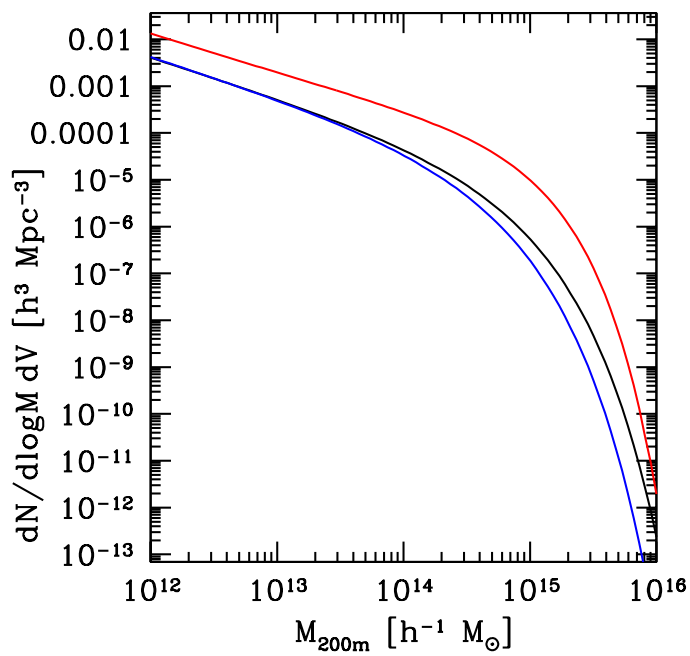

Figure 1.3: Halo mass function at $z = 0$ from the Tinker et al. (2008) fitting formula, plotted from the scale of massive galaxies ($10^{12}h^{-1}M_\odot$) to galaxy groups ($10^{13}h^{-1}M_\odot$) and clusters ($> 10^{14}h^{-1}M_\odot$). Black: fiducial cosmology $(\Omega_\mathrm{m}, \Omega_\Lambda, \sigma_8) = (0.3, 0.7, 0.79)$; red: Einstein-de Sitter universe with same σ_8; blue: lower power spectrum amplitude with $(\Omega_\mathrm{m}, \Omega_\Lambda, \sigma_8) = (0.3, 0.7, 0.7)$.

Figure 1.3 shows the latter mass function for three different cosmologies. Differences become most apparent at the high mass end, where the mass function drops quickly. Even a relatively moderate change in σ_8 causes almost an order-of-magnitude difference in the number of haloes at $M_{200m} > 2 \times 10^{15} h^{-1} M_\odot$. The Einstein-de Sitter scenario of a matter only universe corresponds to a significantly higher density of haloes at all mass scales.

1.2.3 Clusters of galaxies

At the massive end of the collapsed objects that are present in the Universe today, we find structures with virial masses of $10^{14} M_\odot$ to few times $10^{15} M_\odot$: clusters of galaxies. In this section, I will describe some of their basic properties, using the nearby Coma cluster (cf. Fig. 1.4) as an illustrative example.

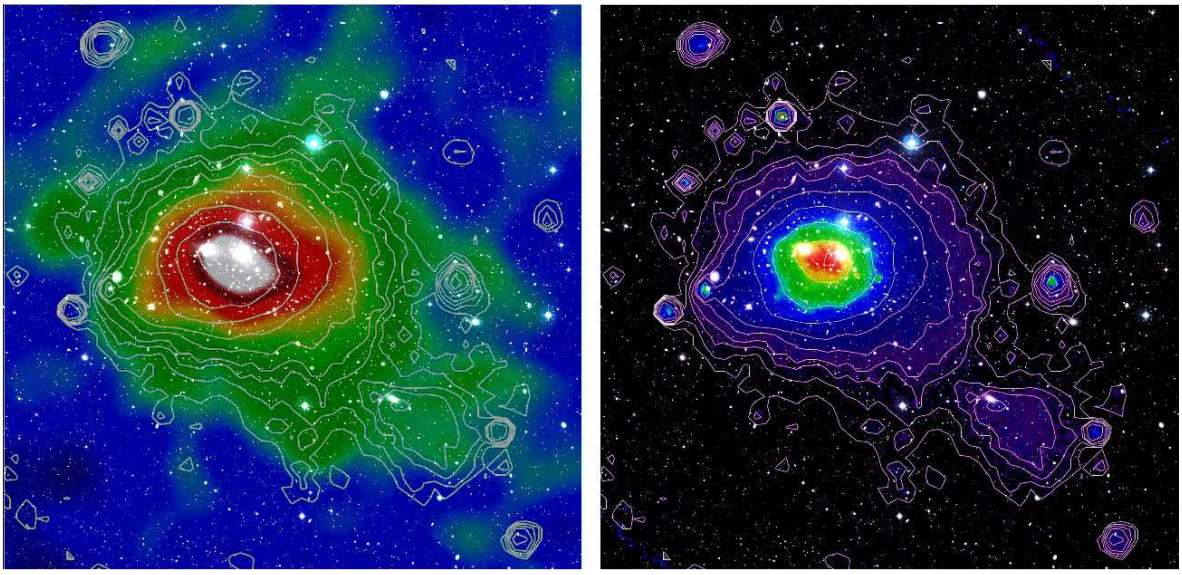

Figure 1.4: The Coma cluster of galaxies as seen in *Planck* SZ (left, shaded color), *ROSAT* X-Ray (right, shaded color and contours in both panels), and optical light (underlaid to both panels). Image credits: ESA / LFI and HFI Consortia (*Planck* image); MPI (*ROSAT* image); NASA/ESA/DSS2 (visible image). Acknowledgment: Davide De Martin (ESA/Hubble).

Clusters, due to their large mass and volume, are representative samples of the cosmic matter content. It is therefore particularly instructive to consider the components of the cluster matter.

Galaxies

The optical photons we'll be interested in studying later are generated in stars inside galaxies. Naturally, clusters of galaxies were first discovered and studied based on observations of the stellar light of their members. Morphologically, these are predominantly elliptical galaxies with red, old stellar populations. The distribution of their luminosity L is described well by a Schechter (1976) function,

$$\frac{\mathrm{d}^2 N}{\mathrm{d}L\,\mathrm{d}V} = n_0 \left(\frac{L}{L^\star}\right)^\alpha e^{-L/L^\star} \,, \tag{1.65}$$

where n_0 is a normalization. The density of objects drops as a power-law with slope α below the characteristic luminosity $L^\star$ and is exponentially truncated at the bright end.

The Coma cluster (whose visible light image is underlaid to both panels of Figure 1.4) is dominated, as are many clusters, by two giant, diffuse (cD-type) elliptical galaxies near its center. The combined luminosity of all cluster members is approximately 10^{13} times that of the sun (Oemler, 1974) which, for an old stellar population with relatively large stellar mass to light ratio, corresponds to a few times $10^{13} M_\odot$ in stellar mass. The redshifts measured for spectral lines of Coma cluster member galaxies shows, however, that these are moving relative to each other with a velocity dispersion of the order of 1000 km s^{-1}. Zwicky (1933) noted this and showed that there is a large discrepancy between the expected virial mass of a gravitationally bound system of the size and velocity dispersion of the Coma cluster (of order $10^{15} M_\odot$) and the observed stellar mass. Indeed, the stellar mass of clusters has consistently been found to be only few per cent of the total mass content.

Intra-cluster gas

The stellar mass is outweighed by baryonic matter in the form of intra-cluster gas by a factor of several. For protons moving at the measured galaxy velocity dispersion, its temperature is of the order of $10^{7\ldots8}$ K. We know about this gas from two observational signatures.

The first is the emission of bremsstrahlung photons at X-ray energies when two particles in the gas collide. The spectral energy distribution of the bremsstrahlung depends on the gas temperature and its intensity on the square of gas density. This makes both properties constrainable with observations with an X-ray telescope, for local clusters and high enough resolution in a spatially resolved fashion. If the gas is in hydrostatic equilibrium, its pressure gradient compensates the gravitational attraction due to the enclosed mass $M(< R)$ at any radius R,

$$\frac{\mathrm{d}p}{\mathrm{d}R} = -\frac{GM(< R)\rho_{\mathrm{gas}}(R)}{R^2} \ . \tag{1.66}$$

Solving for $M(< R)$, using the ideal gas law $p = \rho_{\mathrm{gas}} k_B T$ and $\frac{\mathrm{d}\log y}{\mathrm{d}\log x} = \frac{\mathrm{d}y}{\mathrm{d}x}\frac{x}{y}$, we find the enclosed mass to be related to the observables as (cf., e.g. Rosati et al., 2002, Eqn. 5)

$$M(< R) = -\frac{k_B T R}{G\mu m_p}\left(\frac{\mathrm{d}\log\rho_{\mathrm{gas}}}{\mathrm{d}\log R} + \frac{\mathrm{d}\log T}{\mathrm{d}\log R}\right) \ . \tag{1.67}$$

The second effect could concern the CMB photon that we have been following on its path. When passing through a cluster, a fraction of the low-energy photons interact with high-energy electrons in the intra-cluster gas via inverse Compton scattering. The effect was first described by Sunyaev & Zel'dovich (1972) and is hereafter called the SZ effect. Its amplitude is given by the Compton decrement

$$Y = \frac{\sigma_T}{m_e c^2} k_B \int n_e T \mathrm{d}V = \frac{\sigma_T}{m_e c^2}\int P \mathrm{d}V \ , \tag{1.68}$$

where σ_T is the Thompson cross-section, m_e is the electron mass and n_e is the electron number density. The left panel of Figure 1.4 shows a map of y, the surface density of Y, for the Coma cluster, as it was reconstructed from CMB observations of the *Planck* satellite.

This observable effect is a distortion of the thermal CMB spectrum by increasing the number of high-energy photons at the expense of low-energy ones. The characteristic frequency

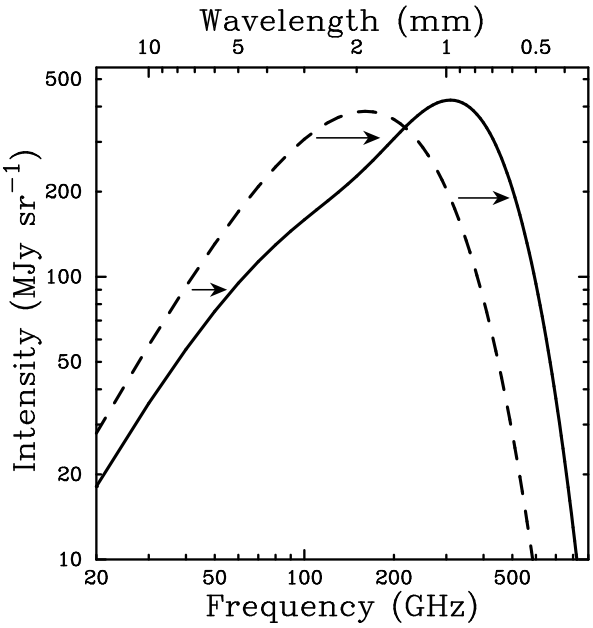

Figure 1.5: Change of CMB Planck spectrum (dashed) by inverse Compton scattering on hot cluster gas (thermal SZ effect) into observed spectrum (solid line). The amplitude of the effect has been strongly increased for illustration purposes. Source: Carlstrom et al. (2002, their Fig. 1).

dependence of derived temperature when observing the CMB through a cluster is shown in Fig. 1.5. Using observations in multiples bands below, at and above the cross-over frequency of ≈ 217 GHz, the signal can be distiguished from other astrophysical sources such as dust or radio emitters. Notably, this fact and the integrated observable at fixed thermal energy (cf. Eqn. 1.68) does not change with cluster redshift.

We can derive the expected scaling laws of the gas observables with cluster mass as follows. To this end, we assume that clusters are isothermal and self-similar, i.e. that objects of different mass are simply re-scaled versions of one another that share the same gas mass fraction $M_{\rm gas}/M$ and gas density profile.

From the virial theorem in a gravitational potential,

$$E_{\rm pot,gas} = -2E_{\rm kin,gas} \ , \tag{1.69}$$

and the proportionalities

$$E_{\rm pot,gas} \propto M_{\rm gas}\, M/R_{\rm vir} \overset{M\propto R_{\rm vir}^3}{\propto} M_{\rm gas}\, M^{2/3} \tag{1.70}$$

$$E_{\rm kin,gas} \propto M_{\rm gas}\, T \tag{1.71}$$

we find

$$T \propto M^{2/3} \ . \tag{1.72}$$

For the bolometric X-ray luminosity, since the mean gas density inside the virial radius is constant and bremsstrahlung emission is proportional to $T^{1/2} \propto M^{1/3}$, we have

$$L \propto V_{\rm vir}\, T^{1/2} \overset{M\propto V_{\rm vir}}{\propto} M^{4/3} \ . \tag{1.73}$$

The Compton parameter scales as

$$Y \propto \int P \, \mathrm{d}V_{\mathrm{vir}} \propto T \int \rho_{\mathrm{gas}} \mathrm{d}V \propto M^{5/3} \, . \tag{1.74}$$

The gas mass fraction of clusters can be measured by comparing X-ray estimates of gas mass with lensing or X-ray hydrostatics based estimates of total mass. It is found to be little more than 10 per cent of the total mass (cf., e.g., Allen et al., 2002).

One important caveat about the described properties of the intra-cluster gas is that the relations are based, in one way or another, on the assumption of hydrostatic equilibrium of an ideal gas with purely thermal pressure. There is, however, also non-thermal pressure supporting the cluster gas from collapse, e.g. from the bulk motion of in-falling gas in mergers (cf. Shi & Komatsu, 2014, for a recent model and review of previous studies). The contribution of these effects to the overall gas pressure is expected to vary from cluster to cluster, causing intrinsic dispersion of the gas observables at fixed mass. But also the mean contribution and its dependence on cluster mass has been measured from hydrodynamic simulations and observations with somewhat varying results. The comparison of hydrodynamic mass estimates and lensing, which is insensitive to the astrophysical state, is therefore one of the purposes of the cluster mass calibration project described in Chapter 5.

Dark matter

The discrepancy between gravitating mass and baryonic matter noted by Zwicky (1933) is thus not solved by the addition of intra-cluster gas. Similarly, rotational velocities (Rubin et al., 1980) and velocity dispersions of stars in galaxies cannot be explained by the self-gravity of visible baryonic matter. In fact, these structures could not have formed at all from the observed tiny relative fluctuations at the time of re-combination if matter was purely baryonic. These observations and the peaks of the CMB power spectrum are evidence for a matter component that does not interact electromagnetically, *dark matter*.

This form of dark matter indeed makes up approximately 85 per cent of the matter content of clusters of galaxies. Simulations with collisionless, cold dark-matter particles evolving in an expanding universe show that the average density profiles of dark matter haloes are well described by the Navarro, Frenk, & White (1997, hereafter NFW) profile,

$$\rho(r) = \frac{\rho_0}{(r/r_{\mathrm{s}})(1 + r/r_{\mathrm{s}})^2} \, , \tag{1.75}$$

with two parameters ρ_0 and r_{s} corresponding to a scale in density and radius.

It is, at the point of this writing, not clear what constitutes dark matter. The most likely candidate is a weakly interacting (i.e., electromagnetically sterile) massive (GeV scale, i.e. non-relativistic during structure formation) particle (WIMP). Attempts to directly detect such a particle through its interaction with matter in a detector (e.g. Angloher et al., 2012) or indirectly through observational signatures of WIMP annihilation in regions of dense dark matter (e.g. Aguilar et al., 2013) are ongoing.

Clusters as cosmological probes

As discussed in Section 1.2.2, the number of massive haloes (i.e. galaxy clusters) to form in the Universe is sensitive to cosmology. The number of clusters to be found in a given volume

is influenced by both the expansion history and the density and degree of inhomogeneity of matter. The growth of these structures is governed by the laws of gravitation. Therefore, both the parameters of a standard cosmological model and tests for deviations from GR are possible with clusters, defining the field of cluster cosmology (cf. Allen et al., 2011, for a recent review).

The most common probe, cluster abundance, is based on three components, namely (i) a list of clusters selected by an observable, such as galaxy count or luminosity, X-ray emission or Compton decrement, (ii) a prediction for the halo mass function and its cosmology dependence (cf. Section 1.2.2), and (iii) a mass-observable relation (MOR), which allows to connect (i) and (ii) in terms of a likelihood.

The latter likelihood describes the probability of finding the observed list of clusters inside the survey volume, conditional on the choice of cosmological parameters. For an ideal observable that yields the true mass of clusters without scatter, this is found by comparing cluster counts in mass-redshift bins to the halo mass function integrated over the respective mass bin and survey volume, based on a Poisson likelihood.

This is complicated by the intrinsic scatter that every cluster observable exhibits at fixed true mass, in addition to measurement related uncertainties. The effects of this are (i) a selection bias of up-scattered objects at the low mass end due to the observable threshold of a survey (commonly referred to as Malmquist bias) and (ii) a preferential up-scatter in the observable due to the fact that lower mass clusters are more numerous (Eddington bias). These effects need to be included in a cluster abundance likelihood, making the intrinsic scatter an important part of the MOR (cf. Lima & Hu, 2005).

1.2.4 Gravitational lensing

The photons we have followed do feel gravity. Even in a Newtonian picture of corpuscular light moving with velocity c, their paths are deflected when passing by a mass. Johann Georg von Soldner, later to be appointed as the director of the Royal Observatory of Bogenhausen, proposed this more than a century before the development of GR (von Soldner, 1804). If a particle of mass m and velocity v passes a spherically symmetric mass M at impact parameter $\xi = CA$ (cf. Fig. 1.6), we can write the final velocity perpendicular to the original direction as

$$mv_\perp = \int \mathrm{d}t\, m\dot{v}_\perp = \int \mathrm{d}t\, F_\perp = \int \mathrm{d}t\, F_g\, \cos\varphi = \int_{-\infty}^{\infty} \frac{\mathrm{d}x}{v} \frac{GmM}{x^2+\xi^2} \frac{\xi}{\sqrt{x^2+\xi^2}}\,, \tag{1.76}$$

where we have used a projection of the gravitational force F_g under the angle φ (cf. Fig. 1.6) to write the force $F_\perp$ that acts perpendicular to the light path. The time integral is expressed as an integral along the unperturbed path $x = -\infty \ldots \infty$, where $x = 0$ corresponds to the point A in Fig. 1.6. It is evaluated to find the deflection angle (ω in Fig. 1.6) as

$$\hat{\alpha}_{\mathrm{Newton}} \approx \frac{v_\perp}{v} = \frac{2GM}{v^2\xi} \xrightarrow{v\to c} \frac{2GM}{c^2\xi}\,. \tag{1.77}$$

This approximation is indeed valid for $\hat{\alpha} \ll 1$, yet breaks in GR as $v \to c$ for the following reason. In GR, the perturbation to the metric that recovers the motion of massive particles in a weak Newtonian potential Φ is given by the line element (cf. Peebles, 1993, Eqn. 10.84)

$$\mathrm{d}s^2 = (1+2\Phi/c^2)c^2\mathrm{d}t^2 - (1-2\Phi/c^2)(\mathrm{d}\boldsymbol{x})^2\,. \tag{1.78}$$

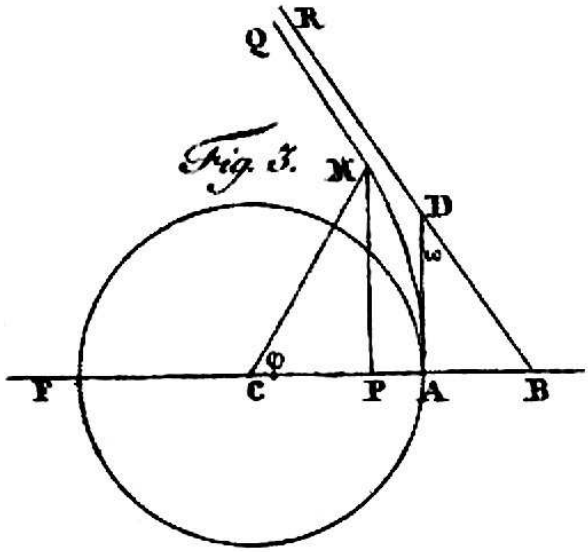

Figure 1.6: Deflection of a light ray that passes a mass, centered at C, at a distance CA, by angle ω. Historical illustration taken from von Soldner (1804).

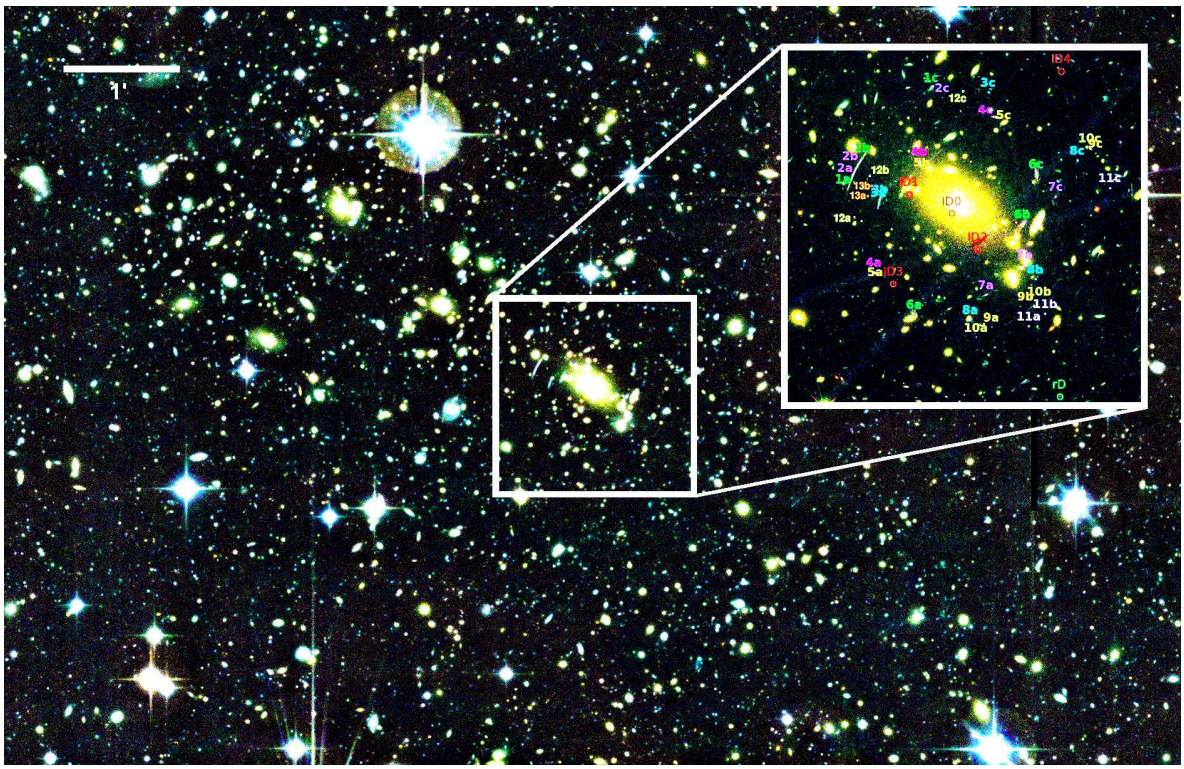

Figure 1.7: Ground based BRI color image of the galaxy cluster RXC J2248.7–4431, with a zoomed cut-out of HST image (from Monna et al., 2014, Fig. 1) of the central region. A large number of cluster member galaxies can be seen as the yellow, diffuse sources. Strong lensing features are visible as giant arcs and multiple images, indicated by colored labels for 13 system with a total of 37 images in the inset. Weak lensing of the background galaxies is analyzed in Gruen et al. (2013, contained in Chapter 4 of this thesis).

For a non-relativistic particle, i.e. an object of non-zero mass with a velocity small compared to the speed of light, the geodesic in this metric corresponds to the path predicted by Newtonian theory, i.e. a deflection according to Eqn. 1.77. In this limit, $\mathrm{d}x/\mathrm{d}t \ll c$ and therefore the time part of the metric dominates Eqn. 1.78.

For a photon, however, $\mathrm{d}s^2 = 0$ and thus time and spatial part of Eqn. 1.78 are of equal magnitude. Consequently, Φ affects the null geodesic twice as strongly. The deflection is therefore

$$\hat{\alpha} = 2\hat{\alpha}_{\mathrm{Newton}} = \frac{4GM}{c^2\xi} \ . \tag{1.79}$$

Based on the observation of deflected light from background stars grazing the surface of the sun during a solar eclipse, Dyson et al. (1920) confirmed this prediction.

The bending of light rays occurs in the vicinity of all massive cosmic bodies. Zwicky (1937) was the first to propose that galaxies could act as gravitational lenses. For gravitational fields that are strong enough, highly distorted arcs and multiple images of background sources can be observed. An example of strong gravitational lensing by the galaxy cluster RXC J2248.7–4431 is shown in the inset of Figure 1.7. Careful analysis of these images can yield detailed information about the mass distribution of the object acting as a lens (see Monna et al., 2014, for the case of RXC J2248.7–4431). Further away from mass aggregations such as galaxy clusters, the observable effect is a differential deflection and merely accounts for small distortions of the observed objects. In Fig. 1.7, this causes a preferential tangential alignment of the mostly blue background galaxies around the center of the cluster. The effect, however, is indiscernible on any individual object due to the dominant and randomly oriented intrinsic ellipticity.

The propagation of light in an inhomogeneous universe can be studied in great generality (Seitz et al., 1994). For weak lensing effects, the mapping of source coordinates to apparent positions can be linearly approximated. The Jacobian, which we are about to derive for the case of a single, thin lens, contains all information about the differential deflection, which can cause a change in apparent size and shape of a lensed source.

Consider a light source that is situated at a small angular distance $\boldsymbol{\beta}$ from the line of sight. The source shall be confined to a plane at angular diameter distance D_s (cf. Eqn. 1.35) from the observer. Its proper position in the lens plane relative to the axis of sight is denoted by $\boldsymbol{\eta}$. A sketch of positions and angles is given in Figure 1.8.

Now consider some massive object between observer and source, confined to a lens plane at angular diameter distance D_d from the observer. The angular diameter distance between lens and source is denoted by D_{ds}.

In the absence of deflection, the angle $\boldsymbol{\theta}$ under which an observer receives photons from the source is equal to its actual position, i.e. $\boldsymbol{\theta} = \boldsymbol{\beta}$. Similarly, if we define $\boldsymbol{\xi}$ as the proper point in the lens plane that the light ray from the source intercepts before it is seen by the observer, we find, using the small angle approximation, $\boldsymbol{\eta} = \frac{D_s}{D_d}\boldsymbol{\xi}$.

With deflection, a path of a photon passing the lens plane at $\boldsymbol{\xi}$ is deflected by some angle $\hat{\boldsymbol{\alpha}}(\boldsymbol{\xi})$ to finally meet the observer. Reconstruction of the position of the source gives

$$\boldsymbol{\eta} = \frac{D_s}{D_d}\boldsymbol{\xi} - D_{ds}\hat{\boldsymbol{\alpha}}(\boldsymbol{\xi}) \ . \tag{1.80}$$

Since what we would like to find is an expression for the true and observed angles of the source rather than its true distance from the origin of the source plane $\boldsymbol{\eta}$, we transform

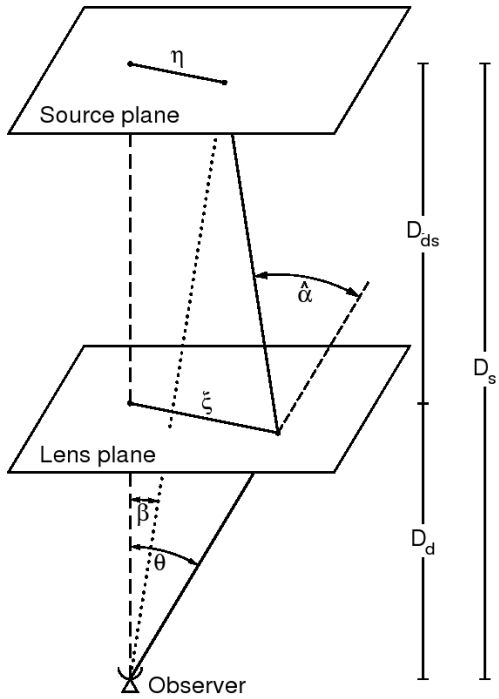

Figure 1.8: Sketch of positions and angles for a lensing configuration. In contrast to the illustration, realistic angles in a lensing scenario are small. Source: Bartelmann & Schneider (2001), p. 45.

Eqn. 1.80 using $\boldsymbol{\beta} = \frac{\boldsymbol{\eta}}{D_s}$ and $\boldsymbol{\theta} = \frac{\boldsymbol{\xi}}{D_d}$ to find the *lens equation*

$$\boldsymbol{\beta} = \boldsymbol{\theta} - \frac{D_{ds}}{D_s}\hat{\boldsymbol{\alpha}}(D_d\boldsymbol{\theta}) = \boldsymbol{\theta} - \boldsymbol{\alpha}(\boldsymbol{\theta}) \ . \tag{1.81}$$

Note the introduction of the scaled deflection angle

$$\boldsymbol{\alpha}(\boldsymbol{\theta}) := \frac{D_{ds}}{D_s}\hat{\boldsymbol{\alpha}}(D_d\boldsymbol{\theta}) \ . \tag{1.82}$$

The $\hat{\boldsymbol{\alpha}}$ in the above equations for a spherical body of mass M, passed by a light ray at distance ξ, is given by Eqn. 1.79. Since the equation is linear, the effect of a more complex mass distribution is expressed by superposition of surface mass elements $\Sigma(\boldsymbol{\xi})\mathrm{d}^2\boldsymbol{\xi}$ as

$$\hat{\boldsymbol{\alpha}}(\boldsymbol{\xi}) = \int \mathrm{d}^2\boldsymbol{\xi}' \frac{4G\Sigma(\boldsymbol{\xi}')}{c^2}\frac{\boldsymbol{\xi} - \boldsymbol{\xi}'}{|\boldsymbol{\xi} - \boldsymbol{\xi}'|^2} \ . \tag{1.83}$$

Introducing the *convergence* κ, the dimensionless surface mass density in units of the critical surface mass density Σ_{crit},

$$\kappa := \frac{\Sigma}{\Sigma_{\mathrm{crit}}}, \quad \Sigma_{\mathrm{crit}} := \frac{c^2}{4\pi G}\frac{D_s}{D_d D_{ds}} \ , \tag{1.84}$$

the scaled deflection angle (cf. Eqn. 1.82) is given by

$$\boldsymbol{\alpha}(\boldsymbol{\theta}) = \frac{D_{ds}}{D_s}\hat{\boldsymbol{\alpha}}(D_d\boldsymbol{\theta}) = \frac{1}{\pi}\int \mathrm{d}^2\boldsymbol{\theta}'\kappa(\boldsymbol{\theta}')\frac{\boldsymbol{\theta} - \boldsymbol{\theta}'}{|\boldsymbol{\theta} - \boldsymbol{\theta}'|^2} \ . \tag{1.85}$$

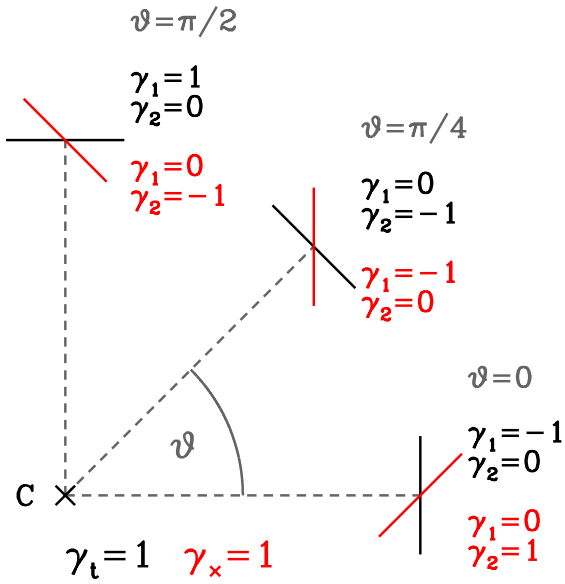

Figure 1.9: Relation of tangential (γ_t, black lines indicate the positive direction at different positions) and cross ($\gamma_\times$, red lines) components of gravitational shear relative to point C to the components $\gamma_{1/2}$ defined in a Cartesian coordinate system.

Since $\boldsymbol{\nabla} \ln|\boldsymbol{\theta}-\boldsymbol{\theta}'| = \frac{\boldsymbol{\theta}-\boldsymbol{\theta}'}{|\boldsymbol{\theta}-\boldsymbol{\theta}'|^2}$ (where $\boldsymbol{\nabla}$ is defined to differentiate w.r.t. $\boldsymbol{\theta}$) we can write the deflection angle as the gradient of a *lensing potential* ψ, $\boldsymbol{\alpha}(\boldsymbol{\theta}) = \boldsymbol{\nabla}\psi(\boldsymbol{\theta})$, with

$$\psi(\boldsymbol{\theta}) = \frac{1}{\pi}\int \mathrm{d}^2\boldsymbol{\theta}'\kappa(\boldsymbol{\theta}')\ln|\boldsymbol{\theta}-\boldsymbol{\theta}'| \,. \tag{1.86}$$

The linear approximation of the lens equation 1.81 is given by the Jacobian A,

$$A = \frac{\partial\boldsymbol{\beta}}{\partial\boldsymbol{\theta}} = \left(\delta_{ij} - \frac{\partial\alpha_i(\boldsymbol{\theta})}{\partial\theta_j}\right) = \left(\delta_{ij} - \frac{\partial^2\psi(\boldsymbol{\theta})}{\partial\theta_i\partial\theta_j}\right) =: \begin{pmatrix} 1-\kappa-\gamma_1 & -\gamma_2 \\ -\gamma_2 & 1-\kappa+\gamma_1 \end{pmatrix} \,. \tag{1.87}$$

Here we have defined the components of *gravitational shear* $\boldsymbol{\gamma}$ as (cf. Fig. 1.9)

$$\begin{aligned} \gamma_1 &= \frac{1}{2}\left(\frac{\partial^2\psi(\boldsymbol{\theta})}{\partial\theta_1^2} - \frac{\partial^2\psi(\boldsymbol{\theta})}{\partial\theta_2^2}\right) \\ \gamma_2 &= \frac{\partial^2\psi(\boldsymbol{\theta})}{\partial\theta_1\partial\theta_2} \end{aligned} \tag{1.88}$$

and used that the deflection potential satisfies the Poisson equation

$$\frac{1}{2}\boldsymbol{\nabla}^2\psi(\boldsymbol{\theta}) = \kappa(\boldsymbol{\theta}) \,. \tag{1.89}$$

With A, the apparent coordinates of a point $\boldsymbol{\theta}$ near $\boldsymbol{\theta}_0$ are locally related to its true coordinates $\boldsymbol{\beta}$ near $\boldsymbol{\beta}_0 = \boldsymbol{\beta}(\boldsymbol{\theta}_0)$ as

$$\boldsymbol{\beta} - \boldsymbol{\beta}_0 \approx \left.\frac{\partial\boldsymbol{\beta}}{\partial\boldsymbol{\theta}}\right|_{\boldsymbol{\theta}_0}(\boldsymbol{\theta}-\boldsymbol{\theta}_0) = A(\boldsymbol{\theta}_0)(\boldsymbol{\theta}-\boldsymbol{\theta}_0) \,. \tag{1.90}$$

Equation 1.87 can be rewritten as

$$A = (1-\kappa)\begin{pmatrix} 1-g_1 & -g_2 \\ -g_2 & 1+g_1 \end{pmatrix} , \tag{1.91}$$

where we have defined the reduced shear

$$\boldsymbol{g} = \boldsymbol{\gamma}/(1-\kappa) . \tag{1.92}$$

It can be seen from Eqns. 1.81 and 1.91 that the effect of lensing is three-fold:

- a displacement of the central position of the image, given by the lens equation 1.81,
- a magnification (or de-magnification) of an object's size, given by the determinant of the Jacobian, i.e. by a factor $(\det A)^{-1}$,
- and a distortion of an object's shape, keeping the size fixed, described at first order by the reduced shear $\boldsymbol{g}$.

It is useful to re-write $\boldsymbol{\gamma}$ (or, equivalently, $\boldsymbol{g}$) in terms of the tangential and cross components relative to a point,

$$\begin{aligned} \gamma_t &= -\gamma_1 \cos 2\vartheta - \gamma_2 \sin 2\vartheta \\ \gamma_\times &= -\gamma_1 \sin 2\vartheta + \gamma_2 \cos 2\vartheta , \end{aligned} \tag{1.93}$$

where orientations and the angle ϑ are defined as indicated in Fig. 1.9. This illustrates that $\boldsymbol{\gamma}$ is a pseudovector (spin-2) field: rotation by 45° transforms one component to the other, rotation by 90° switches the sign and rotation by 180° leaves shear invariant.

Shear and overdensity

A useful interpretation of $\boldsymbol{\gamma}$ is found by applying Gauss's theorem to the gradient of the lensing potential of Eqn. 1.86 (cf. Schneider, 2005, p. 11). The theorem holds that for any vector field (in our case, $\boldsymbol{\nabla}\psi$),

$$\int_{\mathcal{A}} \boldsymbol{\nabla}\cdot\boldsymbol{\nabla}\psi \, \mathrm{d}A = \oint_{\delta\mathcal{A}} \boldsymbol{\nabla}\psi \cdot \boldsymbol{n} \, \mathrm{d}S , \tag{1.94}$$

where the left integral runs over some area $\mathcal{A}$ and the right integral is along a closed path around that area, to which $\boldsymbol{n}$ is a unit normal vector.

Take $\mathcal{A}$ to be a circle of radius θ. From Eqn. 1.89 we see that the left-hand side of Eqn. 1.94 is equal to

$$\int_{\mathcal{A}} \boldsymbol{\nabla}\cdot\boldsymbol{\nabla}\psi \, \mathrm{d}A = 2\int_{\mathcal{A}} \kappa \, \mathrm{d}A = 2\pi\theta^2 \bar{\kappa}(<\theta) , \tag{1.95}$$

where $\bar{\kappa}(<\theta)$ is the mean value of κ inside the circle. For the right-hand side, we use that for our circle $\boldsymbol{\nabla}\psi\cdot\boldsymbol{n} = \frac{\mathrm{d}\psi}{\mathrm{d}\theta}$ to rewrite this as

$$\oint_{\delta\mathcal{A}} \boldsymbol{\nabla}\psi\cdot\boldsymbol{n}\,\mathrm{d}S = \oint_{\delta\mathcal{A}} \frac{\mathrm{d}\psi}{\mathrm{d}\theta}\mathrm{d}S = 2\pi\theta \left\langle \frac{\mathrm{d}\psi}{\mathrm{d}\theta} \right\rangle , \tag{1.96}$$

where the average $\langle \ldots \rangle$ is taken over the azimuthal angle at fixed radius θ. Equating 1.95 and 1.96 and dividing by $2\pi\theta$, we obtain

$$\left\langle \frac{\mathrm{d}\psi}{\mathrm{d}\theta} \right\rangle = \theta\bar{\kappa}(<\theta) \ . \tag{1.97}$$

The last equation can be differentiated w.r.t. θ to find

$$\left\langle \frac{\mathrm{d}^2\psi}{\mathrm{d}\theta^2} \right\rangle = \bar{\kappa}(<\theta) + \theta\frac{\mathrm{d}\bar{\kappa}}{\mathrm{d}\theta} \ . \tag{1.98}$$

The derivative of mean convergence is

$$\frac{\mathrm{d}\bar{\kappa}}{\mathrm{d}\theta} = \frac{\mathrm{d}}{\mathrm{d}\theta}\left[\frac{2}{\theta^2}\int_0^\theta \langle\kappa\rangle(\theta')\theta' \ \mathrm{d}\theta'\right] = \frac{2}{\theta}\left[\langle\kappa\rangle(\theta) - \bar{\kappa}(<\theta)\right] \ . \tag{1.99}$$

Consider now, without loss of generality, a point on the horizontal axis. Here, from Eqns. 1.88, 1.89, and 1.93 we find that $\frac{\mathrm{d}^2\psi}{\mathrm{d}\theta^2} = \frac{\mathrm{d}^2\psi}{\mathrm{d}\theta_1^2} = \kappa + \gamma_1 = \kappa - \gamma_t$. Since we can define the orientation of the axes arbitrarily, the equality of the left and the right-hand term holds anywhere, thus

$$\left\langle \frac{\mathrm{d}^2\psi}{\mathrm{d}\theta^2} \right\rangle = \langle\kappa\rangle(\theta) - \langle\gamma_t\rangle(\theta) \ . \tag{1.100}$$

We insert Eqns. 1.99 and 1.100 into 1.98 to finally find an expression for the mean tangential shear at radius θ as

$$\langle\gamma_t\rangle(\theta) = \bar{\kappa}(<\theta) - \langle\kappa\rangle(\theta) \ . \tag{1.101}$$

Mean tangential gravitational shear thus measures the *overdensity* of projected matter inside a circle relative to its edge. This illustrates how measurements of gravitational shear can constrain the matter profile of cosmic structures (as done for a cluster of galaxies in Chapter 4 and a sample of clusters in Chapter 5).

Inversion of shear

Another interpretation of shear can be given by considering the Fourier space versions of Eqns. 1.88 and 1.89,

$$\frac{\mathscr{F}(\kappa)}{\mathscr{F}(\gamma_1 + i\gamma_2)} = \frac{l_1^2 + l_2^2}{l_1^2 - l_2^2 + 2il_1l_2} = \frac{(l_1 - il_2)^2}{|l|^2} =: \mathcal{D} \ , \tag{1.102}$$

where $\mathscr{F}$ is the Fourier transform, $\boldsymbol{l}$ the coordinate in the Fourier space associated with $\boldsymbol{\theta}$ and we have used the Fourier differentiation theorem $\mathscr{F}\left(\frac{\mathrm{d}f}{\mathrm{d}\theta_i}\right) \propto il_i\mathscr{F}(f)$.

Since the product $\mathcal{D}\mathscr{F}(\gamma_1 + i\gamma_2)$ in Fourier space corresponds to a convolution in real space, we find

$$\kappa(\boldsymbol{\theta}) - \kappa_0 = \left(\mathscr{F}^{-1}(\mathcal{D}) \otimes (\gamma_1 + i\gamma_2)\right)(\boldsymbol{\theta}) \ , \tag{1.103}$$

where the real space version of the kernel $\mathcal{D}$ is

$$[\mathscr{F}^{-1}(\mathcal{D})](\boldsymbol{\theta}) = \frac{1}{\pi(\theta_2 - i\theta_1)^2} \ . \tag{1.104}$$

Note (and see the following section on) the additive constant κ_0, due to the fact that the kernel is undefined at $\boldsymbol{l} = 0$.

Eqn. 1.103 is called Kaiser & Squires (1993) inversion and directly relates the local projected density to a non-local integral over the shear field (cf. Seitz & Schneider, 1996, for a finite-field method).

Mass Sheet Degeneracy

It is important to note that reduced shear $\boldsymbol{g}$ alone does not retain the full information on κ. To see this, consider a transformation

$$\kappa \to \lambda\kappa + (1 - \lambda) \; . \tag{1.105}$$

Since the deflection angle is linear in κ (cf. Eqn. 1.85) and its differential is unchanged by a constant surface mass density, this transforms gravitational shear as

$$\boldsymbol{\gamma} \to \lambda\boldsymbol{\gamma} \; . \tag{1.106}$$

The reduced shear

$$\boldsymbol{g} = \frac{\boldsymbol{\gamma}}{1-\kappa} \to \frac{\lambda\boldsymbol{\gamma}}{\lambda(1-\kappa)} \tag{1.107}$$

is thus degenerate under the transformation of Eqn. 1.105. This means that gravitational shear cannot be used to detect a mass sheet or distinguish between models for surface density that differ only by a mass sheet and a corresponding multiplicative factor.

There are ways of lifting this so-called *mass sheet degeneracy*, e.g. by including measurements of magnification (in terms of number counts or angular size measurements of background galaxies), which independently determine κ, or by means of tomography (measuring the shear of several redshift-binned subsets of background galaxies), for which κ differs by a multiplicative factor D_{ds}/D_s. Similarly, one may fit a functional form of the density profile of the observed cluster to the data. In this case, the degeneracy of the enclosed mass is broken by construction but remains physically unconstrained.

1.3 The finale: Observing the Universe

Despite the great advances of observational astronomy, we should still humbly acknowledge, with Robert Frost, that we can look *neither out far nor in deep. But wherever the truth may be* – it appears we are determined to keep looking. In this section, I introduce some of the aspects related to observation and processing of imaging data. In this, I use a relatively formal approach to emphasize that there is indeed a rigorous, yet complex, connection between the photons we have followed and the images we read out from our telescope camera.

From photons to pixel counts

The optical photons we are interested in were generated in stars. Therefore they allow us to measure the luminosities, positions and, for resolvable light distributions, the shapes of celestial objects.

The photons that end up in the camera of our telescope have traveled through the Universe as described in the previous sections, being redshifted by the expansion of space and deflected by tidal gravitational fields. Some of them have been extincted by intervening baryonic matter, such as Galactic dust, the wavelength dependence of scattering leading to a reddening of colors.

The specific intensity I_λ describes the resulting radiation. It is defined as the transfer of energy per differential unit wavelength $\mathrm{d}\lambda$, time $\mathrm{d}t$, solid angle $\mathrm{d}\Omega$, and collection area $\mathrm{d}A$

whose normal vector is rotated relative to the direction of the incident radiation by an angle θ, as

$$I_\lambda = \frac{\mathrm{d}^4 E}{\mathrm{d}\lambda\,\mathrm{d}t\,\mathrm{d}\Omega\,\cos\theta\,\mathrm{d}A}\ . \tag{1.108}$$

We define a photon count equivalent of this, as measured at a point outside the atmosphere, as

$$f_0(\boldsymbol{\theta},\lambda) = I_\lambda\,\frac{\lambda}{hc}\ , \tag{1.109}$$

where $\boldsymbol{\theta}$ is the position in a sky coordinate system.

On the remaining way onto the focal plane of a telescope, atmospheric extinction, absorption and scattered reflection in the optics, and a filter used in the telescope reduce this photon count by a factor $\mathcal{F}(\boldsymbol{x},\lambda) \leq 1$, which is a function of wavelength λ and position in the focal plane $\boldsymbol{x}$.

In addition, atmospheric turbulence, diffraction, and imperfect optics cause the photon distribution seen in the telescope to be convolved by a kernel, the so-called *point spread function* $\mathrm{PSF}(\boldsymbol{x},\lambda)$. Sky coordinates are mapped onto the focal plane with an *astrometric solution* $\boldsymbol{x}(\boldsymbol{\theta},\lambda)$, which can be described as in Calabretta et al. (2004). Both PSF and astrometric solution are almost constant over the wavelength range of typical filters, which is why we drop the λ dependence (but see, e.g., Plazas & Bernstein 2012; Meyers & Burchat 2014).

The photons from our sources of interest are joined by background light $\mathrm{bg}(\boldsymbol{\theta},\lambda)$ and artifact features due to objects in the sky ($\mathrm{art}_{\mathrm{sky}}$). The latter originate, e.g., from secondary reflections in the telescope optics (so-called ghost images) or unwanted sky features such as satellite trails. Including these effects, the received surface brightness is

$$f_1(\boldsymbol{\theta},\lambda) = \{[f_0(\boldsymbol{\theta},\lambda) + \mathrm{bg}(\boldsymbol{\theta},\lambda)] \otimes \mathrm{PSF}[\boldsymbol{x}(\boldsymbol{\theta}),\lambda]\}\ \mathcal{F}[\boldsymbol{x}(\boldsymbol{\theta}),\lambda] + (\mathrm{art}_{\mathrm{sky}})\ . \tag{1.110}$$

Modern telescopes use charge-coupled device (CCD) detectors. These convert incoming photons into charges via the photoelectric effect. Several different types of CCDs exist, with Fig. 1.10 showing a back-illuminated (i.e., with light falling in from the side opposite to the read-out channels), thick sensor.

A fraction $\mathrm{QE}(\boldsymbol{x},\lambda) \leq 1$ of photons actually succeeds in *charge generation*, where back-illumination helps to reduce absorption in the polysilicon gate structures and thickness allows for efficient conversion of red and infrared photons despite their large penetration depth into the silicon (cf. Janesick, 2001, Sections 3.1 and 3.2).

During integration, *charge collection* is achieved by means of a bias voltage that causes the photo-generated charges to drift towards the gate. Deviations from a perfect pixel grid, diffusion of charges, lateral electric fields due to boundary effects or variations in the already accumulated charge between pixels and saturation effects cause a mapping $\boldsymbol{X}(\boldsymbol{x})$ from focal plane positions onto integer pixel coordinates $\boldsymbol{X}$. The mapping is, in the most general case, dependent on wavelength, position, and the charges already present in the detector. It includes a convolution of the image by the *pixel response function* $\mathrm{PRF}(\boldsymbol{X})$, e.g. a box of the size of the pixel. The area per pixel is denoted by $\mathrm{PA}(\boldsymbol{X})$. The mapping $\boldsymbol{X}(\boldsymbol{x})$ can be defined such that it also includes imperfections in *charge transfer*: while the charges are shifted towards the readout electronics, some are trapped in defects in the silicon and thermally released into trailing pixels.

Spontaneous generation of charge pairs in the silicon causes a *dark current* $d(\boldsymbol{X})$ of charges per pixel per unit time. The analog-digital conversion adds a constant bias $B(\boldsymbol{X})$ at read-out

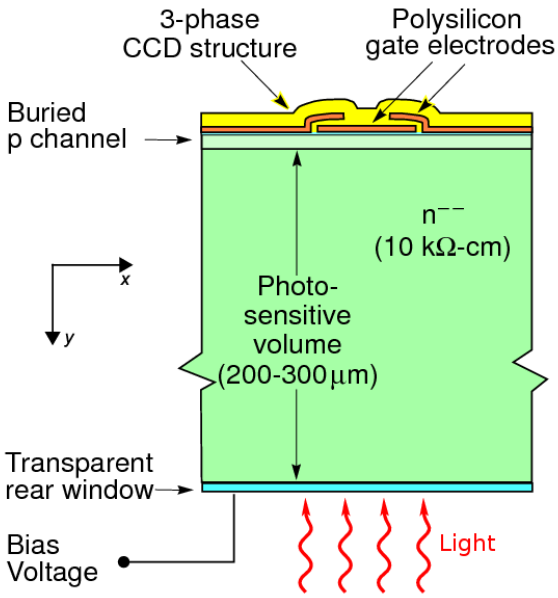

Figure 1.10: Schematic image of a thick, back-illuminated CCD detector similar to the ones used in the Dark Energy Camera. Source: Holland et al. (2003, Fig. 1).

time and converts charges to analog-digital units (ADU) with a gain factor g. Additional artifacts ($\mathrm{art}_{\mathrm{cam}}$) are generated in the camera due to, e.g., cosmic rays, bad pixels or bleeding of charges out of saturated pixels. Combinedly, this yields a time and wavelength integrated $F_{\mathrm{obs}}(\boldsymbol{X})$, as seen by the readout signal chain, as

$$\begin{aligned} F_{\mathrm{obs}}(\boldsymbol{X}) &= \left[\int \mathrm{d}t\, \mathrm{d}\lambda\, \{f_1(\boldsymbol{\theta}[\boldsymbol{x}(\boldsymbol{X})], \lambda) \otimes \mathrm{PRF}(\boldsymbol{X})\}\, \mathrm{QE}[\boldsymbol{x}(\boldsymbol{X}), \lambda]\, \mathrm{PA}(\boldsymbol{X}) + \int \mathrm{d}t\, d(\boldsymbol{X})\}\right] / g \\ &+ B(\boldsymbol{X}) + (\mathrm{art}_{\mathrm{cam}})\ , \end{aligned} \tag{1.111}$$

which can be saved in an image file. The units of F_{obs} are ADU per pixel.

From pixel counts back to photons

We need to reverse these steps to connect the measured F_{obs} to a wavelength integral of the physical $f_0(\boldsymbol{\theta}, \lambda)$ with known filter function. This process is called *data reduction*. Going back step by step:

- $B(\boldsymbol{X})$ can be measured from *bias frames* with zero exposure time and subtracted from F_{obs}.
- $d(\boldsymbol{X})/g$ is derived from *dark frames* taken with closed shutter, i.e. $f_1 = 0$, divided by their exposure time. It can multiplied by the exposure time of the science image and subtracted.
- Since photon counts contain Poissonian noise, the gain g can be measured as the ratio of ADU count level and variance. The image can be multiplied by this to arrive at a photon count map.

- The mapping $\boldsymbol{X}(\boldsymbol{x})$ is close to the identity, and so commonly assumed as $\boldsymbol{X} = \boldsymbol{x}$. Precision measurements, e.g. of weak gravitational shear, can require a more careful treatment to prevent significant systematic errors. An example is the effect of charge self-interaction on $\boldsymbol{X}(\boldsymbol{x})$, for which I describe a correction in Chapter 2.
- The product of $\mathcal{F}(\boldsymbol{\theta}, \lambda)\,\mathrm{QE}(\boldsymbol{x}, \lambda)\,\mathrm{PA}(\boldsymbol{X})$, up to an unknown factor, can be measured from *flat field frames*. These are images with $\boldsymbol{\theta}$ independent (uniform) illumination $f_0(\lambda)$ that should ideally follow the same spectral energy distribution as the objects to be observed. Division by this yields $\int \mathrm{d}t\,\mathrm{d}\lambda\, f_1(\boldsymbol{\theta}, \lambda)$, with a spatially uniform filter function $\mathcal{F}(\lambda)$.[4]
- Artifacts ($\mathrm{art}_{\mathrm{sky}}$) and ($\mathrm{art}_{\mathrm{cam}}$) have to be subtracted or masked out, for which I develop a method in Chapter 3.
- The smooth background light has to be modeled and subtracted. This can include a component from line emission in the sky that is reflected between the front and back side of the CCD to produce an interference pattern of *fringes*.
- The astrometric solution $\boldsymbol{x}(\boldsymbol{\theta})$ can be derived by matching positions of objects among overlapping frames and to a reference catalog with known sky coordinates.
- Finally, the absolute scaling of f_0 can be derived, e.g. by ensuring that the photometric measurements (cf. below) match the known physical values of standard stars.

The result of this procedure is a *reduced image* I representing

$$I(\boldsymbol{\theta}) = \int \mathrm{d}\lambda\, \mathcal{F}(\lambda) \left\{ f_0(\boldsymbol{\theta}, \lambda) \otimes \mathrm{PSF}'[\boldsymbol{x}(\boldsymbol{\theta}), \lambda] \right\} \ , \tag{1.112}$$

where we have defined the effective PSF' as the convolution of PSF and PRF. Images of point sources, e.g. stars, allow the reconstruction of PSF' as a function of position (e.g. Bertin, 2011). The convolution and wavelength integration with the filter function $\mathcal{F}(\lambda)$ are not (fully) reversible and thus we keep them in the image. This corresponds to the fact that information on the spectral energy distribution below the width of the filters and spatial information on scales smaller than the PSF are lost in optical imaging.

Photometry

From the image, we can obtain the flux of an object by integrating I over an aperture $\mathfrak{A}$, e.g., a circle of some fixed angular radius. This yields the aperture flux $\mathfrak{F}_{\mathcal{F},\mathfrak{A}}$ of the object weighted by the filter function $\mathcal{F}(\lambda)$,

$$\mathfrak{F}_{\mathcal{F},\mathfrak{A}} = \int_{\mathfrak{A}} \mathrm{d}^2\boldsymbol{\theta}\, I(\boldsymbol{\theta}) \ . \tag{1.113}$$

We can define the apparent *magnitude* of the object as

$$m = -2.5 \log_{10}(\mathfrak{F}_{\mathcal{F},\mathfrak{A}}/\mathfrak{F}_0) \ , \tag{1.114}$$

[4]Note that in addition to the focused mapping according to the astrometric solution, light also ends up diffusely distributed in the focal plane. The latter is the reason for which flat field images do not fully accurately correct the measured fluxes of point sources for spatial non-uniformity of $\mathcal{F}(\boldsymbol{\theta}, \lambda)$. *Star flats* giving the relative levels of detected flux of point sources as a function of position in the focal plane should be used instead.

where $\mathfrak{F}_0$ is the flux of an object of magnitude 0, as defined by the respective magnitude system.

The difference of magnitudes measured with two different filters defines a *color* and corresponds to the ratio of fluxes in the two bands. The intrinsic spectral energy distributions of distant galaxies are characteristic of the galaxy type and redshifted due to the expansion of the Universe (cf. Eqn. 1.31). Colors can therefore be the basis for *photometric redshift* estimates and can also be used for deriving the geometric scaling factor of the lensing signal (cf. Eqn. 1.84).

Shape measurement

In weak lensing analyses, the observed light of galaxies is used to measure galaxy shapes. This can be done based on second moments of the observed galaxy light distributions. We consider these at three different stages:

- *intrinsic* second moments of the galaxy light, Q^{i}_{ij}, as would be observed in the absence of noise and lensing with a Dirac-δ PSF$'$,
- *lensed* second moments Q_{ij}, transformed from Q^{i} by the lensing Jacobian, and
- *observed* second moments Q^{o}_{ij}, which include the effect of convolution with PSF$'$.

Given an object's centroid $\bar{\boldsymbol{\theta}}$, the 2×2 tensor Q^{o}_{ij} is defined as

$$Q^{\mathrm{o}}_{ij} = \frac{\int \mathrm{d}^2\boldsymbol{\theta}\, w(|\boldsymbol{\theta} - \bar{\boldsymbol{\theta}}|)\, I(\boldsymbol{\theta})\, (\theta_i - \bar{\theta}_i)\, (\theta_j - \bar{\theta}_j)}{\int \mathrm{d}^2\,\boldsymbol{\theta}\, w(|\boldsymbol{\theta} - \bar{\boldsymbol{\theta}}|)\, I(\boldsymbol{\theta})}\ , \tag{1.115}$$

where the presence of noise requires the use of a suitable weight function $w(\theta)$.

Assume, for a minute, that we know the lensed second moments Q_{ij}. The ellipticity of a galaxy can then be defined as

$$\boldsymbol{\varepsilon} := \frac{1}{Q_{11} + Q_{22} + 2\sqrt{Q_{11}Q_{22} - Q_{12}^2}} \begin{bmatrix} Q_{11} - Q_{22} \\ 2Q_{12} \end{bmatrix}\ . \tag{1.116}$$

The intrinsic second moments of the source Q^{i}_{ij} transform with the lensing Jacobian A (cf. Eqn. 1.87) to Q_{ij} as (cf. Bartelmann & Schneider, 2001, Eqn. 4.5)

$$Q^{\mathrm{i}} = AQA^T\ . \tag{1.117}$$

Consider now a source that has some intrinsic ellipticity $\boldsymbol{\varepsilon}^{\mathrm{i}}$. The transformation (derived in Seitz & Schneider, 1997) of intrinsic to lensed ellipticity $\boldsymbol{\varepsilon}$ under gravitational shear $\boldsymbol{g}$ can be approximated as

$$\boldsymbol{\varepsilon} \approx \boldsymbol{\varepsilon}^{\mathrm{i}} + \boldsymbol{g}\ . \tag{1.118}$$

We have left out, in this discussion, the complications due to the convolution of the object image with the point spread function (cf. Eqn. 1.112). For unweighted moments ($w(\theta) = 1$), the convolution could be reverted by subtracting the second moments of the PSF$'$, $Q_{ij} = Q^{\mathrm{o}}_{ij} - Q^{\mathrm{PSF}'}_{ij}$. However, due to the presence of noise, this is unfeasible. For practical application, several different approaches have been developed for overcoming these difficulties, among them moment based methods, model fitting (e.g. Zuntz et al., 2013) or

machine learning (e.g. Gruen et al., 2010). The Kaiser, Squires, & Broadhurst (1995) method uses weighted second moments and a linear correction for the PSF ellipticity and the response of the observed shapes to gravitational shear. It is introduced in more detail in Section 4.5.2 and applied in the analyses of Chapters 4 and 5.

1.4 Closing the loop: Cosmological constraints

The creation of the world did not occur at the beginning of time, it occurs every day, as Proust notes in *The Fugitive*. It is not clear what the universal memory embodied in the photons that we have followed should mean, were it not for us to gradually make sense of it. In this section, I summarize the constraints that we have gained from cosmological observations in the recent past.

As introduced in the previous sections, the most relevant parameters for describing the Universe at the present epoch are:

- the energy density of matter $\Omega_{\rm m}$ at the present epoch (split into baryons and dark matter),
- the energy density of the cosmological constant Ω_Λ (or, more generally, the energy density of dark energy and its equation of state parameter $w_{\rm de}$),
- the amplitude and scale dependence of fluctuations (σ_8 and n_s),
- and the expansion rate given by the Hubble constant H_0.

The most important probes for constraining these parameters are:

- The power spectrum of temperature fluctuations in the CMB. The heights and ratios of the peaks depend on the baryonic and dark matter content of the photon-baryon plasma, with baryons enhancing odd-numbered (compression) peaks and dark matter damping the amplitudes. The first peak position (as a *standard ruler* of known physical size) indicates the spatial scale of the sound horizon in the photon-baryon plasma at the time of decoupling, allowing a measurement of the angular diameter distance to that epoch. The observed temperature of the CMB sets the contribution of radiation to the universal energy density ($\Omega_{\rm r}$), negligible at the present epoch relative to matter and dark energy. The overall tilt of the power spectrum constrains n_s. All-sky CMB power spectrum measurements at high angular resolution were made by the *WMAP* and *Planck* satellites (cf., e.g., Komatsu et al., 2011; Planck Collaboration et al., 2014b).
- A local maximum in the galaxy-galaxy two-point correlation corresponds to the same standard ruler of baryonic acoustic oscillations (BAO), but can be measured at the respective smaller redshift to determine the evolution of the angular diameter distance. Such measurements have been made with galaxy redshift surveys, e.g., by Eisenstein et al. (2005) and Anderson et al. (2012).
- In a similar manner, *standard candles* of known luminosity allow to measure the luminosity distance to their redshift. The most useful such objects are type Ia supernovae (SNIa): they are bright enough to be observable out to redshifts $z > 1$ and exhibit a tight correlation between their observable properties and luminosity. Groundbreaking

measurements that detected an accelerated expansion of the Universe using this method were made by Riess et al. (1998) and Perlmutter et al. (1999), but the recovery of cosmic expansion can also probe non-standard cosmologies (e.g. Weller & Albrecht, 2002).

- The scale and growth of structures can be measured by means of the two-point correlation of weak gravitational *cosmic shear*. This constrains a combination of $\Omega_{\rm m}$ and σ_8 and is, due to the dependence on cosmic expansion history, also sensitive to dark energy. A summary of observational results using a variety of analysis techniques is given in the recent review of Kilbinger (2014).

- Finally, cluster cosmology can constrain both the growth of structures and the volume expansion of the Universe (cf. Section 1.2.3), thereby measuring both the matter content and the effect of dark energy on cosmic expansion (Weller et al., 2002). The redshift evolution of abundance was first used by Bahcall et al. (1997) to detect deviation from an Einstein-de Sitter universe, i.e. $\Omega_{\rm m} < 1$. More recently, studies based on catalogs of optically detected clusters (e.g. Rozo et al., 2010; Mana et al., 2013), X-ray observations (e.g. Allen et al., 2004; Vikhlinin et al., 2009b; Mantz et al., 2015) or the SZ effect (cf. Planck Collaboration et al., 2014c; Benson et al., 2013; Hasselfield et al., 2013, for recent analyses from the Planck, SPT, and ACT surveys) have been made, contributing to competitive constraints on cosmological parameters. Several such studies have used external calibration of the MOR from weak lensing of sets of individual clusters (e.g. Marrone et al., 2009, 2012; Hoekstra et al., 2012; von der Linden et al., 2014a), the main goal of the project described in Chapter 5.

Figure 1.11 shows recent constraints on cosmological parameters derived from these methods individually and in combination (for details, see Mantz et al. 2015). Notably, the probes show sometimes strong degeneracies between the different cosmological parameters. Since these are markedly different between the various probes, there is a large synergy in combining them all. The result is consistent with a flat universe containing 30 per cent of matter and 70 per cent of dark energy, the latter being a cosmological constant.

Constraints on σ_8 from cluster and CMB studies are shown in Figure 1.12, left panel, marginalized with a sharp prior of $\Omega_{\rm m} = 0.3$ to fix the associated degeneracy. Likely cause for the mutual disagreement between some of the cluster measurements are the different approaches used for the MOR calibration (cf. Mantz et al., 2015, Section 4.1 for details). This is illustrated in the right panel, which shows cosmological constraints from *Planck* SZ clusters (Planck Collaboration et al., 2015b), derived with priors on the parameters of the MOR taken from two different cluster weak lensing surveys (von der Linden et al., 2014b; Hoekstra et al., 2015) and CMB lensing.

A real discrepancy of the observed power spectrum amplitude between CMB and clusters, however, is physically possible. For instance, primordial neutrinos suppress structure formation on sufficiently small scales while they are relativistic. The time scale of this depends on the neutrino mass, connecting it to the cluster abundance likelihood. As becomes apparent from this, reliable calibration of cluster masses is a key to fully exploiting cluster cosmology (cf. Chapters 5 and 6 for related projects).

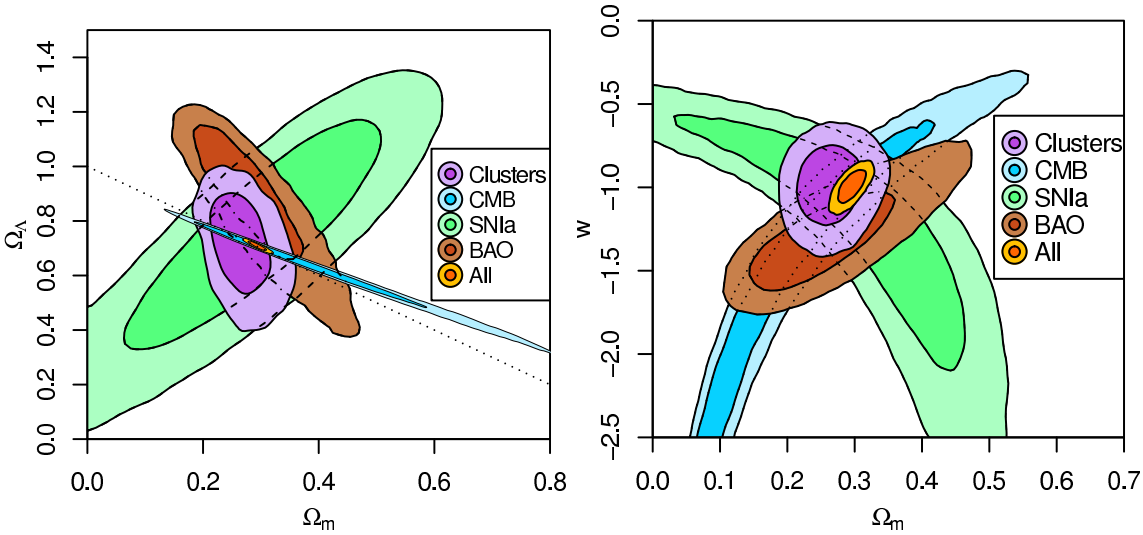

Figure 1.11: Cosmological constraints from (*WMAP* 9-year) CMB, (6dF and SDSS) BAO, (Union 2.1) SNIa, and cluster observations. Left panel: energy density of matter and cosmological constant at present epoch. Flat cosmologies are indicated by dotted line. Right panel: matter density and dark energy equation of state parameter. Figures taken from Mantz et al. (2015, left: their Fig. 5, right: Fig. 4).

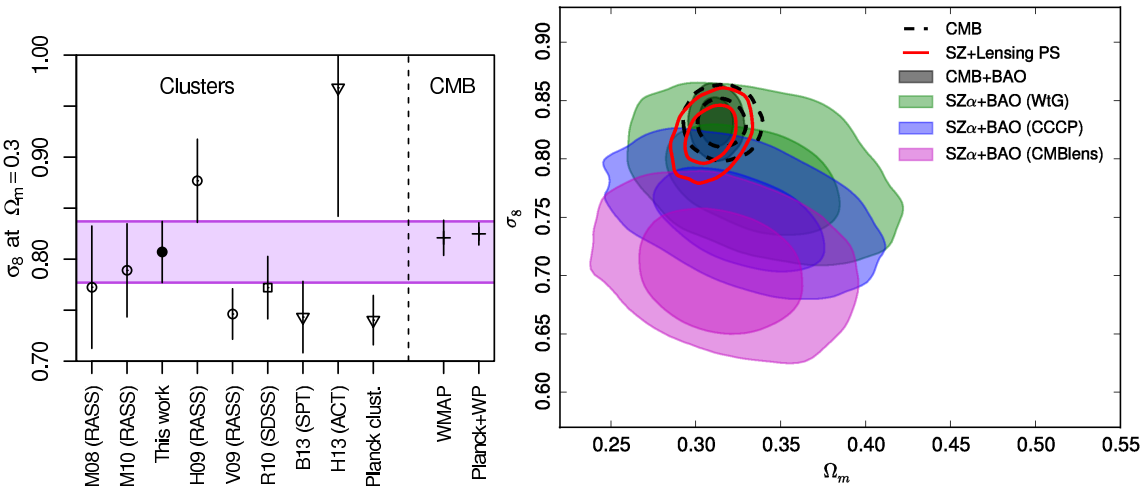

Figure 1.12: Left: Constraints on the amplitude of the matter power spectrum, σ_8, as found by various studies using cluster (left) and CMB observations (right, for *WMAP* and *Planck*+*WMAP* polarization), fixing $\Omega_m = 0.3$. Figure taken from Mantz et al. (2015, their Fig. 2). Right: Constraints on σ_8 and Ω_m from *Planck* SZ clusters with weak lensing MOR calibration from three different studies (shaded regions, von der Linden et al. 2014b; Hoekstra et al. 2015 and *Planck* CMB lensing), showing different levels of consistency with CMB results (black, dashed contours) Figure taken from Planck Collaboration et al. (2015b, their Fig. 7).

Chapter 2

Characterization and correction of charge-induced pixel shifts in DECam

Prologue

We start off where Section 1.3 ended: in the CCD detector of a telescope. The introduction of CCDs was a leap forward for astronomy. Apart from the advantage of their high quantum efficiency, this is primarily due to the fact that they allow, unlike photographic plates, to work with images that are *linear* functions of the surface brightness distribution of the sky. The images can be straightforwardly reduced, combined and interpreted.

During the science verification phase of the Dark Energy Camera, to which I was contributing, we noted, however, a number of non-linear effects: brighter stars looked larger than their faint counterparts, despite being similarly unresolved point sources that should follow the same point spread function; the variance of flat field images was not increasing with the mean level as expected for a Poissonian process; and that mean level was not a perfectly linear function of exposure time for dome flats with fixed illumination.

While the latter is due to non-linearity of the signal chain, the former two effects both appear to be related to interaction of charges already present in the pixel well with newly generated photoelectrons during charge collection, as was first proposed by Antilogus et al. (2014). In this chapter, I describe a characterization and correction of both effects.

The present chapter is based on the paper Gruen, Bernstein, Jarvis, Rowe, Vikram, Plazas, & Seitz (2015a), submitted to JINST as a proceedings to the PACCD 2014 conference at Brookhaven National Laboratory, NY, USA. I exclusively performed the analyses described herein, including data reduction, noise correlation and PSF estimation on the flat and star flat frames, conceptual and technical development of the model fitting scheme, and implementation of the simulation and correction codes. The latter are based on an image processing library written by Gary M. Bernstein. He and Vinu Vikram also contributed data reduction and covariance measurement code. Barnaby T. Rowe and Mike Jarvis helped with the integration of the correction code into GalSim. Andrés A. Plazas provided Figure 2.2. All authors contributed to discussions and proofreading.

After acceptance, the copyright for the paper will be transferred to IOP Publishing Limited and SISSA Medialab Srl. The author rights assigned in the copyright agreement contain the right to include the article in this dissertation.

Abstract

Interaction of charges in CCDs with the already accumulated charge distribution causes both a flux dependence of the point spread function (an increase of observed size with flux, also known as the brighter/fatter effect) and pixel-to-pixel correlations of the Poissonian noise in flat fields. We describe these effects in the Dark Energy Camera (DECam) with charge dependent shifts of effective pixel borders, i.e. the Antilogus et al. (2014) model, which we fit to measurements of flat-field Poissonian noise correlations. The latter fall off approximately as a power-law $r^{-2.5}$ with pixel separation r, are isotropic except for an asymmetry in the direct neighbors along rows and columns, are stable in time, and are weakly dependent on wavelength. They show variations from chip to chip at the 20% level that correlate with the silicon resistivity. The charge shifts predicted by the model cause biased shape measurements, primarily due to their effect on bright stars, at levels exceeding weak lensing science requirements. We measure the flux dependence of star images and show that the effect can be mitigated by applying the reverse charge shifts at the pixel level during image processing. Differences in stellar size, however, remain significant due to residuals at larger distance from the centroid.

2.1 Introduction

An idealized telescope focal plane is covered by a grid of equal-sized pixels that have a linear response to the flux density at their corresponding position in the sky. Charge counts contain Poissonian noise that is independent between any two pixels. The images produced by such a camera then, up to noise, represent the sky convolved with a kernel. The latter, called point spread function (PSF), can be measured from the observed profiles of point sources. The only difference between point sources, e.g. stars, of different flux levels is an amplitude by which the PSF profile is re-scaled.

Real CCDs with large well depth exhibit deviations from this picture, two of which have been known for some time. In exposures of homogeneous flux density (flat fields), the variance V at moderate to high flux levels is not linear in the flat level μ, unlike what is expected for a Poissonian process Downing et al. (2006). Secondly, the size of star images has been found to increase with flux (known as the brighter/fatter effect), e.g. in science verification data from the Dark Energy Camera (DECam), but also in many other cameras (e.g. MegaCam and LSST candidate sensors Antilogus et al. (2014), Euclid candidate sensors Niemi et al. (2014) and the Wendelstein Wide Field Imager Kosyra et al. (2014)).

The brighter/fatter effect is particularly problematic for ongoing and future large weak lensing programs such as the Dark Energy Survey (DES, The Dark Energy Survey Collaboration (2005)), the Hyper Suprime-Cam Survey (HSC, Miyazaki et al. (2012)), the Kilo Degree Survey (KiDS, de Jong et al. (2013)), or the Large Synoptic Survey Telescope (LSST, Ivezic et al. (2008)). The reason for this is that a systematic misrepresentation of the PSF in bright stars (that are used for PSF modeling) biases galaxy shape measurement, to a level that can exceed the acceptable systematics (cf. Section 2.4 and, e.g., Amara & Réfrégier (2008)). Careful correction of this effect is therefore of great importance.

Two physical phenomena have been proposed and examined with analytical and numerical models Holland et al. (2014); Rasmussen et al. (2014) that could be the cause for both observations: (1) lateral electric fields due to differences in electrical potential between pixels of different charge count (put more simply, mutual deflection of accumulating charges) and (2) an increase in lateral diffusion due to lower drift fields in pixels that are partially filled

Holland et al. (2014).

Antilogus et al. (2014); Guyonnet et al. (2015) (hereafter A14) have proposed a phenomenological model for charge self-interaction in CCDs that describes both the variance non-linearity and the brighter/fatter effect. In their model, accumulating charge shifts the effective pixel borders. In a flat field image, a pixel that has at any point during an exposure collected more charges than its neighbors due to positive contributions from Poissonian noise will, effectively, shrink. This decreases the variance and introduces a positive covariance with neighboring pixels. The charges already present in the image of a star shift pixel borders inward, such that the measured image on the pixel grid increases in size. Using laboratory and on-sky measurements with several different cameras, A14 have shown this model to reproduce the observed effects reasonably well. Both lateral electric fields and increased lateral diffusion due to lowered longitudinal electric fields are described by the same phenomenological model.

One of the instruments studied by A14 was DECam Derylo et al. (2006); Holland et al. (2007); DePoy et al. (2008); Diehl et al. (2008); Estrada et al. (2010); Kubik et al. (2010); Flaugher et al. (2012); Diehl & For Dark Energy Survey Collaboration (2012), the 3 sq. deg. camera mounted at the prime focus of the Blanco 4m telescope at the Cerro Tololo Inter-American Observatory (CTIO), currently used for DES and community observing programs. The mosaic consists of 62 fully depleted 2K×4K science CCDs with a thickness of 250μm. During the science verification phase of DECam, we detected a flux dependence of observed sizes of star images, in line with the A14 study, at a level relevant for DES science requirements.

In this work, we aim at correcting the effects of charge self-interaction in DECam images at a level tolerable for DES weak lensing science. In Section 2.2, we qualitatively characterize the brighter/fatter effect from DECam star images. Section 2.3 introduces the A14 model and explains our measurement of the model parameters from flat fields. In Section 2.4 we discuss the effect of charge self-interaction in DECam on galaxy shape measurements for weak lensing. Section 2.5 describes tests of our correction for charge self-interaction by reverse application of the model. We summarize our findings in Section 2.6.

2.2 Brighter/fatter effect in DECam

In this section, we make a phenomenological description of the flux dependence of the PSF in DECam data.

We illustrate the effect in 2D by comparing the profiles of bright and faint stars in DECam images. The left panel of Fig. 2.10 shows the residuals of normalized profiles of stars at a peak flux (SExtractor Bertin & Arnouts (1996) parameter `FLUX_MAX`) of 5000 and 20000, i.e. $(\mathrm{PSF}_{20000} - \mathrm{PSF}_{5000})/\mathrm{PSF}_{5000}$ where PSF_N is the PSF model made from stars around `FLUX_MAX` $= N$. Flux is missing in the central region of the profile and re-appears on an annulus at $\approx 2 - 4$ pix radius.

We use the flux deficit in the central pixel of the normalized PSF model as a metric to answer a number of questions. To this end, we use i band images of the globular cluster ω Centauri taken with DECam during science verification on Feb 02 2013 with homogeneous seeing conditions. We process these as described in Section 2.5, without the reverse charge shift model applied. Fig. 2.1 shows results as a function of `FLUX_MAX` for star images with two different exposure times and for a data reduction scheme applying or not applying,

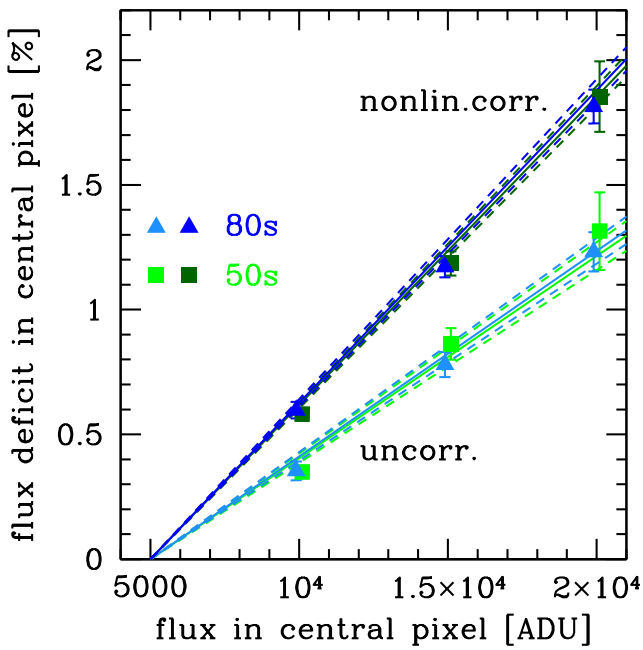

Figure 2.1: Flux deficit of normalized PSF model in central pixel relative to a PSF model made with stars in peak flux (`FLUX_MAX`) bin centered on 5000 ADU. We find that the flux deficit is approximately linear in flux level (solid lines show best linear fit, dashed lines 68 per cent confidence intervals), independent of exposure time (green squares: 50s, blue triangles: 80s), and increases when signal chain non-linearity is corrected for (dark green/blue: corrected, light green/blue: uncorrected).

respectively, a correction for the known signal chain non-linearity of DECam.[1] We find that

- the relative flux deficit in the center of bright stars due to the brighter/fatter effect is well described as linear in flux, as indicated by the solid lines that are good fits to the data points;
- the amplitude of the flux deficit does not depend on exposure time, but only on the measured count level, as visible from the agreement between the blue and green lines (dashed lines give confidence limits for the linear fit); this indicates that the charges must be moved while being collected, not while they are waiting for readout in the pixel potential well;
- the effect is amplified when the high level signal chain non-linearity, a property of the readout electronics, is corrected for; relative photometry of stars in frames with different exposure times shows that correction for high level signal chain non-linearity is necessary for restoring the physical charge level present in the CCDs (cf. Bernstein, presentation at PACCD2013 conference[2]); we will therefore apply the signal chain non-

[1]The non-linearity correction was determined by comparing the mean count levels of dome flats of different exposure time. At the 20k ADU level charge counts are approximately 1% lower than expected from linear response.

[2]See `https://indico.bnl.gov/event/cosmo2013`.

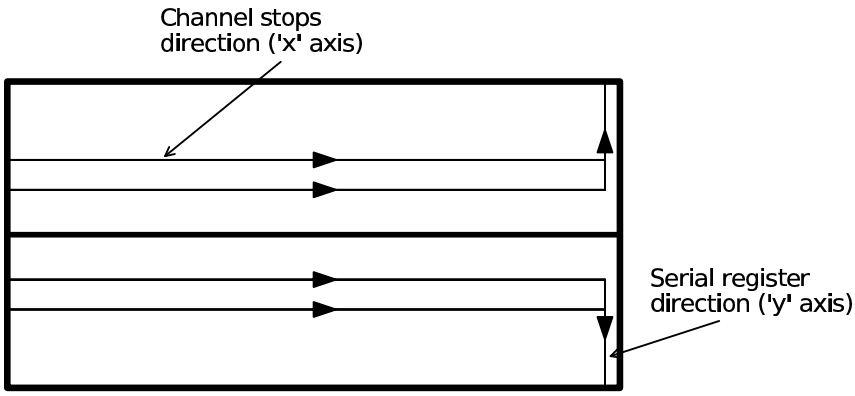

Figure 2.2: Sketch of a DECam CCD and definition of our coordinate system, with the x and y axis parallel to the channel stops and the serial register, respectively. The split of the chip into two amplifier regions is indicated by the central horizontal line.

linearity correction in all following analyses.

2.3 Model

We briefly introduce the model of A14 before we discuss our approach of constraining the model parameters in Sections 2.3.2 and 2.3.3.

The basic idea is that charges q_{kl} in any pixel (k, l) influence the path of newly generated charges on their way into the pixel well.[3] As a result, they induce a shift in the effective border of a pixel (i, j), i.e., they change the mapping of physical area on the chip onto the pixels.

Consider pixel (i, j) and its four borders, which we label as $L = (-1, 0)$, $R = (1, 0)$ (left/right border to neighbors along x axis) and $T = (0, 1)$, $B = (0, -1)$ (top/bottom border to neighbors along y axis). The shift in any of these we call δ_{ij}^X, where $X \in \{L, R, T, B\}$. For a definition of our coordinate system, refer to Fig. 2.2.

We assume the border shift to be linear in the surrounding charge (including charge in pixel (i, j) itself) and dependent on the *lag* $(k - i, l - j)$ between pixel (i, j) and (k, l),

$$\delta_{ij}^X = \sum_{kl} a_{k-i,l-j}^X q_{kl} \ . \tag{2.1}$$

The parameters of the model are the *shift coefficients* a_{ij}^X. In all cases, δ_{ij}^X shall be defined such that the positive direction is outward from pixel (i, j).

The change in charges observed in pixel (i, j) is the sum of $\delta_{ij}^R \frac{q_{ij}+q_{i+1,j}}{2}$ and the corresponding terms for L, T, B. Here, we have approximated the charge density at the pixel border by the mean of the neighboring pixels and defined the δ as fractions of a full pixel width. The observed charge Q_{ij} then becomes

$$\begin{aligned} Q_{ij} = q_{ij} \quad &+ \quad \frac{q_{ij} + q_{i+1,j}}{2} \sum_{kl} a_{k-i,l-j}^R q_{kl} \quad + \quad \frac{q_{ij} + q_{i-1,j}}{2} \sum_{kl} a_{k-i,l-j}^L q_{kl} \\ &+ \quad \frac{q_{ij} + q_{i,j+1}}{2} \sum_{kl} a_{k-i,l-j}^T q_{kl} \quad + \quad \frac{q_{ij} + q_{i,j-1}}{2} \sum_{kl} a_{k-i,l-j}^B q_{kl} \ . \end{aligned} \tag{2.2}$$

[3]Note that this could be due to a combination of lateral fields and changes in lateral diffusion.

2.3.1 A priori symmetries

Assuming conservation of effective area, the area lost in one pixel is gained by its neighbor,

$$\begin{aligned} \delta^R_{ij} &= -\delta^L_{i+1,j} \\ \delta^T_{ij} &= -\delta^B_{i,j+1} \end{aligned} \tag{2.3}$$

Eqn. 2.1 fulfills these equalities for general charge distributions q if and only if

$$\begin{aligned} a^L_{ij} &= -a^R_{i+1,j} \ , \\ a^B_{ij} &= -a^T_{i,j+1} \ . \end{aligned} \tag{2.4}$$

The number of free parameters is further reduced by two parity symmetries. The first is invariance of charge shifts under change of sign of one coordinate axis,

$$\begin{aligned} a^{0,\pm1}_{i,j} &= a^{0,\pm1}_{-i,j} \ , \\ a^{\pm1,0}_{i,j} &= a^{\pm1,0}_{i,-j} \ . \end{aligned} \tag{2.5}$$

Another parity symmetry is that charges on opposite sides of the pixel border cause opposite shifts,

$$\begin{aligned} a^{0,\pm1}_{i,j} &= -a^{0,\pm1}_{i,\pm1-j} \ , \\ a^{\pm1,0}_{i,j} &= -a^{\pm1,0}_{\pm1-i,j} \ . \end{aligned} \tag{2.6}$$

With these symmetries, the free parameters of the model are reduced to, e.g., a^R_{ij} for $i > 0$, $j \geq 0$ and a^T_{ij} for $i \geq 0$, $j > 0$. Note that we discuss further empirically assumed symmetries, necessary to unambiguously constrain the parameters, in Section 2.3.3.

2.3.2 Flat field covariances

The mixing of independent Poissonian processes q into observed counts Q in Eqn. 2.2 causes a correlation of noise in flat-field images. A14 collect the terms at first order in a to find[4]

$$\mathrm{Cov}(Q_{00}, Q_{ij}) = 2\mu^2 \sum_{X=T,B,L,R} a^X_{ij} \ , \tag{2.7}$$

assuming μ is the mean charge count level and Poisson variance $[Var(q) = \mu]$ of charges in pixels in the flat image. We can thus use measurements of flat field covariances to constrain the a parameters under suitable symmetry assumptions. Note that, in addition, there is a change in variance, which can be written using the above symmetries as

$$\Delta\mathrm{Var}(Q_{00}) = -4\mu^2(a^R_{1,0} + a^T_{0,1}) \ , \tag{2.8}$$

equal with negative sign to the sum of all covariances introduced between Q_{00} and the surrounding pixels.

Note that if we convert Q and μ to quantities in ADU with some gain g, Eqns. 2.7 and 2.8 still hold with the same coefficients a. In Eqn. 2.2 we have to multiply the coefficients $a \to a' = ga$ to get the change in observed ADU.

[4]Note that in their definition the a are only half as large, origin of the factor of 2 here.

Measurement pipeline

We measure the covariances as follows, using all 10 s ($\approx$ 15000 ADU) dome flat fields in the r band from the full first year of DECam observations (2013-08-15 until 2014-02-09). We perform overscan and bias subtraction based on the nightly median bias. Inter-CCD cross-talk between the two amplifiers and the signal chain non-linearity are corrected for. Since cosmic rays are systematic contaminants of the observed covariances, we run SExtractor on each flat image to detect all groups of three or more pixels 3σ above the background. For each night, we mask the union of these 2×2 box-convolved object masks, a bad pixel mask, and edge distortions Holland et al. (2009); Kuhlmann et al. (2011); Plazas et al. (2014). We re-scale each flat image so as to make median count levels of all frames taken in the same night match, which changes the levels below the per cent level. From each pixel of the flat images, we subtract the mean of that pixel over all n flats of the night.

From these residual images, we estimate covariances out to lags of $(8, 8)$. We re-scale the residuals by $\sqrt{\frac{n}{n-1}}$ to correct the bias of the maximum likelihood ensemble covariance estimator. Since each chip has two readout channels, we make measurements separately for the 118 halves of chips in DECam,[5] i.e. on a chip by chip and amplifier by amplifier basis.

Covariances are predicted by the A14 model to scale with the square of the count level μ (cf. Eqn. 2.7). We have verified this behavior of measured covariances from a PTC series of pairs of flat fields of different exposure times. For all following results, we therefore normalize our covariance measurements by μ^2 to make them comparable despite somewhat varying flat levels between different nights and filters.

Checks for systematics

Each of the $\approx$1200 flat images yields an independent estimate, such that we can perform a number of systematic checks. For each chip, we make comparisons between different measurements that should give the same result:

- Since the statistics of our covariance estimator is very close to Gaussian, we expect no significant differences between using the mean and median of the $\approx$ 1200 independent measurements. Outliers, however, would influence the mean more strongly than the median.

- Chirally-symmetric lags (e.g. $(1, 1)$ and $(1, -1)$) measure covariances on disjunct sets of pairs of pixels that are, however, predicted to be the same from the model.

- If chips are homogeneous and the model is correct, then $\mathrm{Cov}(Q_{00}, Q_{ij})/\mu^2$ should agree between the two halves of the chip read out by different amplifiers (cf. Fig. 2.2) despite their different gain values.

We find all these measurements to be consistent within the errors with systematic effects that are small compared to our targeted accuracy, out to large lags (cf. Fig. 2.3).

[5] Of the 62 chips, two (N30 and S30, i.e. `CCDNUM` 61 and 02) are damaged and one (S7, `CCDNUM` 31) has a time-varying offset, which is why we exclude them from our analysis.

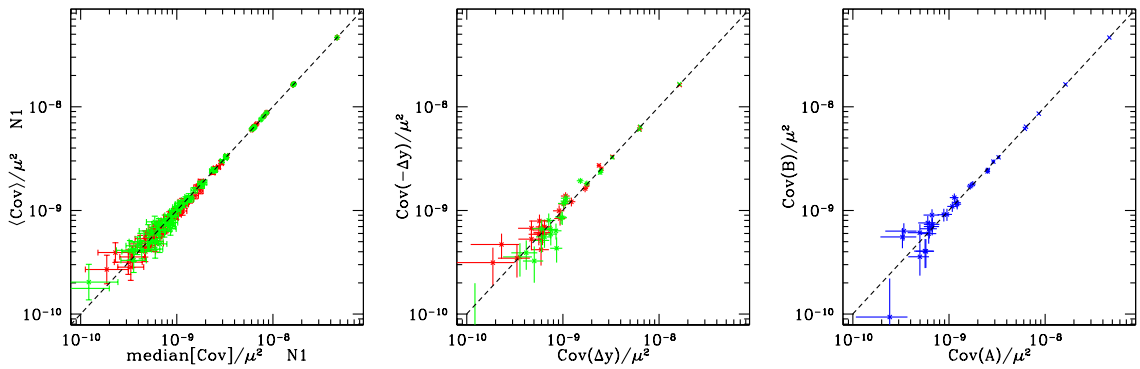

Figure 2.3: Checks for systematics in measured covariances, shown for DECam chip N1. Left: median versus mean value of ≈ 1200 measurements for each lag (red: amplifier A, green: amplifier B). Center: covariances measured at lag (i, j) versus $(i, -j)$. Right: covariances measured in amplifier A region versus amplifier B region. From these tests we conclude that the effect of outliers in measured covariances, artifacts, and differences within the chip are negligible.

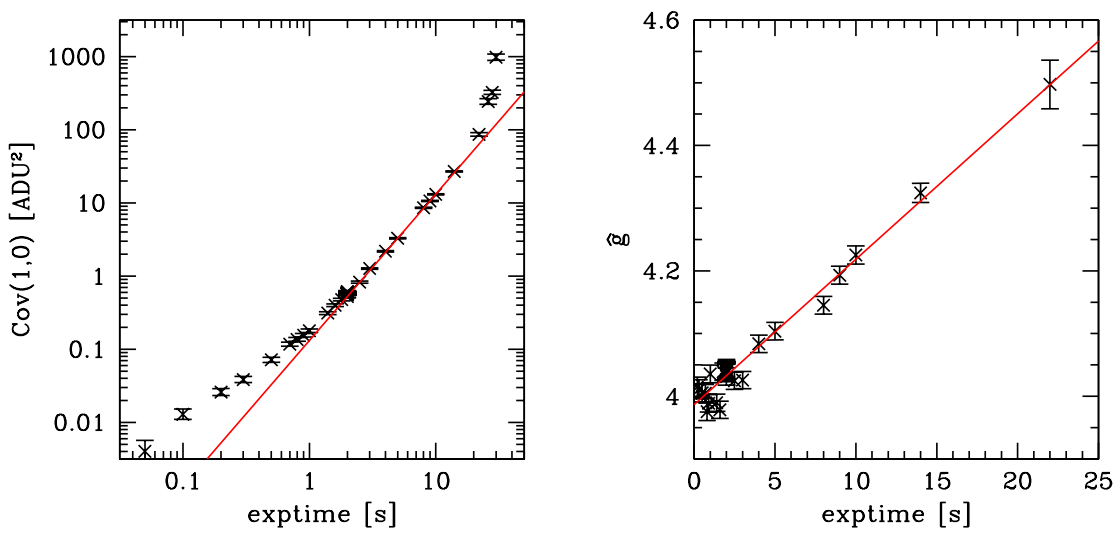

Figure 2.4: Scaling of covariance and measured gain with count level, as measured in a series of pairs of flat field exposures with different exposure time. Left panel: covariance at (1,0) lag, with $\mu^2 \propto t^2$ scaling around the $t = 10$ s point indicated by red line. Right panel: measured gain $\hat{g} = \mu/V$, with the red line as a linear best fit to the data.

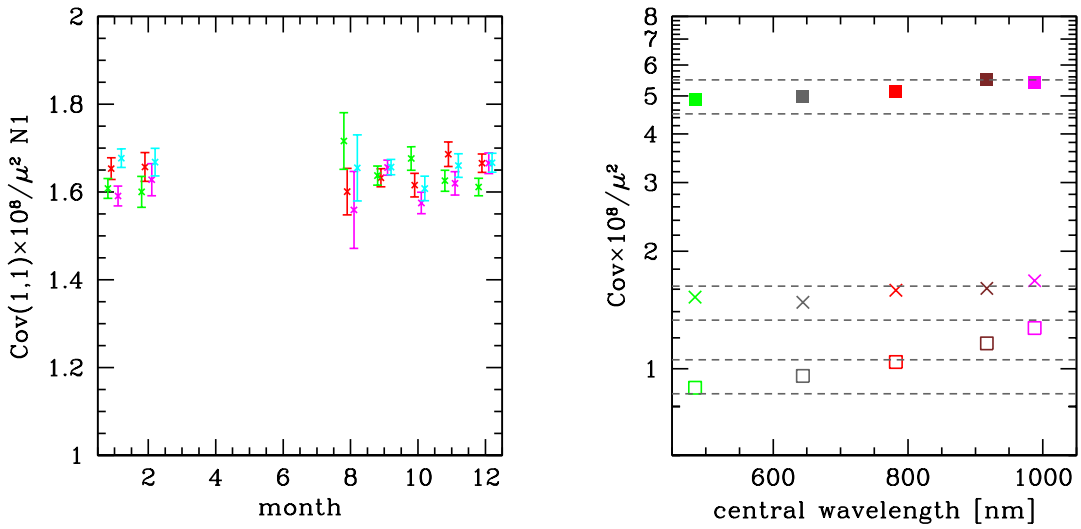

Figure 2.5: Left: Test for time stability of flat field covariances for DECam chip N1. Shown are measurements in flat frames of each month of the DES season of the covariance at lag $(1, 1)$ (red and green for amplifier A and B, respectively) and $(1, -1)$ (magenta and blue). The four measurements are offset on the time axis for readability. No significant time variability is observed. Right: Wavelength dependence of pixel-to-pixel covariances as measured in DECam g, r, i, z, and Y flat field images. Measurements are plotted at the respective central wavelength for lags $(1, 0)$ (solid symbols), $(1, 1)$ (crosses) and $(0, 1)$ (open symbols). Intervals of $\pm 10\%$ around the r band measurements we use to fix the parameters of the model are indicated by dashed lines.

Flux scaling

Covariances of the flat field Poisson noise are predicted to scale with μ^2 according to the model of Eqn. 2.7. Measured gain, i.e. the ratio of count level and variance, is predicted to rise linearly with flux due to the lowered variance. Other effects, such as correlated read noise, charge transfer inefficiency or other non-linearities in the signal chain, could cause different scalings. We test this by measuring covariances and gain at a range of count levels.

To this end, we analyze a photon transfer curve (PTC) series of pairs of flat field images with exposure times of $0.05 \ldots 30$s at a light level of $\approx$ 1500ADU s^{-1}. Figure 2.4 shows covariances and gains measured from each pair, averaged over all valid chips. At very low levels, there is a floor of covariance below Cov < 0.01, which could be due to a small correlation of noise in the signal chain or a low-level non-linearity. At larger levels, correlations rise more quickly than predicted, potentially due to saturation and charge transfer effects. In the range of $2 \ldots 15$ s exposure time, however, the Cov $\propto \mu^2$ scaling describes the measurements well.

Likewise, measured gain is predicted by the model as linearly increasing with count level. Gain measurements in flats of $\approx$20 s exposure time overestimate the true gain by $\approx$10 % and we correct the gains used in the DES data management system Desai et al. (2012); Mohr et al. (2012) for this effect.

Wavelength dependence

A14 found the noise correlations to be achromatic for the e2v-250 CCD run with nominal voltage configuration. This is in line with an effect that acts on the charges primarily in

the last few μm of their drift path and therefore is almost independent of conversion depth. We measure covariances on g, i, z, and Y band flats from 20 nights to test for a potential wavelength dependence. Results for the three innermost lags, averaged over all 59 chips, are shown in the right panel of Fig. 2.5. Both g and i measurements are consistent with the r band baseline model within 10%. For the $(0, 1)$ lag, the increase from g to Y band is at the 40% level between the g and Y band. In $(1, 0)$ and $(1, 1)$ there are indications of an increasing trend, although at a weaker level.

Time stability

We also test our measurements for time stability (cf. Fig 2.5, left panel) by binning the measurements on a monthly basis. We find no evidence for time variation in any of the 59 chips used in our study.

Results

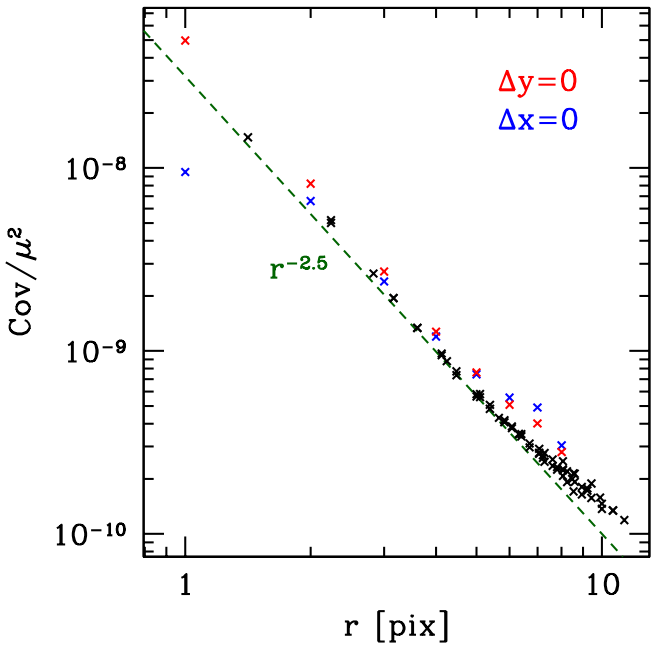

Figure 2.6: Pixel-to-pixel covariance as function of distance $r = \sqrt{i^2 + j^2}$. The long axis and readout direction is defined as x. Correlations with pixels along the same x or y coordinate are plotted in blue and red, respectively. A $r^{-2.5}$ power-law with arbitrary amplitude is indicated by the dashed green line.

We show covariances as a function of lag distance $r = \sqrt{i^2 + j^2}$, averaged over the 59 chips, in Fig. 2.6. We measure positive correlations with a signal-to-noise ratio of ≈ 15 even at the outermost point $r = \sqrt{128}$. Off-axis covariances show a smooth power-law drop-off with radius, with indications for a break at around $r \approx 5$. The behavior of on-axis coefficients is slightly different, with a higher amplitude and a low outlier at the $(0, 1)$ lag, i.e. for neighbors across the channel stop. We note that the ratio $\mathrm{Cov}(1, 0)/\mathrm{Cov}(0, 1) \approx 5$ is in the range

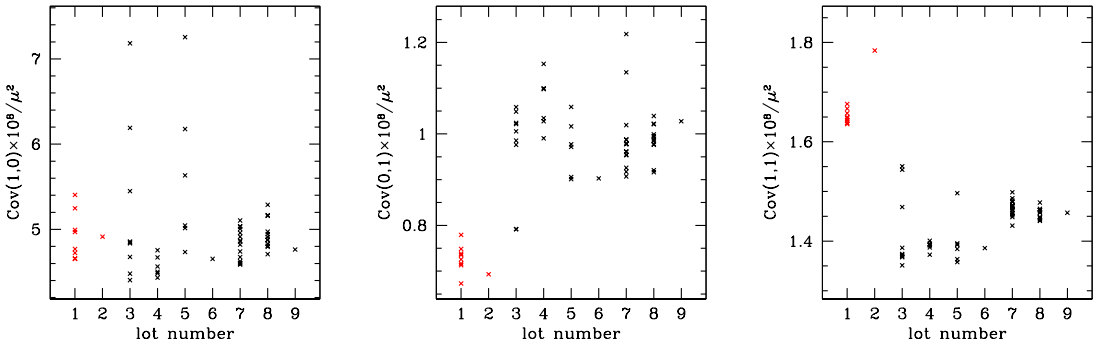

Figure 2.7: Cov/μ^2 measured from flat fields for each of the DECam chips, plotted as a function to CCD production lot. Marked in red are the two high-resistivity lots. Left: $(1,0)$ lag (left/right neighbor along readout direction), center: $(0,1)$ lag (top/bottom neighbor across the channel stop), right: $(1,1)$ lag (diagonal neighbor).

the Rasmussen et al. (2014) simulations predict for reasonable channel stop barrier dipole moments.

We test for variations of the level of covariances between different chips. Since all chips in DECam use the same nominal bias and clock voltages, the reason for such differences would have to be connected to chip properties. The science chips used in DECam were produced in nine different production lots. For simplicity of notation, we label the two high resistivity (10.6-14.2 kΩ cm) lots 107419 and 112094 as 1 and 2 and the remaining lots (with lower resistivity of 4.3-6.2 kΩ cm) 123194, 123195, 124750, 124753, 135959, 135960 and 135961 as 3-9 (in this order). Fig. 2.7 shows results for the three nearest lags. We find variations in amplitude at the $\approx 20\%$ level from lot to lot. Variations within the lots are significantly smaller, although with outliers, particularly at the $(1,0)$ and $(1,1)$ lag in lots 3 and 5.

The two high resistivity lots have covariances $\approx 20\%$ higher (lower) than the low resistivity ones in the $(1,1)$ (the $0,1$) lag. Larger lags show a similar resistivity dependence as $(1,1)$. For the $(1,0)$ lag, no strong resistivity dependence is observed. This is evidence for a mixing of two effects with different dependence on resistivity and distance. While this suggests that resistivity is a relevant factor, other unknown lot-to-lot variations that coincide with resistivity by chance cannot be excluded, particularly since the high resistivity lots were cut from a different boule than the remaining CCDs.

2.3.3 Assumed model symmetries

The parameters of the model are the shift coefficients a from Eqn. 2.1. They are connected to the measured covariances (see Section 2.3.2) by Eqn. 2.7. With only the symmetries of Eqns. 2.4ff, however, the shift coefficients are not unambiguously constrained by flat field covariances (cf. A14).

This is most comprehensibly exemplified by the following degeneracy. Finding all covari-

ance terms that contain any a^X_{ij} with $i < 2$ and $j < 2$

$$\begin{aligned}
\Delta\mathrm{Cov}(Q_{00}, Q_{00}) &= -4\mu^2(a^R_{1,0} + a^T_{0,1}) \\
\mathrm{Cov}(Q_{00}, Q_{0,\pm1}) &= 2\mu^2(a^T_{0,1} - 2a^R_{1,1}) + \ldots \\
\mathrm{Cov}(Q_{00}, Q_{\pm1,0}) &= 2\mu^2(a^R_{1,0} - 2a^T_{1,1}) + \ldots \\
\mathrm{Cov}(Q_{00}, Q_{1,1}) &= 2\mu^2(a^R_{1,1} + a^T_{1,1}) + \ldots
\end{aligned} \tag{2.9}$$

we see that all covariances (including the variance defect ΔCov) are degenerate under the transformation

$$\begin{aligned}
a^R_{1,0} &\rightarrow a^R_{1,0} + \Delta \\
a^T_{0,1} &\rightarrow a^T_{0,1} - \Delta \\
a^R_{1,1} &\rightarrow a^R_{1,1} - \Delta/2 \\
a^T_{1,1} &\rightarrow a^T_{1,1} + \Delta/2
\end{aligned} \tag{2.10}$$

with an arbitrary constant Δ, which compensate the smaller shifts of one pixel border by larger shifts of the perpendicular ones. Clearly, however, the effect on inhomogeneous surface brightness images is not invariant under the above change on model coefficients.

Our approach is to assume two additional symmetries (the rotational and projection symmetry described below) that are suggested by the covariance measurements. For the above degeneracy, this entails setting $a^R_{1,1} = a^T_{1,1}$ and modelling the observed asymmetry in $\mathrm{Cov}(Q_{00}, Q_{0,\pm1}) \neq \mathrm{Cov}(Q_{00}, Q_{\pm1,0})$ by differences in $a^R_{1,0}$ and $a^T_{0,1}$ only.

Rotational symmetry

All off-axis lags rotated by $\pi/2$ have covariances measured to be equal at the level of agreement between the A and B sides of chips, i.e. $\mathrm{Cov}(Q_{00}, Q_{ij}) = \mathrm{Cov}(Q_{00}, Q_{ji})$ for $i > 0$, $j > 0$. This symmetry is predicted by the model if

$$a^R_{ij} = a^T_{ji} \;\; \forall i > 0,\, j > 0\,. \tag{2.11}$$

If we assume this symmetry, we forfeit almost half of our observables (because the covariances at lag (i, j) and (j, i) are now two measurements on the same combination of shift coefficients). In order to break the degeneracies, it would suffice to set $a^R_{i,i} = c_i a^T_{i,i}$, $i > 0$, with a set of assumed ratios c_i. Due to the agreement of measured covariances at rotated lags, however, this would just yield a statistically consistent (yet noisier) model.

Projection symmetry

The lateral electric field due to two charges at the same distance from a border should result from an electrostatic force that has the same amplitude but a different direction.[6] The most similar pairs of charges in terms of distance are ones at lag (i, j) and (j, i). If we assume that the border displacement is proportional to the component of the force projected onto the normal vector of a border, we have (for $i > 1$ or $j > 1$)

$$a^R_{j,i} = r(i, j) a^R_{i,j}\,, \tag{2.12}$$

[6] Note that the situation is different for lateral diffusion, which is affected by the change in the longitudinal electric field. For distant enough pairs, however, lateral electric fields appear to be the dominant effect.

where

$$r(i,j) = \frac{j-0.5}{i-0.5}\sqrt{\frac{(i-0.5)^2+j^2}{(j-0.5)^2+i^2}}\ . \tag{2.13}$$

For a^T, we write the analogous

$$a^T_{j,i} = r^{-1}(i,j)a^T_{i,j}\ . \tag{2.14}$$

As we find from a first iteration of fitting, the fall-off of shift coefficients with radius is close to a power-law with slope $\alpha = -2$. We use that to refine Eqn. 2.13 as

$$r'(i,j) = r(i,j)\sqrt{\frac{(j-0.5)^2+i^2}{(i-0.5)^2+j^2}}^{\alpha} = \frac{j-0.5}{i-0.5}\left(\frac{(i-0.5)^2+j^2}{(j-0.5)^2+i^2}\right)^{3/2} \tag{2.15}$$

and insert r' instead of r in Eqns. 2.12 and 2.14 for our final model.

2.3.4 Fitting of coefficients

Assuming these symmetries, we have reduced the vector $\boldsymbol{a}$ of independent coefficients to $a^R_{1,0}$, $a^T_{0,1}$, $a^R_{1,1}$ and $a^R_{i,j}$ for $1 < i \geq j \geq 0$ (a total number of $\sum_{i=0}^{n}(i+1) = \frac{1}{2}(n+1)(n+2)$ when going out to a maximum of n pixels distance). This matches the dimension of the vector $\boldsymbol{c}$ of independent measured covariances at the same lags.

Out to lags of $\Delta = 3$ we use the direct measurement of covariances of each chip individually. At larger distances, the chip-wise signal-to-noise ratio of the covariances is low. We therefore assume a power-law fall-off of covariances with radius, as observed in Section 2.3.2,

$$\mathrm{Cov}(i,j) = A(i^2+j^2)^{-\beta/2} \tag{2.16}$$

with $\beta = 2.5$. We fit three independent amplitudes (one for lags along the x and y axis and one for off-axis pixels) to the covariances measured between 3 and 5 pixels separation. Covariances out to a maximum lag of 25 are extrapolated from this model.

Using Eqn. 2.7 and the symmetries we express $\boldsymbol{c}$ as a linear function of $\boldsymbol{a}$, $\boldsymbol{c} = M\boldsymbol{a}$. We invert to find $\boldsymbol{a} = M^{-1}\boldsymbol{c}$ as a function of the measured and extrapolated vector of covariances.

We note that this approach is somewhat different from the one proposed by Guyonnet et al. (2015), who model the radial fall-off of the shift coefficients in LSST candidate sensors by an exponential integral.

Tests

We perform two consistency tests of the fitted model.

By comparing to measurements (Fig. 2.8, left panel), we confirm that the model correctly reproduces (at lags ≤ 3) and extrapolates (at larger lags) the observed covariances.

We further compare the fitted coefficients to our gain measurements from the PTC series (cf. Fig. 2.4). The deviation of $\hat{g}$ from the true gain g is predicted to be linear in flux with a slope of $4g(a^R_{1,0} + a^T_{0,1})$. We show the measured slope from the PTC series plotted against model parameters for all chips in Fig. 2.8 (right panel), finding the two to be in agreement at the 10% level. Note that the fitted $a^R_{1,0} + a^T_{0,1}$ are quite sensitive to changes in the shift coefficients at large radii, i.e. the maximum lag used or the power-law coefficient of Eqn. 2.16.

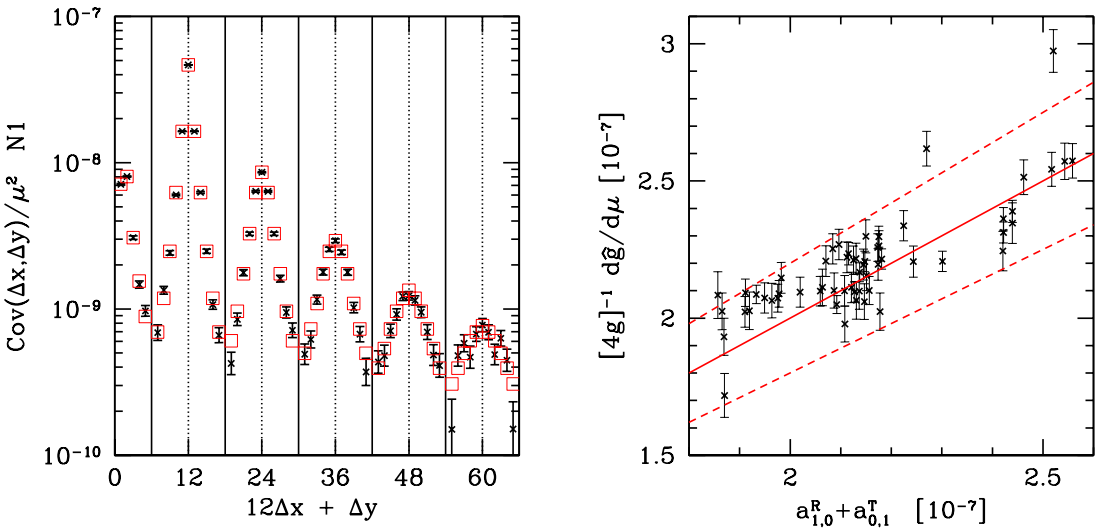

Figure 2.8: Tests of the fitted shift coefficient model. Left panel: measured (black points with error bars) and model (red open squares) covariance coefficients for lags out to 5 for CCD N1. Right panel: comparison of slope of observed gain $\hat{g}$ w.r.t. flat count level μ to sum of model coefficients for all chips. According to Eqn. 2.8, we expect the two quantities to relate with a factor of $4g$ (solid red line). The mean agreement is better than at the ten per cent level (dashed red lines).

Results

We show the fitted shift coefficients a^R of one exemplary chip in Fig. 2.9. The fact that for rows at $\Delta y \geq 2$ there is a maximum at $\Delta x > 1$ (or, equivalently, that curves for constant Δx cross as a function of Δy) is due to projection effects: at larger Δx the separation increases, but the electrostatic force is aligned closer to the normal of the pixel border. Using the projection angle θ, we correct for this effect by normalizing with $\cos\theta = [\Delta x - 0.5]/[\sqrt{(\Delta x - 0.5)^2 + \Delta y^2}]$.

The de-projected coefficients $a^R_{ij}/\cos\theta$ appear to follow a single, power-law radius dependence (Fig. 2.9, right panel). The coefficient $a^T_{0,1}$ is the strongest outlier from this trend. For chip N1, $a^T_{0,1} \approx 1.0 \times 10^{-7}$ whereas $a^R_{1,0} \approx 1.4 \times 10^{-7}$, indicating that an additional physical mechanism acts on directly neighboring pixels.[7] The moderate asymmetry of charge shifting is amplified by the differential nature of how the shift coefficients contribute to the pixel-to-pixel covariance to yield the strong asymmetry between $\mathrm{Cov}(1,0)$ and $\mathrm{Cov}(0,1)$ that we observed in Fig. 2.6.

2.4 Effects on galaxy shape measurement

One of the primary science applications of DES is to probe cosmic shear and the weak gravitational lensing effect of galaxies and clusters of galaxies. The measurement of gravitational shear $\gamma = \gamma_1 + i\gamma_2$ is based on a measurement of galaxy shapes $\epsilon = \epsilon_1 + i\epsilon_2$. The latter can

[7] Compare also to the observed inverted resistivity dependence of the $(0,1)$ lag. Note, however, that from the PTC flat series we find all covariances to be consistent with a μ^2 scaling as predicted by the charge shift model.

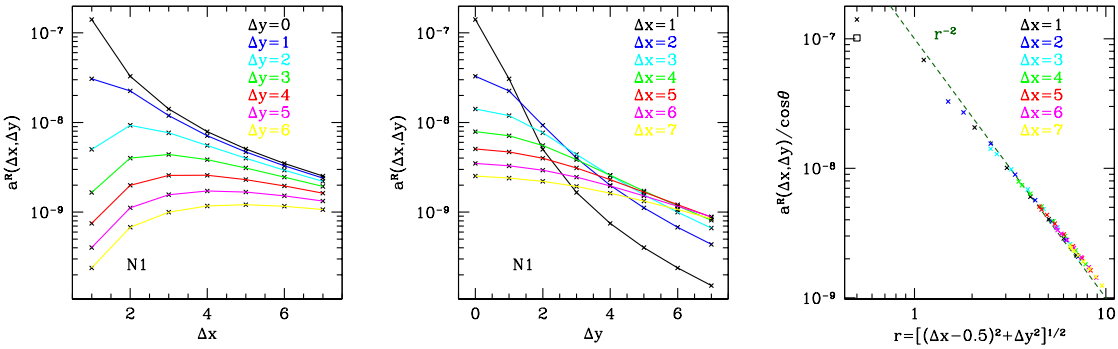

Figure 2.9: Shift coefficients a^R of chip N1 plotted as function of Δx (left panel) and Δy (center). Projection effects are corrected in the right panel, where we normalize coefficients by the cosine of the angle between pixel border normal vector and direction of the lag. This leads to a well-behaved r^{-2}-like power-law behavior (indicated by dotted green line) of the coefficients, with the neighbors $a^R_{1,0}$ and $a^T_{0,1}$ (the latter is overplotted with the open symbol) as outliers.

be defined based on second-order moments of the pre-seeing surface brightness profile $I(\boldsymbol{\theta})$ of a galaxy centered at $\boldsymbol{\theta} = (0, 0)$,

$$\mathcal{Q}_{ij} = \frac{\int I(\boldsymbol{\theta})\theta_i\theta_j \mathrm{d}^2\theta}{\int I(\boldsymbol{\theta})\mathrm{d}^2\theta} \ , \tag{2.17}$$

as

$$\begin{pmatrix} \epsilon_1 \\ \epsilon_2 \end{pmatrix} = \left(\mathcal{Q}_{11} + \mathcal{Q}_{22} + 2\sqrt{\mathcal{Q}_{11}\mathcal{Q}_{22} - \mathcal{Q}_{12}^2}\right)^{-1} \times \begin{pmatrix} \mathcal{Q}_{11} - \mathcal{Q}_{22} \\ 2\mathcal{Q}_{12} \end{pmatrix} \ . \tag{2.18}$$

When second moments are measured with uniform weight as in Eqn. 2.17, deconvolution with the PSF can be performed by subtracting the observed and PSF second moments,[8]

$$\mathcal{Q}_\star^{\mathrm{gal,\ dec}} = \mathcal{Q}_\star^{\mathrm{gal,\ obs}} - \mathcal{Q}_\star^{\mathrm{PSF}} \ . \tag{2.19}$$

Observationally, one estimates $\mathcal{Q}_\star^{\mathrm{PSF}}$ from the second moments of star images. Since the stars used for this are typically at a high flux level in comparison to the galaxy images, the primary effect of charge-self interaction is a misrepresentation of the PSF second moments.[9]

In order to simulate the full effect on charge self-interaction on shape measurement, we implement the A14 model in GalSim Rowe et al. (2014).[10] Simulating PSF-convolved galaxy and star images with the effect applied, we estimate shapes using Eqns. 2.17-2.19. We quantify biases in the measured shape ϵ^{meas} relative to the input galaxy shape ϵ^{true} as

$$\begin{pmatrix} \epsilon_1^{\mathrm{meas}} - \epsilon_1^{\mathrm{true}} \\ \epsilon_2^{\mathrm{meas}} - \epsilon_2^{\mathrm{true}} \end{pmatrix} = \begin{pmatrix} m_1\epsilon_1^{\mathrm{true}} + c_1 \\ m_2\epsilon_2^{\mathrm{true}} + c_2 \end{pmatrix} + \begin{pmatrix} p_1^1 & p_1^2 \\ p_2^1 & p_2^2 \end{pmatrix} \cdot \begin{pmatrix} \epsilon_1^p \\ \epsilon_2^p \end{pmatrix} \ , \tag{2.20}$$

[8]This is a simplified procedure for shape measurement, which in practice needs to use appropriate weighting to prevent the divergence of noise. Biases in real shape measurement pipelines should, however, be similar since the primary effect of charge self-interaction is a change in PSF size due to shifting of charges on scales of its FWHM.

[9]Note that the effect can be alleviated by using fainter stars only, which are less affected by charge self-interaction (for DECam analyses, cf. e.g. Melchior et al. (2014)).

[10]cf. `https://github.com/GalSim-developers/GalSim/`

with multiplicative and additive biases m_i and c_i (e.g. Heymans et al. (2006)) and leakage terms p^i_j of the PSF ellipticity ϵ^p_i into the same and respective other component of shear.

For the fiducial simulation settings, we choose the following conservatively realistic parameters. The pre-seeing galaxy and PSF profile are modelled as Gaussians with full-width at half-maximum $\mathrm{FWHM_{gal}} = 0.5''$ and $\mathrm{FWHM_{PSF}} = 0.9''$, converted to the DECam pixel scale of $0.27''$ per pixel and Gaussian standard deviation $\sigma \approx \mathrm{FWHM}/2.35$. We draw the star image with a FLUX_MAX in the central pixel of 60k charges. The galaxy is chosen to have a total flux of 4000 charges. We add no noise to the image, assume a background level of $b = 0$ in the fiducial settings and set both galaxy and star image centroid to fall on a pixel center. For the shift coefficients, we use the mean values over the individually fitted chips out to lags $\Delta = 8$pix. From determining $\epsilon^{\mathrm{meas}}_{1/2}$ at four different settings (where one of the components of either ϵ^{true} or ϵ^p is set to 0.1 and all others are 0) we fix the eight bias parameters of Eqn. 2.20.

Results for the fiducial settings and a number of variants are shown in Table 2.1. Multiplicative biases are above the per cent level and exceed the DES weak lensing science requirements. For a hypothetical deep all-sky lensing survey, Amara & Réfrégier (2008) have calculated requirements on systematic errors in shape measurement that translate to approximate limits of $|m| > 0.1 \times 10^{-2}$, $|c| > 0.3 \times 10^{-3}$ and $|p| > 0.3 \times 10^{-2}$, all of which are exceeded by the observed biases.

We probe the seeing range typical for DES lensing band data and object sizes between the smallest usable and median angular size of faint galaxies (cf., e.g., Poli et al. (1999)). We note that multiplicative bias is a strong function of the relative size of PSF and galaxy, as expected due to the PSF size misrepresentation in bright stars. High background levels somewhat alleviate the multiplicative bias since the shifting of background charges is a convolution effect that is independent of the object flux. Interestingly, the strong x/y asymmetry of neighbouring pixel covariances in flat fields (cf. Sec. 2.3.2) results in a relatively small additive bias c_1 that disappears when we artificially set $a^T_{0,1}$ to the fitted value of $a^R_{1,0}$.

We apply reverse charge shifts to test the appropriateness of our correction scheme, e.g. use shift coefficients $\boldsymbol{a} \to -\boldsymbol{a}$ and apply Eqn. 2.2. The purpose of this is to test the influence of a number of simplifications in the corrections we make on shape measurement biases (summarized in the second part of Table 2.1). Specifically,

- we correct according to the true model, but only out to lags of $\Delta_{\max} = 5$pix; multiplicative bias is reduced by a factor of ≈ 30 to 8×10^{-5} for the fiducial case and is, as all other bias parameters, within the requirements;

- we apply a maximally asymmetric model, degenerate in terms of flat field covariance measurements ($a^T_{0,1} = 0$ as transformed with Eqn. 2.10), but make a correction for the symmetric model fitted as described in Section 2.3.4; the most significant effect is that additive bias c_1 is corrected only partially, but still below science requirements;

- we apply the model, using a Lanczos-3 interpolated version of the image at the pixel border centers, but for the reverse use the mean counts in the two neighbor pixels in Eqn. 2.2; this leaves a per-mille level multiplicative bias, at the 5% level of the uncorrected case.

We conclude that a $\Delta_{\max} = 5$, symmetric, linearly interpolated correction scheme is sufficient for our scientific requirements. For a deep all-sky lensing survey, the latter two cause residual biases at the limit of acceptable systematic errors.

settings	$m[10^{-2}]$	$c_1[10^{-3}]$	$p_1^1[10^{-2}]$	$p_2^2[10^{-2}]$
fiducial	2.4	-0.5	-0.6	-0.7
$\mathrm{FHWM_{PSF}} = 0.7''$	1.7	-0.5	-0.4	-0.5
$\mathrm{FHWM_{PSF}} = 1.1''$	3.1	-0.5	-0.8	-0.9
$\mathrm{FHWM_{gal}} = 0.3''$	6.9	-1.4	-1.7	-2.0
$\mathrm{FHWM_{gal}} = 0.7''$	1.1	-0.3	-0.3	-0.3
2000 e^- background	2.2	-0.5	-0.6	-0.7
symmetric $a_{ij}^T := a_{ji}^R$	2.5	0.0	-0.6	-0.7
corrected out to $\Delta = 5$ only	0.0	0.0	0.0	0.0
corrected with flat-field degenerate model	0.0	-0.2	0.0	0.0
corrected neglecting interpolation	-0.1	0.0	-0.1	0.0

Table 2.1: Shape biases due to charge self-interaction in DECam as determined from image simulations. Multiplicative biases m, additive biases c and PSF leakage p, defined as in Eqn. 2.20, are measured with fiducial settings (see text in Section 2.4), and the described differences in parameters. Note that biases of approximately $|m| > 0.1 \times 10^{-2}$, $|c| > 0.3 \times 10^{-3}$ and $|p| > 0.3 \times 10^{-2}$ are problematic for a hypothetical deep all-sky lensing survey. For DES, requirements are less stringent but clearly exceeded by the observed multiplicative bias. We always find $m = m_1 \approx m_2$, $c_2 \approx 0$ and $p_2^1 \approx p_1^2 \approx 0$ and omit these from the table.

2.5 Correction on pixel-level basis

In the previous Sections 2.3 and 2.4, we have characterized flat-field noise pixel-to-pixel covariances with the A14 model and shown that the amplitude of charge self-interaction present in DECam is expected to cause shape measurement biases at a critical level. Here, we test whether a correction using our model restores the profiles of bright stars to the shape of their fainter counterparts.

To this end, we analyze a set of 90 r band exposures of moderately dense stellar fields taken between Aug 16, 2013 and Jan 19, 2014. To these we apply overscan and bias subtraction and a correction of inter-CCD cross-talk and signal chain non-linearity. For evaluation of the correction, we generate two versions of the frames, in one of which we apply Eqn. 2.2 with the negative of the fitted shift coefficients (e.g. $\boldsymbol{a} \to -\boldsymbol{a}$). Finally, we divide by a master flat field.

On the reduced frames we run SExtractor Bertin & Arnouts (1996) and split the catalog by brightness. We use the number of counts in the brightest object pixel, `FLUX_MAX`, with four bins centered on `FLUX_MAX` of 5000, 10000, 15000 and 20000 ADU, all sufficiently below the saturation level of DECam. We run PSFEx Bertin (2011) on each of the catalogs to generate a model of the PSF as measured from stars of different flux. We remove a small number of frames for which the fitted PSF models have an irregular appearance visually. We finally stack the PSF models to get the mean PSF profile at each of the flux levels, ensuring that we only use frames where the number of stars in each `FLUX_MAX` bin is sufficient to fit a bilinear model of the spatial variation of the PSF that we always evaluate at the chip center position.

Fig. 2.10 shows a difference image of the `FLUX_MAX` $\approx$ 5000 and 20000 star profile before and after correction. The dominant brighter/fatter feature of a flux deficit in the central pixels is largely removed.

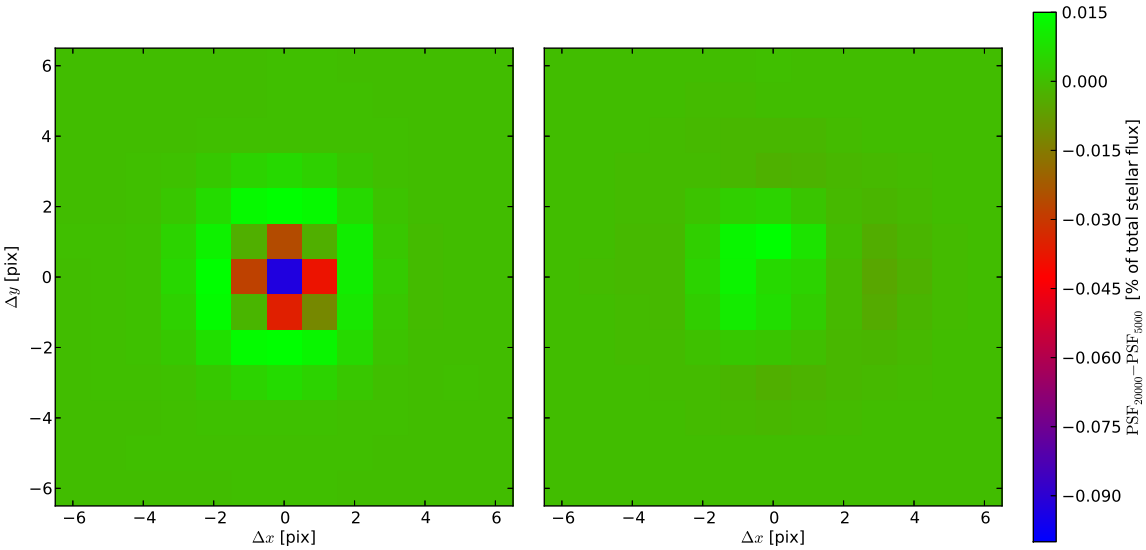

Figure 2.10: Difference image of normalized PSF as measured from stars at `FLUX_MAX` of 20000 and 5000 ADU. Left: without correction, the brighter/fatter effect shows as a flux deficit in the central 9 pixels that is compensated by excess charge on an annulus at ≈2-4 pix radius. Right: after applying the charge shift correction.

We calculate a number of metrics to quantify how well the correction removes the flux dependence of the PSF. Metrics based on the reduction of the residuals in the individual pixels' fluxes (see Fig. 2.11 for flux deficit in central pixel and sum of squared deviations) show a reduction of the effect at the 90 per cent level.

For lensing applications, however, the more relevant quantities are based on second moments of the PSF (cf. Eqns. 2.17ff). Figure 2.12 shows residuals of three combinations of second moments that correspond to the PSF size and the PSF ellipticity between brighter stars and stars of `FLUX_MAX` ≈ 5000. The residuals at somewhat larger radii that remain in the corrected image (cf. Fig. 2.10) have a significant influence on second moments. While the ellipticity effects of charge self-interaction appear corrected for, size residuals are overcorrected significantly. We have checked that this effect is not due to statistical or systematic differences in centroiding of the PSFEx models. Shape biases associated with the observed residuals after correction are likely still problematic.

We were not able to find the cause of the size residuals at the time of this writing. We hypothesize, however, that they could be connected to either a break-down of the model at low charge levels and large distances or one of the simplifying symmetry assumptions required in constraining the model parameters from flat field covariances (cf. Section 2.3.2).

2.6 Summary

We have presented a systematic study of imaging data from DECam and identified two effects of charge self-interaction: (1) a broadening of star images with increasing flux and (2) a correlation of Poisson noise in pairs of pixels in flat field exposures.

The first effect shows as missing flux in the central pixels of bright stars that instead

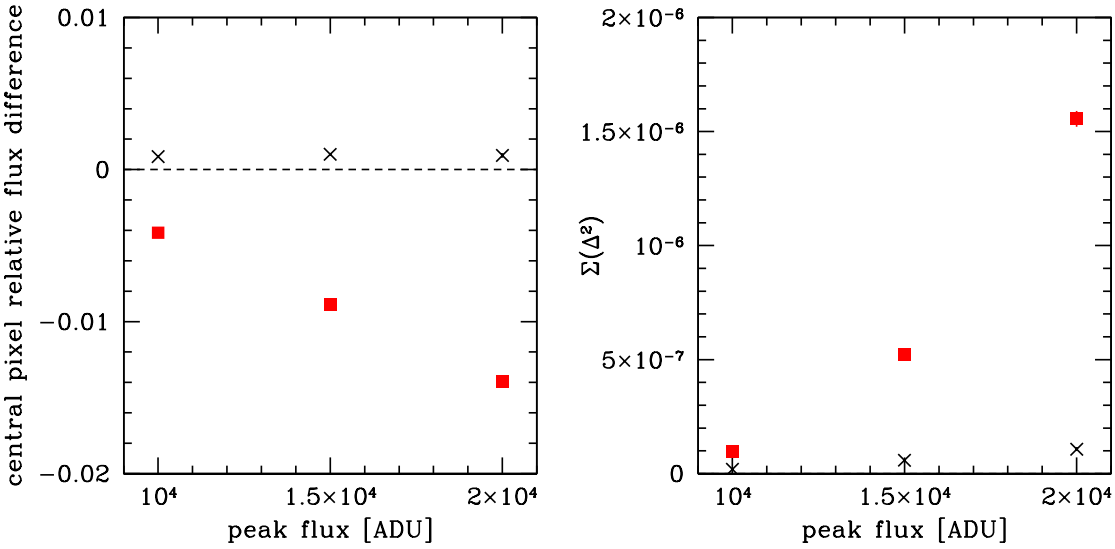

Figure 2.11: Relative change in flux in the central pixel of bright stars (left) and sum of squared residuals between bright and faint stars (right) before correction (red squares) and after applying the reverse charge shifts predicted from the model (black crosses). Both are plotted as a function of peak flux (`FLUX_MAX`) and measured relative to stars of `FLUX_MAX` $\approx$ 5k ADU with bootstrapped error bars.

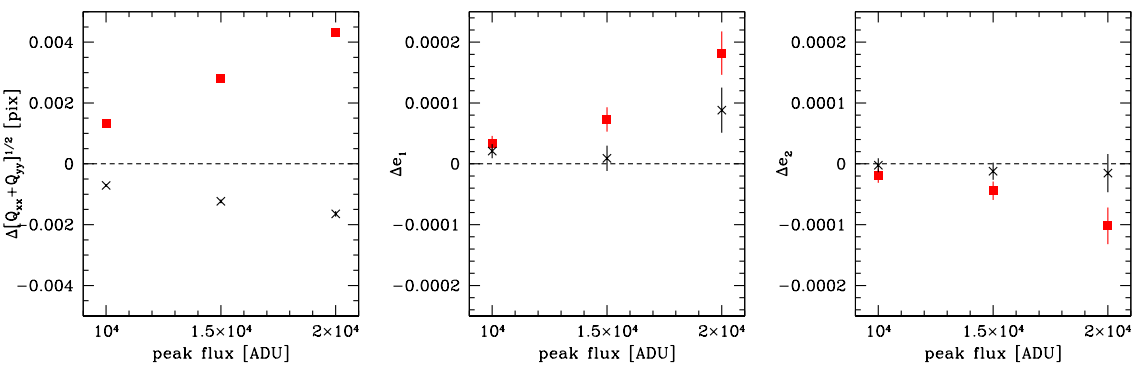

Figure 2.12: Difference in radius (left) and ellipticity (center, right for the two components) between bright and faint stars before correction (red squares) and after applying the reverse charge shifts predicted from the model (black crosses). Quantities are based on second moments Q_{ij} measured with a Gaussian weight function of $\sigma = 3$ pix width. Both are plotted as a function of peak flux (`FLUX_MAX`) and measured relative to stars of `FLUX_MAX` $\approx$ 5k ADU with bootstrapped error bars.

appears at ≈3 pix distance from the center. The difference between bright and faint stars is approximately linear in flux and, at fixed total flux level, independent of exposure time (Section 2.2).

We have measured the second effect with high signal-to-noise ratio out to pixel-to-pixel distances of ≈10 pix (Section 2.3.2). There is a $\approx 5:1$ asymmetry of correlations with the direct neighbor pixels on the same row or column. Correlation amplitudes for more distant pixels are almost isotropic with an approximate power-law fall-off $\propto r^{-2.5}$. Covariances differ from chip to chip at the $\approx 20\%$ level. The DECam chips with higher resistivity show larger correlations with their diagonal and distant neighbors and smaller correlations with the adjacent pixel perpendicular to the read-out direction. There is a color dependence of the measured covariances, which is most severe for the latter pairs (more than 40% increase in correlation from g to Y band) but much weaker for other lags.

Both effects are phenomenologically connected by the A14 charge shift model. From the latter measurements and a number of symmetry assumptions, we fit the model parameters (Section 2.3.3). We simulate the effect of the predicted charge shifts on shape measurement (Section 2.4) and find it to be significant for ongoing Dark Energy Survey weak lensing science, with multiplicative shape measurement biases above the per cent level.

Finally, we test the ability of the charge shift model to remove the flux dependence of the profiles of stellar images (Section 2.5). We find that the flux dependence is strongly reduced in terms of the flux deficit in the central pixels and the overall sum of squared residuals. However, significant flux dependence of stellar sizes remains, indicating that our treatment of the charge self-interaction effects on inhomogeneous surface brightness images is yet incomplete.

Acknowledgments

This project was supported by SFB-Transregio 33 'The Dark Universe' by the Deutsche Forschungsgemeinschaft (DFG) and the DFG cluster of excellence 'Origin and Structure of the Universe'. DG thanks Pierre Astier, Thomas Diehl, Augustin Guyonnet, Stephen Holland, Mihael Kodric, Ralf Kosyra and Andy Rasmussen for helpful discussions. GMB acknowledges support for this work from NSF grant AST-1311924 and DOE grant DE-SC007901. AAP is supported by DOE grant DE-AC02-98CH10886 and JPL, which is run under a contract for NASA by Caltech.

We are grateful for the extraordinary contributions of our CTIO colleagues and the DES Camera, Commissioning and Science Verification teams in achieving the excellent instrument and telescope conditions that have made this work possible. The success of this project also relies critically on the expertise and dedication of the DES Data Management organization.

Funding for the DES Projects has been provided by the U.S. Department of Energy, the U.S. National Science Foundation, the Ministry of Science and Education of Spain, the Science and Technology Facilities Council of the United Kingdom, the Higher Education Funding Council for England, the National Center for Supercomputing Applications at the University of Illinois at Urbana-Champaign, the Kavli Institute of Cosmological Physics at the University of Chicago, Financiadora de Estudos e Projetos, Fundação Carlos Chagas Filho de Amparo à Pesquisa do Estado do Rio de Janeiro, Conselho Nacional de Desenvolvimento Científico e Tecnológico and the Ministério da Ciência e Tecnologia, the Deutsche Forschungsgemeinschaft and the Collaborating Institutions in the Dark Energy Survey.

The Collaborating Institutions are Argonne National Laboratory, the University of Cal-

ifornia at Santa Cruz, the University of Cambridge, Centro de Investigaciones Energeticas, Medioambientales y Tecnologicas-Madrid, the University of Chicago, University College London, the DES-Brazil Consortium, the Eidgenössische Technische Hochschule (ETH) Zürich, Fermi National Accelerator Laboratory, the University of Edinburgh, the University of Illinois at Urbana-Champaign, the Institut de Ciencies de l'Espai (IEEC/CSIC), the Institut de Fisica d'Altes Energies, Lawrence Berkeley National Laboratory, the Ludwig-Maximilians Universität and the associated Excellence Cluster Universe, the University of Michigan, the National Optical Astronomy Observatory, the University of Nottingham, The Ohio State University, the University of Pennsylvania, the University of Portsmouth, SLAC National Accelerator Laboratory, Stanford University, the University of Sussex, and Texas A&M University.

Chapter 3

Implementation of robust image artifact removal in SWarp through clipped mean stacking

Prologue

If we would like to trust any measurements on our images, we need to ensure that they are faithful representations of the sky. In particular, this means they need to be free from artifacts, such as the tracks of energetic particles traversing the CCD detector, satellite and plane tracks in the sky or reflections of bright stars.

In this project, I use the fact that these features appear in the same position in the sky only on a minority of the many overlapping images taken in deep astronomical observations. From a comparison of single frames to the median stack, artifacts can therefore be identified. An important aspect is the feasibility of application on data with moderately varying point spread function. My implementation of the method has since been used in the first weak lensing study with DECam data (Melchior et al., 2014) and included in the latest release of the co-addition software SWarp (Bertin et al., 2002).

The present chapter has been published as Gruen, Seitz, & Bernstein (2014a) in PASP. I conceptionally and technically developed the method and the image simulation code and performed the data reduction of example images. Code for world coordinate mapping was provided by Gary M. Bernstein. All authors contributed to discussions and proofreading.

Non-exclusive permission for publication of the article was granted by the Astronomical Society of the Pacific in the publication agreement. The copyright for the article is with The University of Chicago Press as of the year 2014.

Abstract

We implement an algorithm for detecting and removing artifacts from astronomical images by means of outlier rejection during stacking. Our method is capable of addressing both small, highly significant artifacts such as cosmic rays and, by applying a filtering technique to generate single frame masks, larger area but lower surface brightness features such as secondary (ghost) images of bright stars. In contrast to the common method of building a median stack,

the clipped or outlier-filtered mean stacked point spread function (PSF) is a linear combination of the single frame PSFs as long as the latter are moderately homogeneous, a property of great importance for weak lensing shape measurement or model fitting photometry. In addition, it has superior noise properties, allowing a significant reduction in exposure time compared to median stacking. We make publicly available a modified version of SWarp that implements clipped mean stacking and software to generate single frame masks from the list of outlier pixels.

3.1 Introduction

The creation of stacked images out of multiple single exposures of the same part of the sky is a common problem in astronomy. Important operations, such as object detection or shape measurement, require the combined information to make full use of the individual frame data. In addition, stacking provides the advantage of greatly reducing the amount of data that needs to be analyzed downstream, for many purposes without loss of information.

Usually, images are combined by re-sampling each single frame to a common grid and then taking either the (inverse-variance weighted) mean or median of the individual pixels as the stacked value. Both these methods are implemented, for example, in the most commonly used stacking software SWarp[1] (Bertin et al. 2002, for examples of recent larger applications, see Warren et al. 2007; Gwyn 2008; Mohr et al. 2008). While the inverse-variance weighted mean is statistically optimal in the sense of minimal noise in the resulting stack, it requires a highly complete algorithm for rejecting regions in the individual frames containing artifacts, such as

- *cosmic rays* (CRs), i.e. energetic particles of cosmic or terrestrial origin that hit the detector and cause highly elevated counts in single or few neighboring pixels; the pattern of elevated counts on the CCD they produce depends on the particle and properties of the camera, with charge deposits varying typically between $25 - 75$ electron-hole pairs per μm of the track (Groom, 2002); they can be detected by their peaked profile that is incompatible with the extended point spread function of sources imaged by the atmosphere (e.g. Rhoads 2000 or Gössl & Riffeser 2002 for a method based on detecting features of higher spatial frequency than the PSF, Salzberg et al. 1995 for a machine learning approach or van Dokkum 2001 for a method based on edge detection),

- *tracks* of satellites, meteors, planes and sufficiently rapidly moving objects (e.g. comets and asteroids, which appear at different positions in different exposures) in the solar system are unwanted features in extra-solar astronomy; one method of detecting tracks for automated masking is based on the Hough transform (e.g. in the implementation of Vandame, 2001),

- *ghost images*, which appear as diffuse secondary images of bright stars and can be masked automatically only if accurate knowledge about reflecting surfaces and positions of bright stars is available; charge persistence of bright stars causes similar problems and can depend on several factors (Gössl et al., 2012), and

- *CCD imperfections*, such as saturation features, bad pixels or flat-fielding non-uniformities; these are most often stationary between different exposures and can therefore be

[1] `http://www.astromatic.net/software/swarp`

taken care of with an instrument mask are easy to detect on single frames (e.g., by masking pixels above a saturation threshold), which is why we are not concerned with them in this work.

One major concern is that no algorithm working on the single frames is easily able to detect and correct all of these features that span a wide range in size and apparent surface brightness, while each of them can disturb photometric or shape measurements significantly and, more importantly, potentially cause correlated errors on a certain scale and/or in a certain region of the sky. Mean stacks will, unless these features are detected and masked at the single-frame level, contain a density of artifacts that increases with the number of frames and total exposure time entering the stack. This has led many studies in the past to consider median stacks instead, which are more robust to single outlier frames when a large enough number of overlapping exposures is available.

Median stacks, however, are problematic in two important respects as well. For large, outlier-free samples, the variance of the median is a factor of $\pi/2 \approx 1.57$ larger than the variance of the mean, such that the total exposure time must be increased by more than half if stack images of similar depth are to be produced. They will, however, even then be far from optimal for a variety of analyses for the following reason. If the point spread function (PSF) is not constant over the set of images entering the stack, the resulting stellar images will be a non-linear combination of the individual PSF profiles, piecewise equal to the individual profiles. The transformation of true surface brightness to observed surface brightness will be different for any object, and will no longer be described by a simple convolution, which renders median stacks almost useless for weak lensing shape measurement purposes. For photometry, this also means that PSF-convolved model fitting is not accurate and that the median stack is not necessarily flux conserving.

As an alternative, *clipped mean stacks* have been created before using, for instance, IRAF,[2] Drizzle (Fruchter & Hook, 2002) and related software, THELI (Erben et al., 2005), the O.A.R. IDL Library[3] or non-public software (cf., e.g., Annis et al., 2014; Lin et al., 2012; Hudelot et al., 2012; McCracken et al., 2012).

Three issues remain to be addressed, however. Firstly, clipped mean stacking is not presently implemented in SWarp despite its widespread use. We therefore make publicly available a modification of SWarp that implements this. Secondly, information about outliers with respect to the stack can be used in generating masks for the single frame images included. This is of great value for analyses making use of the set of individual exposures instead of the stack, as is the case for instance for upcoming shear measurement codes. Moreover, the spatial density of outliers can also be used to mask even lower significance features on the single frame level than is possible with clipping alone, and we release a piece of software that implements this. The result, which we call *outlier filtered stack*, is cleaned even of faint tracks and ghost images, and it also provides cleaned single frames useful, for instance, for lensing purposes. Thirdly, we investigate the influence of differences in PSFs between the single frames entering the stack on the performance of these methods. We find that a simple clipped mean can distort the profiles of bright stars even at moderate thresholds. We suggest both a means of mitigating the effect and a metric for determining the required level of allowance for PSF differences.

In Section 3.2, we detail the algorithms used. In Section 3.3, we study the properties of

[2] `http://iraf.noao.edu/`
[3] `http://www.oa-roma.inaf.it/`

the noise in these stacks and analyse the tolerance of the method for PSF inhomogeneity. Section 3.4 shows examples of our application of the algorithm to a set of real and simulated images. Section 3.5 provides practical information for downloading and applying the provided software. Section 3.6 summarizes our findings.

3.2 Method

Consider a set of M overlapping single frames $\mathfrak{F} = \{F_1, F_2, \ldots, F_M\}$. For every position in the overlapping region, we can interpolate each of the images to get the corresponding surface brightnesses at that point, $\mathfrak{f} = \{f_1, f_2, \ldots, f_M\}$. The median of $\mathfrak{f}$ is denoted as μ. Let all frames be background subtracted, i.e. $\mathbb{E}(f_i) = 0$ for pixels not containing astronomical objects. If all frames were on the exact same grid and shared the identical point spread function, then $\mathfrak{f}$ would be a set of independent measurements of the same (convolved) true surface brightness at that point in the sky. Their uncertainties at the given point are denoted as $\{\sigma_1, \sigma_2, \ldots, \sigma_M\}$.

The uncertainty in a given pixel can be written as the sum of several components,

$$\sigma_i^2 = f_{\rm obj}/g + f_{\rm bg}/g + \sigma_{\rm rn}^2 \ , \tag{3.1}$$

where $f_{\rm bg}$ is the background flux, $f_{\rm obj}$ the object flux, both given in analog-digital units (ADU) with gain g, and $\sigma_{\rm rn}$ the read noise (all of which can have pixel-to-pixel variations). The σ_i can, in principle, be taken directly from the weight frames, if these include all components and, in addition, are re-scaled correctly with the respective science images. Neither of this is reliably the case in pipelines in use today. Weight frames are often used merely as *relative* weights

$$w_i = a\,\sigma_{\rm bg}^{-2} \ , \tag{3.2}$$

inversely proportional to the background noise $\sigma_{\rm bg}^2 = f_{\rm bg}/g + \sigma_{\rm rn}^2$ with arbitrary scaling a (for a counter example of a full treatment of noise, see Gössl & Riffeser 2002).[4]

SWarp, which we use as a basis for our implementation, allows various definitions. In the most common relative inverse-variance weight frame format `MAP_WEIGHT`, it determines the scaling factor a in Eqn. 3.2 by matching w_i^{-1} to the empirical variance in empty sky region of the single frames (found by means of σ-clipping to remove object pixels and subtraction of a background map). In addition, SWarp keeps track of the gain in the individual re-scaled single frames. Therefore, we can calculate the full pixel noise as

$$\sigma_i^2 = \mu/g + \sigma_{\rm bg}^2 \ , \tag{3.3}$$

assuming that the median is an artifact-free model for the true surface brightness.

True astronomical single frame images of the same portion of the sky are different in at least four ways beyond having different realizations of noise:

- No two single frames are sampled on exactly the same grid. The astrometric solution allows to map pixel coordinates to common coordinates, and the imperfections due to the interpolation procedure are small.

[4] Note that the background noise only weight has important advantages, since weighted mean stacking according to the full pixel noise σ_i would distort the profiles of bright objects when frames have inhomogeneous PSFs. Object flux uncertainties, on the other hand, can easily be defined to include the photon noise of the object itself, as it is done in SExtractor.

- No two PSFs are the same, at least in ground-based imaging. As a result of this, the *measured* surface brightnesses are different in each of the images because the light is spread out differently. This effect is most severe for point sources. When the ratio of the widths of two PSFs is ν then, given flux normalization, their central amplitudes scale as ν^{-2}.
- There are additional effects of astronomical and terrestrial origin (listed in the Introduction and called artifacts in the following) that are different in each of the single frames; these are exactly what we are trying to detect and mask.
- Variable or transient objects, which are likely to be interpreted by our algorithm as artifacts and clipped as well. Depending on the scientific goal, this can be either a good or an adverse effect.

If there were no difference in PSFs, we could perform a simple $\kappa - \sigma$ clipping to detect points that are influenced significantly by an artifact. Since $\mathfrak{F}$ has a certain distribution of PSFs, however, we will have to allow for PSF related scaling of the flux.

The following criterion takes this into account so as to robustly clip true outlier pixels. Let μ be the median of $\mathfrak{f}$. The value f_i is rejected in our algorithm if

$$|f_i - \mu| > \bar{n}\,\sigma_i + A\,|\mu|\ , \tag{3.4}$$

where $\bar{n}$ and A are two parameters of the clipping specifying the statistical and PSF related leniency of the procedure. Recall that the frames are background-subtracted, i.e. $\mu \approx 0$ in empty sky. The choice of A will depend on the distribution of PSFs and the choice of $\bar{n}$ on the particular purpose, discussed in more detail in Sections 3.2.1 and 3.3.2. For $A = 0$, this produces what is simply a weighted mean stack clipped relative to the median. An exemplary sketch of why $A > 0$ is usually required in the face of PSF inhomogeneity is shown in Figure 3.1.

This procedure works best in the limit of a noiseless median, i.e. with a large number of exposures. We propose the following rule in the case where only two frames are available, i.e. $\mathfrak{f} = \{f_1, f_2\}$: if

$$|f_1 - f_2| > \bar{n}\,\sqrt{\sigma_1^2 + \sigma_2^2} + A\,\left|\frac{f_1 + f_2}{2}\right| \tag{3.5}$$

is true, we discard the pixel information from both frames. The reliability of the algorithm, however, remains strongly dependent on the number of available exposures.

3.2.1 Spatial filtering of outliers

In order not to remove too much information from the image, it is necessary to use a threshold $\bar{n}$ large enough such that most of the f_i enter the weighted mean, i.e. the stacked output value (cf. also Section 3.3.1). Many artifacts, however, are at a surface brightness level which is comparable to the sky noise in a single frame. They obviously cannot be removed reliably on the basis of single pixel clipping. They introduce, however, a higher spatial density of outlier pixels at the artifact position. A first run of the clipped mean stacking with a relatively low threshold can be used to generate a list of outlier pixels. Their density can be used to mask artifacts on the single frame level. A final run which stacks the masked single frames in a mean stack produces an outlier filtered stack with optimal noise properties. This section is concerned with the statistical aspects of such a scheme.

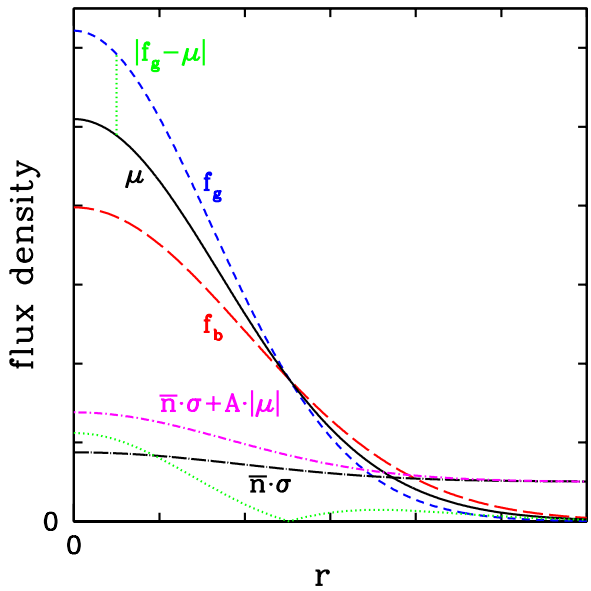

Figure 3.1: Schematic picture of the clipping procedure in the presence of inhomogeneous PSFs. Given a set of frames with varying seeing, the photometrically scaled profile of a point source varies between f_g (blue, short dashed line) at good and f_b (red, long dashed line) at bad seeing conditions. The median profile is μ (black, solid line). The difference between the median profile and the best seeing profile, $|f_g - \mu|$ (green, dotted line) exceeds the threshold $\bar{n}\sigma$ (black, dotted-long-dashed line) in the inner part. When increasing the threshold to $\bar{n}\sigma + A|\mu|$ (magenta, dotted-dashed line), however, this can be compensated and the clipping of artifact-free stars is avoided.

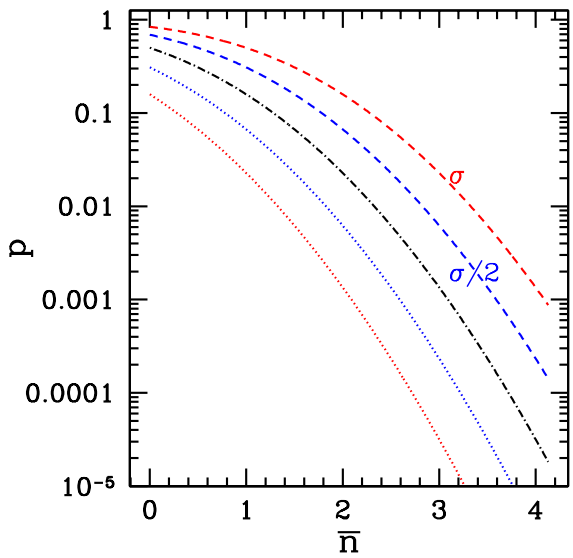

Figure 3.2: Outlier probabilities for Gaussian noise. Plotted are the probability $\hat{p} = \check{p}$ for any pixel to be more than $\bar{n}\sigma$ above (or below) the true value for a correct frame (black, dotted-dashed line) and the corresponding probabilities $\hat{p}$ and $\check{p}$ for being above (dashed lines) or below (dotted lines) if there is an artifact with positive surface brightness of $n\sigma$ (blue, closer to central line: $n = 0.5$; red, further from central line: $n = 1$) present in the pixel.

Consider a Gaussian distribution of noise with zero mean and some standard deviation $\sigma > 0$, which determines the statistical deviation of a pixel from the true surface brightness at the corresponding point in the sky.[5] We can count pixels that are outliers by selecting those which are $\bar{n}\sigma$ or more off (above or below) the expected true surface brightness at the respective point. Due to random fluctuations, this will flag a certain fraction of pixels. Figure 3.2 shows the probability $\hat{p}$ of a pixel being more than $\bar{n}\sigma$ above the true value (dotted-dashed black line), which is related to the Gaussian error function,

$$\mathrm{erf}(x) = \frac{2}{\sqrt{\pi}} \int_0^x e^{-z^2}\, dz \tag{3.6}$$

as

$$\hat{p} = \frac{1 - \mathrm{erf}(\bar{n}/\sqrt{2})}{2} \,. \tag{3.7}$$

With no artifacts present, $\hat{p}$ equals the probability $\check{p}$ of being as far *below* the true value as well.

Now consider an artifact in one frame that raises the surface brightness in some region by $n\sigma$.[6] The probability of high (low) outliers with respect to the true surface brightness will then increase (decrease) for any threshold $\bar{n}$. Figure 3.2 shows the increased per-pixel probability of values more than $\bar{n}\sigma$ above the mean as the dashed curves, which are plotted for $n = +0.5$ and $n = +1$.

In the case of practical application, two complications arise. For one thing, the true surface brightness in a pixel is not known. While the median of a sufficiently large number of frames is a robust estimate, its uncertainty adds to the intrinsic scatter of counts in single-frame pixels, for which some allowance must be made. Secondly, the counts of outlier pixels are increased when inhomogeneity in the PSF profile is present (see also Section 3.3.2). We therefore use the same argument as in Eqn. 3.4 to define

$$n = \mathrm{sgn}(f_i - \mu)\, \frac{\max(|f_i - \mu| - A|\mu|, 0)}{\sigma_i} \tag{3.8}$$

as the outlier significance.

Our concept for masking diffuse artifacts therefore is the following. Since outliers are more likely in an area with systematic surface brightness offsets (even though not all or potentially not even a majority of pixels will be above a sensible threshold) we can find a mask by selecting areas, for instance squares of area N pixels, inside which more than $\bar{N}$ pixels are more than $n > \bar{n}$ off the expected (median) value. Note that in this procedure we discriminate counts of positive and negative outliers, since they are more significant indicators of artifact flux or flux decrement when used individually rather than added. The question which thresholds and mask sizes should be used is discussed further in the following and in Section 3.4.

Statistics of Outlier Counts

In our simple outlier filtering algorithm, an area of N pixels shall be masked if more than $\bar{N}$ pixels are (without loss of generality) positive outliers by more than $\bar{n}$ standard deviations.

[5] The noise is in fact Poissonian, but at large enough background levels as they are common in optical imaging this can safely be approximated by a Gaussian distribution.

[6] Note that for an artifact of given physical surface brightness, n depends on the noise level at the particular position. This corresponds to the fact that an artifact of fixed surface brightness will be more difficult to detect in regions where background noise or shot noise from bright objects are larger.

n	number of standard deviations σ by which a pixel deviates from the true surface brightness
$\bar{n}$	threshold of $\lvert n \rvert$ above which a pixel is counted as an outlier
N	number of pixels of a rectangle that is being tested for artifacts
$\bar{N}$	threshold of the number of same-sided outlier pixels in a rectangle above which it is considered contaminated by artifacts and masked
$\hat{p}$	$\hat{p} = \mathrm{Prob}(n > \bar{n})$ for one pixel and the selected threshold $\bar{n}$
$\hat{P}$	probability of finding more than $\bar{N}$ high outliers above $\bar{n}$ inside one rectangle of N pixels

Table 3.1: Reference of common symbols for Section 3.2.1.

The purpose of this section is to determine optimal thresholds $\bar{N}$ and $\bar{n}$ as a function of area size N, which allow the detection of low surface brightness features at a small false positive rate. Our simplifying assumption in this context is that the artifact surface brightness is a noiseless constant multiple of the pixel noise over the size of the mask. For an overview of the quantities used in this context, we refer the reader to Table 3.1.

The probability $\hat{P}$ of finding more than $\bar{N}$ high outliers in N pixels can be calculated using the Binomial probability distribution,

$$\hat{P} = \sum_{m=\bar{N}}^{N} \mathcal{B}(m; N, \hat{p}) \ , \tag{3.9}$$

where

$$\mathcal{B}(m; N, \hat{p}) = \begin{pmatrix} N \\ m \end{pmatrix} \hat{p}^m \, (1 - \hat{p})^{N-m} \tag{3.10}$$

is the probability of finding the sum m of the results of N Bernoulli experiments with success probability $\hat{p}$ (i.e. m out of N pixels as high outliers). For $N\hat{p} > 10$ and $N(1 - \hat{p}) > 10$ we approximate Eqn. 3.10 by a Normal distribution, including the continuity correction (Feller, 1945), as

$$\hat{P} \approx \left(1 - \mathrm{erf} \left(\frac{\bar{N} - N\hat{p} - 0.5}{\sqrt{2N\hat{p}(1 - \hat{p})}} \right) \right) / 2 \ . \tag{3.11}$$

For the other limiting case of $N > 20$ and $\hat{p} < 0.05$ we use the Poissonian approximation,

$$\mathcal{B}(m; N, \hat{p}) \rightarrow \frac{\lambda^m \, e^{-\lambda}}{m!} \ , \tag{3.12}$$

with $\lambda = N\hat{p}$, which can be applied equivalently for $\hat{p} > 0.95$ when replacing the event by the non-event accordingly.

We make an a priori choice of the mask size N and the tolerable false-positive rate $\hat{P}_{\mathrm{max}}$ that we are willing to accept. The problem is then to find thresholds $\bar{N}$ and $\bar{n}$ for optimal detection of low surface brightness features under these conditions. This can be done in two steps,

i) by finding the $\bar{N}$ as a function of $\bar{n}$ where the false positive rate is below $\hat{P}_{\mathrm{max}}$ and

ii) by determining the surface brightness of outliers that could be detected as a function of threshold $\bar{n}$ when the above method of choosing $\bar{N}$ is applied (i.e., when the false positive rate is limited to a fixed value).

The first step can be solved by iteratively applying Eqn. 3.9. Figure 3.3 shows this for $\sqrt{N} = 3, 10, 50$.

For the second step, we again apply Eqn. 3.9 to find the surface brightness in units of the standard deviation as a function of $\bar{n}$ that are detected at 1σ, 2σ and 3σ significance (i.e., in approximately 68%, 95% and 99% of the cases) at the tolerated false positive rate. The result of this calculation is shown in Figure 3.4.

The curves in Figure 3.4 have minima at low thresholds, which consequently yield the largest amount of information about potential artifacts. However, the loss of detection significance is relatively small when increasing $\bar{n}$ from, for instance, 1 to 2.5 (in the case of $N = 50 \times 50$, for example, this increases the detectable artifact surface brightness level from approximately 0.25σ to 0.5σ, which is still sufficiently low). This allows us to limit the analysis to the more significant outliers whose rareness speeds up the processing time of the procedure considerably.

In order to be sensitive to a range of scales, we recommend to use three $\sqrt{N} = 3, 10, 50$.

- At $N = 3 \times 3$, one can detect small outliers such as cosmic rays. These have high significance, may in the extreme case be limited to one pixel, however. For $\bar{N} = 1$ and a corresponding $\bar{n} = 4.5$ the false detection rate is below 10^{-4}.

- At $N = 10 \times 10$ and $\bar{n} = 2.5$, our false detection criterion is fullfilled at $\bar{N} = 7$. This allows the detection of 95% of homogeneous artifacts with a surface brightness of 1.2σ (cf. Fig. 3.4). The filter has the additional advantage that also thin linear features like tracks, for which $\bar{N} \approx \sqrt{N}$, are detected (although for successful detection they of course need to be of higher significance than homogeneous artifacts).

- At $N = 50 \times 50$, $\bar{n} = 2.5$ and $\bar{N} = 35$ yield a 2σ detection of large artifacts of a surface brightness $n = 0.5$.

We note that these filters can be used independently, combining the resulting masks. Alternatively, it is possible to use one after another at increasing mask size, disregarding outliers which were masked by a smaller filter for the application of the larger one. Especially the criterion for $N = 50 \times 50$ is very sensitive to low surface brightness features, and may be found to be masking large areas around linear features or regions with slight background subtraction offsets, in which case thresholds can be increased. When the PSF has significant differences between the single frames entering the stack, additional care must be taken to not suffer from clipping bright stars (cf. Section 3.3.2).

We release a piece of software that maps the outlier pixels to the single frame coordinate systems and generates masks by counting outliers in all square boxes of a set of sizes. The processor time for the generation of masks from the outlier list is less than one second for a 2k×4k frame on a 2GHz core.

3.3 Properties of the stack

In this section we consider two properties of the stacked images created with the schemes described above. For clipped mean stacks, the pixel noise is always increased relative to a mean stack, which is discussed in Section 3.3.1. Both the clipped mean stack and outlier filtered stack are tolerant only to some degree of difference between the PSFs of the individual frames, which we take into consideration in Section 3.3.2.

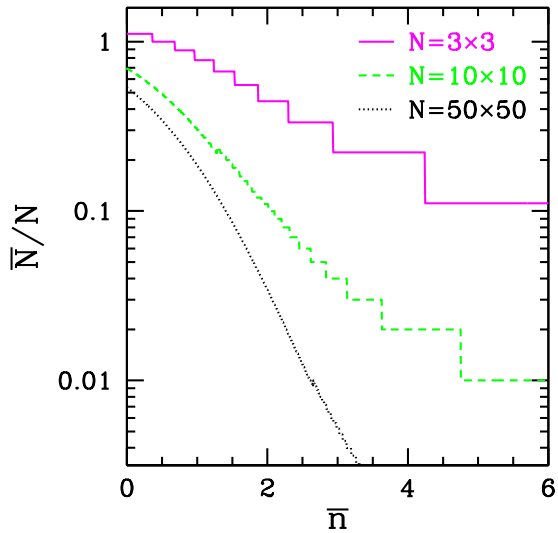

Figure 3.3: Lowest $\bar{N} \in \mathbb{N}$ for which the probability of false detection of non-artifact area as an artifact is $\hat{P} < \hat{P}_{\max} = 10^{-4}$ as a function of outlier threshold $\bar{n}$. With decreasing $\bar{n}$ and N there is a strongly increasing chance of a large fraction of pixels being random outliers. For instance, for the smallest 3×3 box *one* outlier pixel at 4.5σ significance is unlikely enough by chance ($\hat{P} < \hat{P}_{\max}$), but even *all* pixels being above the mean ($\bar{n} = 0$) is more likely than $\hat{P}_{\max}$.

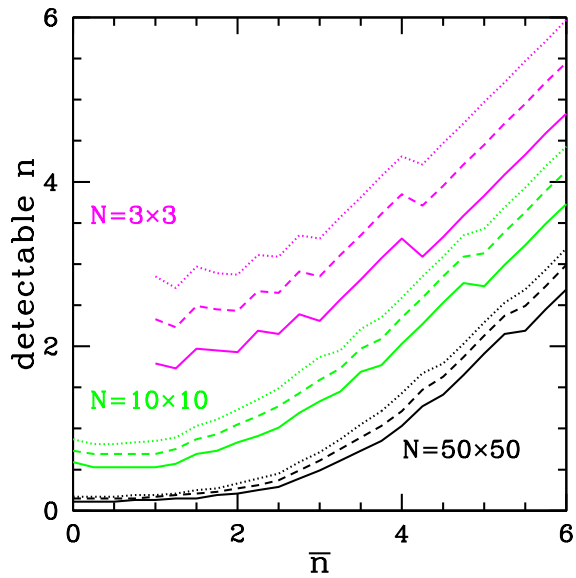

Figure 3.4: Surface brightness level n in units of sky noise detectable when filtering for outlier pixels in boxes of size $N = 3 \times 3$ pixels (upper, magenta lines), 10×10 (middle, green lines) and 50×50 (lower, black lines). Shown are the levels at which 68% (solid lines), 95% (dashed lines) and 99% (dotted lines) of artifacts are detected using outlier counts above a threshold of $\bar{n}$, all at a false positive rate $\hat{P} < 10^{-4}$ (cf. Fig 3.3). For the 3×3 box, outliers of 2σ significance can be detected when using a threshold of $\bar{n} = 2$. For the largest 50×50 box and a threshold of $\bar{n} = 2.5$, features with a homogeneous surface brightness of only half the pixel noise can be detected in 99% of the cases.

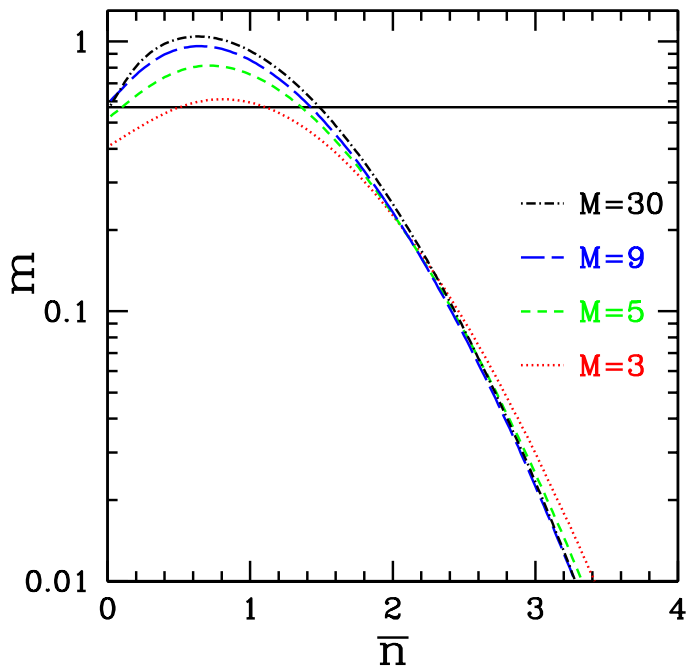

Figure 3.5: Variance levels in images created with clipping at different numbers of overlapping frames $M = 3, 5, 9, 20$ as a function of clipping threshold $\bar{n}$. The excess variance m is defined in Eqn. 3.13, with $m = 0$ for a weighted mean and $m = 1$ for a method that produces stacks of twice the pixel variance. All results are shown for $A = 0.3$ using Eqn. 3.4 and normalized by the variance of a mean stack. The solid horizontal line shows the noise level for a median stack in the limit of infinitely many exposures.

3.3.1 Noise

We study the level of noise in clipped mean images created using our algorithm as described in the first part of Section 3.2. One can define a variance multiplier m such that

$$\sigma^2(\bar{n}) = [1 + m(\bar{n})]\ \sigma^2\ , \tag{3.13}$$

where σ^2 is the sky variance of a mean stack, assuming Gaussian noise, and $\sigma^2(\bar{n})$ is the variance of a clipped mean stack with $\bar{n}$ and $A = 0.3$ according to Eqn. 3.4. Plots for different numbers of overlapping frames are shown in Figure 3.5.

We conclude that unless the clipping threshold is set below $\bar{n} < 3$, the excess noise due to a simple clipping scheme is at or below the per cent level. Very low clipping thresholds should be avoided (except for the identification and masking of artifacts, cf. Section 3.2.1) and a median stack should be used instead. For the removal of low surface brightness features, we recommend the filtering scheme of Section 3.2.1. The weighted mean of single frames with artifacts masked by means of this allows for an outlier-free mean stack with optimal noise properties.

3.3.2 Point spread function

The ideal stack has a PSF equal to a linear combination of the individual frame PSFs scaled according to their weight. This is what is the case for a mean stack, but it is not true for a

median image. Here we discuss the influence of PSF inhomogeneity on the clipped mean or outlier filtered stack.

Let $s_{i,\boldsymbol{x}}$ denote the pixel at position $\boldsymbol{x}$ of the normalized PSF profile in a single frame $i = 1 \ldots M$. The median value in that pixel among the frames shall be $\mu_{\boldsymbol{x}}$. We can count the number of pixels in which the difference from the median is above the threshold,

$$\frac{\mathcal{F} \max(|s_{i,\boldsymbol{x}} - \mu_{\boldsymbol{x}}| - A|\mu_{\boldsymbol{x}}|, 0)}{\sigma_i} > \bar{n} \ , \tag{3.14}$$

where we have calculated the deviation according to Eqn. 3.8 and scaled the normalized PSF by the total flux $\mathcal{F}$ of the brightest usable (i.e., non-saturated) stars. Where the count of either positive or negative outliers exceeds $\bar{N}$, a filter will clip a large fraction of bright stars. The resulting distortion of the PSF profile is problematic in similar ways as in a median stack, which is why it should be avoided.

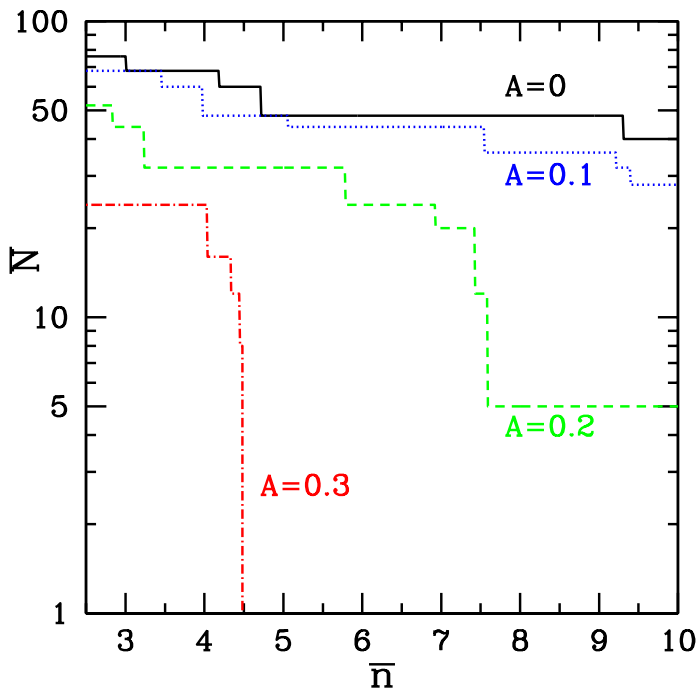

Figure 3.6: Number of outliers expected for bright stars as a function of threshold $\bar{n}$. At the random distribution of PSF widths with $\sigma_{\log_{10}\mathrm{FWHM}} = 0.05$ used here, only $A \geq 0.3$ allows clipping of outliers at $\approx 5\sigma$ without a distortion of the stacked profile of bright stars. Even then, additional allowance for the number of $\leq 4\sigma$ outliers has to be made for outlier filtering schemes.

We show results of calculating this metric for a set of 9 frames with circular Gaussian PSF of varying width. The widths are drawn from a log-normal distribution, centered on a FWHM of 4 pixels with $\sigma_{\log_{10}\mathrm{FWHM}} = 0.05$ (approximately 10%). This is an achievable configuration, although atmospheric seeing can potentially also vary considerably more. Figure 3.6 shows the maximum number of outliers $\bar{N}$ among all frames across a stellar image with flux $f = 10^4\sigma$ as a function of threshold $\bar{n}$ for different parameters $A = 0, \ldots, 0.3$. Similar curves for a set of actual single frame PSFs can be calculated using the software PSFHomTest (see Section 3.5).

We find that at $A = 0$, the common outlier clipping, the removal of even highly significant artifacts leads to a distortion of the PSF by clipping bright stars in the most extreme frames of the sample. In this case, a clipping scheme can only provide clean images with undisturbed PSF if high enough $A \geq 0.3$ are used. Additionally, some allowance in the $\bar{N}$ thresholds chosen for outlier filtering must be made, since even then bright stars can lead to a large number of outliers with low individual significance.

We conclude that clipping schemes should only be applied when testing the homogeneity of the PSF and choosing parameters A, $\bar{n}$ and $\bar{N}$ for which the PSF is left undisturbed. A practicable way is to pick parameters $N = 3\times3, 10\times10, 50\times50$, get $\bar{n}$ and $\bar{N}$ from Figures 3.4 and 3.3. At what parameter A these can be used without clipping bright stars can be tested with PSFHomTest (see Section 3.5). If the PSF inhomogeneity requires a large parameter $A > 0.5$, it is recommendable to increase the thresholds $\bar{n}$ and $\bar{N}$ instead or split the set of frames in two or more seeing bins, as otherwise a high A decreases the sensitivity to outliers blending with real objects. An alternative but computationally much more challenging approach would be the PSF homogenization or deconvolution of single frames before detecting outliers.

3.4 Application to astronomical images

3.4.1 Simulations

We simulate three main applications of the masking, namely cosmic ray, track and ghost image removal, to quantify the reliability of the algorithm in a more realistic manner. As a measure of efficiency, we use

$$\eta = \frac{\text{artifact flux masked}}{\text{total artifact flux}} \,. \tag{3.15}$$

Cosmic rays

The signature of cosmic rays on a CCD detector are most typically straight lines, while the counts and length depends on the particle energy and angle of entry. For a given energy spectrum, the mean length and count per pixel also vary with the thickness of the CCD (cf. Groom, 2002). We use a simple model to test the sensitivity of our algorithm, with a log-normal distribution of track length

$$p(\log[l/\text{pix}]) \propto \exp\left[-(\log[l/\text{pix}] - 1)^2/(2\sigma_l^2)\right] \tag{3.16}$$

with $\sigma_l = 0.3 \approx \log(2)$. The width of the track is set to only one pixel. Assuming a deposit of 1000 charges per pixel (cf. Groom, 2002), we include shot noise in our simulations. We test the completeness of the masking with 9 simulated overlapping frames, a density of 2×10^{-5} events/pix and varying levels of count deposit per pixel.

Because of the narrowness of the features, interpolation influences the detection probabilities most severely among the artifacts studied in this section. We therefore compare the efficiencies of different masking and interpolation schemes. For the baseline masking parameters, we choose a mask size of $N = 3 \times 3$ pixels at a threshold of $\bar{n} = 4.5$ and $\bar{N} = 1$ with $A = 0.3$. Without interpolation (or with nearest-neighbor interpolation, which does not dilute the artifact signal), the result is shown as the solid line in Fig. 3.7. The other lines show the result for interpolated frames, where the cosmic ray flux is distributed over neighboring

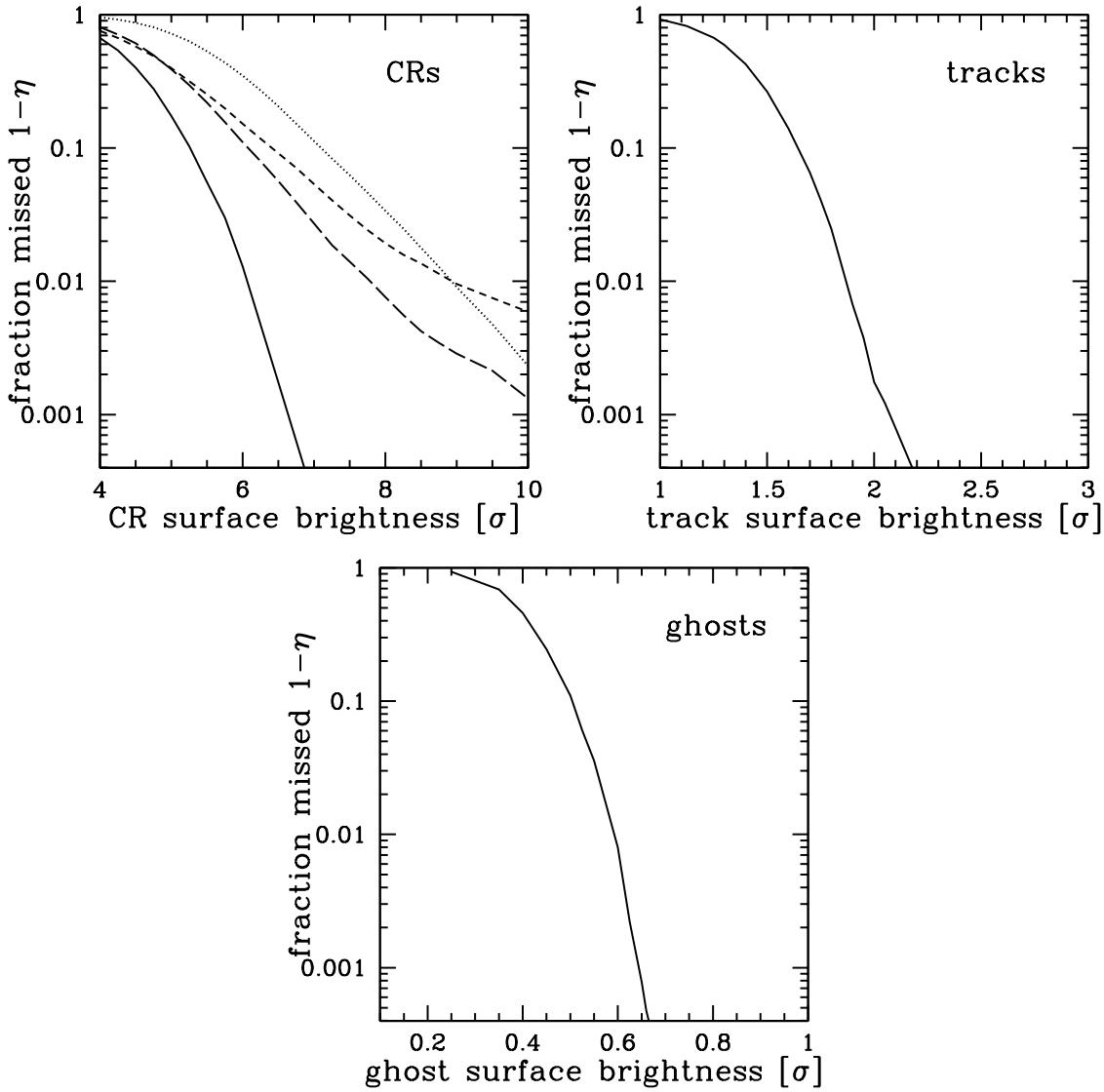

Figure 3.7: Completeness of masking as a function of surface brightness in units of the sky noise for cosmic rays, tracks and ghost images. For cosmic rays, because they are most severely influenced by interpolation, we show different masking schemes: $N = 3 \times 3$ with $\bar{n} = 4.5$ and $\bar{N} = 1$ (solid line) on frames without interpolation, interpolated frames with the same settings (dotted line) and with $\bar{n} = 3, \bar{N} = 2$ (short dashed line), and interpolated frames with $N = 4 \times 4$ boxes and $\bar{n} = 3.5, \bar{N} = 2$ (long dashed line).

pixels. Consequently, completeness of the masking is significantly lower when using the same box size and thresholds as before (dotted line). Detection probabilities can be improved by demanding at least $\bar{N} = 2$ outlier pixels either in a $N = 3 \times 3$ box with $\bar{n} = 3$ (short dashed) or in an $N = 4 \times 4$ box with $\bar{n} = 3.5$ (long dashed).

Note that cosmic rays in realistic images typically have an even higher significance than the regime probed here, typically above 10σ, and will therefore be masked with almost perfect completeness in any of these schemes.

Tracks

Moving objects in the sky such as satellites cause track-like features which are a nuisance to astronomy. We test our algorithm for track masking by simulating images with linear features of a Gaussian profile, where the surface brightness in a pixel at a separation d from the line is set to

$$f(d) = n \exp\left[-d^2/(2\sigma_d^2)\right] \ , \tag{3.17}$$

where we use a full-width at half-maximum of 5 pixels and a truncation at $d > 5$ pixels, corresponding to a hardly resolved object after convolution with a ground-based PSF.

We use a mask of $N = 10 \times 10$ pixels with the settings $\bar{n}_0 = 2.5$, $\bar{N}_0 = 7$ and $A = 0.3$. Results are shown in Figure 3.7. At a track surface brightness of twice the sky noise, the masking becomes very efficient. Below this, a larger filter could still be used successfully (see Ghost image simulations), yet with a large area masked around the track.

Ghost images

Secondary (so-called ghost) images of bright stars come in a wide variety of forms, connected to the many different light paths possible in a complex optical system. We simulate a type of ghost image similar to the most common one in the WFI camera on the ESO/MPG 2.2m telescope (Baade et al., 1999).

We model these ghost images as an annulus between 50 and 100 pixels. The shape of the image is distorted to an ellipse with axis ratio q, uniformly distributed in $q \in [0.3, 1]$, keeping the area constant. The ring is filled with constant surface brightness and offset far from the primary image. We simulate such features with a density of 1×10^{-6} per pixel.

Figure 3.7 shows that a mask with size $N = 50 \times 50$ pixels and thresholds of $\bar{n}_0 = 2.5$ and $\bar{N}_0 = 35$ with $A = 0.3$ is capable of highly complete removal of ghost images, even when the surface brightness of the feature is only a fraction of the sky noise.

3.4.2 Example images

We show an example of a frame observed with the WFI camera on the ESO/MPG 2.2m telescope (Baade et al., 1999). Our sample contains 18 400 s and 600 s R band exposures of a field containing a bright star with a ghost image inside the field of view, all with a PSF FWHM below 0.9 arcsec (3.78 pixels). The single frames are reduced using the pipeline based on Astro-WISE[7] (Valentijn et al., 2007) as described in Gruen et al. (2013), which masks cosmic rays with high confidence, tracks with a somewhat lower success rate and has in its standard form no ghost image masking technique available. We apply outlier masking with $A = 0.3$ and three filter sizes of $N = 3 \times 3$, $\bar{n} = 5$, $\bar{N} = 1$ for small artifacts, $N = 10 \times 10$,

[7] http://www.astro-wise.org/

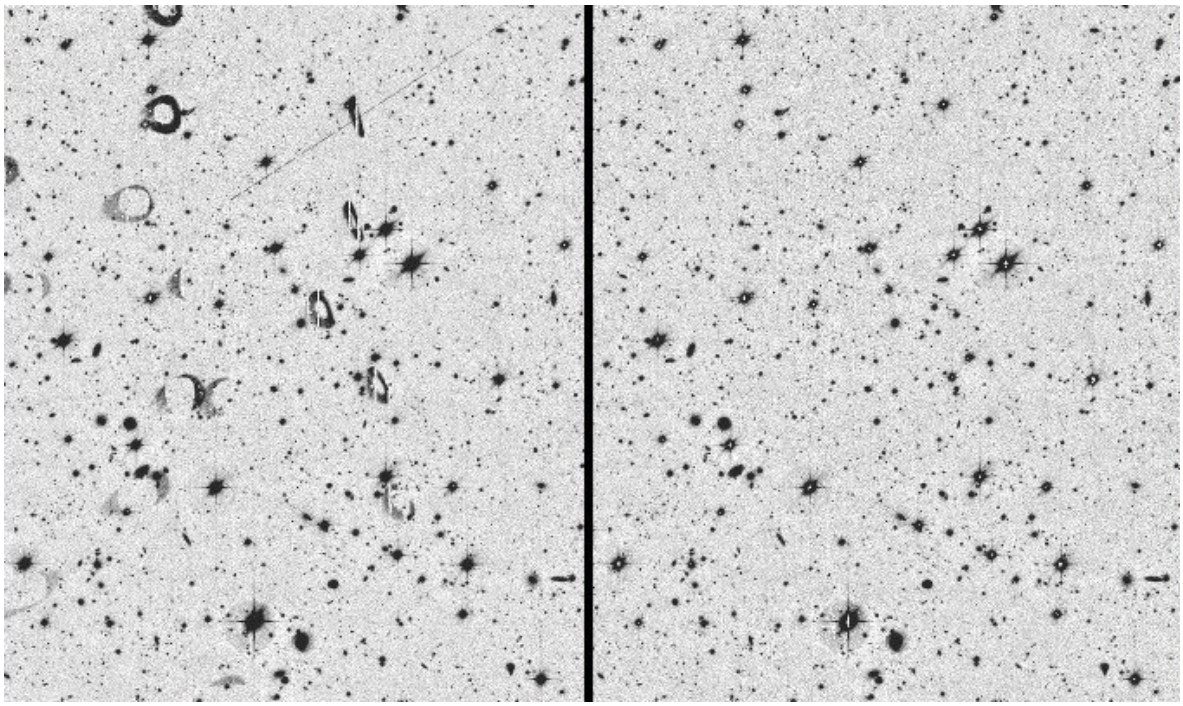

Figure 3.8: Common mean stack (left panel) and outlier filtered stack (right panel) of a cutout from a field containing a bright star. Both ghost images and a satellite track are successfully removed from the image by outlier filtering.

$\bar{n} = 3$, $\bar{N} = 10$ and $N = 50 \times 50$, $\bar{n} = 2.5$, $\bar{N} = 85$ for larger features, lenient enough for the small PSF variations in the sample.

Figure 3.8 shows a mean stack and an outlier filtered stack with the described settings. Both the multiple ghost images and a satellite track are successfully removed, while the depth of the image is conserved. The pupil ghost image close to saturated stars remains present since it does not change greatly between our exposures, which have only small dithers. Figure 3.9 shows a single frame image of a double ghost, overlaid with the mask generated with outlier filtering. Since the surface brightness of the fainter ghost is very low, only the combined information from a larger region is sufficient for detection and masking. The data cleaned from ghost images using the method described herein have been used successfully for cluster weak lensing analyses by Gruen et al. (2014b).

3.5 Download and application

In this section we note some relevant details of our implementation of the described algorithm in SWarp and outline the procedure for practical application.

3.5.1 Implementation

SWarp applies a two-step forward mapping procedure to generate a stack out of single frames. In a first stage, images are background subtracted, resampled onto a common grid and saved temporarily. In a second stage, these images are combined into a stack according to a user

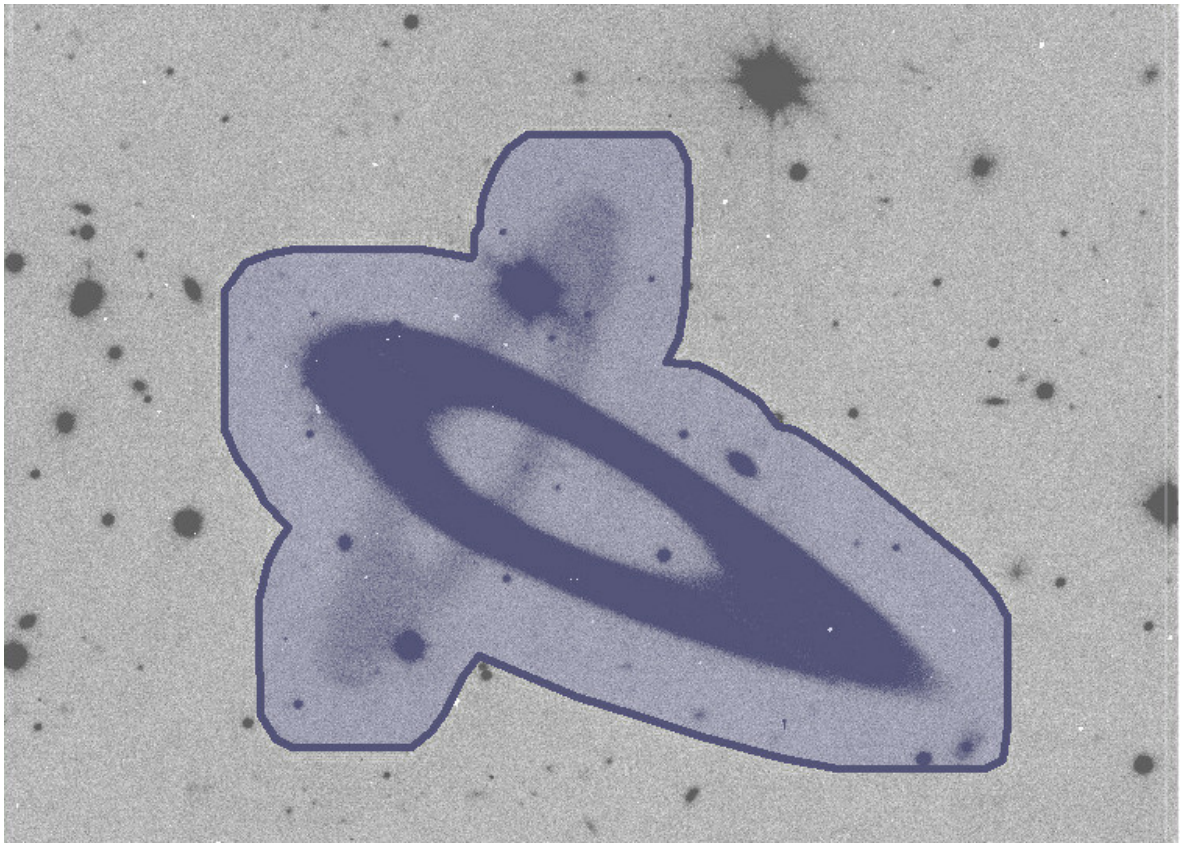

Figure 3.9: Single frame with ghost image consisting of orthogonal bright and faint components. Since the surface brightness of the latter feature is less than 3σ above the background, a simple clipping cannot remove it reliably. The outlier filter mask (shaded region, edge marked as line for clarity), however, detects and masks the feature entirely.

selected COMBINE_TYPE (such as WEIGHTED for weighted mean, MEDIAN or the CLIPPED mode implementing the algorithm described in this work). Both steps are frequently performed at different times, particularly in survey operations. This scheme implies that clipping can only happen at the second stage, where single frames are present in a comparable (background subtracted, flux scaled and re-sampled) form.

This also means that unlike in the implementation of clipping in Drizzle (Fruchter & Hook, 2002), we cannot access the single frames on their original grid for comparison with a re-sampled median image, but must perform the clipping on re-sampled single frames. Consequently, it is more difficult to detect small features on the single frame which are smeared out by interpolation, although experience with cosmic rays at typical levels shows that they remain significant enough (cf. Section 3.4.1). The scheme, however, also has the advantage not only of being more efficient computationally and from a pipeline perspective, but also of comparing two frames interpolated one time each instead of a non-interpolated and a doubly-interpolated version of the sky. Note that the masks found by means of outlier filtering are of course mapped back to the single frame grid straightforwardly.

One important issue is the correct treatment of pixel noise (cf. Section 3.2). When the weight map provided is based on background noise only (which is also true for weight maps generated by SWarp internally from the background level) and the individual frame gain keywords or the GAIN_DEFAULT configuration parameter are set correctly, our calculation of pixel noise according to Eqn. 3.3 works as intended. Alternatively, if the input weight map is based on the pixel noise including shot noise from object photons, gain should be set to 0, as otherwise the object contribution to the noise is added twice. Note that the latter setting is not recommended for the purpose of generating a weighted mean or clipped weighted mean stack, since it distorts surface brightness profiles in the presence of inhomogeneous PSFs (it can be used for outlier detection and masking on the single frame as described below, however).

3.5.2 Practical use

Configuration

For the basic configuration of SWarp, we refer the reader to the official documentation.[8] The modifications of configuration parameters for clipped mean stacking are the following:

- COMBINE_TYPE has a new option CLIPPED
- CLIP_SIGMA specifies the threshold parameter $\bar{n}$ from Eqn. 3.4 (default: 4.0)
- CLIP_AMPFRAC specifies the parameter A from Eqn. 3.4 (default: 0.3)
- CLIP_NAME specifies the filename for the outlier list to be written (to be used for generating single frame masks, default: clipped.tab)

Procedure

We recommend the following procedure for generating clipped-mean or outlier filtered stacks. To remove highly significant outlier pixels in a clipped-mean stack,

[8] http://www.astromatic.net/software/swarp

i) generate single-frame PSF models with PSFEx,

ii) determine suitable clipping parameters with PSFHomTest, in particular make sure that the clipping threshold $\bar{n}$ and parameter A do not clip pixels on bright stars, and

iii) create a clipped mean stack with the modified version of SWarp.

To produce an outlier filtered stack free of ghost images or faint tracks,

i) generate single-frame PSF models with PSFEx,

ii) determine suitable clipping parameters with PSFHomTest, in particular make sure that the combinations of $\bar{n}$ and $\bar{N}$ used for the filters later do not mask bright stars for the choice of A taken,

iii) create a clipped mean stack with the modified version of SWarp at a relatively low clipping threshold,

iv) run MaskMap to generate single frame mask images from the outlier list,

v) multiply single frame weight images by the mask and

vi) run SWarp again, yet in usual `WEIGHTED` mean mode.

PSFEx and the regular version of SWarp are available from `http://www.astromatic.net`. The modified version of SWarp, PSFHomTest and MaskMap are available for download.[9] They include a C++ class for accessing PSFEx models, which might be useful for other purposes, too.

3.6 Summary

We presented a method of outlier rejection and filtering that successfully detects and masks unwanted features in astronomical images by comparison to the median stack. Simple outlier rejection removes highly significant outliers very efficiently. Calculations, simulations and practical application show that the outlier filtering method can be used to also mask lower surface brightness features such as tracks at more than twice and large area features such as ghost images at more than half the sky noise level above the background. It also has the benefit of generating single frame level masks that can be applied in analyses running on the single frame images.

One important caveat is that all clipping methods rely on some degree of homogeneity of the PSF. Simple outlier clipping changes the stacked profile of bright stars even at a relatively low level of PSF variation and moderate to high clipping thresholds. Differences in PSF profiles therefore must and can be accommodated, both for single pixel clipping and outlier filtering, but should be tested with the knowledge of single frame PSF models before the application of the scheme.

All software required and described in this paper is available for download (see Section 3.5).

[9] see `http://www.usm.uni-muenchen.de/~dgruen/`

Acknowledgements

This work was supported by SFB-Transregio 33 'The Dark Universe' by the Deutsche Forschungsgemeinschaft (DFG) and the DFG cluster of excellence 'Origin and Structure of the Universe'.

We acknowledge the contribution of Emmanuel Bertin, the author of SWarp, which is a core component of the scheme presented here. The authors thank Arno Riffeser for helpful comments on the manuscript and Peter Melchior and Eric Suchyta for additional testing of the code.

Chapter 4

Weak lensing analysis of RXC J2248.7–4431

Prologue

After preparing the data, we can use the signatures of the distorted paths of photons, generated in galaxies when the Universe was half its current age, to study an exceptional cluster of galaxies: RXC J2248.7–4431. One of the 20 most X-ray luminous clusters in the *ROSAT* south Galactic pole region (Cruddace et al., 2002), with a galaxy velocity dispersion of over 1500km/s (Gómez et al., 2012), detected by both the SPT, *Planck* and ACT SZ surveys, RXC J2248.7–4431 has been selected as a gravitational telescope for the CLASH survey (Postman et al., 2012) and as a Hubble Frontier Field.[1] With our multi-band MPG/ESO 2.2-m data, we were the first to measure its mass and density profile with weak gravitational lensing and study the cluster galaxy population in detail.

This chapter is based on the paper Gruen, Brimioulle, Seitz, Lee, Young, Koppenhoefer, Eichner, Riffeser, Vikram, Weidinger, & Zenteno (2013), published in MNRAS. Data reduction, photometric and astrometric calibration, galaxy shape measurement (including PSF modelling and implementation and application of the shape measurement code), lensing analysis code for NFW fitting, mass measurement, and the analysis in Section 4.7 was exclusively done by me. Fabrice Brimioulle contributed aperture photometry and photometric redshifts, code for fitting the SIS profile, and performed part of the analyses based on cluster member photometry in Sections 4.4.1 and 4.4.2. Telescope time allocation and observation planning was done by Stella Seitz. Julia Young contributed image simulations and statistics on the shape catalogs that I used for shape bias calibration. Vinu Vikram provided the plot in Fig. 4.12 based on the shape catalog. Thomas Eichner and Stella Seitz performed the strong lensing fit of the secondary cluster strong lensing candidate feature in Section 4.8. Alfredo Zenteno ran his luminosity function fitting code on the photometric catalogs. Chien-Hsiu Lee, Johannes Koppenhoefer, Thomas Eichner, Arno Riffeser and Thomas Weidinger observed the cluster with the MPG/ESO-2.2m telescope. All authors contributed to discussions and proofreading.

Permission for non-commercial re-use of the material included in this thesis has been confirmed by the MNRAS editorial office. Oxford University Press holds the copyright on the paper.

[1] cf. `http://www.stsci.edu/hst/campaigns/frontier-fields/`

Abstract

We present a weak lensing analysis of the cluster of galaxies RXC J2248.7–4431, a massive system at $z = 0.3475$ with prominent strong lensing features covered by the Cluster Lensing And Supernova survey with Hubble (CLASH). Based on *UBVRIZ* imaging from the Wide-Field Imager camera at the MPG/ESO 2.2-m telescope, we measure photometric redshifts and shapes of background galaxies. The cluster is detected as a mass peak at 5σ significance. Its density can be parametrized as a Navarro-Frenk-White (NFW) profile with two free parameters, the mass $M_{200m} = 33.1^{+9.6}_{-6.8} \times 10^{14} M_\odot$ and concentration $c_{200m} = 2.6^{+1.5}_{-1.0}$. We discover a second cluster inside the field of view at a photometric redshift of $z \approx 0.6$, with an NFW mass of $M_{200m} = 4.0^{+3.7}_{-2.6} \times 10^{14} M_\odot$.

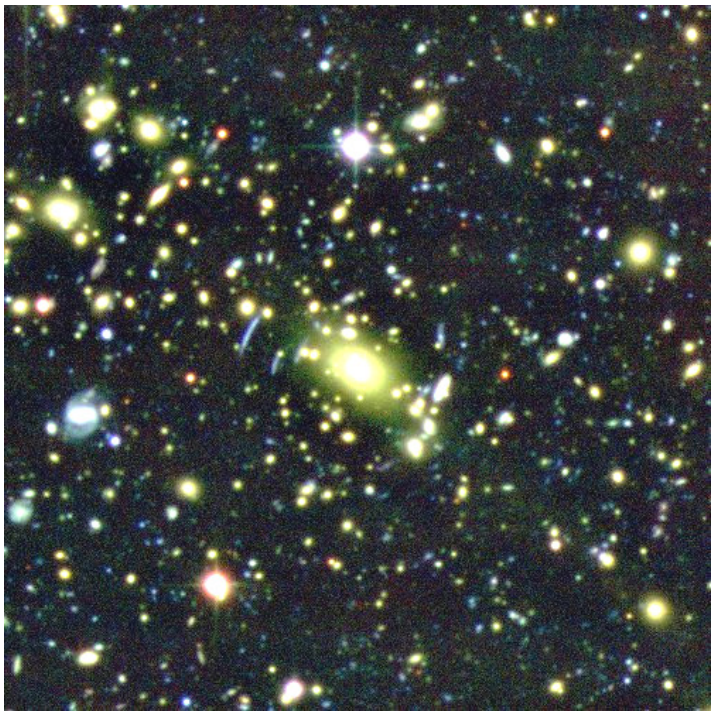

Figure 4.1: BRI colour image of the central 200×200 arcsec^2 of RXC J2248.7–4431. Clearly visible are the brightest cluster galaxy and several gravitational arcs, along with a high concentration of yellow cluster member galaxies.

4.1 Introduction

Clusters of galaxies, such as RXC J2248.7–4431 (cf. Fig. 4.1) studied in this work, are the most massive gravitationally bound objects that have formed in the Universe to date. What makes them interesting for cosmology is that they lie at an intersection of the two potentially most important unresolved questions: their mass content is dominated by dark matter - and their formation and evolution is strongly influenced by the interplay of matter density and dark energy. For this reason, studying clusters of galaxies is also a powerful probe of cosmological parameters and models (e.g. Wang & Steinhardt, 1998; Holder et al., 2001; Weller et al., 2002).

Perhaps the most important property of a cluster of galaxies with respect to cosmology is its virial mass, which can be determined in several different ways. The number and the velocity dispersion of cluster member galaxies are related to the total mass of the system. One can use larger fractions of the overall mass as a proxy by observing the hot intracluster gas, which emits X-ray radiation (e.g. Böhringer et al., 2004a; Sahlen et al., 2009; Piffaretti et al., 2011) and changes the cosmic microwave background spectrum due to inverse Compton scattering (Sunyaev-Zel'dovich, SZ, effect; cf. Sunyaev & Zel'dovich, 1972; Haiman et al., 2001; Battye & Weller, 2003). The latter observables can be related to mass by astrophysical modelling or self-calibration (Hu, 2003; Majumdar & Mohr, 2004).

Despite this, however, weak gravitational lensing is a valuable ingredient since the tangential alignment of background galaxy images is directly proportional to overdensity of all cluster matter - luminous or dark - alike and is insensitive to the astrophysical state of the cluster. This allows for unbiased mass measurements of single clusters and improved calibration of other mass-observable relations (e.g. Allen et al., 2002; Okabe et al., 2010; Hoekstra et al., 2011a). Furthermore, gravitational lensing straightforwardly allows the probing of additional properties of the density profiles of dark matter haloes, such as their concentrations, for which predictions in a cosmological model can be made and from which additional constraints can be drawn (see for instance the Cluster Lensing And Supernova survey with *Hubble* (CLASH), in which RXC J2248.7–4431 is also observed; cf. Postman et al., 2012).

In this work we analyse the weak lensing effect of the cluster RXC J2248.7–4431 based on background galaxy shapes and photometric redshifts measured from *UBVRIZ* multiband imaging by the Wide-Field Imager (WFI) on the 2.2-m MPG/ESO telescope at La Silla. In Section 2, we introduce the basic properties of the data used and our data reduction. Section 3 summarizes previous optical, X-ray and SZ observations of RXC J2248.7–4431. We give an overview of the photometric analysis, including photometric redshifts, cluster member photometry and morphology, in Section 4. Technical aspects of our weak lensing measurements are discussed in Section 5. The analysis of the weak lensing effect of RXC J2248.7–4431 is presented in Section 6. Results for a second cluster found in the field of view at $z \approx 0.6$ are shown in Section 7. We summarise our results in Section 8.

All numerical values given in this work are calculated for cosmological parameters $H_0 = 72$ km s^{-1} Mpc^{-1} and $\Omega_m = 1 - \Omega_\Lambda = 0.27$. Where applicable, measurements from the literature have been converted to this cosmology as well. We denote the radii of spheres around the cluster centre with fixed overdensity as $r_{\Delta\mathrm{m}}$ and $r_{\Delta\mathrm{c}}$, where Δ is the overdensity factor of the sphere with respect to the mean matter density ρ_m or critical density ρ_c of the Universe at the cluster redshift. Masses inside these spheres are labelled and defined correspondingly as $M_{\Delta\mathrm{m}} = \Delta \times \frac{4\pi}{3} r_{\Delta\mathrm{m}}^3 \rho_\mathrm{m}$ and $M_{\Delta\mathrm{c}} = \Delta \times \frac{4\pi}{3} r_{\Delta\mathrm{c}}^3 \rho_\mathrm{c}$.

4.2 Observations and data reduction

This analysis is based on observations made with the WFI on the 2.2-m MPG/ESO telescope at La Silla. The sensitivity of the instrument and the filters available spans all optical wavelengths and with its field of view of 33×33 arcmin^2 it is well suited for weak lensing cluster analyses with photometric redshifts.

The observations in U (#877), B (#842), V (#843), R (#844), I (#879) and Z (#846) band[2] used in this work were taken in the years 2009-2010. Details of integration time as a

[2] https://www.eso.org/lasilla/instruments/wfi/inst/filters/

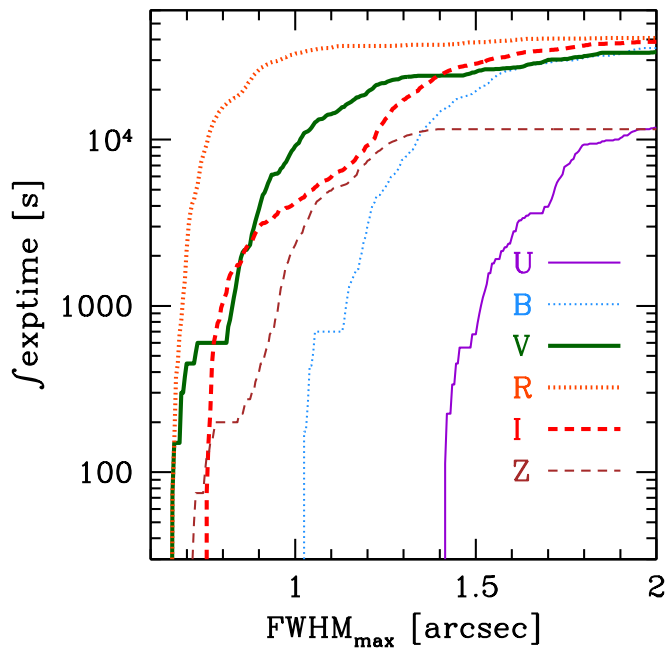

Figure 4.2: Cumulative exposure time as a function of limiting seeing in WFI frames of RXC J2248.7–4431 used in this work. Bold lines show the bands used for shape measurement, where we have applied seeing FWHM cuts at 0.9 arcsec (1.0 arcsec) in R (V and I) band, respectively.

function of limiting point spread function (PSF) full-width at half-maximum (FWHM) are shown in Fig. 4.2. The excellent depth and seeing in R band (with over 9 hours of exposure time at sub-arcsecond seeing, yielding a coadded image with 0.8 arcsec PSF FWHM and limiting magnitude of $m_{R,\mathrm{Vega,lim}} = 26.7$ for a 5σ detection inside a 1 arcsec diameter aperture) make it our primary lensing band, but also in V (0.9 arcsec seeing with $m_{V,\mathrm{Vega,lim}} = 26.4$) and I band (0.9 arcsec PSF FWHM with $m_{I,\mathrm{Vega,lim}} = 24.4$) shape measurements of background galaxies are feasible.

We perform de-biasing, flat fielding, masking of bad pixels in all bands and fringe pattern correction in the I and Z band using the Astro-WISE[3] pipeline (Valentijn et al., 2007). Background subtraction, final astrometry and co-addition of suitable frames is done externally using SCAMP[4] (Bertin, 2006) and SWarp[5] (Bertin et al., 2002). The central part of a colour image based on these co-added frames is shown in Fig. 4.1.

For photometry, we take observations of standard star fields in B, V and R to fit zero-points for each CCD individually and extinction coefficients globally. From nights which we confirm to be photometric according to their standard star measured zero-points we build a photometric B, V and R stack. We build deeper stacks including frames from all available nights with relative photometry fitted by SCAMP and match the magnitudes measured from these stacks to the photometric ones in order to find zero-points for the deep stacks. Alternatively, fixing the R band zero-point, we find U, B, V, I and Z zero-points by minimizing

[3] http://www.astro-wise.org/
[4] http://www.astromatic.net/software/scamp
[5] http://www.astromatic.net/software/swarp

residuals in colour-colour diagrams with respect to the stellar library of Pickles (1998). The stellar locus zero-points found in this way for B and V agree within 0.02 mag with the photometric zero-points found by matching the two versions of the stacks, confirming that our photometric pipeline provides consistent results.

4.3 Previous work on RXC J2248.7–4431

The cluster RXC J2248.7–4431 studied in this work is also known as Abell S1063 or MACS 2248-4431. Here we give an overview of all literature on the cluster published previously to this work, including detections and redshift estimates, X-ray observations and SZ measurement. We discuss the more detailed findings of Gómez et al. (2012) and compare them to our own analyses in Section 4.7.

RXC J2248.7–4431 was first listed by Abell et al. (1989) with a background-corrected galaxy count of 74. It was independently detected by the *ROSAT* All-Sky Survey (de Grandi et al., 1999), who quote a redshift estimate of $z = 0.252$, which was, however, only weakly determined based on the Abell et al. (1989) distance class. Cruddace et al. (2002) give its redshift as $z = 0.1495$ based on private communications with Andernach (private communication). Böhringer et al. (2004a) finally quote a spectroscopic redshift of $z_{\rm cl} = 0.3475$, which is what we adopt for this work. This is confirmed by spectroscopy of 51 cluster members with a mean redshift of $z = 0.3461^{+0.0010}_{-0.0011}$ (Gómez et al., 2012).

Gómez et al. (2012) find the spectroscopic velocity dispersion of to be $\sigma_v = 1660^{+230}_{-150}$km s^{-1}, which corresponds to a mass of $M_{200c} = 42^{+17}_{-9} \times 10^{14} M_\odot$ according to the relation of Evrard et al. (2008).

Cruddace et al. (2002) quote an X-ray temperature of 7.823 keV from the *ROSAT* All-Sky Survey (RASS). Maughan et al. (2008) give the X-ray temperature within R_{500} as $11.1^{+0.8}_{-0.9}$keV and parametrize the cluster profile as slightly elliptical with $1 - b/a = 0.2$ based on *Chandra* ACIS-I data. Both values are based, however, on earlier erroneous cluster redshifts ($z = 0.1495$ for Cruddace et al. 2002 and $z = 0.252$ for Maughan et al. 2008). The Planck Collaboration et al. (2011b) quote an X-ray mass based on their follow-up with *XMM-Newton* of $M_{500c} = (12.25 \pm 0.21) \times 10^{14} M_\odot$ which they use to calibrate their SZ MOE. Comis et al. (2011) determine $M_{2500c} = (5.3 \pm 2.6) \times 10^{14} M_\odot$ from *Chandra* X-ray data and Gómez et al. (2012) give a consistent value from independent data reduction of the same data of $M_{2500c} = (6.0 \pm 1.6) \times 10^{14} M_\odot$.

Plagge et al. (2010) parametrize the SZ profile measured with the South Pole Telescope (SPT) with a β parameter of (0.86 ± 0.02) arcmin at a scaling of $\Delta T \approx 1$ mK. Williamson et al. (2011) quote an SZ signal-to-noise ratio (S/N) of 20.7 and a SZ mass of $M_{200m} = (28.2 \pm_{\rm stat} 3.6 \pm_{\rm sys} 9.3) \times 10^{14} M_\odot$. The Planck Collaboration et al. (2011a) detect the SZ effect of RXC J2248.7–4431 at 13.93σ significance. From the *Planck* SZ observable and scaling relation (Planck Collaboration et al., 2011b) the SZ mass is $M_{500c} = (11.5 \pm_{\rm stat} 2.6 \pm_{\rm sys} 0.5) \times 10^{14} M_\odot$.

Guzzo et al. (2009) and Plagge et al. (2010) show X-ray and SZ imaging of the cluster, respectively. The cluster is also covered by the CLASH project (Postman et al., 2012; Monna et al., 2014).

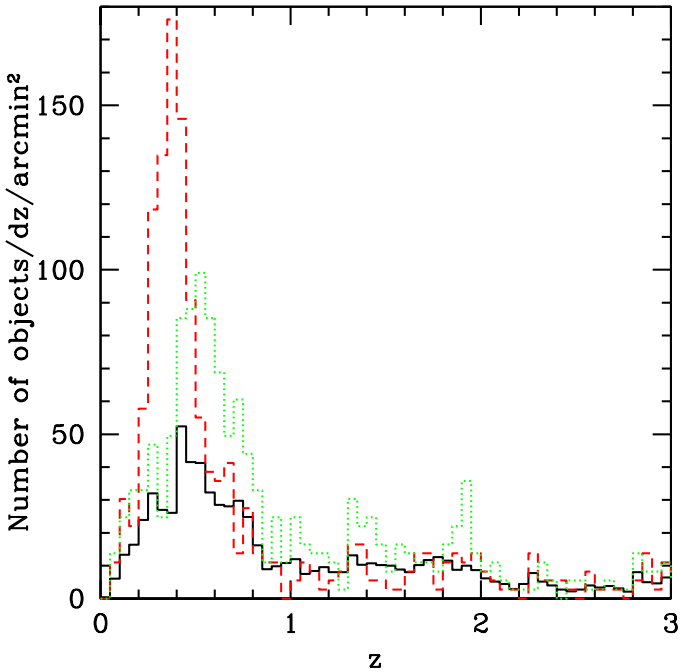

Figure 4.3: Three-dimensional galaxy density as a function of photometric redshift in the WFI field (black, solid lines) and inside a circle of radius 100 arcsec around the brightest cluster galaxy of RXC J2248.7–4431 (red, dashed lines). The cluster at a redshift of $z_{\rm cl} = 0.3475$ (Böhringer et al., 2004a) can be clearly seen as a peak in this smaller field. The green, dotted line shows objects within a radius of 100 arcsec around the BCG of the $z \approx 0.6$ cluster described in Section 4.8.

4.4 Photometric analysis

4.4.1 Photometric redshifts

The multicolour catalogue creation and photometric redshift estimation follow the procedure described in Brimioulle et al. (2013). Here we only give a brief overview. We convolve all data with a Gaussian kernel to match the seeing to the band where it is largest (in this case the U band). This equalization of the PSF is required for reliable aperture colours in the different filters. We then run SExtractor[6] in dual-image mode to extract fluxes, including weight images and masks of bad areas in the detection and extraction frame. We detect the objects on the unconvolved R band with a S/N threshold of 2σ on at least four contiguous pixels. Flux and magnitude information is extracted from the convolved images. We correct for extinction and zero-point accuracies by comparing the stellar locus in colour-colour diagrams to the stellar library of Pickles (1998). We then use the photometric template-fitting algorithm of Bender et al. (2001) to estimate photometric redshifts.

The density of galaxies in redshift space is shown in Fig. 4.3. The cluster is clearly visible as a redshift density peak around the spectroscopic $z_{\rm cl} = 0.3475$, which is also true for the second cluster at a mean photometric redshift of $z \approx 0.6$, described in detail in Section 4.8.

In our weak lensing analysis we only consider background galaxies with a minimum pho-

[6] http://www.astromatic.net/software/sextractor

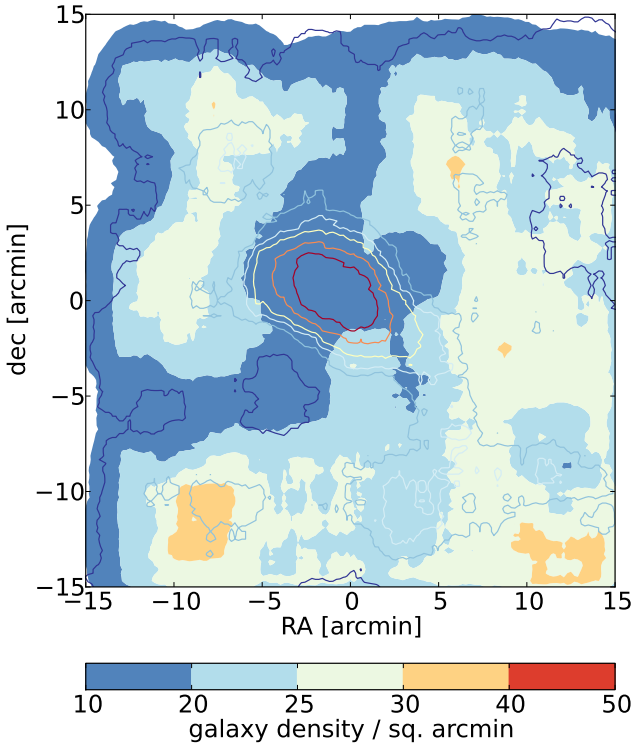

Figure 4.4: Density of galaxies in our photometric redshift catalogue in a map centred on the BCG position, averaged in angular boxes of 4×4 arcmin^2 size. Contour lines show density per arcmin^2 per redshift interval for sources with $|z - z_{\rm cl}| < 0.04(1 + z_{\rm cl})$. The background colour shows the overall density of sources above the redshift cut of equation (4.1). The depletion of background galaxies at the cluster position is an indication that our background sample is pure. The high background density observed in the lower left of the map is due to the system discussed in Section 4.8.

tometric redshift of

$$z_{\rm source} > 1.1 z_{\rm cl} + 0.15 \approx 0.53 \ . \tag{4.1}$$

We include objects up to a maximum photometric redshift of $z = 4$. We verify that this excludes redshift mismeasurement of cluster galaxies into the background sample by means of redshift density maps at the cluster redshift and for objects selected by the background cut of equation (4.1) in Figure 4.4. Indeed, the cluster is seen as a highly significant overdensity of objects around $z_{\rm cl}$, while the density of background sources near the cluster is smaller than in the field. This is expected owing to the area covered by cluster light and indicates that background contamination is not a significant issue, as expected for the red cluster galaxies whose redshift can be determined photometrically to good accuracy.

4.4.2 Cluster member SEDs

We investigate photometric properties and spectral energy distribution (SED) types of the cluster member galaxies of RXC J2248.7–4431 and the second cluster at $z \approx 0.6$ (cf. Sec-

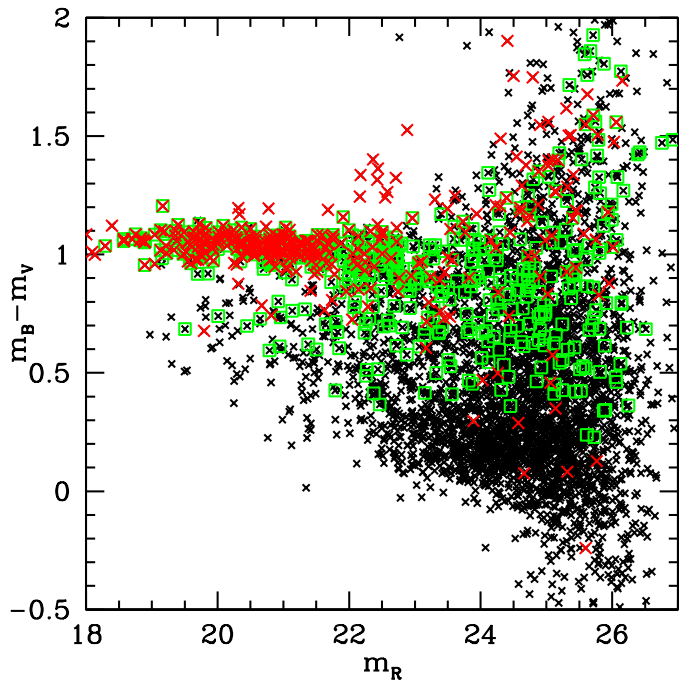

Figure 4.5: Colour-magnitude diagram of galaxies within 5 arcmin projected separation from the BCG, using B-V aperture colours and R band MAG_AUTO magnitudes and showing all objects (black, small crosses), objects with red spectral energy distribution types (cf. Dahlen et al., 2005; Brimioulle et al., 2013) (red, large crosses) and marking objects in a redshift slice $|z - z_{\rm cl}| \leq 0.04(1+z_{\rm cl})$ around the cluster by a green open square.

tion 4.8).

The brightest cluster galaxy (BCG) of RXC J2248.7–4431 has a photometric redshift of 0.4 and an absolute magnitude of $M_{R,\rm Vega} = -24.81$. Its counterpart in the $z \approx 0.6$ cluster has a photometric redshift of 0.66 and an absolute magnitude of $M_{R,\rm Vega} = -25.1$.

Cluster members galaxies are preferentially of early type and, at a given redshift, lie on a relatively tight sequence in colour-magnitude space, the red sequence. We plot B-V aperture colours, which are particularly indicative of the D4000 break, against R band MAG_AUTO magnitudes in Fig. 4.5. The red sequence is clearly detected and dominant among cluster members. We measure the fraction of red galaxies on a sample of cluster members selected by their photometric redshift $|z - z_{\rm cl}| \leq 0.04(1 + z_{\rm cl})$ for both RXC J2248.7–4431 and the second cluster found at $z \approx 0.6$. Fig. 4.6 shows the fraction of these galaxies which are classified photometrically as having a red SED (cf. Dahlen et al., 2005; Brimioulle et al., 2013), $N_{\rm red}/N_{\rm total}$, as a function of projected separation from the cluster in units of its r_{200m} according to our best-fitting Navarro-Frenk-White (NFW) models (see Sections 4.6.5 and 4.8) and as a function of depth.

The latter is fixed relative to the characteristic luminosity of the Schechter function, $L^\star$. $L^\star$, or in this case $m^\star$, is estimated by fitting a Schechter function to the statistically background corrected cluster luminosity function (as in Zenteno et al. 2011). The limiting depth for the fit is chosen at $m^\star + 4$, where $m^\star$ is found iteratively. The offset of 4 limits the magnitude range so it is well sampled for both clusters. In this way we find characteristic

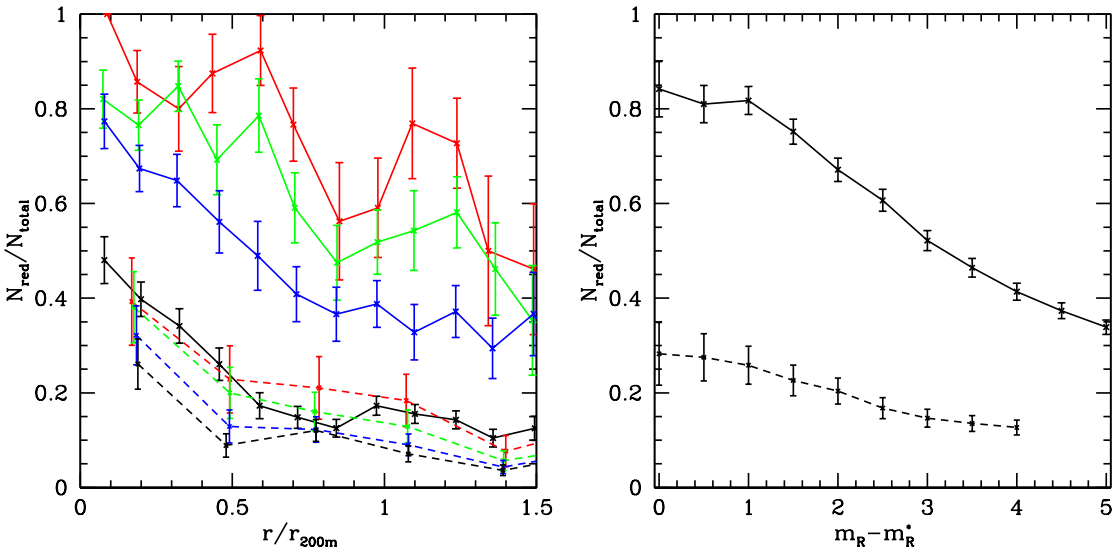

Figure 4.6: Fraction of galaxies having a red SED type in the redshift slice and projected vicinity of RXC J2248.7–4431 (solid lines) and the second cluster at $z \approx 0.6$ (dashed lines). The left panel shows the red fraction as a function of radius from the BCG in units of r_{200m} of the respective system with magnitude limits at $m_R^\star + 1$ (red), $m_R^\star + 2$ (green), $m_R^\star + 3$ (blue) and our detection limit (black). The right panel shows the red fraction inside r_{200m} of the respective system as a function of magnitude limit, which reaches the overall detection limit at $m_R^{\rm lim} - m_R^\star \approx 4$ for the $z \approx 0.6$ system. Error bars are calculated from the Poissonian noise in the number counts of red and blue galaxies in each bin.

magnitudes of $m^\star_{R,\rm Vega} = 19.3^{+0.5}_{-0.6}$ ($m^\star_{R,\rm Vega} = 22.2^{+0.9}_{-1.7}$ for the $z \approx 0.6$ cluster) for apparent R band and $M^\star_{r,\rm AB} = -23.4^{+0.3}_{-0.3}$ ($M^\star_{r,\rm AB} = -23.9^{+0.9}_{-1.0}$) for absolute magnitudes in Sloan Digital Sky Survey (SDSS) r' band.

We conclude that approximately 50 per cent of cluster members are red galaxies near the core of RXC J2248.7–4431, and that this fraction continuously drops towards the outskirts, where it is below 20 per cent. For the higher redshift system, the fraction of red galaxies in the cluster is significantly lower (which is known as the Butcher-Oemler effect, Butcher & Oemler 1978). The fraction of red galaxies decreases both towards fainter magnitudes, larger separations from the core and higher redshift.

4.4.3 Mass from richness and luminosity

We can find an independent estimate of cluster mass by means of mass-observable relations of richness and absolute luminosity. To this end, we apply the prescription of Wen, Han, & Liu (2010). For our cluster member catalogue we select luminous galaxies inside a projected radius of 1Mpc around the BCG within $|z - z_{\rm cl}| \leq 0.06(1 + z_{\rm cl})$ and with magnitudes $M_{r'} \leq -21$, where we use absolute magnitudes in SDSS r' band (Gunn et al., 1998). The size and r' band luminosity of the sample is 64 and $L_{r'} = 3.0 \times 10^{12} {\rm L}_\odot$. After subtracting the mean number and luminosity of similar object selected from a region of the field more than 3 Mpc from the BCG, we find a background corrected richness of $R = 54$ and luminosity of $L_{r'} = 2.6 \times 10^{12} {\rm L}_\odot$.

Applying the scaling relations of Wen et al. (2010), this yields

$$\begin{aligned} \log M_{101c}/(10^{14}h^{-1}M_\odot) &= (-1.57 \pm 0.12) + 1.55 \log R \\ &= 1.12 \pm_{\rm stat} 0.09 \pm_{\rm sys} 0.12 \end{aligned} \tag{4.2}$$

from richness as the mass proxy with systematic and statistical uncertainty. Alternatively, one can use the net luminosity to obtain

$$\begin{aligned} \log M_{101c}/(10^{14}h^{-1}M_\odot) &= (-2.03 \pm 0.06) + 1.49 \log L_{r'}/(10^{10}h^{-2}\mathrm{L}_\odot) \\ &= 1.14 \pm_{\rm stat} 0.09 \pm_{\rm sys} 0.06 \,. \end{aligned} \tag{4.3}$$

Since the errors of these two estimates are highly correlated we use the less uncertain equation (4.3), which yields a mass of $M_{101c} = 19 \pm 6 \times 10^{14} M_\odot$.

4.5 Weak lensing measurement

Weak gravitational lensing changes the ellipticities of the images of galaxies in the background of massive structures. Its measurement therefore requires the determination of pre-seeing galaxy shapes. In this section we describe our shape measurement, while the analysis of the signal is presented in Section 4.6.

4.5.1 Model of the point spread function

Any estimate of the pre-seeing shape of a galaxy requires knowledge of the point spread function (PSF). For a successful and unbiased weak lensing analysis it is most crucial to model the PSF accurately (cf. Kitching et al., 2013), since mismatches in ellipticity and size of the PSF model cause additive and multiplicative systematic errors in the shape estimate, respectively.

We use PSFEx[7] (Bertin, 2011) for determining the profile of the PSF as a polynomial function of the position in the co-added focal plane. To this end, we perform a pre-selection of stars according to size, S/N and the SExtractor[8] neural network star classifier (Bertin & Arnouts, 1996). The pre-selected stars (cf. Fig. 4.7) are used to determine the PSF model, which is then checked using the following diagnostics:

i) mean and scatter of residual ellipticities and sizes to check for remaining offsets and quality of the fit;

ii) whisker plot of residual ellipticities to exclude failure of the fit in specific regions of the focal plane;

iii) two-point autocorrelations of ellipticity residuals (D_1) and cross-correlation of residuals and measured star ellipticities (D_2) to exclude under- and overfitting, as defined in Rowe (2010), equations (13) and (14).

We verify, in particular, that a star pre-selection is necessary for the size of the PSFEx model to match the size of the PSF well enough. In R and V a smooth PSF model over the

[7] http://www.astromatic.net/software/psfex
[8] http://www.astromatic.net/software/sextractor

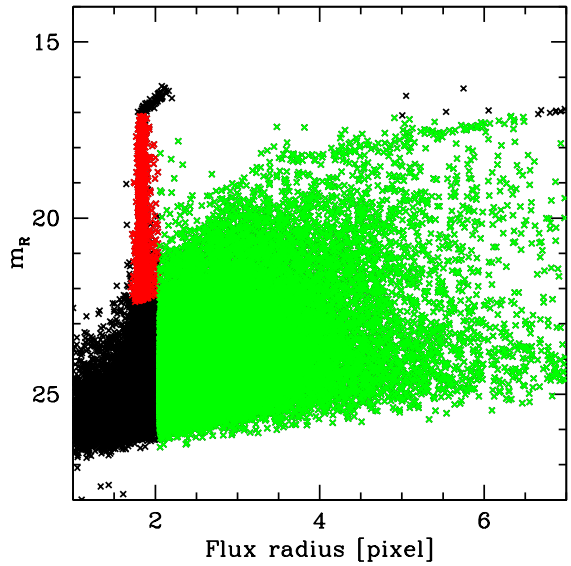

Figure 4.7: Selected stars for PSF modelling (red) and sources initially accepted for shape measurement (green).

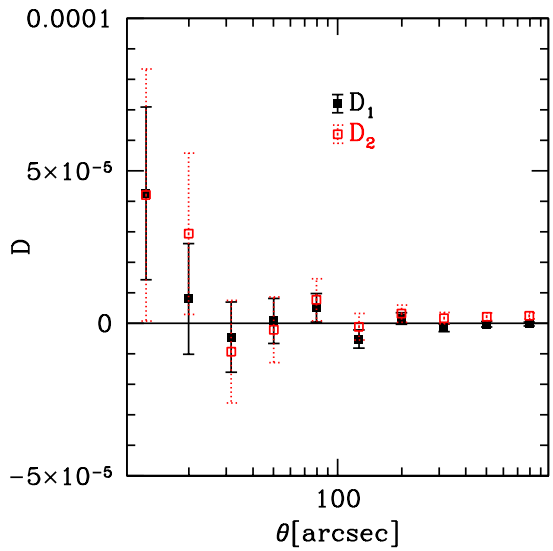

Figure 4.8: Autocorrelation of PSF model ellipticity residuals (D_1) and cross-correlation of residuals and measured ellipticity (D_2) according to Rowe (2010) for a fifth order polynomial PSF model in the R band co-add. While lower orders show signs of underfitting (D_1 and/or D_2 significantly non-zero on some scales), higher orders do not improve the model further and show signs of overfitting (D_2 significantly negative on some scales).

whole focal plane is a sufficient description of the observed pattern. We find that, similar to other exposures from the WFI camera we have analysed in the past, the I-band PSF is more difficult to model. Only when masking the border regions between neighbouring chips and discarding all stars and galaxies in those regions can we describe the PSF with a simple polynomial dependence on position to sufficient accuracy. For these tests we find that the method of Rowe (2010) is particularly helpful, and use it to determine the correct polynomial order of the spatial variation [5 (7) for the R (V and I) band, respectively], which match the observed PSF without clear signs of over- or underfitting (cf. Fig. 4.8).

4.5.2 Shape Measurement

We run an implementation of the KSB+ method (Kaiser, Squires, & Broadhurst 1995, hereafter KSB; Luppino & Kaiser 1997; Hoekstra et al. 1998) using the PSFEx PSF model (KSBPSFEx) that has been tested against simulations at intermediate to large tangential shears and proven to be viable in the cluster shear regime (Young et al., in preparation). The pipeline includes the following preparation steps for the KSB+ shape measurement:

i) unsaturated sources with flux radii larger than the stellar flux radius and zero SExtractor flags are filtered;

ii) postage stamps of 64 × 64 pixels size are extracted and neighbouring objects according to the SExtractor segmentation map are masked;

iii) the SExtractor photometric background estimate at the object position is subtracted from the image in order to compensate for small-scale background variations insufficiently modelled by the data reduction pipeline;

iv) bad and masked pixels are interpolated using a Gauss-Laguerre model of the galaxy (Bernstein & Jarvis, 2002), where we discard objects with more than 20 per cent of postage stamp area or 5 per cent of model flux falling on to bad or masked pixels.

As the final step of the shape measurement, KSB+ is run on the cleaned postage stamp of the galaxy and the sub-pixel resolution PSF model at the galaxy position. For details, we refer the reader to the papers introducing and extending the method. Here we only give a brief summary.

KSB measure polarizations,

$$\boldsymbol{e} = \frac{1}{Q_{11} + Q_{22}} \begin{pmatrix} Q_{11} - Q_{22} \\ 2Q_{12} \end{pmatrix} , \tag{4.4}$$

using second moments calculated inside a Gaussian aperture,

$$Q_{ij} = \int d^2\theta I(\boldsymbol{\theta}) w(|\theta|) \theta_i \theta_j , \tag{4.5}$$

of the surface brightness distribution of the galaxy $I(\boldsymbol{\theta})$ with a Gaussian weight function $w(|\theta|)$ centred on the galaxy centroid. In our implementation, the weight function for measuring the galaxy and PSF moments is scaled with the measured half-light radius of the observed galaxy.

Cluster weak lensing analyses require the ensemble measurement of reduced shear (cf. Bartelmann & Schneider, 2001, p.60). In the presence of an elliptical PSF, the linear approximation of how observed post-seeing polarization $\boldsymbol{e_o}$ reacts to a reduced shear $\boldsymbol{g}$ can be expressed as

$$\boldsymbol{e_o} = \boldsymbol{e}_i + \mathbf{P}^{\mathrm{sm}}\boldsymbol{p} + \mathbf{P}^{\gamma}\boldsymbol{g} \ , \tag{4.6}$$

where $\boldsymbol{e}_i$ is the intrinsic post-seeing ellipticity of the galaxy, $\mathbf{P}^{\mathrm{sm}}$ is a 2×2 tensor quantifying the response of observed shear to PSF polarisation $\boldsymbol{p}$ and $\mathbf{P}^{\gamma}$ is the shear responsivity tensor. Inverting $(\mathbf{P}^{\gamma})^{-1} \approx \frac{2}{\mathrm{tr}\mathbf{P}^{\gamma}}$ and assuming that $(\mathbf{P}^{\gamma})^{-1}\boldsymbol{e}_i$ is zero on average because of the random intrinsic orientation of galaxies, this yields the ensemble shear estimate

$$\langle \boldsymbol{g} \rangle = \langle \boldsymbol{\epsilon} \rangle = \left\langle \frac{2}{\mathrm{tr}\mathbf{P}^{\gamma}} \left(\boldsymbol{e_o} - \mathbf{P}^{\mathrm{sm}}\boldsymbol{p} \right) \right\rangle \ . \tag{4.7}$$

We remove objects with failed KSB+ measurements and objects with $\mathrm{tr}\mathbf{P}^{\gamma} < 0.1$ from the final shape catalogue. The latter is a requirement owing to the noisiness of measured $\mathrm{tr}\mathbf{P}^{\gamma}$, which otherwise greatly amplifies the uncertainty of equation (4.7) (cf. Schrabback et al., 2007; Romano et al., 2010; Applegate et al., 2014; Newman et al., 2013, for similar clipping schemes at various levels of $\mathrm{tr}\mathbf{P}^{\gamma}$). We match R, V and I band shape catalogues and take the arithmetic mean of all available bands as the individual object shape and match against the photometric redshift catalogue to select valid background galaxies and assign redshift scalings. This and the S/N cut introduced in Section 4.5.3 leaves us with an average of nine galaxies per square arcminute in the background of RXC J2248.7–4431 with a mean ratio of angular diameter distances of $\langle D_{ds}/D_s \rangle = 0.59$ (cf. Section 4.6.1).

4.5.3 Noise bias calibration

Biases of shape estimators are commonly expressed as a multiplicative and an additive term (Heymans et al., 2006), where the additive component is typically due to imperfect correction for the ellipticity of the PSF. The latter effect is particularly relevant for cosmic shear analyses, where auto-correlations of the shear field are calculated and auto-correlations of the PSF ellipticity field would enter the equation by means of an additive bias (for a more detailed study of the influence of shape biases on cosmic shear, see Amara & Réfrégier, 2008). All analyses we do in this cluster weak lensing study, however, deal with shear estimates averaged in an annulus, in which case any constant additive bias cancels out. Pixel noise, on the contrary, typically causes multiplicative biases at the per cent level over a wide range of observational conditions, which would directly enter our cluster weak lensing model (Melchior & Viola, 2012). This and the fact that we do not observe significant additive biases on simulated images with elliptical PSF is the reason for limiting our calibration to the most important factor, namely noise-dependent multiplicative bias.

Shape measurement, primarily because it involves division by noisy quantities, suffers from a noise bias, which is negligible for bright galaxies but becomes troublesome for the faint end of background galaxies in a weak lensing analysis (Kaiser, 2000; Bernstein & Jarvis, 2002; Melchior & Viola, 2012; Refregier et al., 2012; Kacprzak et al., 2012). Many studies in the past have applied a global correction factor to their KSB shape catalogue (see Schrabback et al. 2007; Clowe et al. 2012; Ragozzine et al. 2012; Newman et al. 2013 for a range of factors used), but there also have been cases where calibration has been matched to galaxy S/N and sometimes also size using simulated galaxy images (Schrabback et al., 2010; von der

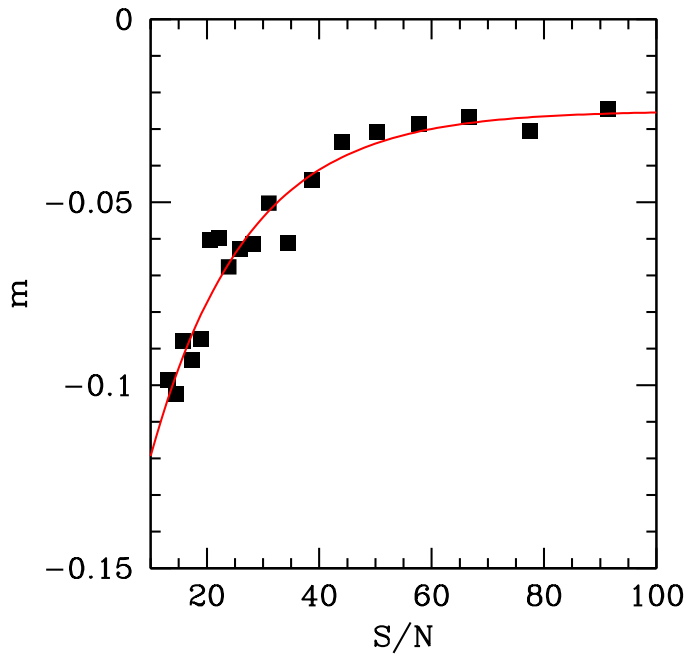

Figure 4.9: Multiplicative bias m as a function of S/N for our shape pipeline, as measured using image simulations with a range of PSF sizes, shears and galaxy properties typical for a weak lensing cluster study like ours. The results are well fit by equation (4.9) with best-fitting parameters $A = 0.025$, $B = 0.17$ and $C = 17$ (red line).

Linden et al., 2014a). We quantify the magnitude of noise bias in our pipeline using image simulations with a range of PSF sizes, shears and galaxy properties typical for a weak lensing cluster study like ours (Young et al., in preparation).

If a shear estimator g_o only has multiplicative bias m, it can be written as

$$g_o = (1 + m)g + N \ , \tag{4.8}$$

where g is the true shear and N is a noise term with zero mean. We fit m for simulated sets of galaxies and show the results in Fig. 4.9 as a function of S/N measured according to the prescription of Erben et al. (2001). The multiplicative bias is fit well by the functional form

$$m = -A - B \exp(-(\mathrm{S/N})/C) \ , \tag{4.9}$$

with best-fitting values of $A = 0.025$, $B = 0.17$ and $C = 17$ down to a S/N of 10.

We discard objects outside the regime this calibration was tested on (i.e. where S/N$<$ 10 (Erben et al., 2001) or $(\mathrm{S/N})_{\mathrm{iso}} < 15$ as measured inside an isophotal aperture of 1.5σ significance per pixel over the background). The remainder of our sample is calibrated with the m of equation (4.9), by multiplying shape estimates by a factor of $1/\left[1 + m(\mathrm{S/N})\right]$.

4.6 Weak Lensing Analysis

4.6.1 Introduction

Cluster weak lensing analysis aims to reconstruct properties of the density field of clusters of galaxies from the reduced shear they impose on the images of background galaxies. We refer the reader to the review of Bartelmann & Schneider (2001) for an in-depth introduction and only give a brief overview of the main concepts here.

Gravitational shear $\boldsymbol{\gamma}$ relates to reduced shear $\boldsymbol{g}$ as

$$\boldsymbol{\gamma} = \boldsymbol{g}(1-\kappa) \ , \tag{4.10}$$

where κ is the projected surface mass density in units of the critical surface density, $\kappa = \Sigma/\Sigma_c$, with

$$\Sigma_c = \frac{c^2}{4\pi G}\frac{D_s}{D_d D_{ds}} \ . \tag{4.11}$$

The latter contains a geometric factor composed of angular diameter distances $D_{s,d,ds}$ from observer to source, from observer to lens and from lens to source, respectively.

The surface mass density is related to the mean tangential component of the shear on a circle, $\gamma_t(r)$, by the simple equation

$$\gamma_t(r) = \langle \kappa(<r) \rangle - \kappa(r) \ , \tag{4.12}$$

the difference between mean κ inside and on the edge of the circle.

Equations (4.10) and (4.12) show that the observable $\boldsymbol{g}$ is invariant under mass sheet transformations, $\kappa \to \lambda\kappa + (1-\lambda)$, a degeneracy which can be broken for instance by assuming a functional form of $\kappa(r)$.

In the following we use two common density profiles, the singular isothermal sphere (SIS) and the NFW profile (Navarro, Frenk, & White, 1996). Their densities are given by

$$\rho_{\rm SIS}(r) = \frac{\sigma_v^2}{2\pi G r^2} \ , \tag{4.13}$$

with a constant velocity dispersion σ_v, and

$$\rho_{\rm NFW}(r) = \frac{\rho_0}{(r/r_s)(1+r/r_s)^2} \ . \tag{4.14}$$

The NFW profile has two free parameters which are commonly expressed in terms of the mass and concentration $c_{\Delta m} = r_{\Delta m}/r_s$ or $c_{\Delta c} = r_{\Delta c}/r_s$ instead of the central density ρ_0 and the scale radius r_s used in the equation above.

The projected surface mass density and tangential shear profiles of a SIS can be readily integrated as

$$\kappa(r) = \gamma_t(r) = 2\pi \left(\frac{\sigma_v}{c}\right)^2 \frac{D_{ds}}{D_s}\frac{1}{r} \ . \tag{4.15}$$

For the NFW profile, we refer the reader to the calculations in Wright & Brainerd (2000).

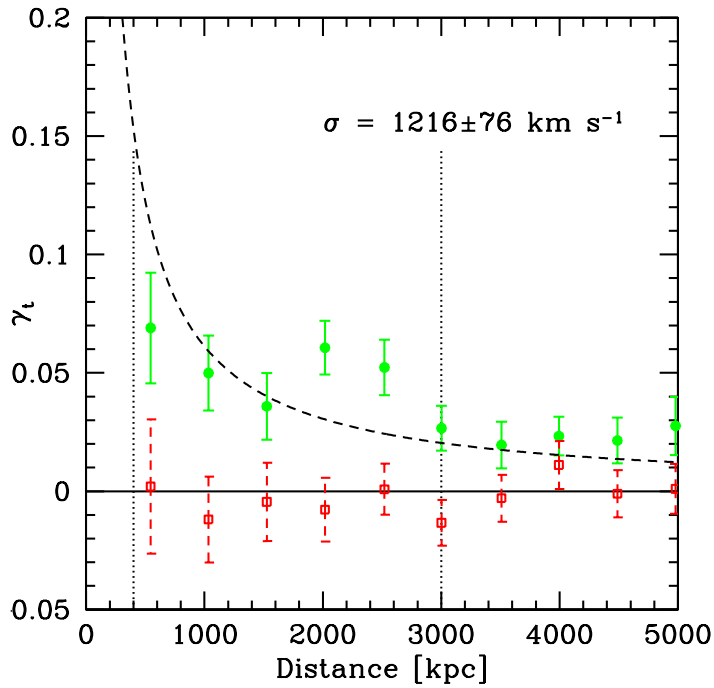

Figure 4.10: Tangential alignment (green circles), B mode (red squares) and SIS fit (dashed line) inside the interval delimited by dotted vertical lines. Note that the B mode is consistent with 0 as expected for a bias-free shape catalogue.

4.6.2 Tangential alignment

We first measure the tangential alignment signal around the brightest cluster galaxy (cf. Fig. 4.10). For this we calculate the mean reduced tangential shear g_t in radial bins and convert it into tangential gravitational shear γ_t assuming a SIS profile, for which (cf. equations 4.10 and 4.15)

$$\gamma_t = \frac{g_t}{1+g_t} \ . \tag{4.16}$$

The effective distance ratio D_{ds}/D_s is calculated from the mean individual galaxy values in each bin. The SIS fit yields a velocity dispersion of $\sigma_v = 1216 \pm 76$ km s^{-1}, measuring in the radial range of 400-3000 kpc projected distance. As it follows from equation (4.13),

$$r_{200c} = \frac{\sqrt{2}\sigma_v}{10H(z)} = (2025 \pm 126) \text{ kpc and} \tag{4.17}$$

$$r_{200m} = \frac{\sqrt{2}\sigma_v}{10H_0\sqrt{\Omega_m(1+z)^3}} = (2979 \pm 184) \text{ kpc} \ , \tag{4.18}$$

which implies a mass of $M_{200c,\mathrm{SIS}} = (14.0 \pm 2.6) \times 10^{14}\ M_\odot$ and $M_{200m,\mathrm{SIS}} = (21.0 \pm 3.8) \times 10^{14}\ M_\odot$.

4.6.3 Significance map

For a first two-dimensional view of the lensing signal, we measure the surface mass density or, equivalently, tangential gravitational shear inside circular weighted apertures, so-called

	NFW fit	Literature value	Source	Method
M_{200m}	$33.1^{+9.6}_{-6.8}$	$28.2 \pm_{\rm stat} 3.6 \pm_{\rm sys} 9.3$	Williamson et al. (2011)	SZ
M_{101c}	$32.2^{+9.3}_{-6.6}$	19 ± 6	Section 4.4.3 / Wen et al. (2010)	Luminosity
M_{200c}	$22.8^{+6.6}_{-4.7}$	42^{+17}_{-9}	Gómez et al. (2012)	Kinematics
M_{500c}	$12.7^{+3.7}_{-2.6}$	12.25 ± 0.21	Planck Collaboration et al. (2011b)	X-ray / *XMM-Newton*
		$11.5 \pm_{\rm stat} 2.6 \pm_{\rm sys} 0.5$	Planck Collaboration et al. (2011b)	SZ
M_{2500c}	$2.8^{+0.8}_{-0.6}$	5.3 ± 2.6	Comis et al. (2011)	X-ray / *Chandra*

Table 4.1: Best-fitting mass and confidence region of our NFW model (M_{200m}) converted to other definitions of mass inside spherical overdensity using the best-fitting concentration of $c_{200m} = 2.6$. All values are given in units of $10^{14} M_\odot$.

aperture masses (Schneider, 1996). We show the significance of aperture masses above zero as a function of position in Fig. 4.11. For this we use a Gaussian weight function

$$w(|\boldsymbol{\theta}|) \propto \begin{cases} \exp\left[-|\boldsymbol{\theta}|^2/(2\sigma_w^2)\right] & |\boldsymbol{\theta}| < 3\sigma_w \ , \\ 0 & \text{otherwise} \end{cases} \tag{4.19}$$

to calculate the significance, defined as the ratio between aperture mass and its uncertainty, $M_{\rm ap}/\sigma_{M_{\rm ap}}$ (Bartelmann & Schneider 2001, their Section 5.3 and Schirmer et al. 2004), with

$$\begin{aligned} M_{\rm ap}(\boldsymbol{\theta}) &= \sum_i w(|\boldsymbol{\theta} - \boldsymbol{\theta_i}|) g_{i,t} \\ \sigma_{M_{\rm ap}} &= \sqrt{\frac{1}{2} \sum_i w^2(|\boldsymbol{\theta} - \boldsymbol{\theta_i}|)|g_i|^2} \ , \end{aligned} \tag{4.20}$$

where $g_{i,t}$ is the tangential reduced shear of galaxy i measured with respect to $\boldsymbol{\theta}$. For the width of the aperture we use $\sigma_w = 3$ arcmin.

We detect the cluster as a peak in the aperture significance map with a significance of 5σ, centred on the BCG with a deviation of only few arcseconds. The significance map indicates an anisotropic distribution of mass around its centre, with additional peaks towards the north-eastern, south-western and southern direction from the BCG. We also check the significance of aperture B mode peaks and find them to be consistent with a random field.

4.6.4 Mass density map

We calculate a density map using the method of Kaiser & Squires (1993). For this we use all sources that satisfy the background cut of equation (4.1). These sources have a mean ratio of angular diameter distances of $\langle D_{ds}/D_s \rangle = 0.59$. The κ map has a pixel size of 1 arcmin and is smoothed with a Gaussian of $\sigma = 1.2$ arcmin width. The map is shown in Fig. 4.12 for the full field of view.

4.6.5 NFW model

We further perform a likelihood analysis (see Schneider, King, & Erben 2000) for a two-parametric NFW profile (Navarro et al., 1996) of the halo, fitting the concentration parameter c_{200m} and the mass M_{200m} simultaneously. We use background galaxies above a projected separation of 1 Mpc at the cluster redshift, since inside this limit some of the tested models

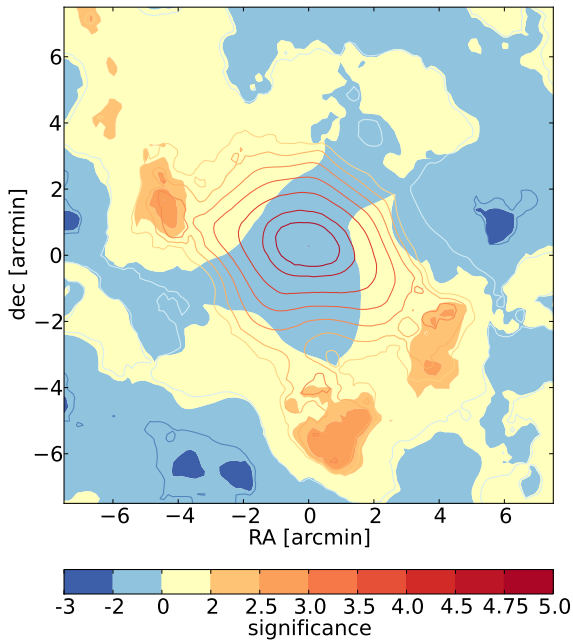

Figure 4.11: Aperture mass significance map calculated according to equations (4.19) and (4.20). Contour lines show the significance of aperture mass measured on background galaxies according to the cut of equation (4.1), which is centred on the BCG at a significance of 5σ. The background colour shows the aperture mass significance of the residual shape catalogue after subtracting the best-fitting NFW model of the central halo (cf. Section 4.6.5). Towards the lower left is the south-eastern corner of the image.

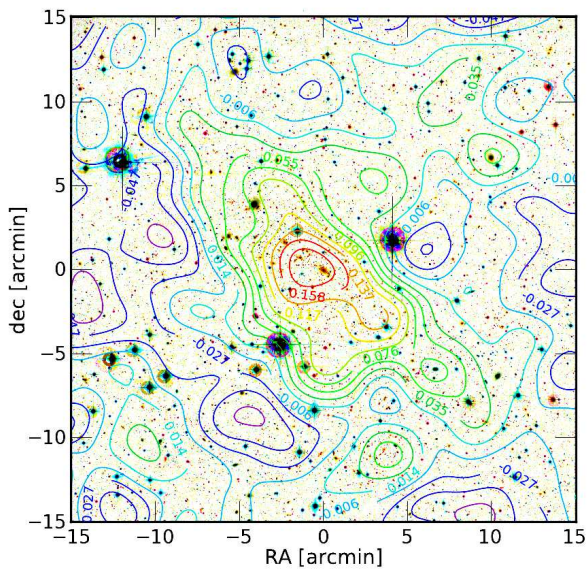

Figure 4.12: Density map, overlayed on colour image of RXC J2248.7–4431.

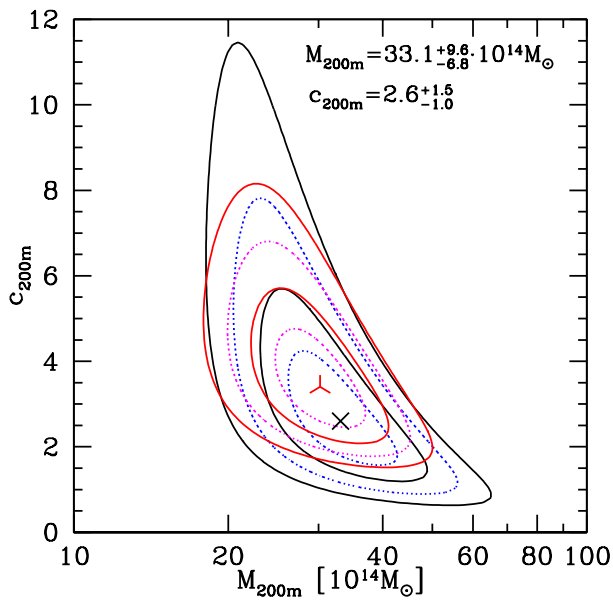

Figure 4.13: Likelihood contours of the two-parametric NFW profile of RXC J2248.7–4431. Black, solid (blue, dotted) contours show the combined (projected) confidence regions (intervals) for M_{200m} and c_{200m} with no concentration prior. Red, solid (magenta, dotted) contours for the combined (projected) confidence regions (intervals) using the concentration prior of Bullock et al. (2001) and Duffy et al. (2008). All contours are drawn at the 1σ and 2σ confidence levels. The black cross (red triangular symbol) indicate the best-fitting solution without (with) concentration prior.

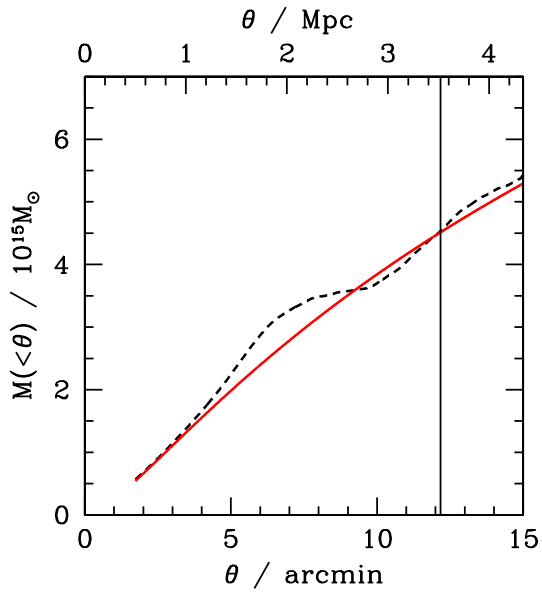

Figure 4.14: Projected excess mass inside a circle around the BCG of RXC J2248.7–4431, shown for the best-fitting NFW model (red, solid line) and directly measured from the observed tangential shear profile (black, dashed line), fixed at r_{200m} (vertical line).

predict shear above the weak regime and, in addition, astrophysical effects near the core of the cluster disturb the expected signal most (cf. Mandelbaum et al., 2010). This justifies the assumption of a model-independent dispersion of intrinsic shapes in equation (15) of Schneider et al. (2000). We use $\sigma_\epsilon = 0.3$, the dispersion of our best-fitting subtracted shape residuals, and determine confidence limits using the $\Delta\chi^2$ statistics of Avni (1976).

The 1σ confidence limits for mass and concentration individually are $M_{200m} = 33.1^{+9.6}_{-6.8} \times 10^{14} M_\odot$, $c_{200m} = 2.6^{+1.5}_{-1.0}$, where because of a degeneracy the very high masses only occur at unlikely low concentrations. Confidence contours are shown in Fig. 4.13.

Since there is prior knowledge about the concentration of dark matter haloes at given mass and redshift, we can reduce the uncertainty of our measurement by multiplying the likelihood with a concentration term

$$p(c|M,z) = e^{-[\log c - \log c(M,z)]^2/(2\sigma^2_{\log c})} \,, \tag{4.21}$$

where we adopt the mass-concentration relation $c(M,z)$ of Duffy et al. (2008) and a lognormal distribution of concentrations according to Bullock et al. (2001) with $\sigma_{\log c} = 0.18$. This leads to confidence limits of $M_{200m} = 30.2^{+6.1}_{-5.1} \times 10^{14} M_\odot$ and $c_{200m} = 3.4^{+1.3}_{-0.9}$.

For reference and comparison, we give corresponding masses in different definitions of spherical overdensity in Table 4.1. Our result is consistent inside the error limits with the X-ray mass of the Planck Collaboration et al. (2011b) and the SZ masses of Williamson et al. (2011) and Planck Collaboration et al. (2011b). The X-ray mass at high overdensity of Comis et al. (2011) is higher than our best fit, yet relatively uncertain and likely dominated by highly concentrated baryonic matter in and around the BCG, which is not correctly modelled by a global NFW halo. The mass calculated from richness and luminosity in Section 4.4.3 is significantly lower than our weak lensing result, yet likely contains systematic uncertainties because it was calibrated with different data. Spectroscopic velocity dispersion of cluster members yields a significantly higher mass estimate (Gómez et al., 2012), discussed in more detail in Section 4.7. In addition, we plot mass enclosed in a cylinder of varying radius, centred on the BCG, in Fig. 4.14.

Deviations from the spherically symmetrical NFW profile are known to exist in several different forms, such as correlated secondary haloes, asphericity of the main halo or filamentary structures (Dietrich et al., 2012b) and can influence the accuracy of weak lensing cluster analyses significantly (Gruen et al., 2011). In order to investigate these effects, we plot the aperture mass significance map on a shape catalogue with the signal of the best-fitting model subtracted in Fig. 4.11. While the central peak is described well by the spherical profile, we find that there are additional peaks towards the north-eastern, south-western and southern direction from the BCG, with the northern one potentially highly elongated towards the north-north-east. This is in line with the density map (cf. Section 4.6.4) and the shape of the galaxy concentration in three dimensional space (cf. Fig. 4.4). These structures therefore most likely represent correlated structures physically close to the main halo of RXC J2248.7–4431.

4.7 On the hypothesis of a recent merger in RXC J2248.7–4431

Gómez et al. (2012) present evidence for a recent merger of RXC J2248.7–4431 based on optical imaging, spectroscopy of 51 cluster members and analysis of the X-ray emission of the

system. We briefly recollect their findings and compare them with our results from deeper images with photometric redshift information and weak lensing.

4.7.1 Galaxy number density

The cluster member number density, selected either based on spectroscopic redshift or in colour-magnitude space, is found by Gómez et al. (2012) to be multimodal (their Figs. 7-9). We study the projected density of galaxies in the region of the cluster in Fig. 4.15. The multimodality is confirmed, where the two peaks of Gómez et al. (2012) form a highly enlongated central region of approximately 2 arcmin diameter. An additional peak towards the east-north-eastern (ENE) direction (not inside the field of view of the images used by Gómez et al. 2012) and a less dense but still visible peak towards the south-western (SW) direction (also identified by Gómez et al. 2012, but below their significance threshold).

Our mean photometric redshifts of galaxies inside a cylinder of 1 arcmin radius around all three peaks are mutually consistent with each other and with the spectroscopic mean cluster redshift. The uncertainty of the ensemble mean of $\delta z \approx 0.005$ for each peak, however, would only allow a significant detection of peculiar motions of several 1000 km s^{-1} along the line of sight.

Comparing the galaxy density map with Fig. 4.11, we find a rough correspondence of the two galaxy density sub-peaks with the two residual peaks in the aperture mass significance after subtracting the best-fitting model for the central halo. The third significant additional aperture significance peak towards the south does not correspond to a structure clearly visible in the galaxy number density.

4.7.2 Galaxy SEDs

We examine the distributions of best-fitting SED types from the photometric redshift code for the galaxy density peaks identified in Gómez et al. (2012) and in the previous section. To this end, we select galaxies inside cylindrical volumes of 1 arcmin (0.5 arcmin) radius and $|z - z_{cl}| < 0.06(1 + z_{cl})$ around the three peaks (and the two central peaks of Gómez et al. 2012). Results are shown in Fig. 4.15 and Table 4.2, discriminating red, moderately star-forming Sb/c-like and star-forming SEDs.

The galaxy populations in the ENE and SW peak contain a smaller fraction of red galaxies than in the very centre of the cluster, yet a larger one than elsewhere at similar separation from the BCG (in the region labelled O).

Even if their distance from the centre in three dimensions is higher than in projection, the latter observation cannot be explained by the environmental influence of the core of RXC J2248.7–4431 alone and indicates that ENE and SW are evolved neighbouring structures in the outskirts of a major cluster.

For the two peaks identified by Gómez et al. (2012), the galaxy populations are too small to make significant statements about differences in SED distribution (cf. Table 4.2, central 0.5 arcmin and NE).

4.7.3 Centroid offsets

Gómez et al. (2012) note an offset between the BCG and the centroid of X-ray emission when measuring the latter on larger radii. We note that the point of highest significance of the lensing signal (cf. Fig 4.11) is less than 20 arcsec off the BCG, which is consistent with the

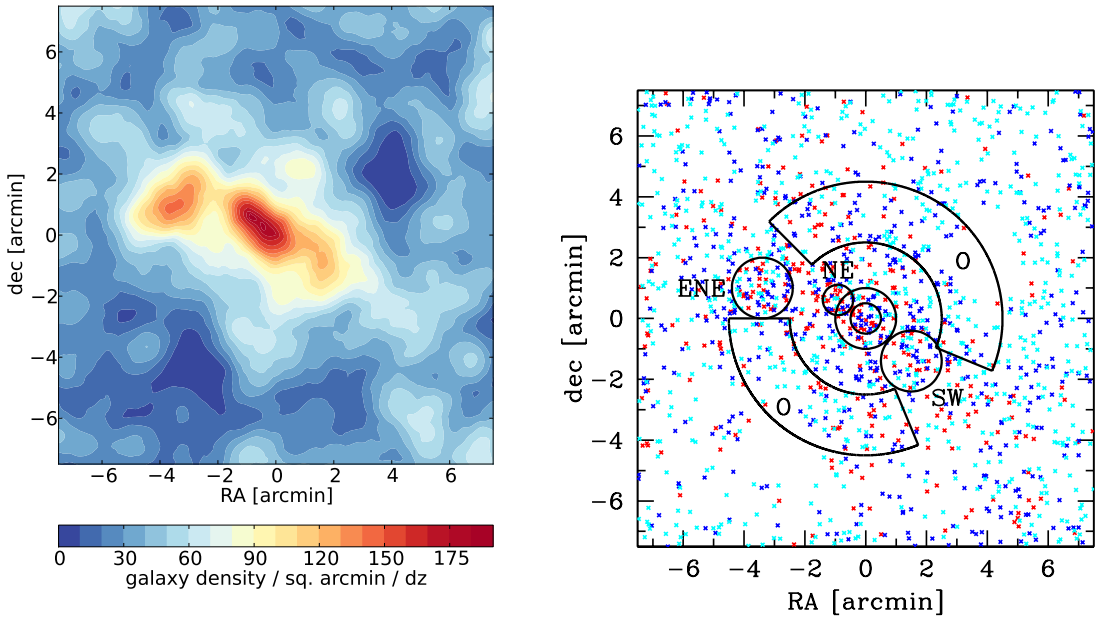

Figure 4.15: Left-hand panel: density of galaxies with $|z - z_{\rm cl}| < 0.06(1+z_{\rm cl})$ in our photometric redshift catalogue centred on the BCG position, measured as a kernel density with the minimum-variance (Epanechnikov) kernel of 1 arcmin radius. Right-hand panel: positions of red (red), moderately star-forming Sb/c-like (blue) and star-forming (cyan) galaxies around the centre of RXC J2248.7–4431 in the same redshift slice. The areas delineated by black lines indicate the regions used for the SED analysis in Table 4.2. The two empty regions visible at radii of ≈5 arcmin from the center correspond to positions of bright stars and their associated masks.

Peak	$N_{\rm gal}$	Red [%]	Mod. SF [%]	SF [%]
Central 1'	78	41 ± 6	41 ± 6	18 ± 4
ENE	67	33 ± 6	37 ± 6	30 ± 6
SW	50	32 ± 7	36 ± 7	32 ± 7
O	239	22 ± 3	36 ± 3	42 ± 3
Central 0.5'	29	48 ± 9	41 ± 9	11 ± 6
NE	29	51 ± 9	28 ± 8	21 ± 8

Table 4.2: Fractions of galaxies by SED type for the galaxy density peaks identified in Section 4.7.1.

random offsets expected from shape noise (cf. Dietrich et al., 2012a). The strong lensing model of RXC J2248.7–4431 (Monna et al., 2014) also shows no offset between the central galaxy and the peak of the projected density field.

4.7.4 Discrepancy between lensing and other mass estimates

Weak lensing mass estimates are not influenced by the astrophysical state of a system, unlike estimates based on the dynamic state of cluster members or the intra-cluster gas. Therefore a discrepancy between weak lensing and other mass estimates could suggest the influence of dynamic astrophysical processes such as mergers. Gómez et al. (2012) hypothesize that a lensing mass significantly lower than the dynamical and X-ray masses found for RXC J2248.7–4431 could help confirm merger activity.

The mass calculated by Gómez et al. (2012) based on the velocity dispersion of cluster members is slightly inconsistent with our weak lensing mass on the high side ($M_{200c}^{\rm dyn} = 42^{+17}_{-9} \times 10^{14} M_\odot$ versus $M_{200c}^{\rm WL} = 22.8^{+6.6}_{-4.7} \times 10^{14} M_\odot$), indicating that opposite bulk motion of different galaxy populations along the line of sight could be present. Whether there is indeed substructure in the velocity fields of the cluster members, for which Gómez et al. (2012) find marginal evidence will be investigated in detail with the forthcoming VLT-CLASH large spectroscopic programme (P. Rosati, private communication).

We see no significant discrepancy, however, of weak lensing with X-ray or SZ mass estimates of the cluster. Gómez et al. (2012) find an inconsistency between masses inside 110 kpc apertures from X-ray modelling in hydrostatic equilibrium and a strong lensing model. The latter, however, is based on a candidate multiply imaged system identified in their relatively shallow photometry which deeper observations have revealed to be not from the same source (Monna et al., 2014). At this point, there is therefore also no compelling evidence of a discrepancy between lensing and X-ray mass estimates in the core of RXC J2248.7–4431.

4.7.5 Influence of neighbouring structures on lensing mass

We attempt to quantify the influence of the structures in the environment of RXC J2248.7–4431 on its weak lensing mass estimate by fitting a model with multiple haloes to the observed shear signal. To this end, we place two haloes with fixed concentration-mass relation (Duffy et al., 2008) at the position of the BCG and the centre of the east-northeastern peak (cf. Section 4.7.1). The confidence region for the mass of the secondary peak is in this case $M_{200m}^{ENE} = 4.2^{+2.2}_{-1.9} \times 10^{14} M_\odot$. Subtracting the best-fitting model of the secondary peak and fitting the central halo of RXC J2248.7–4431 with two free parameters yields $M_{200m} = 24.0^{+6.1}_{-5.8} \times 10^{14} M_\odot$ and $c_{200m} = 2.8^{+3.0}_{-1.2}$. The corresponding mass for comparison with other estimates is $M_{500c} = 9.6^{+2.5}_{-2.3} \times 10^{14} M_\odot$.

We note that this lower mass of the central peak is still in agreement with the SZ and X-ray masses listed in Table 4.1. Is is unclear whether or not the mass of the secondary peak should in fact be included in a M_{200m} estimate of RXC J2248.7–4431 since the projected separation of 3.5 arcmin is well below r_{200m} of the central system. While this exemplifies the sensitivity of cluster weak lensing to correlated structures (Gruen et al., 2011), it does not change the conclusions of Section 4.7.4.

4.8 Secondary cluster at $z \approx 0.6$

In redshift space density maps we detect a secondary peak around

$$(\alpha, \delta) = (22^{\mathrm{h}}49^{\mathrm{m}}37.1^{\mathrm{s}}, -44^{\circ}43'04'') \ ,$$

at the position of a bright early-type galaxy with photometric redshift of $z = 0.66$ and corresponding absolute rest-frame magnitude of $M_{R,\mathrm{Vega}} = -25.1$ which appears to be at the centre of another cluster of galaxies. At a separation of 14.5 arcmin from the centre of RXC J2248.7–4431, this configuration of lenses is significantly more separated than the cases of cluster-cluster lensing discussed in Zitrin et al. (2012b). In the following, we present a weak lensing and a simple strong lensing analysis of the newly discovered cluster.

The mean redshift of the 12 closest, visually colour-selected member galaxies is $z = 0.58$, which is the redshift we use for the following weak lensing analysis. After subtracting the best-fitting NFW model of the central peak of RXC J2248.7–4431 (cf. Section 4.6.5), we model this structure as an NFW halo positioned on the BCG using the concentration prior of equation (4.21) and a radial range of 0.5 Mpc $\leq r \leq$ 3 Mpc. The confidence contours are shown in Fig. 4.16. As a result of the low background number density and location of the cluster near the edge of the image, the mass is only weakly constrained and not detected at the 2σ level. We find the confidence region to be $M_{200m} = 4.0^{+3.7}_{-2.6} \times 10^{14} M_{\odot}$ at a concentration of $c_{200m} = 4.3^{+2.2}_{-1.4}$. Owing to the lack of completeness at the required depth, a richness and luminosity derived mass estimation (cf. Section 4.4.3) is not feasible. Fig. 4.17 shows a colour image of the central part of the system.

We identify four blue sources in a cross-like orientation around the BCG with separations of ~ 8 and ~ 17 arcsec along the small and large axis, respectively, as a candidate of multiple imaging. Assuming a cluster redshift of $z_l = 0.58$, the redshift of the blue source at its photometric value of $z_s = 1.58$, and a halo with projected ellipticity and orientation following the light distribution of the BCG, we can build a strong lensing model. For a non-singular halo with 4 arcsec (27 kpc) core radius, we get a mass of $\sim 1.4 \times 10^{13} M_{\odot}$ within a radius of 6.8 arcsec, the Einstein radius at this redshift.

4.9 Conclusions

We present the first weak lensing analysis of the cluster of galaxies RXC J2248.7–4431. We calculate photometric redshifts of background and cluster galaxies and determine the richness and total luminosity of the system. We find the mass and concentration of RXC J2248.7–4431 in a NFW likelihood analysis to be equal to $M_{200m} = 33.1^{+9.6}_{-6.8} \times 10^{14} M_{\odot}$, in good agreement with previous X-ray and SZ mass estimates, and $c_{200m} = 2.6^{+1.5}_{-1.0}$, which is in the lower range of expected concentration for a system of the given mass and redshift. The subtraction of the best-fitting model leaves three marginally significant aperture mass peaks in the vicinity of the main halo, which likely correspond to substructure and surrounding structures of RXC J2248.7–4431. We confirm and add to some of the evidence given by Gómez et al. (2012) for an ongoing major merger of the system in terms of the multimodal galaxy density field and a discrepancy between (low) weak lensing and (high) dynamical mass estimate. We do not, however, find a tension between X-ray hydrostatic masses and the weak lensing mass of the cluster. This remains to be true even when a secondary peak of galaxy density at 3.5 arcmin

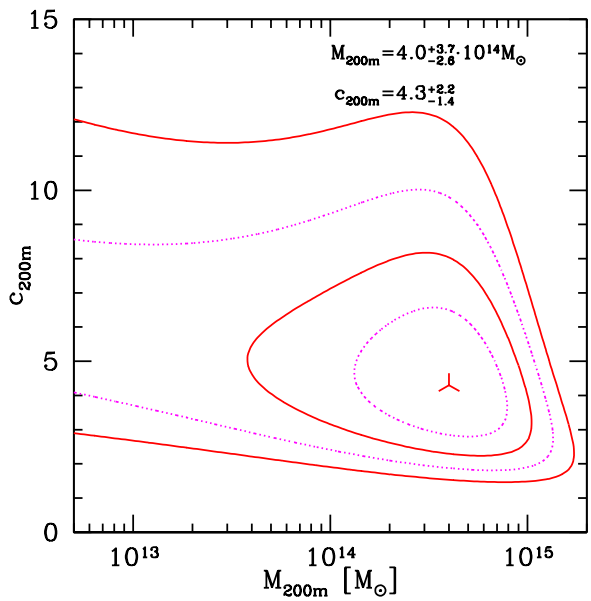

Figure 4.16: Likelihood contours of the two-parametric NFW profile of secondary cluster with $z = 0.58$. Red, solid (magenta, dotted) contours for the combined (projected) confidence regions (intervals) for M_{200m} and c_{200m} using the concentration prior of Bullock et al. (2001); Duffy et al. (2008). Both contours are drawn at the 1σ and 2σ confidence levels. The triangular symbol indicates the best-fitting solution.

Figure 4.17: Colour image of second cluster at $(\alpha, \delta) = (22^{\mathrm{h}}49^{\mathrm{m}}37.1^{\mathrm{s}}, -44°43'04'')$, $z \approx 0.6$, with a size of 2×2 arcmin^2. Note the redder colour of BCG and cluster member galaxies compared to RXC J2248.7–4431 (cf. Fig. 4.1) and the four symmetric blue sources along the major and minor axes of the BCG (the former ones highly blended with the BCG itself) at $z_{\mathrm{phot}} \approx 1.5 - 1.8$.

separation of the core of RXC J2248.7–4431 is independently included in the weak lensing model.

We detect a second cluster at $z \approx 0.6$ inside our field of view, whose weak lensing mass is weakly constrained at $M_{200m} = 4.0^{+3.7}_{-2.6} \times 10^{14} M_\odot$ with a concentration of $c_{200m} = 4.3^{+2.2}_{-1.4}$. In this system a strong lensing analysis of a candidate multiply imaged source is possible.

Acknowledgements

This work was supported by SFB-Transregio 33 'The Dark Universe' by the Deutsche Forschungsgemeinschaft (DFG) and the DFG cluster of excellence 'Origin and Structure of the Universe'. The authors thank Megan Donahue, August E. Evrard and the anonymous referee for useful comments on the manuscript. VV thanks Bhuvnesh Jain for helpful discussions.

Chapter 5

Weak lensing analysis of SZ-selected clusters of galaxies from the SPT and Planck surveys

Prologue

Sunyaev-Zel'dovich (SZ) surveys are a particularly useful way of compiling samples of clusters for the purpose of cluster cosmology, since the Compton decrement is expected to tightly scale with cluster mass and to be nearly redshift independent. An important obstacle, however, is the accurate connection of the SZ signal to the cluster mass. The purpose of this project, therefore, was to measure the masses of a sample of SZ selected clusters with weak lensing and use this to constrain the mass-observable relations of the *Planck* and SPT surveys.

This chapter is based on the paper Gruen, Seitz, Brimioulle, Kosyra, Koppenhoefer, Lee, Bender, Riffeser, Eichner, Weidinger, & Bierschenk (2014b), published in MNRAS. Relative to the published version, Fig. 5.28 and the related description in the text are corrected in this thesis for a typo in an internal data table, the effect of which on the original analysis was, however, minor. Data reduction, photometric and astrometric calibration, conceptual development and implementation of the background galaxy selection scheme, galaxy shape measurement (including PSF modelling and shape measurement code), lensing analysis code for mass measurement, interpretation of the *Planck* likelihoods, likelihood code for constraining the mass-observable relations, hypothesis tests and comparison of SZ catalogs were exclusively performed by me. Mass mapping from the shape catalogs was done by Stella Seitz. Aperture photometry and photometric redshifts in the cluster fields and the ESO-DPS reference catalogs were provided by Fabrice Brimioulle. Ralf Kosyra contributed to literature search on nearby structures and prepared some of the cluster maps. Telescope time allocation and observation planning was done by Stella Seitz and Ralf Bender. Johannes Koppenhoefer, Chien-Hsiu Lee, Arno Riffeser, Thomas Eichner and Thomas Weidinger observed the cluster fields with the MPG/ESO-2.2m telescope. All authors contributed to discussions and proofreading.

Permission for non-commercial re-use of the material in this thesis has been confirmed by the MNRAS editorial office. Oxford University Press holds the copyright on the paper.

Abstract

We present the weak lensing analysis of the **W**ide-Field **I**mager **SZ** **C**luster of galax**y** (WISCy) sample, a set of 12 clusters of galaxies selected for their SZ effect. After developing new and improved methods for background selection and determination of geometric lensing scaling factors from absolute multi-band photometry in cluster fields, we compare the weak lensing mass estimate with public X-ray and SZ data. We find consistency with hydrostatic X-ray masses with no significant bias, no mass dependent bias and less than 20% intrinsic scatter and constrain $f_{\mathrm{gas},500c} = 0.128^{+0.029}_{-0.023}$. We independently calibrate the South Pole Telescope significance-mass relation and find consistency with previous results. The comparison of weak lensing mass and Planck Compton parameters, whether extracted self-consistently with a mass-observable relation (MOR) or using X-ray prior information on cluster size, shows significant discrepancies. The deviations from the MOR strongly correlate with cluster mass and redshift. This could be explained either by a significantly shallower than expected slope of Compton decrement versus mass and a corresponding problem in the previous X-ray based mass calibration, or a size or redshift dependent bias in SZ signal extraction.

5.1 Introduction

As the end product of hierarchical structure formation, clusters of galaxies are particularly sensitive to the cosmological interplay of dark matter and dark energy. Studies of individual clusters and, even more so, large surveys have for this reason been considered a valuable cosmological probe for several decades (see Allen et al. 2011 for a recent review).

The framework for cosmological interpretation of cluster surveys consists, on the theoretical side, of a halo mass function that predicts the dependence of the number density of clusters as a function of mass and redshift on cosmology (e.g. Press & Schechter, 1974; Sheth & Tormen, 1999; Tinker et al., 2008). The observational task consists in providing an ensemble of clusters detected with a well-determined selection function and measurements of an observable that can be related to their mass.

Most observations that allow a sufficiently high signal-to-noise ratio (S/N) detection of sufficiently many clusters to date relate to the minority of cluster matter that is of baryonic origin (but see Gavazzi & Soucail 2007; Miyazaki et al. 2007; Schirmer et al. 2007 for lensing-detected surveys). In particular, use has been made of the density of red galaxies (e.g. Gladders & Yee 2005, Koester et al. 2007 or Rykoff et al. 2014 for observations and Rozo et al. 2010 or Mana et al. 2013 for cosmological interpretation) or the hot gas in the intracluster medium (ICM) that can be detected by its X-ray emission (e.g. Piffaretti et al. 2011 for a meta-catalogue and Vikhlinin et al. 2009b or Mantz et al. 2010b for cosmological interpretation).

Another observable effect is due to the inverse Compton scattering of cosmic microwave background (CMB) photons by the ICM, the Sunyaev & Zel'dovich (1972, hereafter SZ) effect. The scattering distorts the CMB spectrum such that below (above) a global null-point frequency of approximately 220 GHz, a decrease (an increase) in microwave flux density is observed in galaxy clusters. The effect at any point scales with the integrated electron pressure P along the line of sight, which defines the dimensionless Compton parameter y,

$$y = \frac{\sigma_{\mathrm{T}}}{m_{\mathrm{e}}c^2} \int P \, dl \, , \tag{5.1}$$

where σ_T is the Thomson cross-section and $m_e c^2$ the rest energy of electrons.

Integration of y over the angular extent of the cluster, $Y = \int y \, d\Omega$, yields a volume integral of electron pressure,

$$D_A^2 Y = \frac{\sigma_T}{m_e c^2} \int P \, dV \tag{5.2}$$

with the angular diameter distance D_A used to convert apparent angles to physical scales. Note that the volume integral of pressure equals the thermal energy and is therefore expected to be closely related to cluster mass.

Large surveys of the SZ sky have been and are currently being performed by the *Planck* Satellite (e.g. Planck Collaboration et al. 2014a), the South Pole Telescope (SPT; Carlstrom et al. 2011) and the Atacama Cosmology Telescope (ACT; e.g. Marriage et al. 2011).

5.1.1 Calibration of the SZ mass-observable relation

As a connection between cosmological models and SZ surveys, it is necessary to establish a mass-observable relation (MOR) between SZ observable and cluster mass. As important as the mean relation is the intrinsic scatter of the MOR (Lima & Hu, 2005), since the steepness of the halo mass function causes preferential up-scatter of the (more numerous) less massive haloes. There are a number of ways of achieving this calibration.

External mass calibration is not strictly required for the cosmological interpretation of an SZ survey, since large surveys can determine both cosmological parameters, a parametrized MOR and the intrinsic scatter simultaneously (Hu, 2003; Majumdar & Mohr, 2004; Lima & Hu, 2005) by requiring that cluster counts as a function of observable be consistent with the halo mass function of the respective cosmology. The fewer assumptions about the form and evolution of the MOR are made, however, the less well-constrained cosmological parameters become in such a scheme.

Previous studies have used astrophysical modelling (e.g. Mroczkowski 2011) or X-ray mass estimates for SZ-selected systems (Planck Collaboration et al., 2011b, 2014c) to constrain the MOR. These approaches require assumptions about the astrophysical state of clusters, e.g. virialization and hydrostatic equilibrium (HSE), and are complicated by the variety of evolutionary states clusters are in fact found to be in. One important example of this is the question of hydrostatic mass bias, i.e. a mean underestimation of true mass by X-ray analyses based on HSE (Nagai et al., 2007; Piffaretti & Valdarnini, 2008), which has been investigated with controversial results (e.g. Mahdavi et al. 2008; Zhang et al. 2010; Mahdavi et al. 2013; Planck Collaboration et al. 2013a).

Weak lensing (WL) constraints on the MOR are a complement to these approaches. A moderate number of accurately measured masses greatly reduces the uncertainty of self-calibration schemes (e.g. Majumdar & Mohr, 2004). WL can measure masses and mass-observable scatters for samples of clusters selected according to the respective survey with the important advantage that it is sensitive to all matter regardless of its astrophysical state.

In practice, however, WL also faces observational challenges. Biases in WL measurements of the mass due to, for instance, shape measurement bias (e.g. Young et al., in preparation), cluster orientation (Corless & King, 2007) or uncertain determination of source redshifts (Applegate et al., 2014) have been explored. Increased uncertainty of observed mass due to unrelated projected structures (Hoekstra, 2001, 2003; Spinelli et al., 2012) or deviations of individual systems from the common assumption of spherical, isolated Navarro, Frenk, & White (1997, hereafter NFW) haloes (Becker & Kravtsov, 2011; Gruen et al., 2011) is

an issue of similar importance. Despite the need of reducing and quantifying these effects, gravitational lensing remains the best candidate for an unbiased mass measurement of galaxy clusters to date. For this reason, the WL analysis of SZ selected samples of clusters has been the focus of a number of recent studies [cf. McInnes et al. 2009 (3 SPT systems), Marrone et al. 2009, 2012 (a total of 29 systems with pointed SZ observations at $z = 0.15 \ldots 0.3$, 25 of which are also detected by Planck), High et al. 2012 (5 SPT systems), AMI Consortium: Hurley-Walker et al. 2012 (6 systems with pointed SZ observations) and Hoekstra et al. 2012 (a total of 30 systems with SZ observations, mostly at $z = 0.15, \ldots, 0.3$, 18 of which are also detected by Planck Collaboration et al. 2011a in the early data release)].

This work aims to be complementary to the aforementioned studies. Our sample of 12 clusters with an overlap of only one is a significant addition in terms of statistics to the present list of SZ clusters with WL measurements. We probe a wide range of $0.10 < z < 0.69$, extending to higher redshift than typical previous studies. Seven systems from our sample can be compared to the 2013 *Planck* release, and this is the first study to compare the 2013 *Planck* catalogue and MOR to independent measurements of cluster mass with lensing. Finally, we pay particular attention to the aspects of shape measurement calibration, background selection and modelling of neighbouring structures, improving upon methods commonly used to date and reducing potential biases resulting from the incomplete treatment of these effects.

This paper is structured as follows. Section 5.2 gives an overview of our sample and the data reduction procedure up to photometric catalogues. Section 5.3 describes our background galaxy selection including an improved method based on multi-band photometry without photometric redshifts. Our methodology for the measurement and interpretation of the WL signal is laid out in Section 5.4. Our use of SZ data, including the calculation of self-consistent Planck SZ masses, is detailed in Section 5.5. Section 5.6 contains individual analyses for each cluster of the Wide-Field Imager SZ Cluster of Galaxy (WISCy) sample. The main result of this work is presented in Section 5.7, where we compare our WL measurements to the SZ observables and X-ray mass estimates. We conclude in Section 5.8.

In this paper we adopt a Λ cold dark matter (ΛCDM) cosmology with $H_0 = 70$ km s^{-1} Mpc^{-1} and $\Omega_\mathrm{m} = 1 - \Omega_\Lambda = 0.3$. To accommodate different conventions used in the literature, we consistently mark published masses with $h = H_0/(100$ km s^{-1} Mpc$^{-1})$ or $h_X = H_0/(X$ km s^{-1} Mpc$^{-1})$. We denote the radii of spheres around the cluster centre with fixed overdensity as $r_{\Delta\mathrm{m}}$ and $r_{\Delta\mathrm{c}}$, where Δ is the overdensity factor of the sphere with respect to the mean matter density ρ_m or critical density ρ_c at the cluster redshift. The mass inside these spheres is labelled and defined correspondingly as $M_{\Delta\mathrm{m}} = \Delta \times \frac{4\pi}{3} r_{\Delta\mathrm{m}}^3 \rho_\mathrm{m}$ and $M_{\Delta\mathrm{c}} = \Delta \times \frac{4\pi}{3} r_{\Delta\mathrm{c}}^3 \rho_\mathrm{c}$. When comparing masses, we convert according to differences in h but ignore small differences in Ω_m (which would require to assume a density profile to be corrected). All magnitudes quoted in this work are given in the AB system. All maps and images assume a tangential coordinate system where north is up and east is left.

5.2 Sample and data

Our sample contains 12 clusters of galaxies. Of these, five and seven are detected by SPT and *Planck*, respectively, of which four and two are in fact discovered by their SZ signal in these surveys.

The set of clusters was selected from four parent samples. We selected four objects (SPT-CL J0551–5709, SPT-CL J0509–5342, SPT-CL J2332–5358, SPT-CL J2355–5056) from the

detection-limited sample of 2008 SPT observations (Vanderlinde et al., 2010) based on their visibility in the observing time allocated to us at the 2.2m MPG/ESO telescope. By a similar selection, we added two systems (PLCKESZ G287.0+32.9, and PLCKESZ G292.5+22.0) from the Planck early SZ catalog (Planck Collaboration et al., 2011a) and two known strong lensing systems (MACS J0416.1–2403 and RXC J2248.7–4431) from the Cluster Lensing And Supernova survey with Hubble (CLASH; Postman et al. 2012), for which we expected later SZ detection by Planck at the time. Note that both of these were recently selected as *Hubble Space Telescope* (HST) Frontier Fields.[1] Finally, we added all systems detected by Planck in the 2013 catalogue (Planck Collaboration et al., 2014a) that were covered serendipitously by the Canada-France-Hawaii Telescope Legacy Survey (CFHTLS) in its final public data release (PSZ1 G168.02–59.95, PSZ1 G230.73+27.70, PSZ1 G099.84+58.45, PSZ1 G099.48+55.62).

The sample spans a wide dynamic range. In terms of mass it reaches from $1 \times 10^{14} M_\odot$ to several $10^{15} M_\odot$, in terms of redshift from the almost local Universe at $z \approx 0.1$ close to the limit of feasible ground-based WL at $z \approx 0.7$. Table 5.1 gives an overview of the sample.

5.2.1 Data reduction and photometry

For eight of the clusters, observations were made with the Wide-Field Imager (WFI; Baade et al. 1999) on the 2.2 m MPG/ESO telescope at La Silla. Seeing and photometric depth is typically best in R band, although in some cases additional bands can be used for shape measurement of galaxies (see Table 5.1). The raw images are de-biased, flat-fielded and bad pixels are masked in all bands and fringe patterns are corrected in the I and Z band using the ASTRO-WISE[2] framework (Valentijn et al., 2007). Background subtraction, final astrometry and co-addition of suitable frames is done with custom scripts using SCAMP[3] (Bertin, 2006) and SWARP[4] (Bertin et al., 2002). For fields highly contaminated with bright star ghost images, we use the outlier masking method of Gruen et al. (2014a, see their Fig. 8 for an example of an R band stack of SPT-CL J0551–5709) to remove artefacts from the stack.

Observations of the fields in photometric nights together with fields of standard stars are used to fix the photometric zero-points in R band of all WFI clusters except PLCKESZ G287.0+32.9 and PLCKESZ G292.5+22.0. Due to the unavailability of standard star observations during the nights in which the latter two were observed, we use 2MASS (Cutri et al., 2003) *JHK* infrared magnitudes of stars in their field of view and the stellar colours of the Pickles (1998) library to fix their R and I zeropoints. Comparison with V band magnitudes of a single exposure of PLCKESZ G287.0+32 shows that the R-I colour is recovered correctly by this procedure. The same stellar locus method is also used to fix the zeropoints of the remaining bands of the WFI fields. This is verified against standard star observations in additional filters in the field of SPT-CL J2248–4431 (Gruen et al., 2013, their Section 2). Extinction corrections of Schlegel et al. (1998) are applied consistently. We note that for the relatively low galactic latitude fields of PLCKESZ G287.0+32.9 and PLCKESZ G292.5+22.0, significant uncertainty (comparing the Galactic extinction models of Schlegel et al. 1998 and Schlafly & Finkbeiner 2011) and spatial variation of extinction of ≈ 0.15 mag likely cause systematic offsets of our magnitudes in those fields.

[1] Observations for MACS J0416.1–2403 have already been performed while for RXC J2248.7–4431 they are scheduled for year 3 of the survey and contingent on results from the previously observed fields.

[2] `http://www.astro-wise.org/`

[3] `http://www.astromatic.net/software/scamp`

[4] `http://www.astromatic.net/software/swarp`

#	SZ name	Assoc. names	z	RA	Dec	WFI	CFHTLS
1	SPT-CL J0509–5342	ACT-CL J0509–5341	0.4626^a	05:09:21	-53:42:18	$B\boldsymbol{VR}I$	-
2	SPT-CL J0551–5709	-	0.4230^a	05:51:36	-57:09:22	$B\boldsymbol{R}I$	-
3	SPT-CL J2332–5358	SCSO J233227–535827	0.4020^b	23:32:27	-53:58:20	$B\boldsymbol{R}I$	-
4	SPT-CL J2355–5056	-	0.3196^c	23:55:49	-50:56:13	$B\boldsymbol{R}I$	-
5	PLCKESZ G287.0+32.9	-	0.3900^d	11:50:51	-28:04:09	$V\boldsymbol{RI}$	-
6	PLCKESZ G292.5+22.0	-	0.3000^d	12:01:00	-39:51:35	$\boldsymbol{RI}$	-
7	-	MACS J0416.1–2403	0.3970^e	04:16:09	-24:04:04	$\boldsymbol{BVRI}$	-
8	SPT-CL J2248–4431	ACO S 1063 PLCKESZ G349.46-59.94 RXC J2248.7–4431	0.3475^f	22:48:44	-44:31:48	$UB\boldsymbol{VRI}Z$	-
9	PSZ1 G168.02–59.95	ACO 329 RXC J0214.6–0433 RCC J0214.6–0433	0.1456^g	02:14:41	-04:33:22	-	$ug\boldsymbol{r}\boldsymbol{i}z$
10	PSZ1 G230.73+27.70	MaxBCG J135.43706-01.63946 XCC J0901.7-0138	0.2944^h	09:01:30	-01:39:18	-	$ug\boldsymbol{r}\boldsymbol{i}z$
11	PSZ1 G099.84+58.45	SL2S J141447+544703	0.6900^i	14:14:47	+54:47:04	-	$ug\boldsymbol{r}\boldsymbol{i}z$
12	PSZ1 G099.48+55.62	ACO 1925 RXC J1428.4+5652	0.1051^j	14:28:26	+56:51:36	-	$ug\boldsymbol{r}\boldsymbol{i}z$

Table 5.1: Overview of WISCy sample. The first and second columns give an ID and the name given by the respective SZ survey, both to be used in the rest of this work. Additional names are shown in the third column. Available photometric bands are shown in the last two columns, marking bands used for shape measurement in bold print. Redshift references: (a) High et al. 2010, (b) Song et al. 2012, (c) Reichardt et al. 2013, (d) Planck Collaboration et al. 2011c, (e) Ebeling et al. 2014, (f) Böhringer et al. 2004b, (g) Mirkazemi et al. 2015, (h) photometric redshift of Koester et al. (2007), (i) median photometric redshift of 32 visually selected cluster member galaxies (this work), (j) Struble & Rood 1999, citing Lebedev & Lebedeva 1991.

For the four clusters in our sample covered by the CFHTLS, we use photometric redshifts from the Brimioulle et al. (2013) pipeline, re-run on the latest publicly available stacks.[5] Since no public shape catalogue is complete in a region of sufficient diameter around the two clusters, we process these co-added images with our own shape pipeline (see Section 5.4).

The multi-band aperture photometry of the WFI and Canada-France-Hawaii Telescope (CFHT) fields is extracted using the procedure described in Brimioulle et al. (2013) and Gruen et al. (2013).

5.3 Background selection

The overall lensing signal at a given lens redshift z_d scales with a factor

$$\frac{D_d(z_d)D_{ds}(z_s, z_d)}{D_s(z_s)} = D_d(z_d) \times \beta(z_s, z_d)\,, \tag{5.3}$$

where D are angular diameter distances. The subscripts d and s denote deflector and source position and ds the distance between the two. Since lens redshifts are known accurately in the case of cluster lensing, we have factored out the dependence on source redshift in $\beta(z_s, z_d)$, which is zero for $z_s < z_d$, then rises steeply before it approaches the asymptotic value at $z_s \to \infty$. This fact requires an accurate estimation of β for galaxies in the shape catalogue in order to select a suitable background sample and correctly scale the signal in the lensing analysis.

Precise photometric source redshifts can, when available, be simply inserted in the above equation to get the scaling of the lensing effect. For the CFHTLS fields and SPT-CL J2248–4431 the photometric information in 5 and 6 bands, respectively, allows fitting the redshifted galaxy spectral energy distribution (SED) of individual sources over a wide wavelength range. In these cases, we therefore use photometric redshifts as provided by Gruen et al. (2013) and a re-run of the Brimioulle et al. (2013) pipeline on the latest CFHTLenS data reduction (Erben et al., 2013).

The fewer bands exist, however, the less well determined any single object's redshift becomes. Limiting, for the purpose of testing this effect, the number of bands used for the template fitting in the case of SPT-CL J2248–4431, the field with the otherwise best wavelength coverage, we verify that estimates of β are in fact biased when using simply the best fitted but noisy photometric z_s, and in particular when selecting by them. We note that this is a natural consequence of the non-linear propagation of errors from redshifts to geometric scaling factors in equation (5.3) (cf. Applegate et al. 2014 and Section 5.3.1).

5.3.1 β from limited photometric information

Even when photometric redshifts are not feasible, use of the full photometric information allows for an optimal background selection. While in some studies magnitude cuts in a single band have been used (cf., e.g., Erben et al. 2000; Romano et al. 2010; Israel et al. 2012), the inclusion of additional bands can greatly improve the separability of foreground and background objects (see, for instance, High et al. 2012 for a comparison of two-band versus three-band information). We will show that using not only the colour but also including the apparent magnitude of objects can be beneficial (see also Fig. 5.3 and discussion below).

[5] cf. Erben et al. (2013), `http://www.cfhtlens.org/astronomers/data-store`

We therefore develop a probabilistic method of calculating the appropriate β factor to use for a galaxy with limited photometric information in this section. The basis of our method is the position of the galaxy in magnitude space, which we compare to a deeper reference catalogue with accurate redshift information. In this way we use not just the available magnitudes of galaxies in our cluster field, but also the empirical distribution of unavailable magnitudes for galaxies similar to them, to estimate the geometrical scaling of the WL signal. We note that this method shares some characteristics with the one described by Lima et al. (2008) and Cunha et al. (2009).

The reference catalogue and basics of the method are explained in Sections 5.3.1 and 5.3.1. In addition, we correct for contamination with cluster member galaxies (described in Section 5.3.1) and calculate the optimal minimal β (Section 5.3.1) above which galaxies should be used as sources in a WL analysis.

Reference catalogue

The method used in this work requires a catalogue with magnitudes and accurate photometric redshifts to which sources in our cluster fields can be compared. In our case, this catalogue is extracted from stacks of the ESO Deep Public Survey (ESO-DPS; Erben et al., 2005; Hildebrandt et al., 2006). The optical data are taken with the WFI camera on the MPG/ESO 2.2 m telescope, the primary instrument also used in the WISCy sample. We use six pointings (named Deep1a, 1b, 2b, 2c, 3a and 3b in Hildebrandt et al. 2006) for which photometric information is complete in the WFI filters *UBVRI* and data is available in *JK* from an additional infrared survey with NTT/SOFI (Olsen et al., 2006a,b). These yield approximately 200 000 galaxies at similar or significantly better depth than our cluster fields. Photometric redshifts are calculated with the template-fitting algorithm of Bender et al. (2001) as described in Brimioulle et al. (2013). Fig. 5.1 shows a comparison of photometric redshifts of objects in Deep2c to spectroscopic measurements from the overlapping VIMOS VLT Deep Survey (Le Fèvre et al., 2005). The quality of photometric redshifts, as a result of wavelength coverage, depth and calibration, is excellent, a prerequisite for using the catalogue as a reference.

Any selection effects from photometric objects in our cluster fields into the catalogue of successful shape measurements that are potentially redshift dependent must be done similarly when selecting objects from the reference field into a reference catalogue for the redshifts of lensing sources. While magnitude dependent selection is taken into account automatically by the scheme described below, we therefore apply a size-dependent cut as in the cluster fields (cf. Section 5.4.2) to our reference catalogues. This has a small but significant effect, particularly for faint galaxies (cf. Fig. 5.3).

β in magnitude space

Given a set of magnitudes $\boldsymbol{m} = \{m_i\}$, in our case $i = R, I(, B, V)$, consider the spherical volume in $2-4$ dimensional magnitude space centred on $\boldsymbol{m}$ with a radius of $|\Delta\boldsymbol{m}| = 0.1$ and select a reference sample from that volume. For any fixed cluster redshift, the mean $\beta(\boldsymbol{m})$ of the reference sample and, in addition, the fraction of objects from the reference sample which are in the foreground ($P_{\rm fg}(\boldsymbol{m})$ for $z < z_{\rm cl} - 0.06 \times (1 + z_{\rm cl})$) or near the cluster redshift ($P_{\rm cl}(\boldsymbol{m})$ for $|z - z_{\rm cl}| \leq 0.06 \times (1 + z_{\rm cl})$) can be calculated and assigned to the objects of interest. For the case of two available bands, this is visualized in Fig. 5.2.

We note that it is common in WL analyses to use only colour information, i.e. the

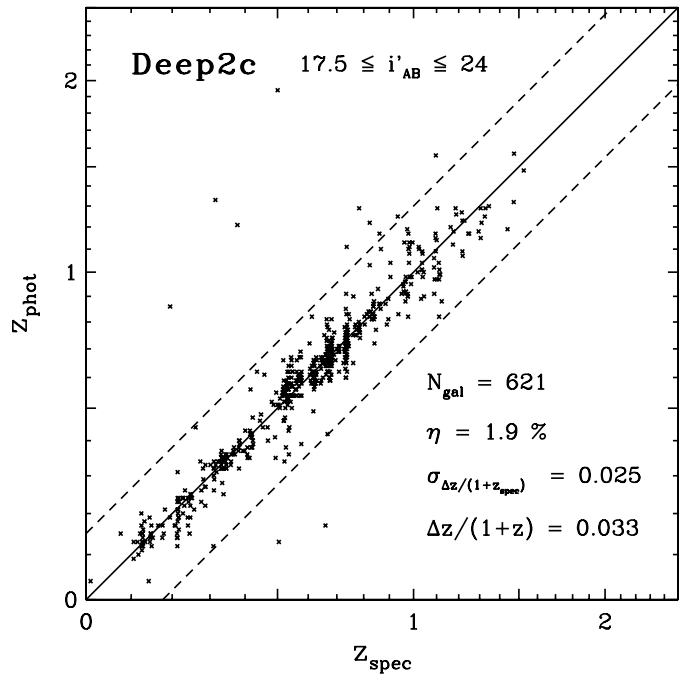

Figure 5.1: Photometric and spectroscopic redshifts of objects in the ESO-DPS Deep2c field. For the matched 621 objects, the outlier rate η, scatter $\sigma_{\Delta z/(1+z)}$ and bias $\Delta z/(1+z)$ (as defined in Brimioulle et al. 2013, equations 38-40) are excellent down to the depth of the spectroscopic survey at $m_R \approx 24$.

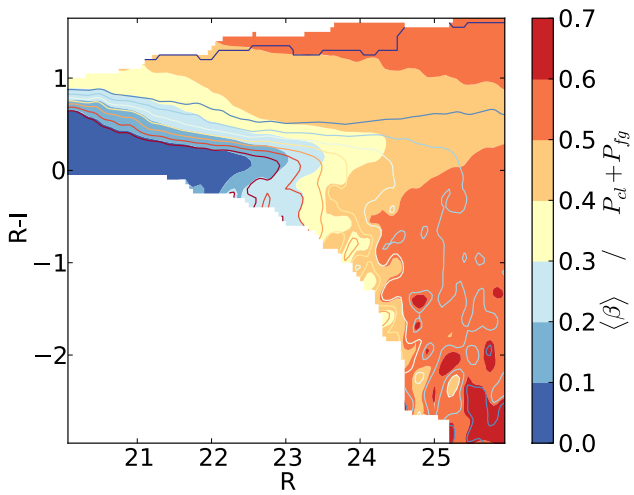

Figure 5.2: Mean value of $\beta = D_{ds}/D_s$ as a function of R and I magnitude for a hypothetical lens redshift $z_{\rm cl} = 0.4$ (coloured area). Note that while regions of high and low mean β are easy to separate, contamination with objects in the foreground or close to the cluster redshift is problematic (see the contour lines giving the combined probabilities for both cases in the field) and will have to be corrected in the central part of the cluster where such galaxies are overabundant relative to the field.

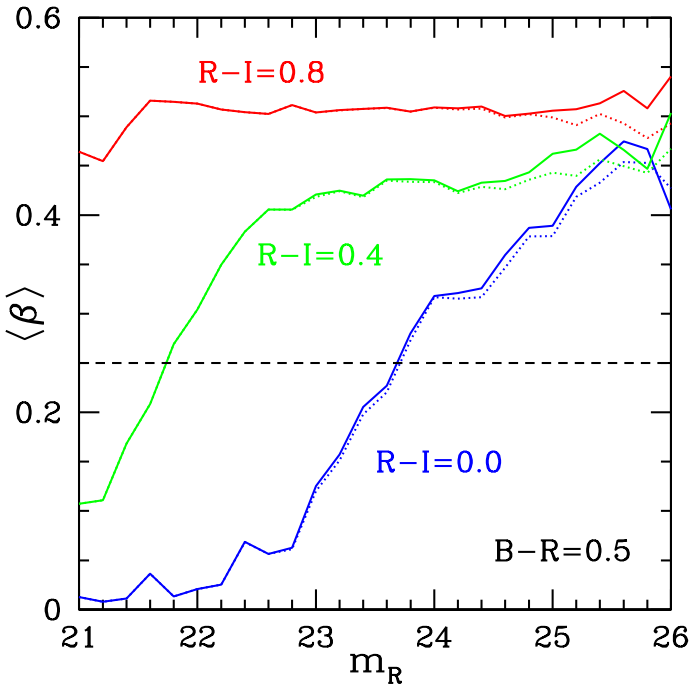

Figure 5.3: Mean value of β as a function of R magnitude in bins of R-I colour for fixed B-$R = 0.5$ at a hypothetical $z_{\rm cl} = 0.4$. The horizontal dashed line indicates a typical level of β below which objects add more noise than signal (see equation 5.11). While for the reddest bin β is determined from the B-R and R-I colours and virtually independent of m_R, full magnitude information improves the background selection in the other colour bins (R-I = 0.0, 0.4). Here, only by including m_R we can discriminate objects with low β that add excess noise from objects with high β that yield an improved signal, which are both contained in the same colour bin. The solid and dotted lines show results for a reference sample selected for our lensing catalogue size cut at 0.5 arcsec `FLUX_RADIUS` and for the complete reference sample, respectively, indicating that at magnitudes fainter than $m_R \approx 24$ this is a relevant effect.

difference of the magnitudes of a galaxy in different bands (cf. e.g., Medezinski et al. 2010, High et al. 2012 or Okabe et al. 2013 for recent examples). Magnitude cuts are used, too, yet typically in cases where only one or two bands are available (cf., e.g., Nakajima et al. 2009, Romano et al. 2010 or Okabe et al. 2011). When only colours are used, one discards the magnitude offset that corresponds to a scaling of apparent flux for background selection. In contrast, our method includes the complete information. Fig. 5.3 shows that, depending on the position in colour space, the apparent magnitude does indeed help to discriminate low and high redshift objects. While for sufficiently many bands the colour information might constrain the source redshift well enough, for few bands and certain regions in colour colour space, therefore, complete magnitude information should be used in order to exploit the full power of photometric information for background estimation.

Correction for cluster members

The treatment presented above would be sufficient if the distribution of galaxies in our fields was similar to the reference field. However, our fields contain rich clusters of galaxies, and the

excess of cluster members, which is also a strong function of the separation from the cluster centre, has not been considered so far. As has typically also been done in previous studies, positional information must be used to correct the background sample for a dilution with cluster members.

Where additional galaxies at the cluster redshift exist, β is overestimated by assuming the distribution of galaxies in magnitude-redshift space to be equal to an average field, when in fact a larger than usual fraction of galaxies is situated at the cluster redshift with $\beta = 0$.[6] Estimates of cluster member density based on counts alone inevitably come with high uncertainty and systematic problems due to blending, masked areas and the intrinsic clustering of galaxies, at least in the case of single clusters.

Our method of determining the cluster member contamination is based on decomposing the distribution of β that we measure in an annulus around the cluster centre into the known distributions of β for galaxies at the cluster redshift and in fields without excess galaxies at the cluster redshift. The coefficients of both components then give the proportion of excess galaxies at the cluster redshift in that region.

In this we make only the following weak assumption, namely that the measured distribution of $\beta(\boldsymbol{m})$ of galaxies at the cluster redshift and in the field is constant over the image. We can calculate $p_c(\beta)$, the distribution of β in a redshift slice around the cluster, and $p_f(\beta)$, the distribution of β outside the cluster region, by binning the $\beta(\boldsymbol{m})$ determined as described above. In the first case, we weigh objects by their probability of being near the cluster redshift, $P_{\rm cl}(\boldsymbol{m})$. In the second case we limit the analysis to the part of the field sufficiently separated from the cluster core and use all objects with equal weight. Fig. 5.4 shows $p_{\rm cl}(\beta)$ and $p_{\rm f}(\beta)$ for an exemplary cluster redshift of $z_{\rm cl} = 0.4$ as calculated in one of our fields on *RI*, *BRI* and *BVRI* colour information. Fortunately, the two distributions are distinct in all these cases, such that a decomposition is possible.

As a function of radius from the cluster centre, we fit a parameter $0 \leq f_{\rm cl}(r) \leq 1$ for the fraction of cluster member galaxies in our shape catalogue at that separation. This is done by demanding that

$$p(\beta, r) = f_{\rm cl}(r) \times p_{\rm cl}(\beta) + [1 - f_{\rm cl}(r)] \times p_{\rm f}(\beta) \ , \tag{5.4}$$

which can be optimized in terms of $f_{\rm cl}(r)$ using minimum χ^2 with Poissonian errors. In practice, we do this in bins of 1 arcmin width out to a radius of 6 arcmin. For application to individual objects, we linearly interpolate $f_{\rm cl}(r)$ to the galaxy position.

Results for $f_{\rm cl}(r)$ are shown in Fig. 5.5. The overall profile of cluster member galaxies is of the order of 50 per cent in the central region and drops smoothly towards the outskirts. We note that the data are fitted best not by a single power law but by a broken power -aw profile with logarithmic slope near 0 at small and -2 at large radii. This is consistent with the expected NFW profile of cluster member number density (cf. Carlberg et al., 1997; Lin et al., 2004; Zenteno et al., 2011; Budzynski et al., 2012) rather than a single power law (but cf. Hoekstra et al. 2012, who find a global r^{-1} dependence).

Knowing $f_{\rm cl}(r)$, we can correct the probabilities for a galaxy of belonging to the foreground,

[6]This misestimation of course can only happen in regions of magnitude space that are populated with galaxies at the cluster redshift. Due to the presence of non-red cluster members particularly at larger cluster redshifts and in the deeper data used in WL studies, however, these regions are larger than the commonly excised red sequence.

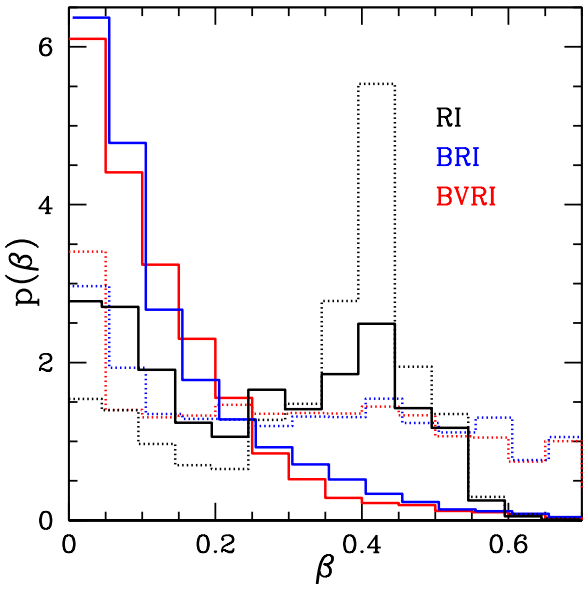

Figure 5.4: Distributions of β determined by magnitude space position for galaxies at a hypothetical lens redshift $z_{\rm cl} = 0.4$ (solid lines) and field galaxies (dotted lines), in both cases assuming a lens redshift $z_l = 0.4$, illustrated using subsets of the $BVRI$ photometry in the field of SPT-CL J0509–5342. When photometry in B, R and I is available, the distributions are well discriminable. Adding V band does not improve the separation much. Limiting the information to R and I only makes the situation significantly worse, although the two components are still distinguishable.

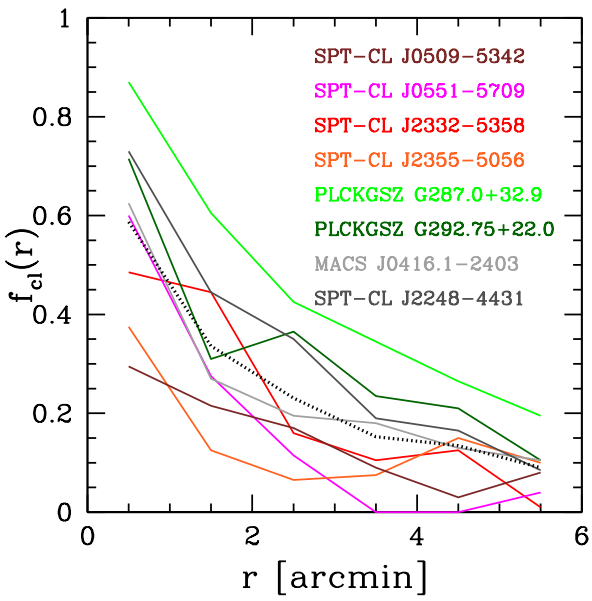

Figure 5.5: Cluster member fraction $f_{\rm cl}$ in the photometric catalogue as a function of radius for the cluster field without photometric redshift information. Colour coding for individual clusters as indicated, with the mean value given by the dotted black line. The richest among these clusters, PLCKESZ G287.0+32.9 (light green), is visually confirmed to contain numerous cluster member galaxies spread over a large region.

the cluster redshift region and the background as

$$(P_{\rm fg}, P_{\rm cl}, P_{\rm bg}) \rightarrow (P'_{\rm fg}, P'_{\rm cl}, P'_{\rm bg}) = \frac{(P_{\rm fg}, P_{\rm cl} b_{\rm cl}, P_{\rm bg})}{1 + (b_{\rm cl} - 1) P_{\rm cl}} \ , \tag{5.5}$$

where we have defined the cluster member bias $b_{\rm cl}$ as

$$b_{\rm cl} - 1 = f_{\rm cl}(r) \times (1/\langle P_{\rm cl} \rangle - 1) \ , \tag{5.6}$$

with $\langle P_{\rm cl} \rangle$ the fraction of galaxies in the field which lie in the cluster redshift slice.

The true field population appears reduced to a fraction $(1+(b_{\rm cl}-1)P_{\rm cl})^{-1}$ due to the excess cluster members. For any galaxy, the probability of actually belonging to the background population and with it β therefore decrease by that same factor,

$$\beta \rightarrow \beta' = \beta \times (1 + (b_{\rm cl} - 1) P_{\rm cl})^{-1} \ . \tag{5.7}$$

Note that for galaxies in regions of magnitude space unlikely to be populated with galaxies at the cluster redshift ($P_{\rm cl} \approx 0$), no correction is necessary. Indeed, we find that the changes to the best-fitting mass when not applying the cluster member correction are typically below 5% in our sample.

In the case where β is to be calculated for a secondary lens at a redshift different from the cluster, a small generalization to equation (5.7) must be made. The relevant mutually exclusive and collectively exhaustive cases here are $P_{\rm cl}$, the probability of a galaxy belonging to the main cluster redshift slice, and $P_{\rm fg\neg cl}$ and $P_{\rm bg\neg cl}$, the probabilities for a galaxy to be in the foreground or background of the secondary lens, but now explicitly excluding the cluster redshift slice in both. These three probabilities transform exactly as in equation (5.5). However, the initial estimate for β is composed of

$$\beta = P_{\rm cl} \beta(z_{\rm cl}) + P_{\rm bg\neg cl} \beta_{\rm bg\neg cl} \ . \tag{5.8}$$

Note that cluster member galaxies could have $\beta(z_{\rm cl}) > 0$ if the cluster is in the background of the secondary lens, in which case equation (5.7) is no longer correct. Rather then,

$$\begin{aligned} \beta \rightarrow \beta' &= \beta(z_{\rm cl}) P'_{\rm cl} + P'_{\rm bg\neg cl} \beta_{\rm bg\neg cl} \\ &= \frac{\beta(z_{\rm cl}) P_{\rm cl}(b_{\rm cl} - 1) + \beta}{1 + (b_{\rm cl} - 1) P_{\rm cl}} \ . \end{aligned} \tag{5.9}$$

For $\beta(z_{\rm cl}) = 0$, this reduces to equation (5.7).

Optimised β threshold

One can finally make optimised cuts by selecting objects whose β is above some threshold. A threshold too high would remove too many actual background objects and increase the shape noise. A threshold too low would increase the noise by including objects for which the lensing effect is small compared to the intrinsic ellipticity scatter. The optimum can be found as follows.

Let the density of objects in β space be given by $p(\beta)$, such that $\int_0^{\beta(z_s \rightarrow \infty)} p(\beta) \, d\beta = 1$. If we assume a constant shear γ_t for objects at a hypothetical $\beta = 1$, a constant shape noise of σ_ϵ and a β threshold $\beta_{\rm min}$, then the S/N of the measurement will be

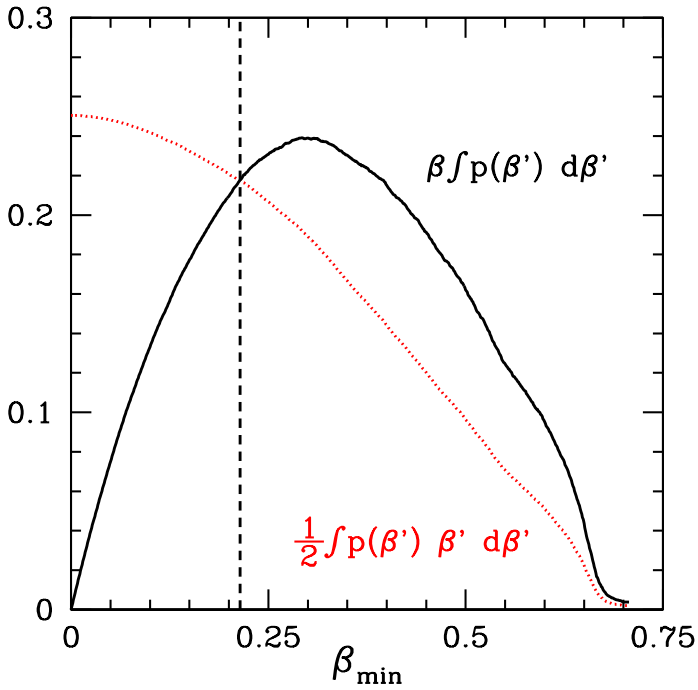

Figure 5.6: Both sides of equation (5.11) plotted against the β threshold $\beta_{\rm min}$, illustrated for a hypothetical lens redshift $z_{\rm cl} = 0.4$ based on *BVRI* photometry in the field of SPT-CL J0509–5342. The optimal threshold is in this case $\beta_{\rm min,opt} \approx 0.214$ as indicated by the dashed vertical line.

$$\mathrm{S/N} = \frac{\sqrt{N_{\rm gal}}\gamma_t}{\sigma} \frac{\int_{\beta_{\rm min}}^{\beta(z_s\to\infty)} p(\beta)\beta\ d\beta}{\sqrt{\int_{\beta_{\rm min}}^{\beta(z_s\to\infty)} p(\beta)\ d\beta}}\ , \tag{5.10}$$

where $N_{\rm gal}$ is the number of galaxies in the sample.

A maximum of the S/N can be found at some $\beta_{\rm min,opt}$ where $\frac{\mathrm{dS/N}}{\mathrm{d}\beta_{\rm min}} = 0$. This entails

$$\beta_{\rm min,opt} \int_{\beta_{\rm min,opt}}^{\beta(z_s\to\infty)} p(\beta)\mathrm{d}\beta = \frac{1}{2}\int_{\beta_{\rm min,opt}}^{\beta(z_s\to\infty)} p(\beta)\beta\mathrm{d}\beta\ . \tag{5.11}$$

The above equation can be solved numerically for any ensemble of galaxies to which β values have been previously assigned, as is illustrated in Fig. 5.6.

Uncertainty in β and reduced shear

The observed shear signal is not the gravitational shear γ itself, but rather the reduced shear

$$g = \frac{\gamma}{1-\kappa}\ . \tag{5.12}$$

Note that, unlike γ or convergence κ, this is not linear in β. When a model predicts some value γ_1 and κ_1 for a hypothetical $\beta = 1$, the expectation value for a galaxy whose β is determined with non-zero uncertainty is (Seitz & Schneider 1997, cf. also Applegate et al.

2014)

$$\langle g \rangle = \frac{\langle \beta \rangle \gamma_1}{1 - \frac{\langle \beta^2 \rangle}{\langle \beta \rangle} \kappa_1} \ , \tag{5.13}$$

which includes a correction for the non-linear response of equation (5.12) to the dispersion of β.

While the $\beta(\boldsymbol{m})$ determined above equals $\langle \beta \rangle$ in equation (5.13), $\langle \beta^2 \rangle$ can be determined in an equal fashion by taking the mean of β^2 in a magnitude space volume around the position of the source galaxy. Likewise, equation (5.9) can be used to correct the estimate for cluster members by substituting $\beta^2(z_{\rm cl})$ for $\beta(z_{\rm cl})$. Compared to the direct application of equation (5.12), this correction yields a 1% decrease in best-fitting mass for our clusters, where the effect is, as expected, strongest for the most massive systems, for which the approximation $\kappa \ll 1$ does not hold.

For the analysis of the two CFHTLS WISCy clusters with photometric redshifts, we also account for the non-singular probability distribution (cf. Applegate et al., 2014). In this case we approximate the uncertainty by a scatter of photometric redshifts of $\sigma_{\Delta z/(1+z)} = 0.03$ and an outlier rate $\eta = 0.04$, as defined and measured against spectroscopic samples in Brimioulle et al. (2013). From the simulated distribution, $\langle \beta \rangle$ and $\langle \beta^2 \rangle$ are calculated for the individual galaxy and then used in equation (5.13).

Comparison to photometric redshifts

We finally make a comparison between the $\beta(\boldsymbol{m})$ determined by colour-magnitude matching as described above and the alternative method of calculating $\beta(z_{\rm phot})$ directly from best-fitting photometric redshifts. In particular, we are interested in how biased $\langle \beta(z_{\rm phot}) \rangle$ becomes when estimated from photometric redshifts in various regimes.

To this end, we use the galaxies from the DPS reference catalogue with *UBVRIJK* magnitude information. We generate photometric redshifts for these galaxies, limiting the bands used to either *BVRI* or *UBVRI* only. We select objects either by their $\beta(BRI) > 0.22$ estimated as described above from *BRI* magnitudes only or by these *BVRI* or *UBVRI* photometric redshifts. In the latter case, we select the background by the condition

$$z_s > 1.1 \times z_l + 0.15 \ . \tag{5.14}$$

The conservative offset of $z_s - z_l > 0.1 \times z_l + 0.15$ is meant to prevent significant scatter of foreground galaxies into the background (Brimioulle et al., 2013). In all cases, we compare the mean β of the sample selected and estimated with the respective method to the mean β of the sample based on the *UBVRIJK* photometric redshifts. This corresponds to a comparison to the truth under the assumption that the latter are accurate redshifts, an approximation justified by their excellent quality with respect to the spectroscopic control sample (cf. Fig 5.1).

Fig. 5.7 shows these comparisons both in an empty field (solid lines) and in a region heavily populated with cluster galaxies (half of the galaxies at the cluster redshift in excess of the field distribution, i.e. $f_{\rm cl} = 0.5$, typical for the central region of our cluster pointings, cf. Fig. 5.5). We note the following points.

- Photometric redshifts from a limited number of bands show little bias, in particular at low to medium cluster redshifts, in the field. For *UBVRI*, the bias in $\langle \beta \rangle$ is below 3% up to $z_{\rm cl} \approx 0.35$.

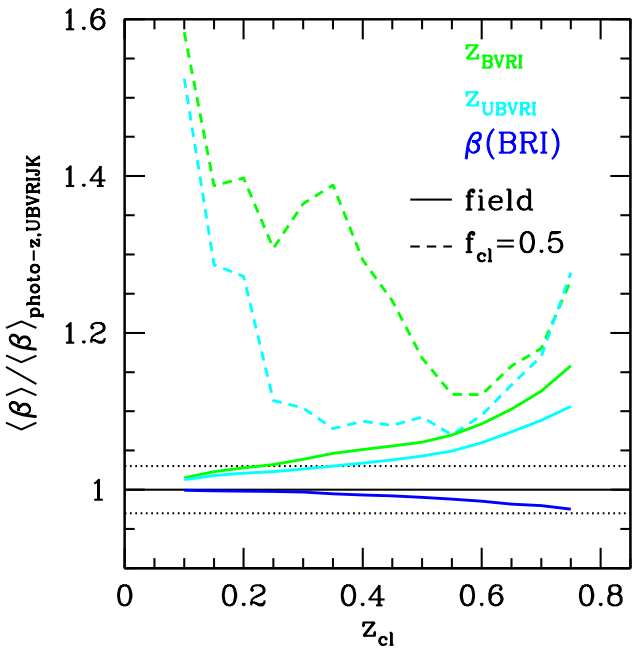

Figure 5.7: Bias in estimated mean β for background galaxy samples selected by various methods compared to the β estimated from *UBVRIJK* photometric redshifts.

- The ability of photometric redshifts with a limited number of bands to yield an unbiased background selection and β estimate is strongly degraded by the presence of excess cluster members. This is also a strong function of the available bands, as can be seen in the case of *BVRI* and *UBVRI* redshifts for $z_{\rm cl} \approx 0.4$ and $f_{\rm cl} = 0.5$: here the *BVRI* background sample has a $\approx 35\%$ bias in β, while *UBVRI* is closer to a $\approx 10\%$ bias.

- The β(m) method described in this section is always biased below the 3% level. The small systematic effect is caused by our symmetric weighting over the magnitude space sphere despite the non-uniform magnitude space density of galaxies. Note that the curve of β(BRI) for $f_{\rm cl} = 0.5$ and in the field are identical by definition in this plot due to our cluster member correction (cf. Section 5.3.1).

These observations are consistent with our data: for six of our clusters with sufficiently deep WFI multi band photometry (namely SPT-CL J2332–5358, SPT-CL J0551–5709 and SPT-CL J2355–5056 with *BRI*, SPT-CL J0509–5342 and MACS J0416.1–2403 with *BVRI* and SPT-CL J2248–4431 with *UBVRIZ*), we perform single halo NFW fits on the same shape catalogue, supplying β with either method. The best-fitting masses measured with these photo-z values are, in all cases, significantly lower than the ones we find with $\beta(\boldsymbol{m})$, on average by 30% (cf. also the similar effect noted in Applegate et al. 2014). The difference in $\Delta\Sigma$ profiles is primarily in the central region, in line with the observation that the bias of photometric redshift based β is a strong function of excess cluster member density. For the photometric redshifts calculated with the better spectral coverage and greater depth of the field of SPT-CL J2248–4431, best-fitting masses agree between both methods at the level of shape noise expected from the different object selection.

#	$\beta_{\rm min}$	$\langle\beta\rangle$	$z(\beta_{\rm min})$	$z(\langle\beta\rangle)$	$N_{\rm gal,bg}$
1	0.20	0.40	0.60	0.85	8316
2	0.21	0.42	0.55	0.80	4307
3	0.23	0.46	0.54	0.83	9152
4	0.25	0.51	0.44	0.72	6259
5	0.19	0.38	0.49	0.67	5763
6	0.23	0.46	0.40	0.60	7467
7	0.23	0.46	0.54	0.82	8663
8	-	0.59	-	-	8045
9	-	0.77	-	-	10639
10	-	0.60	-	-	8067
11	-	0.34	-	-	2628
12	-	0.83	-	-	10053

Table 5.2: Background sample statistics for WISCy clusters. IDs are taken from Table 5.1. β is determined as described in Section 5.3.1. The threshold $\beta_{\rm min}$ is found by means of equation (5.11). The remaining columns give the mean of β in the selected background, the corresponding source redshifts and the number of background galaxies with successful shape measurements selected inside the $\approx 30 \times 30$ arcmin^2 WFI pointing. For the five clusters where photometric redshifts are used, only $\langle\beta\rangle$ and $N_{\rm gal,bg}$ of the photo-z selected background sample are given. For the four CFHT clusters 9-12, source counts are within a WFI pointing centred on the cluster for direct comparison.

Background samples

For the background samples determined as above, we present some fundamental metrics in Table 5.2.

The remaining SPT-CL J2248–4431 WFI data and the CFHT fields have sufficient coverage in five or more bands for the determination of photometric redshifts. In these cases, we select sources by equation (5.14).

5.4 Weak lensing analysis

Weak gravitational lensing changes the positions, sizes and shapes of background galaxy images. While the effect on position is indeterminable and changes in size induce changes in the observed surface density of galaxies which depend on the less than fully known intrinsic distribution of galaxy sizes and magnitudes, the weak assumption that the orientations of galaxies are intrinsically random allows an unbiased measurement of the mass density field.

One important difficulty is that this requires the accurate measurement of pre-seeing galaxy shapes in the presence of a point spread function (PSF) with size of the order of or exceeding that of small background galaxies and ellipticity similar to the gravitational shear signal. This step can be divided into making a model of the PSF at the galaxy position in the image and measuring the pre-seeing galaxy shape using this model. The pipeline used in this work performs these tasks with the publicly available software PSFEX[7] (Bertin, 2011) and an implementation of the shape measurement method of Kaiser et al. (1995, hereafter KSB). It

[7] http://www.astromatic.net/software/psfex

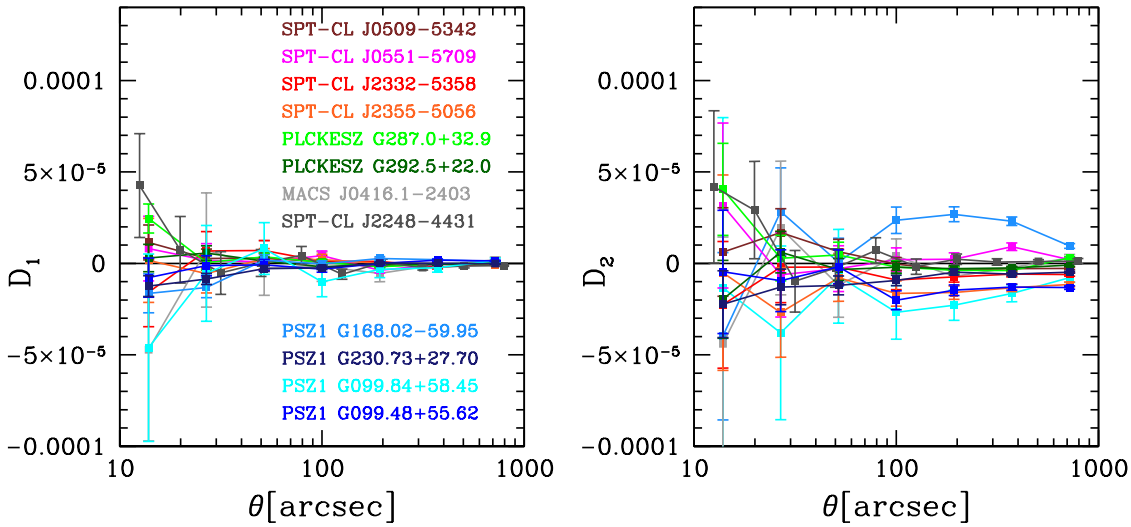

Figure 5.8: Rowe (2010) statistics for the main lensing bands of the WISCy sample. The left- (right)-hand panel shows the autocorrelation of stellar ellipticity residuals (cross-correlation of residual and measured ellipticity). We note that the requirement $|D_i(\theta)| < 10^{-5}$ is always fulfiled for D_1, the component that directly connects to spurious E/B modes due to PSF mismodelling. For D_2, it is violated moderately for three of the four CFHT fields (PSZ1 clusters) and SPT-CL J2355–5056, yet to a level that can be tolerated in cluster analyses.

is described also in Gruen et al. (2013), and we only give a summary here, with emphasis on aspects particular to the WISCy sample.

5.4.1 Model of the point spread function

From bright but unsaturated stars without significant blending selected in a radius-magnitude diagram, we generate a model of the PSF using PSFEX (Bertin, 2011). The model assigns a value to each pixel in a centred vignet image of the star that is a polynomial of the x and y coordinate in the field of view.

It is necessary to ensure that the model represents the PSF accurately. The most important metrics for the purpose of WL are residuals in size and shape. Both are based on second moments of the PSF profile (cf. Kitching et al. 2013), which we calculate from actual star images and the model vignets at star positions.

The main requirement for WL is that PSF sizes and shapes are modelled accurately with low statistical uncertainty and without spatial coherence in the residuals. The latter could cause a systematic signal, since it induces a spatially coherent additive and/or multiplicative component on the measured shear field. We therefore accept a PSF model only if the residual between measured stars and the model at the same position are small. Our qualitative and quantitative criteria are as follows:

- no offset of the residual histogram from zero mean for both size and shape,
- no regions of visibly problematic fit for either size or shape,
- root-mean-squared residual ellipticity below 0.004 in any single component, and

- auto-correlation of ellipticity residuals $D_1(\theta)$ and cross-correlation of residuals and measured stellar ellipticity $D_2(\theta)$, i.e. the Rowe (2010) statistics (defined as in their equations 13 and 14), are consistent with $|D_i(\theta)| < 10^{-5}$ at a separation angle of $\theta \geq 100$ arcsec, the scales relevant to our analysis.

The last criterion is a useful test of having selected the correct polynomial order of PSF interpolation, since it is sensitive to both over- and underfitting (Rowe, 2010). Fig. 5.8 shows D_1 and D_2 for the main lensing band of all our clusters. In each frame, we use the lowest order at which the D_i statistics are either consistent with zero or do not significantly improve when increasing the orders further.

For the subsample of eight clusters from the WISCy sample imaged with WFI, it is always possible to fulfill the PSF model quality criteria for the R-band stack and in several cases also in other bands (cf. Table 5.1 for the list of bands with successful shape measurement). The negative D_2 of SPT-CL J2355–5056 (cf. Fig. 5.8) is a minor exception. Since this is in principle a sign of overfitting despite the use of a polynomial of only 4th order, we conclude that it is likely a statistical effect and accept the model regardless. In some of the I band frames it is not possible to control D_2 to an acceptable level, and we reject these frames for shape measurement. For the four clusters imaged by CFHTLS, the criteria of root-mean-square (rms) residual and $|D_i(\theta)| < 10^{-5}$ prove to be too strict to be fulfilled for the models tested. Modelling the PSF on individual chips while excluding the chip gaps and regions of the field where the PSF model is visibly problematic, we accept the frames despite a slightly higher D_2. We note that this higher level of PSF complexity is typical for the CFHTLS frames (cf. also Brimioulle et al. 2013, their section 3.4).

5.4.2 Shape measurement

We run an implementation of KSB+ (KSB; Luppino & Kaiser 1997 and Hoekstra et al. 1998) which uses the PSFEX PSF model (KSBPSFEX). Galaxies are prepared for shape measurement by the following steps:

- unsaturated, reasonably isolated sources with SExtractor flags ≤ 3 are selected,
- postage stamps of 64×64pix size are extracted and neighbouring objects are masked according to the SExtractor segmentation map,
- the SExtractor photometric background estimate at the object position is subtracted from the image in order to compensate for small-scale background variations insufficiently subtracted by the data reduction pipeline,
- bad and masked pixels are interpolated using a Gauss Laguerre model of the galaxy (Bernstein & Jarvis, 2002), discarding objects with more than 20 per cent of postage stamp area or 5 per cent of model flux in bad or masked pixels.

For the actual shape measurement, KSB+ is run on the prepared postage stamp of the galaxy and the sub-pixel resolution PSF model at the same position. Here we only give a brief summary of this step, referring the reader to the original papers for further details.

KSB measure polarizations

$$\boldsymbol{e} = \frac{1}{Q_{11} + Q_{22}} \begin{pmatrix} Q_{11} - Q_{22} \\ 2Q_{12} \end{pmatrix} \tag{5.15}$$

defined by second moments calculated inside an aperture with Gaussian weight,

$$Q_{ij} = \int \mathrm{d}^2\theta \, I(\boldsymbol{\theta}) \, w(|\theta|) \, \theta_i \, \theta_j \ , \tag{5.16}$$

of the surface brightness distribution of the galaxy $I(\boldsymbol{\theta})$ with a weight function $w(|\theta|)$ centred on the galaxy centroid. Our implementation allows measuring the galaxy and PSF moments with the identical weight function, scaled with the observed half-light radius of the galaxy.

In the presence of an elliptical PSF, the linear approximation of how observed post-seeing polarization $\boldsymbol{e_o}$ reacts to a reduced shear $\boldsymbol{g}$ (cf. Bartelmann & Schneider 2001, p. 60) can be expressed as

$$\boldsymbol{e_o} = \boldsymbol{e}_i + \hat{P}^{\mathrm{sm}}\boldsymbol{p} + \hat{P}^{\gamma}\boldsymbol{g} \ , \tag{5.17}$$

where $\boldsymbol{e}_i$ is the intrinsic post-seeing ellipticity of the galaxy, $\hat{P}^{\mathrm{sm}}$ is a 2×2 tensor quantifying the response of observed shear to PSF polarization $\boldsymbol{p}$ and $\hat{P}^{\gamma}$ is the shear responsivity tensor. We invert $(\hat{P}^{\gamma})^{-1} \approx \frac{2}{\mathrm{tr}P^{\gamma}}$ and assume that $(\hat{P}^{\gamma})^{-1}\boldsymbol{e}_i$ is zero on average (because of the random intrinsic orientation of galaxies) to find the ensemble shear estimate

$$\langle \boldsymbol{g} \rangle = \langle \boldsymbol{\epsilon} \rangle = \left\langle \frac{2}{\mathrm{tr}P^{\gamma}} \left(\boldsymbol{e_o} - \hat{P}^{\mathrm{sm}}\boldsymbol{p} \right) \right\rangle \ . \tag{5.18}$$

We apply some final filtering and corrections to our catalogue, namely

- removing objects with any of $\mathrm{tr}P^{\gamma} < 0.1$, half-light radius less than 5% larger than the PSF half-light radius or S/N as defined by Erben et al. (2001) smaller than 10, since these give extremely noisy shape estimates prone to selection effects and noise biases,
- for objects with measured $|\boldsymbol{\epsilon}| > 1 + \sqrt{\Delta\epsilon_1^2 + \Delta\epsilon_2^2}$, which can happen due to noise, rescaling ellipticity to $|\boldsymbol{\epsilon}| = 1 + \sqrt{\Delta\epsilon_1^2 + \Delta\epsilon_2^2}$ where $\Delta\epsilon_i$ is the Gaussian error of measured pre-seeing ellipticity from pixel noise; note that a strict clipping at $|\boldsymbol{\epsilon}| = 1$ could potentially induce biases since it asymmetrically limits the measurement errors on objects with non-zero ellipticity,
- correcting for shape measurement biases (see Section 5.4.3 for details), and
- merging shape catalogues measured on different bands (or, in the case of the CFHTLS, overlapping pointings), where they exist, into one; since due to differences in depth and colour the statistical uncertainty of these shape estimates can greatly differ between bands, we use for any galaxy the inverse-variance ($\Delta\epsilon^{-2}$) weighted average of all shape estimates.

These catalogues are then matched against photometry extracted as described in Section 5.2.1.

5.4.3 Correction of shape measurement bias

Biases of shape estimators are commonly expressed as a multiplicative and an additive term (see, e.g., Heymans et al., 2006),

$$\epsilon_{\mathrm{obs}} - \epsilon_{\mathrm{true}} = m \times \epsilon_{\mathrm{true}} + c \ . \tag{5.19}$$

It is known from programmes testing shape measurement methods on simulated images with known shear (cf. Heymans et al., 2006; Massey et al., 2007; Bridle et al., 2010; Kitching et al., 2012, Young et al., in preparation) that even under these well-controlled conditions shape measurement biases exist in virtually all pipelines, at least at the typical low levels of S/N that one must deal with in WL studies.

Multiplicative biases $m \neq 0$ translate directly to a bias in the amplitude of the shear signal and, consequently, the mass. Additive biases $c \neq 0$, while severely hindering cosmic shear analyses where the two-point correlation of shapes is measured, average out in spherically symmetric shear analyses such as the ones presented here. They can, however, still influence our analysis in the case of significant masked regions or near the image borders, where spherical averaging is incomplete. We therefore decide to test for and, where necessary, calibrate both effects, using a combination of simulated and real galaxy images.

For calibrating the multiplicative bias, we use a set of simulations of galaxy images with realistic distributions of size, ellipticity and Sérsic parameter convolved with circular and elliptical Gaussian PSFs (Young et al., in preparation). The images are resampled using the same Lanczos kernel as in our stacks, applying a random sub-pixel shift, before galaxies are selected and their shapes measured with our pipeline. S/N is a parameter known to relate to several effects relevant for multiplicative shape bias (Kaiser, 2000; Bernstein & Jarvis, 2002; Refregier et al., 2012; Kacprzak et al., 2012; Melchior & Viola, 2012). We therefore determine the multiplicative bias as the deviation of the ratio of mean measured shapes to known true shears from one as a function of S/N. We note that the magnitude of multiplicative bias and also its observed increase towards lower S/N is typical for present shape measurement pipelines (e.g. Schrabback et al., 2010; von der Linden et al., 2014a). The fitted functional form for multiplicative bias is shown in Gruen et al. (2013, equation 9) and the corresponding correction is applied to our shape catalogues.

No significant additive bias is detected in our simulations, yet could potentially be caused in real data by more intricate observational effects not present in the former. The fact that the mean ellipticity of galaxies in an unbiased catalogue should be zero can be used to empirically calibrate constant additive biases directly from the data (cf. e.g., Heymans et al., 2012). In our initial catalogues, we found a significantly negative ϵ_1 component, indicating preferential orientation of objects along the vertical direction. We trace this back to a selection effect in the latest public version of SExtractor.[8] Related to buffering with insufficiently large memory settings (Melchior, Bertin, private communication), horizontally elongated objects are preferentially deselected (`FLAG`=16). An increase of `MEMORY_BUFSIZE` fixes this and yields shape catalogues without significant additive bias.

5.4.4 Mass mapping

The WL shear field can be used to estimate the surface mass density as a function of position. We create such maps for the eight WFI clusters in the WISCy sample. They are shown in the respective subsections of Section 5.6 and used for the purpose of illustrating the cluster density fields only.

For the surface density reconstruction we use the finite field reconstruction technique described in Seitz & Schneider (1996). From the observed galaxy ellipticity we estimate the reduced shear using equations 5.4 to 5.7 in Seitz & Schneider (1996). We choose a smoothing

[8] Version 2.8.6, cf. `http://www.astromatic.net/software/sextractor`

length of 1.5 arcmin for the spatial averaging of the galaxy ellipticities (their equation 5.7), accounting for the relatively low galaxy density (of order 10 galaxies per square arcminute) of background objects used for the reconstruction. The κ-maps are obtained on a 100×100 grid for the FOV of shear data of typically 28×28 arcmin^2. Spatial resolution is limited by the required large smoothing length and not by the grid on which κ is calculated.

As was pointed out by Schneider & Seitz (1995) and Seitz & Schneider (1995, 1997), as long as one uses shear data (at one effective redshift) only, the surface density maps can only be obtained up to the mass sheet degeneracy. We thus arbitrarily fix this constant such that within the reconstructed field the mean density is $\kappa = 0.01$ (accounting for the fact that the field is not empty but contains a massive cluster with approximately this mean surface density). If we would have chosen this constant differently the contour-pattern of course would not change, but the values would be slightly altered as described by the mass sheet degeneracy.

For the four clusters imaged by the CFHTLS, masking of the chip border areas is required in our shape catalogue, since the complex and discontinuous behaviour of the stack PSF in this region cannot be controlled well enough. As a result, two-dimensional density mapping is extremely noisy, and consequently we do not provide density maps for them.

5.4.5 Mass measurement

For the interpretation of the WL signal in each of our cluster fields, we follow the scheme described in this section. We follow two different approaches, one ignoring secondary structures along the line of sight (as is commonly done in similar WL studies) and one explicitly modelling these. The following sections detail the components of this procedure.

Density profile

It is supported by a range of observational and simulation studies that dark matter haloes of clusters of galaxies on average follow the profile described first by NFW. We also adopt this mass profile, with the three-dimensional density $\rho(r)$ at radius r given as

$$\rho(r) = \frac{\rho_0}{(r/r_\mathrm{s})(1 + r/r_\mathrm{s})^2} \ . \tag{5.20}$$

The profile can be rewritten in terms of two other parameters such as mass M_{200m} and concentration $c_{200m} = r_{200m}/r_\mathrm{s}$ instead of the central density ρ_0 and scale radius r_s. Expressions for the projected density and shear of the NFW profile are given by Bartelmann (1996) and Wright & Brainerd (2000).

The two parameters of the NFW profile are not independent, but rather connected through a concentration-mass relation. This can be used, for instance, in cases where the data are not sufficient for fitting the two parameters simultaneously. It also allows for proper marginalization over concentration from the two-dimensional likelihood in cases where one is only interested in mass. In our analysis, we assume the concentration-mass relation of Duffy et al. (2008) with a lognormal prior (Bullock et al., 2001) with $\sigma_{\log c} = 0.18$. Offsets of the assumed concentration-mass relation from the truth, which can be due to differences between assumed and true cosmology or imperfect simulations from which the relation is drawn, impact the mass measurement, however only mildly (see, for example, the discussion in Hoekstra et al. 2012, their section 4.3).

Unless otherwise noted, we use the brightest cluster galaxy (BCG) position as the centre of the halo (cf. also Hoekstra et al. 2012 and section 5.7.5 for a discussion for choosing the centre for lensing analyses). In order to be less sensitive to miscentring, heavy contamination with cluster members, very strong shears and possible deviations from the NFW profile, a central region of 2 arcmin radius around the BCG is not used in our likelihood analysis (see following section). This is in line with previous studies (cf. Applegate et al. 2014 and Hoekstra et al. 2012, who exclude the central projected 750 and 500 kpc, respectively, or Mandelbaum et al. (2010), who propose an aperture mass measurement insensitive to surface mass density inside $r_{200c}/5$ and discuss, in more detail, the reasons why this is beneficial for the mass determination). Note, however, that we a posteriori find the measured central shears to be consistent with the prediction from our fit (cf. Section 5.7.5).

Likelihood analysis

Assuming Gaussian errors of the shape estimates, the likelihood of any model can be calculated from the shear catalogue by means of the χ^2 statistics. Given model predictions $\hat{g}_{i,j}$ for the i component of the shear on background galaxy j (which depend on the masses and concentrations of one or more haloes in the model and the estimates of β and β^2 of the background galaxy, cf. Section 5.3.1), the likelihood L can be written as

$$-2\ln\mathcal{L} = \sum_{i,j} \frac{(\hat{g}_{i,j} - \epsilon_{i,j})^2}{\sigma_{i,j}^2 + \sigma_{\rm int}^2} + \text{const} \ . \tag{5.21}$$

Here $\epsilon_{i,j}$ is the corresponding shape estimate with uncertainty $\sigma_{i,j}$ and the intrinsic dispersion of shapes is $\sigma_{\rm int} \approx 0.25$. The shape measurement uncertainty is calculated by the KSBPSFEX pipeline based on linear error propagation and then multiplied with an empirically calibrated factor of 1.4 to approximate non-linear effects. The latter can be estimated by assuming that the observed variance of shape estimates around the true mean of 0 be equal to the sum of measurement and intrinsic variance, which, unlike the measurement error, is constant under different observing conditions. In addition, the factor is confirmed by a comparison of uncertainties measured on CFHT data with our pipeline with the uncertainties given in the CFHTLenS shape catalogues (cf. Miller et al. 2013 and Heymans et al. 2012).

Equation (5.21) readily allows finding maximum-likelihood solutions. Marginalisation over the concentration parameter can easily be done if a sufficiently large range in concentration around the concentration prior is probed (cf. Section 5.4.5). By means of the $\Delta\chi^2$ method (Avni, 1976), we can also determine projected or combined confidence regions in the parameter space of our model.

Single halo versus multiple halo analysis

Our measurement of masses is done with two different fitting procedures, which we denote in the following as the *single halo* and *multiple halo* analysis.

For the single halo analysis, we fit only the central halo of the SZ cluster, placing its centre at the brightest cluster galaxy.

However, no cluster of galaxies is completely isolated in the field. Rather, both uncorrelated structures along the line of sight and correlated structures in the vicinity of the cluster contain additional matter and therefore cause a lensing signal of their own.

It is in this important sense that while lensing accurately weights the *matter* along the line of sight (up to the mass sheet degeneracy), a *mass* estimate for a cluster is the result of our interpretation of the signal. In the same way as in the case of full knowledge (as it is available only in a high-resolution simulation), the mass we determine therefore differs by method, yet in the case of lensing with the additional difficulty of projection.

Several studies in the past have shown that the accuracy of WL analyses depends on proper modelling of such projected structures (see, for example, Dodelson 2004 and Maturi et al. 2005 for minimizing the impact of uncorrelated structures, Hoekstra et al. 2011b for the effect of modelling massive projected structures and Gruen et al. 2011 for the impact of correlated structures). Projected structures, depending on their position, can bias the mass estimate in either direction, requiring a modelling of the particular configuration rather than a global calibration.

For each of the systems considered here, our multiple halo analysis is therefore done as follows. From known clusters and density peaks identified visually and in photometric redshift catalogues we compile a list of candidate haloes within the WFI field of view. Details of this procedure are given in the respective subsection of Section 5.6 and Table 5.5 in the appendix.

We determine the redshift of each of the candidate haloes by three different strategies, depending on the field. In the case of PSZ1 G168.02–59.95 and PSZ1 G099.84+58.45, coverage with spectroscopy from SDSS DR 10 (Ahn et al., 2014) is used where candidate structure members have been observed. In the fields with ≥ 5 bands, the median photometric redshift of visually selected cluster members is taken. For the remaining seven WFI fields without accurate photometric redshifts, a different scheme is applied.

In these cases, from a list of visually identified red member galaxies, we find the median colours with respect to the R-band magnitude. These could be compared to a red galaxy template, yet it is known that the SED of red galaxies indeed changes with redshift and shows significant variability even at fixed redshift (Greisel et al., 2013). We therefore determine the mean B-R, V-R and R-I colours of red galaxies in redshift bins from the DPS catalogues (cf. Section 5.3.1). Fitting a parabola to the squared deviations between these colours and the median colour of red member galaxies of the candidate clusters, we find its minimum χ^2 redshift. Excluding the outlier of SPT-CL J0551–5709 (where our estimate of $z \approx 0.30$ deviates from the spectroscopic value of 0.423, potentially due to residual star-forming activity in cluster member galaxies), this estimate yields a root-mean-squared error of $\sigma_z = 0.02$ w.r.t. known redshifts in our WFI cluster fields.

In order to remove the effect of projected structures on the mass estimate of the central halo, we then determine the maximum-likelihood masses for each of the candidate haloes in a combined fit, assuming a fixed concentration-mass relation. As a first-order approximation, in this analysis we assume simple addition of reduced shears due to multiple lenses. Where the best-fitting masses of candidate off-centre haloes deviate from zero, we subtract the signal of the best-fitting haloes from the shear catalogue, on which we then perform the same two-parameter likelihood analysis as in Section 5.4.5.

5.5 Sunyaev-Zel'dovich catalogues

The comparison of our WL results to the SZ effect of the clusters is performed purely on the basis of publicly available catalogues. This section lists the data and our methods of using the catalogues.

5.5.1 South Pole Telescope

The SPT is presently performing multiple surveys of 2500 deg^2 of the southern sky in three microwave bands, one of its goals being a cosmological analysis of the SZ signal of clusters of galaxies (Staniszewski et al., 2009; Vanderlinde et al., 2010; Williamson et al., 2011; Reichardt et al., 2013). Five of our clusters have been observed in SPT surveys and four of them are indeed SPT discovered.

SPT mass estimates are based on the detection significance ζ in the band where it is maximal. In this work, we take Vanderlinde et al. (2010) as the primary reference for mass calibration. They calibrate the mass-significance relation in SPT empirically as

$$\zeta = A \times \left(\frac{M_{200m}}{5 \times 10^{14} h^{-1} M_\odot} \right)^B \times \left(\frac{1+z}{1.6} \right)^C , \tag{5.22}$$

with parameters calibrated from simulations as $A = 5.62$, $B = 1.43$ and $C = 1.40$ (Vanderlinde et al., 2010). Here ζ is the SPT detection significance corrected from the observed significance ξ for several noise dependent biases, namely first the preferential selection of objects for which intrinsic and measurement noise have a positive contribution to the signal and secondly the preferential up-scatter of intrinsically less massive objects because of the steepness of the mass function. These effects are sometimes called the Malmquist and Eddington bias, and are indeed related to the works by Malmquist (although only widely and with varying definition) and Eddington (1913). A third effect particular to SPT is an additional bias on measured significances, caused by the fact that these are measured at the position where they are highest (instead of the unknown true position of the cluster). While the first and third effect can be corrected directly, the second requires to assume a mass function, which in turn depends on cosmology. Where we use ζ in our analysis, we therefore calculate it from the mass estimate published by the SPT collaboration (Vanderlinde et al. 2010 for two of our clusters, Reichardt et al. 2013 for two of the clusters where new spectroscopic redshifts had become available in the meantime and Williamson et al. 2011 for SPT-CL J2248–4431, all of which have made corrections for all three effects), which we insert into equation (5.22) or (5.23).

As an alternative calibration based on a very similar scheme, we also compare to the mass estimates of Reichardt et al. (2013). Using a different mass definition and redshift scaling, Reichardt et al. (2013) and Benson et al. (2013) define the MOR as

$$\zeta = A \times \left(\frac{M_{500c}}{3 \times 10^{14} h^{-1} M_\odot} \right)^B \times \left(\frac{E(z)}{E(0.6)} \right)^C , \tag{5.23}$$

with $E(z) = \sqrt{\Omega_\mathrm{m}(1+z)^3 + \Omega_\Lambda}$. The parameters are determined from survey simulations as $A = 6.24 \pm 1.87$, $B = 1.33 \pm 0.27$ and $C = 0.83 \pm 0.42$ (Reichardt et al., 2013), taking into account modelling uncertainty. Posterior scaling parameters from the combined cosmological analysis including X-ray cluster measurements and CMB are reported in Benson et al. (2013) as $A = 4.91 \pm 0.71$, $B = 1.40 \pm 0.15$ and $C = 0.83 \pm 0.30$ with an intrinsic scatter of ζ at fixed mass corresponding to lognormal $\sigma_{\mathrm{int},\log_{10}} = 0.09 \pm 0.04$.

5.5.2 *Planck*

Planck is a mission complementary to SPT in its SZ applications. Unlike SPT, which has imaged a relatively small area, *Planck* detects an all-sky catalogue of the SZ-brightest objects

with sufficient angular extent. However, while the SPT produces arcminute-resolution images, the Planck SZ analyses are complicated by the much lower resolution (above 4 arcmin full width at half-maximum even for the bands with smallest beam size), which leaves most clusters unresolved and high redshift clusters hard to detect, and the inhomogeneity of noise over the observed area.

For this reason, Compton parameters Y are provided by Planck Collaboration et al. (2014a) only in the form of a two-dimensional likelihood grid in terms of $Y = Y_{5\theta_{500c}}$, integrated inside a spherical a volume of $5 \times \theta_{500c}$ radius, and the angular size $\theta_\mathrm{s} = r_\mathrm{s}/D_A(z)$, where r_s is the scale radius of the generalized NFW profile (cf. Arnaud et al., 2010) of the intracluster gas.[9] Due to the large beam size, the Compton parameter can only be confined well if prior information on θ_s is available.

De-biasing

As a first step, Compton parameters Y measured near the detection limit must be (Malmquist) noise-bias corrected. At the detection limit, there exists a selection effect based on the preferential inclusion (exclusion) of objects whose signal scatters up (down) from the fiducial value. Consequently, a majority of objects near the detection limit have a positive noise and intrinsic scatter contribution.[10] The resulting multiplicative bias in

$$Y_\mathrm{obs} = b_m \times Y_\mathrm{true} \tag{5.24}$$

can be estimated as (Vikhlinin et al., 2009a)

$$b_m = \exp\left[\sigma \times \frac{\exp(-x^2/2\sigma^2)}{\sqrt{\pi/2}\mathrm{erfc}(x/\sqrt{2}\sigma)}\right] , \tag{5.25}$$

where

$$x = -\ln[(\mathrm{S/N})_0/(\mathrm{S/N})_\mathrm{cut}] , \tag{5.26}$$

$$\sigma = \sqrt{\ln^2[(\mathrm{S/N}+1)/(\mathrm{S/N})] + [\ln(10)\sigma_{\mathrm{int},\log 10}]^2} , \tag{5.27}$$

with the nominal S/N according to the MOR at the mass of the cluster $(\mathrm{S/N})_0$, the threshold of the catalogue $(\mathrm{S/N})_\mathrm{cut} = 4.5$ and the ln-normal scatter of the MOR σ. We adopt a value of the lognormal intrinsic scatter of $\sigma_{\mathrm{int},\log 10} \approx 0.07$ (Planck Collaboration et al., 2014a). As done by Planck Collaboration et al. (2014a), we simply divide the Compton decrement by b_m.[11]

For the seven *Planck*-detected clusters in the WISCy sample, $b_m \in (1.00, 1.10)$. Note that for a higher $\sigma_{\mathrm{int},\log_{10}}$ as suggested by previous studies (Marrone et al., 2009; Hoekstra et al., 2012; Marrone et al., 2012), b_m and with it Y_true and estimated mass for our clusters change significantly, in particular for the low S/N detections.

[9] For a detailed description of the format, please refer to `http://www.sciops.esa.int/wikiSI/planckpla/index.php?title=Catalogues&instance=Planck_Public_PLA`

[10] This is true even without the Eddington bias (preferential up-scatter of less massive haloes due to the steepness of the mass function), an effect ignored here for consistency with the Planck Collaboration et al. (2014a) calibration.

[11] We consistently work with the natural logarithm here. Planck Collaboration et al. (2014a) appear to use log and ln interchangeably in their equation 8 and the following description.

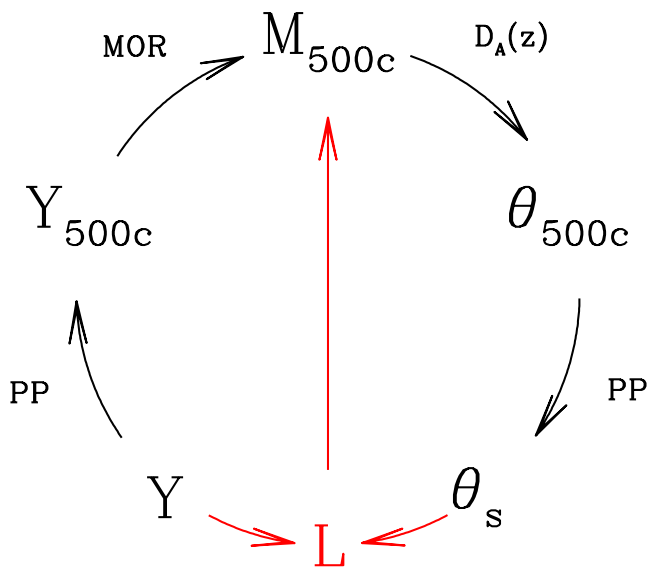

Figure 5.9: Self-consistent mass estimation from *Planck* likelihood in θ_s-Y space. The diagram illustrates how, assuming a pressure profile (PP), a mass-observable relation (MOR) and the angular diameter distance of the cluster $D_A(z)$, θ_s is a function of Y (and vice versa). The likelihood for mass need then be evaluated only for consistent tuples of Y and θ_s.

θ_s-Y degeneracy

How can the degeneracy between angular size and integrated Compton parameter be broken? In this work we use two different schemes of calculating mass estimates from the Planck SZ signal. For their own calibration, the Planck Collaboration uses subsets of clusters with X-ray mass estimates. From these and assumptions about the pressure profile (PP; see below) they derive θ_s, thereby breaking the θ_s-Y degeneracy. We perform a similar analysis, using X-ray mass estimates for our sample from various sources. The resulting SZ mass estimates, however, are not made truly independently from the SZ information, since in fact prior information on the mass itself is used. In addition, we therefore develop a scheme of self-consistent SZ masses, similar to the one suggested by Planck Collaboration et al. (2014a, their section 7.2). It is illustrated in Fig. 5.9.

Likelihoods are given by Planck Collaboration et al. (2014a) in terms of Compton parameters Y and angular scale radii θ_s.[12] A value for θ_{500c} corresponding to an external X-ray mass estimate can be converted to θ_s by means of the PP concentration parameter $c_{P,500c}$=1.1733 (Arnaud et al., 2010; Planck Collaboration et al., 2014a). At the fixed value of θ_s, we obtain a confidence interval of Y (see Fig. 5.10 for an illustration), which can be converted to the spherical estimate Y_{500c} and to M_{500c} with the prescriptions of Planck Collaboration et al.

[12]These likelihoods are provided by Planck Collaboration et al. (2014a) for different extraction methods. We will use the Matched Multi-filter method (MMF3) catalogues of Melin et al. (2006) for consistency with Planck Collaboration et al. (2014c) in version R1.11.

SZ name	θ_{500c}	S/N	$Y_{500c}^{R_X}$	$M_{500c}^{\mathrm{SZ},R_X}$	$M_{500c}^{\mathrm{SZ,sc}}$
PLCKESZ G287.0+32.9	4.85	17.2	3.43 ± 0.29	$17.7^{+0.8\ +1.7\ +2.7}_{-0.9\ -1.5\ -3.6}$	$18.2^{+1.0\ +1.7\ +2.8}_{-0.9\ -1.6\ -3.7}$
PLCKESZ G292.5+22.0	5.00	8.9	1.76 ± 0.29	$10.3^{+0.9\ +1.0\ +1.5}_{-1.0\ -0.9\ -2.1}$	$10.6^{+1.1\ +1.0\ +1.5}_{-1.1\ -0.9\ -2.1}$
SPT-CL J2248–4431	4.93	16.7	2.71 ± 0.23	$14.5^{+0.7\ +1.4\ +2.1}_{-0.7\ -1.2\ -2.9}$	$14.8^{+0.8\ +1.4\ +2.2}_{-0.8\ -1.3\ -3.0}$
PSZ1 G168.02–59.95	5.97	5.4	1.21 ± 0.33	$4.6^{+0.6\ +0.4\ +0.7}_{-0.8\ -0.4\ -0.9}$	$5.0^{+0.9\ +0.5\ +0.7}_{-0.9\ -0.4\ -1.0}$
PSZ1 G230.73+27.70	3.71	5.4	0.69 ± 0.20	$6.0^{+0.9\ +0.6\ +0.9}_{-1.0\ -0.5\ -1.2}$	$6.2^{+1.2\ +0.6\ +0.9}_{-1.3\ -0.5\ -1.3}$
PSZ1 G099.84+58.45	2.98	5.9	0.58 ± 0.14	$8.6^{+1.1\ +0.8\ +1.2}_{-1.2\ -0.7\ -1.7}$	$8.3^{+1.2\ +0.8\ +1.2}_{-1.3\ -0.7\ -1.7}$
PSZ1 G099.48+55.62	6.27	7.0	1.08 ± 0.23	$3.2^{+0.4\ +0.3\ +0.5}_{-0.4\ -0.3\ -0.7}$	$3.8^{+0.5\ +0.4\ +0.6}_{-0.5\ -0.3\ -0.8}$

Table 5.3: Mass estimates from the Planck Collaboration et al. (2014a) SZ catalogue. $M_{500c}^{\mathrm{SZ},R_X}$ is calculated using X-ray mass estimates for determining the aperture size θ_{500c}. $M_{500c}^{\mathrm{SZ,sc}}$ uses the self-consistent mass determination algorithm described herein. All Compton parameters have been corrected for Malmquist bias by means of equation (5.25) according to their S/N in the MMF3 catalogue. Masses are given in units of $10^{14} h_{70}^{-1} M_\odot$. The Compton parameter integrated inside a sphere of the size of the X-ray r_{500c}, $Y_{500c}^{R_X}$, is given in units of 10^{-3} arcmin^2. The M^{SZ} estimates are listed with statistical, intrinsic and systematic uncertainties.

(2011b, 2014a), namely

$$Y_{500c} = 0.5567 \times Y \tag{5.28}$$

(cf. also Arnaud et al. 2010, their section 6.3.1) and

$$E(z)^{-2/3} \times \left(\frac{D_A^2 \times Y_{500c}}{\mathrm{Mpc}^2} \right) = 10^A \times \left(\frac{M_{500c} \times (1-b)}{6 \times 10^{14} h_{70}^{-1} M_\odot} \right)^B \tag{5.29}$$

with $E(z) = \sqrt{\Omega_\mathrm{m}(1+z)^3 + \Omega_\Lambda}$ and fiducial calibration parameters $A = -4.19 \pm 0.02$, $B = 1.79 \pm 0.08$ and $b = 0.2^{+0.1}_{-0.2}$ (cf. Planck Collaboration et al., 2014c, their equation A.15). We find that the value of $Y_{500c}^{R_X} = (2.36 \pm 0.20) \times 10^{-4}$ Mpc^{-2} determined such from the Planck Collaboration et al. (2014a) likelihoods for SPT-CL J2248–4431 is consistent with the value given by Planck Collaboration et al. (2011b) from earlier *Planck* data, also using X-ray priors on size, of $Y_{500c}^{R_X} = (2.21 \pm 0.16) \times 10^{-4}$ Mpc^{-2}. For PLCKESZ G287.0+32.9 and PLCKESZ G292.5+22.0, Planck Collaboration et al. (2011a) give Compton decrements as $Y = (6.1 \pm 0.6) \times 10^{-3}$arcmin^2 and $Y = (3.7 \pm 0.6) \times 10^{-3}$arcmin^2. These are again consistent with the values we extract of $Y = (6.16 \pm 0.52) \times 10^{-3}$ and $Y = (3.16 \pm 0.52) \times 10^{-3}$arcmin^2, respectively.

The second option we use is to calculate, by way of equations 5.28 and 5.29, for any Y the corresponding

$$\theta_\mathrm{s} = \theta_{500c}[M_{500c}(Y)]/c_{P,500c}\ . \tag{5.30}$$

For the PP concentration we again use the fixed value of $c_{P,500c} = 1.1733$.

Equation (5.30) is a criterion of self-consistency, namely that the analysis result in a mass to which corresponds the virial radius used in the extraction of the signal. The likelihood is then evaluated at the combination of Y and θ_s matched by equation (5.30). Thereby we reduce the dimensionality of the likelihood analysis by one, applying only knowledge about the angular diameter distance to the system and no mass information external to the Planck SZ signal. An illustration of the method is given in Fig. 5.10 for one of our clusters.

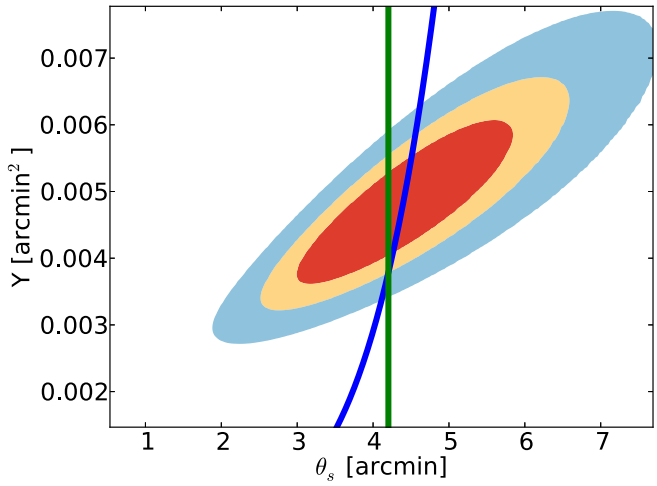

Figure 5.10: Mass estimation from *Planck* likelihood in Y-θ_s space for SPT-CL J2248–4431. From the tabulated likelihood (Planck Collaboration et al., 2014a) we determine the confidence interval in Y using a fixed prior for the scale angle from X-ray measurements (green line) and using self-consistency with the MOR (blue line). Colour contours indicate the 68, 90 and 99 per cent confidence levels for two degrees of freedom.

Mass estimates

We give confidence intervals for the mass estimates based on the Planck Collaboration et al. (2014a) catalogues in Table 5.3, listing three separate uncertainties:

- the statistical uncertainty of Y_{500c}, extracted from the likelihood as described above,
- the intrinsic scatter of Y_{500c} at fixed mass (and, conversely, mass at fixed Y_{500c}, which we approximate as $\sigma_{\log Y_{500c}|M_{500c}} = 0.07$, and
- the systematic uncertainty based on the confidence regions of parameters A, B and b in equation (5.29), where we assume all deviations from the fiducial values to be uncorrelated.

5.6 Individual cluster analysis

This section presents the individual analyses of the WISCy sample. The subsections are ordered by cluster ID (cf. Table 5.1) and contain information on the following:

i) *Visual appearance.* Including a colour image of the central parts and a map of projected galaxy density,

ii) *Previous work.* With a review of published optical, spectroscopic, X-ray, radio and SZ observations and known neighbouring projected structures,

iii) *Weak lensing analysis.* Including shear profile, individual mass estimates and remarks on particularities of the analysis, especially in terms of the modelling of nearby structures, and

iv) *Strong lensing.* With a review of previous strong lensing analyses and strong lensing candidates discovered in our cluster fields.

5.6.1 SPT-CL J0509–5342

Visual appearance

The centre of SPT-CL J0509–5342 (cf. Fig. 5.11, top panel, showing a 4×4 arcmin^2 region) is marked by a diffuse BCG, embedded in a number of relatively bright foreground stars and neighboured by at least two giant gravitational arcs of background galaxies strongly lensed by the system.

The central panel of Fig. 5.11 shows the three-dimensional density of galaxies in a 30×30 arcmin map around the cluster, smoothed with a minimum-variance (Epanechnikov) kernel of radius 1 arcmin and corrected for masked area. Galaxies are selected by their photometric redshift within $|z - z_{\rm cl}| \leq 0.06 \times (1 + z_{\rm cl})$. Note that the photometric redshifts used here are very noisy due to the small number of bands and are therefore provided for illustrative purposes only. The colour image cutout, as in the respective figures of all following clusters, corresponds to the red frame in the overview map (central panel).

Previous work

Staniszewski et al. (2009) describe the system as one of the first clusters discovered in an SZ survey. Its detection significance is quoted by Vanderlinde et al. (2010) as $\xi = 6.61\sigma$. Menanteau et al. (2010a) independently discover the SZ signal of the cluster and label it as ACT-CL J0509-5341. The cluster coincides with the source 1RXS J050921.2-534159 from the *ROSAT* faint source catalogue (Voges et al., 2000).

High et al. (2010) determine a spectroscopic redshift of the cluster of $z = 0.4626$, which we adopt in this analysis. The independent spectroscopy of Menanteau et al. (2010a) yields $z = 0.461$.

Using *griz* data from the Blanco Cosmology Survey and Magellan, High et al. (2010) provide an optical richness of $N_{\rm gal} = 41 \pm 8$, corresponding to their mass estimate of $M_{200m}(N_{\rm gal}) = (3.3 \pm 2.0 \pm 1.0) \times 10^{14} h^{-1} M_\odot$. Zenteno et al. (2011) fit the luminosity function and the number density profile of cluster member galaxies, noting that there is no indication that this and the other clusters in their SZ-selected sample differ in their properties from samples selected by other kinds of observations.

Sifón et al. (2013) use spectroscopic redshifts of 76 cluster members to determine a velocity dispersion of (846 ± 111)km s^{-1} and a corresponding dynamical mass estimate of $M_{200c} = (5.5 \pm 2.1) \times 10^{14} h_{70}^{-1} M_\odot$.

The SZ mass of the system is estimated by Vanderlinde et al. (2010) based on the significance-mass relation, yielding $M_{200m} = (5.09 \pm_{\rm stat} 1.02 \pm_{\rm sys} 0.69) \times 10^{14} h^{-1} M_\odot$. The unbiased significance according to equation (5.22) is $\zeta = 5.08$.

The independent discovery of the cluster by ACT is listed as ACT-CL J0509–5341 (Marriage et al., 2011). The SZ mass is given by Hasselfield et al. (2013) as $M_{500c} = (4.0 \pm 0.8) \times 10^{14} h_{70}^{-1} M_\odot$.

Andersson et al. (2011) present the system in their X-ray measurements of SPT clusters with *Chandra*, finding $T = 7.0^{+1.4}_{-1.1}$keV, $M_{g,500} = 5.6^{+0.2}_{-0.2} \times 10^{13} h_{70.2}^{-1} M_\odot$ and a corresponding $Y_{X,500c} = (4.3 \pm 0.8) \times 10^{14} h_{70.2}^{-1} M_\odot$keV. Using the MORs of Vikhlinin et al. (2009a) with mean values calibrated from local clusters under the assumption of HSE, they estimate $M_{500c} =$

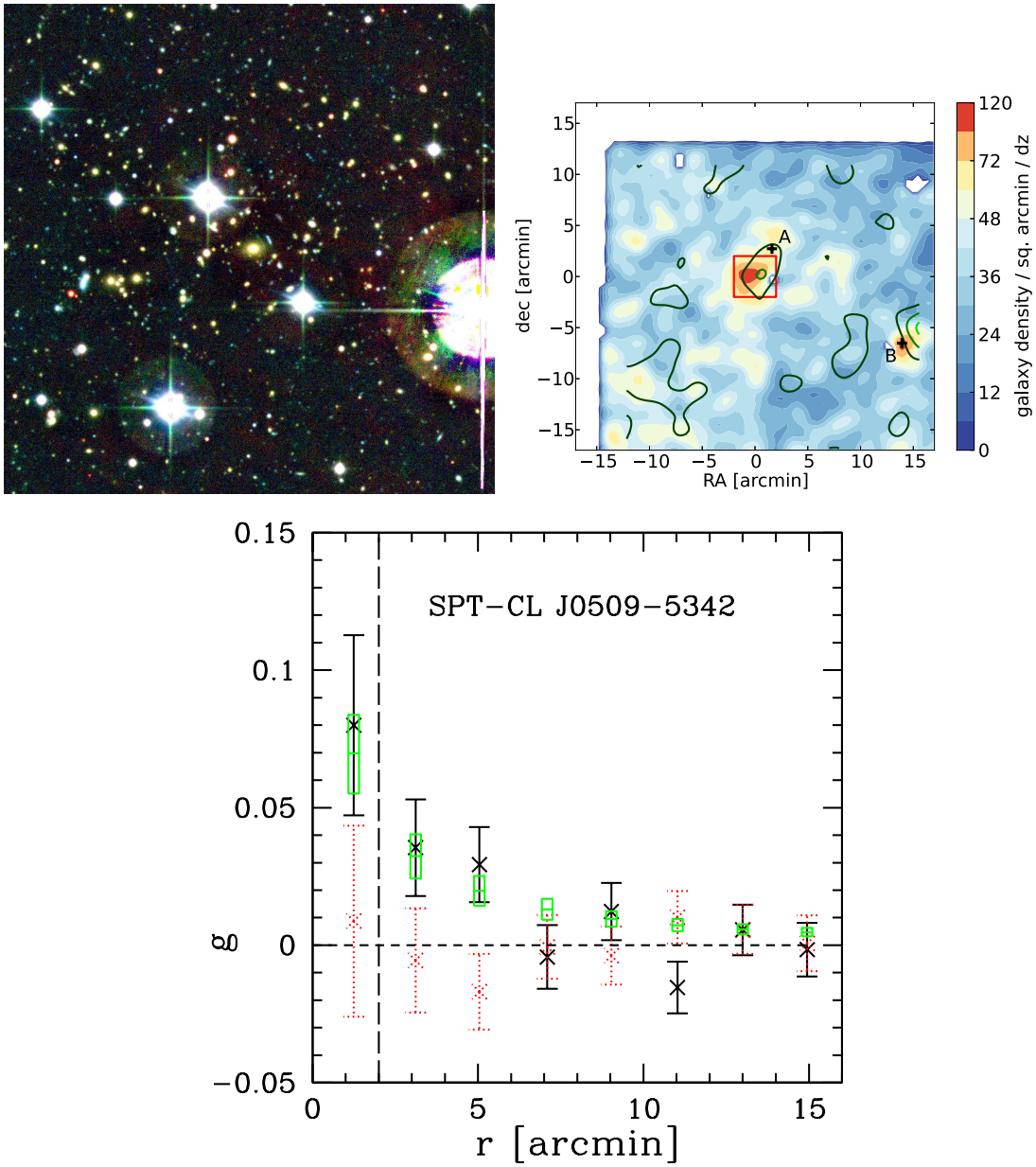

Figure 5.11: Colour image (top left panel) from *VRI* frames of the central 4×4 arcmin region of SPT-CL J0509–5342, corresponding to the red square in the three-dimensional galaxy density map (top right panel) with overlaid κ contours at $\kappa = 0.05, 0.10, 0.15$. The bottom panel shows shear profile with tangential shear (black), cross-shear (red, dotted) and NFW fit (green boxes), using only data > 2 arcmin from the centre (long dashed line).

$(5.43 \pm 0.60) \times 10^{14} h_{70.2}^{-1} M_\odot$ from $Y_{X,500c}$ and $M_{500c} = (6.71 \pm 1.69) \times 10^{14} h_{70.2}^{-1} M_\odot$ from the temperature. In this work, we will adopt the weighted mean value $M_{500c} = (5.57 \pm 0.56) \times 10^{14} h_{70.2}^{-1} M_\odot$.

Andersson et al. (2011) classify SPT-CL J0509–5342 as a merger at an early stage based on the double-peaked X-ray centre. In contrast, Semler et al. (2012) find the system to have a moderate cool core.

Reichardt et al. (2013) quote a combined SZ+X-ray mass of $M_{500c} = (5.36 \pm 0.71) \times 10^{14} h_{70}^{-1} M_\odot$.

McInnes et al. (2009) perform a WL analysis of the system as one of the first SZ detected clusters. They calculate KSB shapes on i band and photometric redshifts on g-, r-, i-, and z-band public imaging data from the Blanco Cosmology Survey. Their mass estimate from an NFW fit is $M_{200m} = 3.54^{+2.07}_{-1.68} h_{71}^{-1} \times 10^{14} M_\odot$.

Weak lensing analysis

The κ map (Fig. 5.11, central panel) contains peaks at the centre of SPT-CL J0509–5342 and at a secondary location near the western edge of the field (B). The latter is the location of the candidate strong lensing feature discussed in the following section and shown in Fig. 5.12.

A single halo fit, fixing the centre at the BCG and marginalizing over concentration, yields $M_{200m} = (8.4^{+3.4}_{-2.9}) \times h_{70}^{-1} 10^{14} M_\odot$ ($M_{500c} = (4.7^{+1.9}_{-1.7}) \times h_{70}^{-1} 10^{14} M_\odot$). The observed shear profile and the confidence interval of the NFW fit are shown in Fig. 5.11 (bottom panel).

Given the correlated shape noise, this result is inconsistent with the earlier analysis of McInnes et al. (2009), although without a cross-match to their photometric redshift catalogue the significance of inconsistency cannot be estimated confidently. We hypothesize that the photometric redshifts calculated by McInnes et al. (2009) on four bands only, the bluest being the g band, could be a cause for a low bias in their mass estimate (cf. Section 5.3.1 and Applegate et al. 2014). We note that there is additional evidence from the strong lensing feature (cf. Section 5.6.1) and the consistency of our result with all SZ and X-ray based measurements supporting our higher mass estimate.

After subtracting the maximum likelihood signal of surrounding structures fitted simultaneously, the resulting mass estimate for the central halo is slightly lower at $M_{200m} = (6.6^{+3.1}_{-2.6}) \times h_{70}^{-1} 10^{14} M_\odot$ ($M_{500c} = (3.8^{+1.7}_{-1.5}) \times h_{70}^{-1} 10^{14} M_\odot$).

Both our mass estimates are in agreement with the SZ masses of Vanderlinde et al. (2010) and Hasselfield et al. (2013), the X-ray masses of Andersson et al. (2011), the combined SZ+X-ray mass of Reichardt et al. (2013) and the dynamical mass of Andersson et al. (2011).

Strong lensing

Two giant arcs are visible in Fig. 5.11 towards the north-eastern direction from the BCG, as previously reported by Menanteau et al. (2010a). At a separation of $\theta_1 = 4.8$ arcsec and $\theta_2 = 8.7$ arcsec from the BCG they correspond to the Einstein radii of the best-fitting NFW profile at source redshifts $z_{s,1} = 1.75$ and $z_{s,2} = 5.7$. For the 68% upper limit of our NFW fit, the corresponding redshifts are at more plausible values of $z_{s,1} = 1.37$ and $z_{s,2} = 2.6$.

We note that these strong lensing features pose additional evidence for our mass estimate that significantly exceeds the previous one by McInnes et al. (2009). An NFW profile following the concentration-mass relation (Duffy et al., 2008) at their best-fitting mass (their upper limit), $M_{200m} = 3.59 \times 10^{14} h_{70}^{-1} M_\odot$ ($5.69 \times 10^{14} h_{70}^{-1} M_\odot$), has a limiting Einstein radius of

Figure 5.12: Colour image of strong lensing candidate in the field of SPT-CL J0509–5342. The cutout is centred at $(\alpha, \delta) = (05^{\mathrm{h}}07^{\mathrm{m}}47.1^{\mathrm{s}}, -53°48'40.9'')$ and 0.5×0.5 arcmin^2 in size.

4.7 arcsec (7.6 arcsec) for $z_s \to \infty$. Likewise, at their best-fitting mass, a high concentration of $c_{200m} = 8.6$ (an outlier from the mean by $\approx 1.5\sigma$) is required to reproduce the outer arc for a hypothetical source redshift of $z_s = 2$. Since the BCG is visibly elliptical at an axis ratio of $A/B = 1.27$, a strongly increased projected concentration is, however, unlikely.

In addition, the field contains a strangely shaped blue structure around a red galaxy at the centre of a group in the west of the main cluster (Fig. 5.12). At a radius of $r \approx 4$ arcsec and for the 68% upper limit of the group mass of $M_{200m} = 1.8 \times 10^{14} M_\odot$ (although not constrained well due to its vicinity to the edge of the field) and red sequence colour redshift (cf. Section 5.4.5) of $z_l = 0.41$, the Einstein radius for plausible source redshifts is smaller by a factor of at least 1/2. Considering this, the inhomogeneity of the surface brightness of the feature and its unusual geometry, we conclude that the candidate is more likely to be a pair of interacting galaxies, yet higher resolution imaging would be needed to unambiguously explore its nature.

5.6.2 SPT-CL J0551–5709

Visual appearance

The central part of SPT-CL J0551–5709 (cf. Fig. 5.13, top panel, showing a 4×4 arcmin^2 region) is formed by three galaxies of similar brightness aligned in almost north-south direction. Clean imaging of the cluster is impaired by the nearby bright star HR 2072 of magnitude $m_V \approx 6$ at approximately 6 arcmin separation, and a large area has to be masked for the purpose of photometry and shape measurement.

Previous work

The cluster was detected in SZ by SPT (Vanderlinde et al., 2010) at a significance of $\xi = 6.13\sigma$.

Its spectroscopic redshift is given as $z = 0.423$ (Vanderlinde et al., 2010).

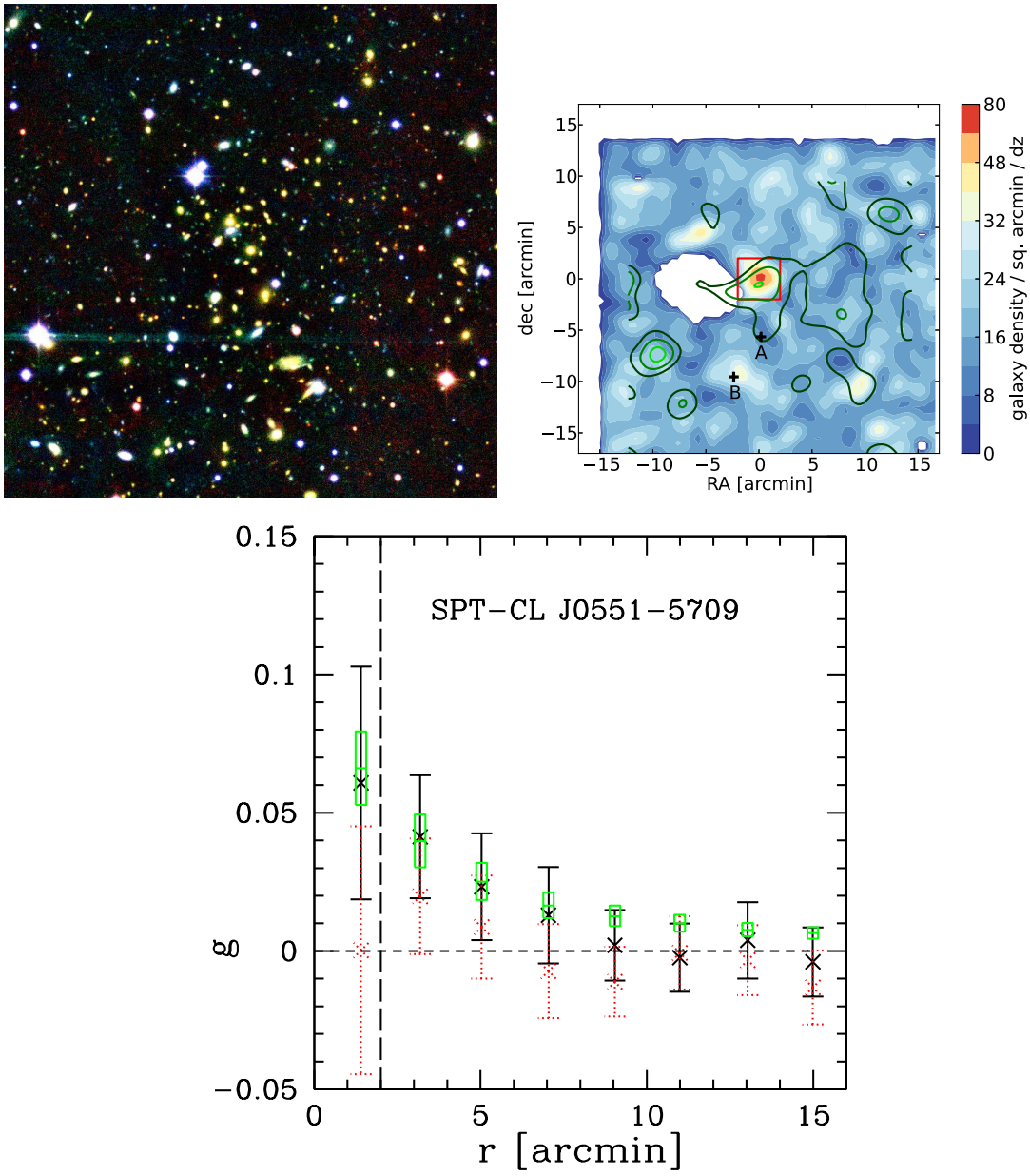

Figure 5.13: Colour image from *BRI* frames (top left panel), three-dimensional galaxy density and κ contours (top right panel) and shear profile (bottom panel) of SPT-CL J0551–5709. See Fig. 5.11 and Section 5.6.1 for details.

Using *griz* data from the Blanco Cosmology Survey and Magellan, High et al. (2010) provide an optical richness of $N_{\rm gal} = 54 \pm 15$, which they relate to a mass of $M_{200m}(N_{\rm gal}) = (5.4 \pm_{\rm stat} 3.8 \pm_{\rm sys} 1.6) \times 10^{14} h^{-1} M_\odot$.

Vanderlinde et al. (2010) give the SZ mass estimate at $M_{200m} = (4.84 \pm_{\rm stat} 1.06 \pm_{\rm sys} 0.68) \times 10^{14} h^{-1} M_\odot$. The de-biased significance according to equation (5.22) is $\zeta = 4.55$.

Andersson et al. (2011) present the first X-ray measurements SPT-CL J0551–5709 with *Chandra*. Their analysis is updated in Reichardt et al. (2013) with deeper data, finding $T = 4.0^{+0.6}_{-0.6}$keV, $M_{g,500c} = 5.1^{+0.6}_{-0.6} \times 10^{13} h^{-1}_{70.2} M_\odot$ and a corresponding $Y_{X,500c} = (1.9 \pm 0.4) \times 10^{14} h^{-1}_{70.2} M_\odot$keV. Using the MORs of Vikhlinin et al. (2009a) with mean values calibrated from local clusters under the assumption of HSE, they convert the X-ray measurements to a mass estimate of $M_{500c} = (3.4 \pm 0.4) \times 10^{14} h^{-1}_{70.2} M_\odot$.

Andersson et al. (2011) identify the cluster as a merger based on its disturbed X-ray morphology. This is consistent with the analysis of the X-ray surface brightness concentration by Semler et al. (2012), who classify the system as a non cool-core cluster with a relatively large offset of 82 ± 3kpc between BCG and X-ray centroid.

Reichardt et al. (2013) quote a combined SZ+X-ray mass of $M_{500c} = (3.82 \pm 0.54) \times 10^{14} h^{-1}_{70} M_\odot$.

The foreground cluster Abell S 552 (with lowest Abell richness class, Abell et al. 1989) lies at 5 arcmin separation from SPT-CL J0551-5709. High et al. (2010) give its photometric redshift as $z = 0.09$, the value we adopt in this analysis. Our red galaxy method (cf. Section 5.4.5) yields a consistent value of $z = 0.08$.

Weak lensing analysis

The κ mapping (Fig. 5.13, central panel) of SPT-CL J0551–5709 is made difficult by the large masked area around the bright star towards the east from the cluster. Nevertheless, a density peak is identified in the central region of the cluster, its odd shape likely being a result of the masking. The secondary κ peak in the south-eastern direction from SPT-CL J0551–5709 is associated only with a diffuse galaxy overdensity at $z \approx 0.2 \ldots 0.3$ and also noisified by a number of moderately bright stars that mask out background galaxies near the peak position.

A single halo fit, fixing the centre at the BCG and marginalizing over concentration, yields $M_{200m} = (11.7^{+5.1}_{-4.2}) \times 10^{14} h^{-1}_{70} M_\odot$ ($M_{500c} = (6.6^{+2.6}_{-2.4}) \times 10^{14} h^{-1}_{70} M_\odot$). The observed shear profile and the confidence interval of the NFW fit are shown in Fig. 5.13 (bottom panel).

When including nearby structures in a combined fit and subtracting their best-fitting NFW signal from the shear catalogue, this result is unchanged. The WL mass measurement is consistent with the combined X-ray and SZ estimate of Reichardt et al. (2013) and the SZ mass estimate at the 1σ level and with the X-ray estimate of Andersson et al. (2011) at $\approx 1.2\sigma$.

For the purpose of our WL analysis, we have set the centre to be the central cluster galaxy, even though the northern one is the most luminous of the central trio, brighter by 0.13 magnitudes in R. We test the impact of this and find that the best-fit mass at the position of the northern, brighter galaxy is lower by less than 10 per cent of the statistical error (less than 4 per cent of the mass), indicating that WL does not yield significant information on the true centring of the system, but that our off-BCG centring approach following the overall light of the brightest cluster galaxies is reasonable.

Strong lensing

We find no compelling evidence for strong lensing features in the field of SPT-CL J0551–5709.

5.6.3 SPT-CL J2332–5358

Visual appearance

SPT-CL J2332–5358 (cf. Fig. 5.14, top panel, showing a 4×4 arcmin^2 region) appears regular with a single dominant brightest cluster galaxy (BCG) and no obvious massive structures in the vicinity. The elongation of the galaxy distribution along the north-south direction is clearly visible, in accordance with the BCG orientation.

Previous work

SPT-CL J2332–5358 was discovered by SPT (Vanderlinde et al., 2010) at an SZ significance of $\xi = 7.3\sigma$. It is also identified as SCSO J233227-535827 after its optical detection by the Southern Cosmology Survey (Menanteau et al., 2010b) and associated with 1RXS J233224.3-535840, a source in the *ROSAT* bright source catalogue (Voges et al., 1999). Šuhada et al. (2010) independently discover the cluster in X-ray observations as part of the *XMM-Newton* Blanco Cosmology Survey, making the system one of the first clusters to be detected independently both by X-ray and SZ surveys.

Its redshift was initially estimated photometrically as $z = 0.32$ (High et al., 2010), but has been determined more recently spectroscopically to be $z = 0.402$ (Song et al., 2012).

Using *griz* data from the Blanco Cosmology Survey and Magellan, High et al. (2010) provide an optical richness of $N_{\rm gal} = 42 \pm 8$, which they translate to a mass of $M_{200m}(N_{\rm gal}) = (3.5 \pm 2.1 \pm 1.1) \times 10^{14} h^{-1} M_\odot$ including statistical and systematic uncertainty, although using the erroneous redshift $z = 0.32$.

An SZ mass estimate based on a significance-mass relation is given by Vanderlinde et al. (2010) as $M_{200m} = (6.21 \pm_{\rm stat} 1.15 \pm_{\rm sys} 0.94) \times 10^{14} h^{-1} M_\odot$, yet calculated at the erroneous redshift of $z = 0.32$ and with the caveat of potential blending with a radio point source. The more recent measurement of Reichardt et al. (2013) reports a higher $M_{500c} = (6.5 \pm 0.79) \times 10^{14} h_{70}^{-1} M_\odot$ at the spectroscopic redshift, which is the value we will compare to in this work. The de-biased significance according to equation (5.23) is $\zeta = 9.91$, which yields $M_{200m} = (12.1 \pm 1.4) \times 10^{14} h_{70}^{-1} M_\odot$ by means of equation (5.22).

X-ray imaging of the cluster exists from *XMM-Newton*, analysed by Šuhada et al. (2010) and Andersson et al. (2011) at the erroneous photometric redshift of $z = 0.32$. The analysis is repeated by Benson et al. (2013) for the correct redshift. They find a temperature of $T = 7.8^{+1.0}_{-0.9}$keV, a gas mass of $M_{g,500c} = 7.6^{+0.2}_{-0.3} \times 10^{13} h_{70.2}^{-1} M_\odot$ and a corresponding $Y_{X,500c} = (6.1 \pm 0.8) \times 10^{14} h_{70.2}^{-1} M_\odot$keV. Using the MORs of Vikhlinin et al. (2009a) with mean values calibrated from local clusters under the assumption of HSE, they convert the X-ray measurements to a mass estimate of $M_{500c} = (6.7 \pm 0.5) \times 10^{14} h_{70.2}^{-1} M_\odot$.

Andersson et al. (2011) characterize the cluster as relaxed based on its X-ray morphology.

The combined SZ+X-ray mass estimate of Reichardt et al. (2013) is $M_{500c} = (6.54 \pm 0.82) \times 10^{14} h_{70}^{-1} M_\odot$.

Greve et al. (2012) describe a candidate strongly lensed sub-mm galaxy with multiple images at approximately 0.5 arcmin separation from the cluster centre with a spectroscopic redshift of $z = 2.7$.

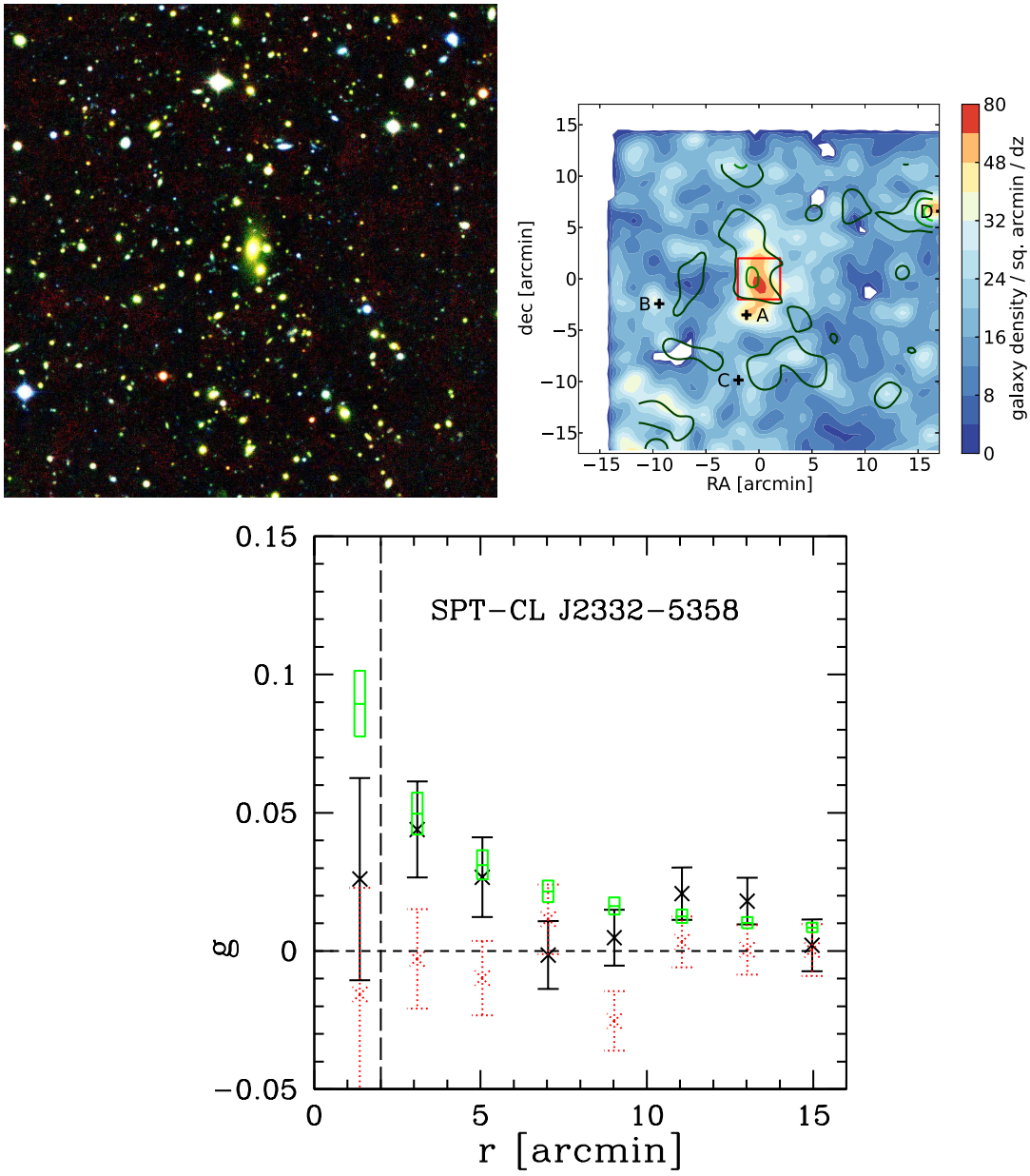

Figure 5.14: Colour image from *BRI* frames (top left panel), three-dimensional galaxy density and κ contours (top right panel) and shear profile (bottom panel) of SPT-CL J2332–5358. See Fig. 5.11 and Section 5.6.1 for details.

The nearby system SCSO J233231.4-540135.8 at $\theta \approx 4$ arcmin separation is a cluster of galaxies optically discovered by Menanteau et al. (2009), at a photometric redshift of $z = 0.33$. Using the relation of Reyes et al. (2008), they calculate mass estimates based on a combination of BCG luminosity and either richness or total luminosity of $M_{200m} = 4.1 \times 10^{14} h_{70}^{-1} M_\odot$ and $M_{200m} = 1.7 \times 10^{14} h_{70}^{-1} M_\odot$, respectively.

Weak lensing analysis

The κ map (Fig. 5.14, central panel) shows that the cluster is elongated along the north-south axis, aligned with the BCG ellipticity. An overdensity of galaxies at an estimated $z \approx 0.24$, 18 arcmin from the BCG at the western edge of the field, is associated with a clear peak in κ and included in the multi-halo fit (see below).

A single halo fit, fixing the centre at the BCG and marginalizing over concentration, yields $M_{200m} = (14.5^{+4.0}_{-3.5}) \times 10^{14} h_{70}^{-1} M_\odot$ ($M_{500c} = (7.5^{+1.8}_{-1.7}) \times 10^{14} h_{70}^{-1} M_\odot$). The observed shear profile and the confidence interval of the NFW fit are shown in Fig. 5.14 (bottom panel).

When including nearby structures in a combined fit and subtracting their best-fitting NFW signal from the shear catalogue, a repeated fit of the central halo yields a slightly higher $M_{200m} = (15.3^{+4.2}_{-3.6}) \times 10^{14} h_{70}^{-1} M_\odot$ ($M_{500c} = (7.9^{+1.8}_{-1.7}) \times 10^{14} h_{70}^{-1} M_\odot$).

Both results are mildly higher than the SPT SZ mass estimate of Vanderlinde et al. (2010) at $\approx 1.5\sigma$, yet in good agreement with the X-ray, SZ and combined mass estimate of Reichardt et al. (2013).

Strong lensing

We find several small blue background sources in the south-east and south-west from the BCG. It is unclear from our data whether any of these are multiply imaged or correspond to the strongly lensed system discovered by Greve et al. (2012).

5.6.4 SPT-CL J2355–5056

Visual appearance

The central part of SPT-CL J2355–5056 (cf. Fig. 5.15, upper panel, showing a 17×6 arcmin^2 region) features a single large and diffuse BCG. However, the cluster is neighboured by structures towards the East and est at separations of 3-4 arcmin, which from visual inspection seem to have similar red galaxy colours and thus redshifts. There is no indication for the neighbouring structures from the archival *Chandra* X-ray data, although the field of view is not large enough for a conclusive statement.

Previous work

SPT-CL J2355–5056 is discovered by SPT (Vanderlinde et al., 2010) at a significance of 5.89σ.

Song et al. (2012) and Reichardt et al. (2013) provide a spectroscopic redshift of 0.3196, correcting the previous photometric estimate of 0.35 (High et al., 2010).

Using *griz* data from the Blanco Cosmology Survey and Magellan, High et al. (2010) provide an optical richness of $N_{\rm gal} = 55 \pm 5$, on which they base a mass estimate of $M_{200m}(N_{\rm gal}) = (5.6 \pm 3.0 \pm 1.7) \times 10^{14} h^{-1} M_\odot$ when assuming the slightly erroneous redshift of $z = 0.35$.

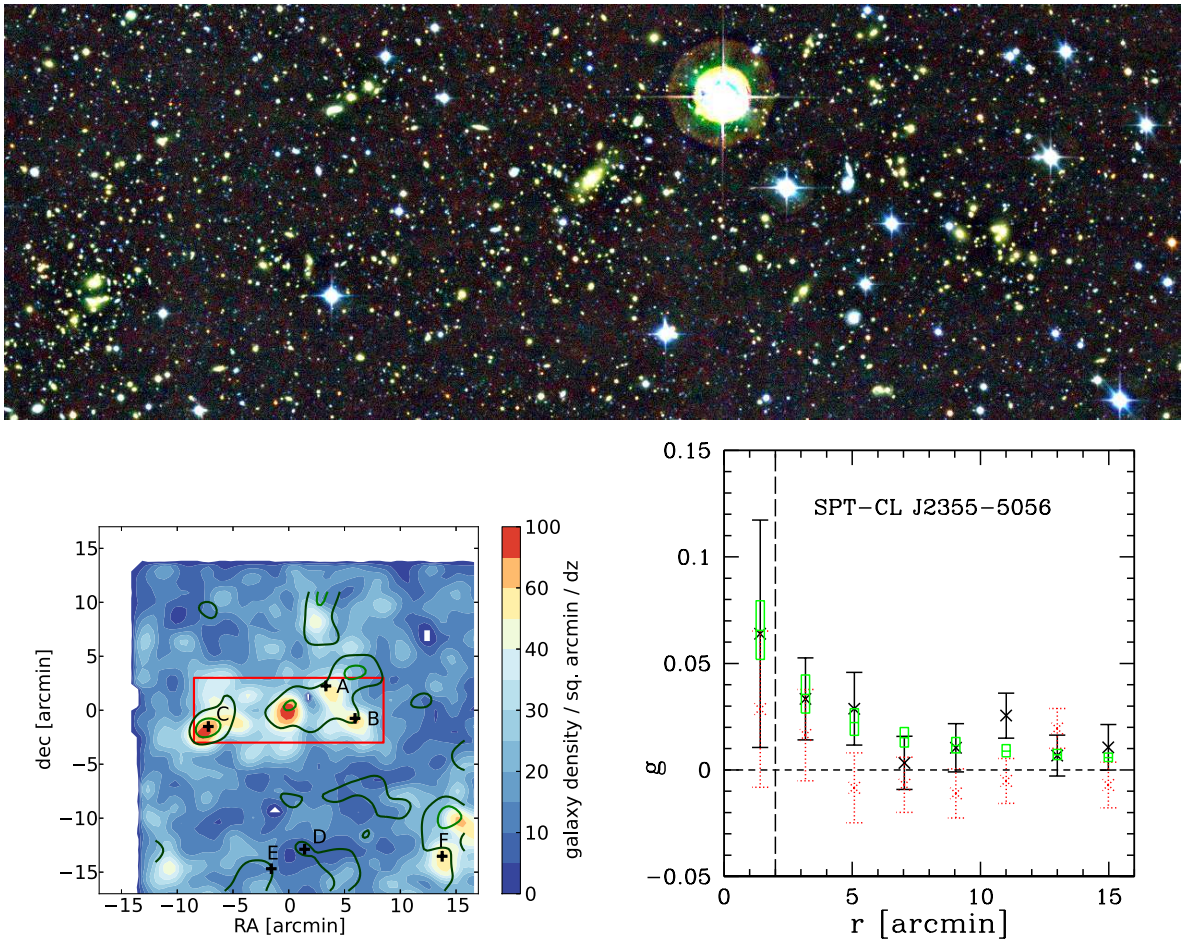

Figure 5.15: Colour image from *BRI* frames of the central 17×6 arcmin region (top panel), three-dimensional galaxy density and κ contours (bottom left panel) and shear profile (bottom right panel) of SPT-CL J2355–5056. See Fig. 5.11 and Section 5.6.1 for details.

An SZ mass estimate is given by Vanderlinde et al. (2010), yet at the erroneous $z = 0.35$. The more recent measurement of Reichardt et al. (2013) reports $M_{500c} = (4.07 \pm 0.57) \times 10^{14} h_{70}^{-1} M_\odot$ at the spectroscopic redshift, which is the value we will compare to in this work. The de-biased significance according to equation (5.23) is $\zeta = 5.12$, which yields $M_{200m} = (7.6 \pm 1.0) \times 10^{14} h_{70}^{-1} M_\odot$ by means of equation (5.22).

Andersson et al. (2011) present the first X-ray measurements SPT-CL J2355–5056 with *Chandra*. Their analysis is updated in Reichardt et al. (2013) for the corrected redshift, finding $T = 5.3^{+0.9}_{-0.7}$keV, $M_{g,500c} = 3.9^{+0.2}_{-0.1} \times 10^{13} h_{70.2}^{-1} M_\odot$ and a corresponding $Y_{X,500c} = (2.2 \pm 0.4) \times 10^{14} h_{70.2}^{-1} M_\odot$keV. Using the MORs of Vikhlinin et al. (2009a) with mean values calibrated from local clusters under the assumption of HSE, they convert the X-ray measurements to a mass estimate of $M_{500c} = (3.8 \pm 0.4) \times 10^{14} h_{70.2}^{-1} M_\odot$.

Andersson et al. (2011) report the cluster to be relaxed based on its X-ray morphology, likely with a cool core. Semler et al. (2012) consistently classify the system as a cool core cluster, with a relatively small offset of 6.7 ± 2.3kpc between BCG and X-ray centroid.

Reichardt et al. (2013) quote, using the spectroscopic redshift, a combined SZ+X-ray mass of $M_{500c} = (4.11 \pm 0.54) \times 10^{14} h_{70}^{-1} M_\odot$.

The APM Galaxy Survey (Dalton et al., 1997) lists the cluster APMCC 936 at $(\alpha, \delta) = (23^{\mathrm{h}}53^{\mathrm{m}}21.5^{\mathrm{s}}, -51°26'57'')$, ≈ 14 arcmin separated from SPT-CL J2355–5056. They estimate its redshift at $z = 0.118$ with a richness of $R = 61.6$.

Weak lensing analysis

The κ map (Fig. 5.15, central panel) nicely maps the complex structure of the multiple components in the field of SPT-CL J2355–5056. Aside the central region, the galaxy peak near the south-western corner of the field is associated with a κ overdensity and red galaxy population at $z \approx 0.42$, included as a component in the multi-halo fit (see below).

A single halo fit, fixing the centre at the BCG and marginalizing over concentration, yields $M_{200m} = (8.0^{+3.7}_{-3.1}) \times 10^{14} h_{70}^{-1} M_\odot$ ($M_{500c} = (4.1^{+1.7}_{-1.5}) \times 10^{14} h_{70}^{-1} M_\odot$). The observed shear profile and the confidence interval of the NFW fit are shown in Fig. 5.15 (lower right panel).

When including nearby structures in a combined fit and subtracting their best-fitting NFW signal from the shear catalogue, a repeated fit of the central halo yields a significantly lower $M_{200m} = (3.8^{+2.4}_{-2.0}) \times 10^{14} h_{70}^{-1} M_\odot$ ($M_{500c} = (2.1^{+1.4}_{-1.1}) \times 10^{14} h_{70}^{-1} M_\odot$). In return, significant mass is attributed to the eastern peak ≈ 7 arcmin from the BCG ($M_{200m} = (4.5^{+1.7}_{-1.7}) \times 10^{14} h_{70}^{-1} M_\odot$ at $z \approx 0.24$) and a northern and southern component of the western peak ($M_{200m} = (1.2^{+1.7}_{-1.2}) \times 10^{14} h_{70}^{-1} M_\odot$ and $M_{200m} = (6.7^{+3.0}_{-2.1}) \times 10^{14} h_{70}^{-1} M_\odot$ at redshifts consistent with the central cluster, respectively).

The single-peak analysis is consistent with the X-ray, SZ and combined result of Reichardt et al. (2013), while the WL result with neighbouring structures subtracted is 1σ below. The large uncertainty in the WL analysis of this complex system allows for no significant conclusions on the effect of blending on the SZ analysis. Yet we note that the structure of the cluster warrants deeper follow-up, since the interplay of cluster gas and dark matter might be interesting.

Strong lensing

Apart from inconclusive arc-like features around the BCG, two candidate strong lensing features can be seen towards the east. One is a potential arc at a separation of $\theta \approx 20.6$ arcsec

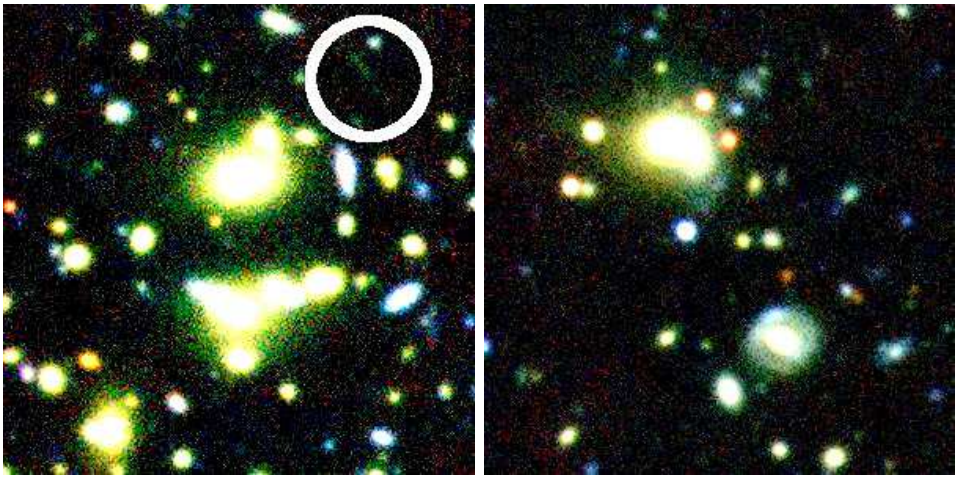

Figure 5.16: Colour images of strong lensing candidates in the field of SPT-CL J2355–5056. Left panel is centred at $(\alpha, \delta) = (23^{\mathrm{h}}56^{\mathrm{m}}33.1^{\mathrm{s}}, -50°57'20'')$, right panel is centred at $(\alpha, \delta) = (23^{\mathrm{h}}56^{\mathrm{m}}30.4^{\mathrm{s}}, -50°53'08'')$, both are 1×1 arcmin^2 in size.

from the main galaxy of the eastern structure ≈ 7 arcmin from the centre of the field (left panel of Fig. 5.16). The other is composed of a blue symmetric ring with radius $\theta \approx 3.3$ arcsec around a red galaxy and a bluish structure blended with two red foreground galaxies close in projection (right panel of Fig. 5.16). Both features are at unexpectedly large radii given the likely mass of the lenses, and deeper follow-up observations at higher resolution would be required to confirm their strong lensing nature.

5.6.5 PLCKESZ G287.0+32.9

Visual appearance

PLCKESZ G287.0+32.9 features a large number of cluster member galaxies, with a clear brightest galaxy in the centre and numerous gravitational arcs visible near cluster members at arcminute separations from the core (cf. Section 5.6.5). Fig. 5.17 shows a *VRI* colour image, using the single V band frame available.

Previous work

The cluster was discovered by its SZ signal, detected by Planck (Planck Collaboration et al., 2011a) at a significance of 10.62σ.

A redshift estimate is given by Planck Collaboration et al. (2011c) at $z = 0.39$, although based on X-ray emission lines and therefore not of optimal confidence.

The cluster is followed-up with X-ray observations with *XMM-Newton*. The Planck Collaboration et al. (2011c) find from these data a temperature of $T = (12.86 \pm 0.42)$keV, $M_{g,500c} = (2.39 \pm 0.03) \times 10^{14} h_{70}^{-1} M_\odot$ and a corresponding $Y_{X,500c} = (30.69 \pm 0.36) \times 10^{14} h_{70}^{-1} M_\odot$keV. From a Y_X MOR calibrated with relaxed objects under the assumption of HSE (Arnaud et al., 2010), they calculate a mass of $M_{500c} = (15.72 \pm 0.27) \times 10^{14} h_{70}^{-1} M_\odot$.

Bagchi et al. (2011) investigate non-thermal radio emission from the cluster. They find a double radio relic, which is an indication of a major merger. Notably, the double relic has a projected separation of over 4 Mpc, the largest found to date at a redshift as high as

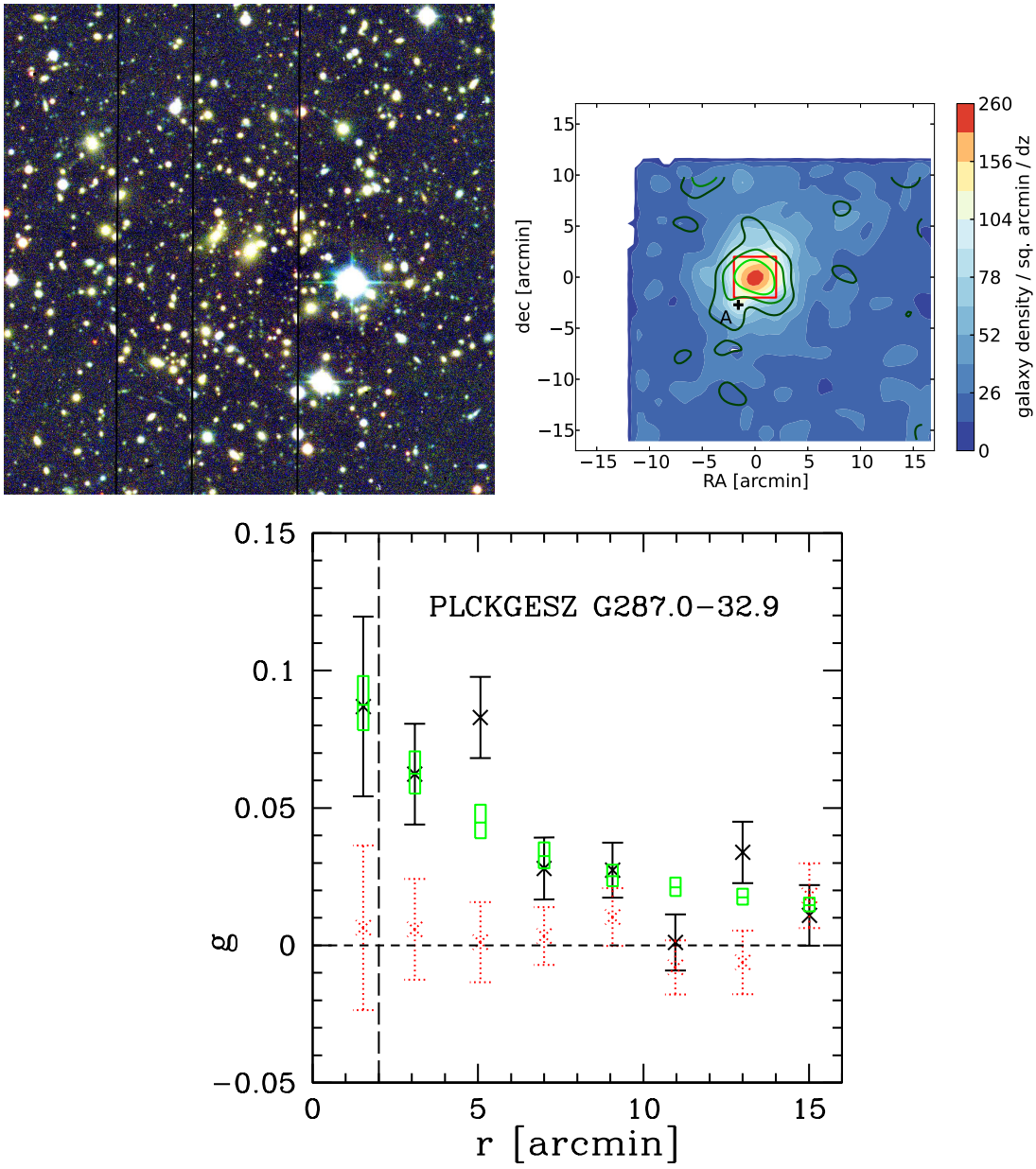

Figure 5.17: Colour image (top left panel), galaxy density weighted with $P_{\rm cl}$ (cf. Section 5.3.1) and κ contours (top right panel) and shear profile (bottom panel) of PLCKESZ G287.0+32.9. See Fig. 5.11 and Section 5.6.1 for details.

$z = 0.39$ (Bagchi et al., 2011). They characterize the X-ray morphology based on the same *XMM-Newton* that is used by Planck Collaboration et al. (2011c) as disturbed, consistent with the merger hypothesis. They find the X-ray peak to be separated from the BCG by a large distance of 410 kpc.

From the catalogued SZ likelihood of Planck Collaboration et al. (2014a) we calculate mass estimates using the X-ray θ_{500} as a fixed size and the self-consistency method as $M_{500c} = 17.7^{+0.8}_{-0.9} \times 10^{14}$ and $18.2^{+0.9}_{-1.0} \times 10^{14} h_{70}^{-1} M_\odot$, respectively.

Weak lensing analysis

The κ map (Fig. 5.17, central panel) is dominated by the central peak, which has symmetric appearance and a central value of $\kappa = 0.22$.

A single halo fit, fixing the centre at the BCG and marginalizing over concentration, yields $M_{200m} = (37.7^{+9.5}_{-7.6}) \times 10^{14} h_{70}^{-1} M_\odot$ ($M_{500c} = (19.5^{+3.3}_{-3.2}) \times 10^{14} h_{70}^{-1} M_\odot$). The observed shear profile and the confidence interval of the NFW fit are shown in Fig. 5.17 (bottom panel).

We note that the excess shear at 5 arcmin radius is potentially due to the added mass from the structure A in Fig. 5.17 at that projected separation. Subtracting the maximum likelihood signal of structure A from a combined fit, the resulting mass is slightly lower at $M_{200m} = (35.4^{+8.9}_{-7.1}) \times 10^{14} h_{70}^{-1} M_\odot$ ($M_{500c} = (18.7^{+3.2}_{-3.1}) \times 10^{14} h_{70}^{-1} M_\odot$).

We note that both results are consistent with previous X-ray observations (Planck Collaboration et al., 2011c) and the Planck-based SZ mass estimate (Planck Collaboration et al. 2014a; this work).

Strong lensing

The central region of PLCKESZ G287.0+32.9 shows several arc-like features, marked in the enlarged view in Fig. 5.18. Candidate features can be found over a large region, the two most separated ones $2\theta \approx 165$ arcsec apart. Even at the 68% upper limit of the NFW fit and for a hypothetical source redshift of $z_s = 5$, the predicted Einstein radius is only $\theta_E \approx 37$ arcsec, although a larger than mean concentration can increase this value considerably. It is the most likely explanation that the features seen are therefore either not actual multiple images or caused by the particular geometry of the system and its subcomponents (e.g. a major merger as indicated by the radio signature, cf. Bagchi et al. 2011). Despite this, the unusual constellation merits follow-up with spectroscopy and higher-quality imaging, since it would, if confirmed, make PLCKESZ G287.0+32.9 potentially the largest strong lens known to date and a candidate for the largest strong lens in the Universe, with some tension with ΛCDM (cf. Medezinski et al. 2013, who find MACS J0717.5+3745 at $\theta_E \approx 55$ arcsec for $z_s \approx 3$ and Oguri & Blandford 2009, Waizmann et al. 2012, and Redlich et al. 2012).

5.6.6 PLCKESZ G292.5+22.0

Visual appearance

PLCKESZ G292.5+22.0 has a central region dominated by the brightest cluster galaxy (cf. Fig 5.19), with a highly magnified strongly gravitationally lensed image of a background galaxy between it and a bright galaxy towards the southern direction.

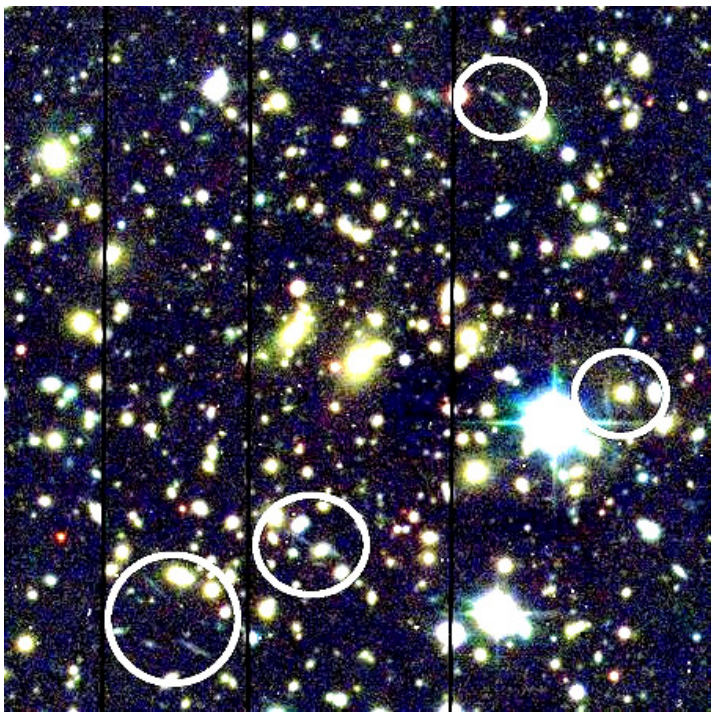

Figure 5.18: Colour image of centre of PLCKESZ G287.0+32.9, arc candidates marked with circles. The cutout size is 3×3 arcmin^2, making this an exceedingly large region for strong lensing features even for a massive cluster.

Previous work

This cluster was discovered by its SZ signal, detected by Planck Collaboration et al. (2011a) at a significance of 6.88σ.

Planck Collaboration et al. (2011c, 2012) provide a redshift of $z = 0.31$ using X-ray spectral fitting and of $z = 0.29$ from V-, R- and I-band optical photometry. In this paper we adopt $z = 0.30$, noting that spectroscopic confirmation would benefit the analysis.

The cluster is followed-up with X-ray observations with *XMM-Newton*. The Planck Collaboration et al. (2011c) find from these data a temperature of $T = (9.82 \pm 0.84)$keV, $M_{g,500c} = (1.17 \pm 0.04) \times 10^{14} h_{70}^{-1} M_\odot$ and a corresponding $Y_{X,500c} = (11.49 \pm 1.33) \times 10^{14} h_{70}^{-1} M_\odot$keV. From a Y_X MOR calibrated with relaxed objects under the assumption of HSE (Arnaud et al., 2010), they calculate a mass of $M_{500c} = (9.25 \pm 0.60) \times 10^{14} h_{70}^{-1} M_\odot$.

The Planck Collaboration et al. (2011c) report the cluster to have a disturbed X-ray morphology.

From the catalogued SZ likelihood of Planck Collaboration et al. (2014a) we calculate mass estimates using the X-ray θ_{500} as a fixed size and the self-consistency method as $M_{500c} = 10.3^{+0.9}_{-1.0} \times 10^{14}$ and $10.6^{+1.1}_{-1.0} \times 10^{14} h_{70}^{-1} M_\odot$, respectively.

Weak lensing analysis

Our κ map of PLCKESZ G292.5+22.0 shows a rather complex structure. The central peak is not as strong as a second structure towards the north. The latter is approximately centred on a diffuse galaxy $\Delta m_R = 0.98$ brighter than the BCG of PLCKESZ G292.5+22.0 and at a

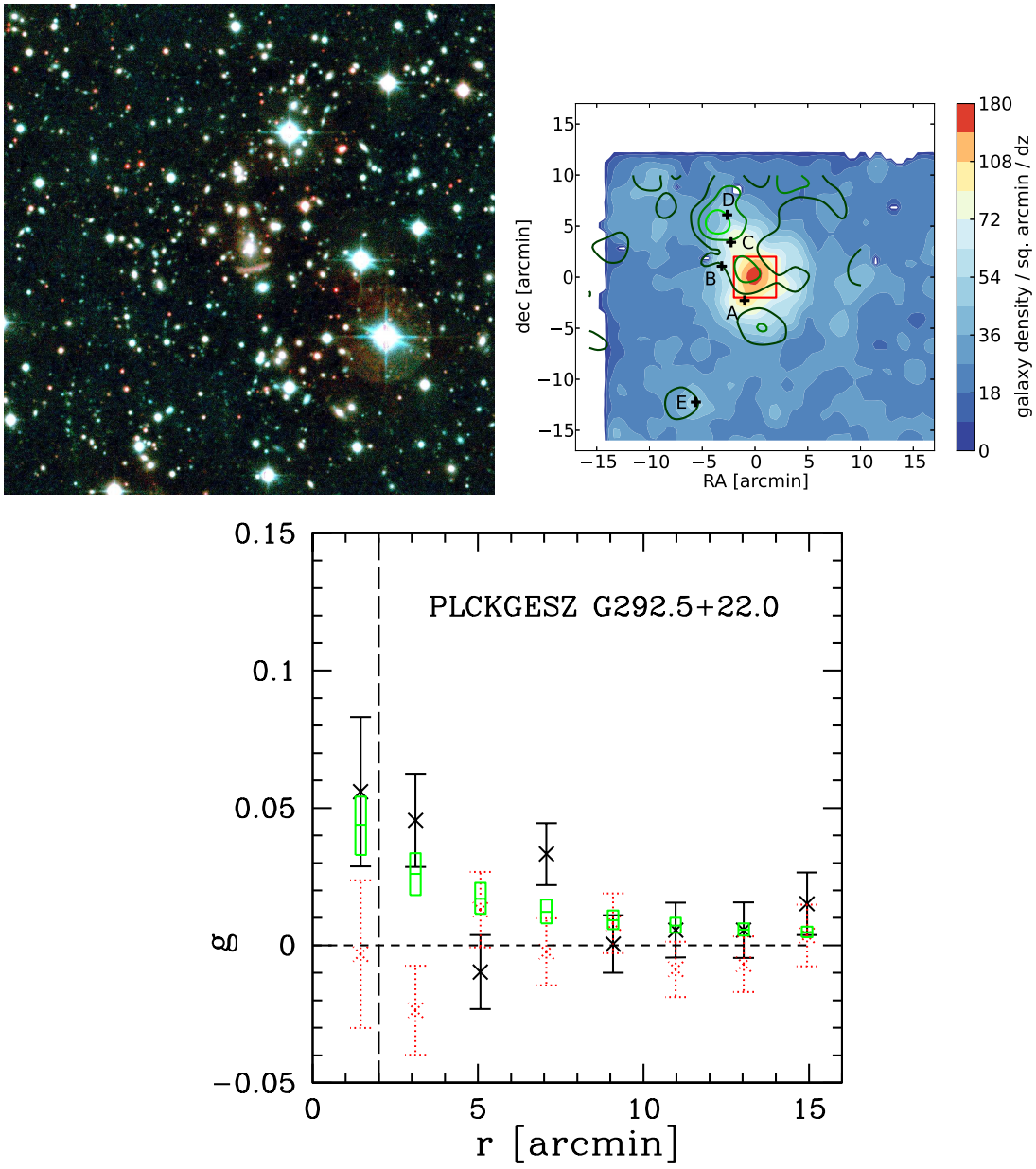

Figure 5.19: Single colour image from *RI* frames (top left panel), galaxy density weighted with $P_{\rm cl}$ (cf. Section 5.3.1) and κ contours (top right panel) and shear profile (bottom panel) of PLCKESZ G292.5+22.0. See Fig. 5.11 and Section 5.6.1 for details.

redshift that is indiscriminable based on the R-I colour.

The shear profile (Fig. 5.19, bottom panel) has clear signs of this structure, the dip in tangential shear at 5 arcmin and counter-excess at 7 arcmin indicating that an overdensity is present at ≈ 5 arcmin projected separation from the BCG.

A single halo fit, fixing the centre at the BCG and marginalizing over concentration, yields $M_{200m} = (6.8^{+3.8}_{-3.0}) \times 10^{14} h_{70}^{-1} M_\odot$ ($M_{500c} = (3.4^{+1.7}_{-1.4}) \times 10^{14} h_{70}^{-1} M_\odot$). The observed shear profile and the confidence interval of the NFW fit are shown in Fig. 5.19 (bottom panel).

The best-fitting mass is reduced considerably when modelling multiple nearby structures. We then find $M_{200m} = (5.0^{+3.1}_{-2.5}) \times 10^{14} h_{70}^{-1} M_\odot$ ($M_{500c} = (2.7^{+1.5}_{-1.3}) \times 10^{14} h_{70}^{-1} M_\odot$). Two structures (D and E) are assigned masses of close to $M_{200m} = 10^{15} h_{70}^{-1} M_\odot$ in this combined analysis. Their influence is seen from the tangential shear profile (Fig. 5.19, bottom panel) as a low outlier around 5 arcmin (and a high outlier at 7 arcmin) radius, where the BCG-centred overdensity is decreased (increased) by matter on the edge of (inside) the respective annulus.

We hypothesize that this vicinity of other massive structures might be the reason for the $\approx 4\sigma$ discrepancy between our mass estimate and the X-ray and SZ results.

Strong lensing

There is one more interesting feature in the field of PLCKESZ G292.5+22.0 beside the strongly magnified image of a background galaxy lensed between the BCG and another bright foreground galaxy (see Fig. 5.19). This other feature is a symmetric ring around a red galaxy (R-I colour of 0.59, redshift not well constrained by this particular colour but consistent with the cluster redshift) with bluer colour (R-$I \approx 0.3$) at a radius of $\theta \approx 4$ arcsec (see Fig. 5.20). The WL analysis shows no significantly massive halo centred at this position, making it doubtable whether the feature is a star-forming physically associated ring or indeed lensed. However, the lensing strength of the red galaxy could also be boosted by the projected dark matter density of the surrounding cluster haloes sufficiently to allow for such a large Einstein radius.

5.6.7 MACS J0416.1–2403

Visual appearance

A view of the central part of MACS J0416.1–2403 (cf. Fig 5.21) reveals its highly elongated shape, with a chain of bright cluster member galaxies along the north-east to south-western direction. Several strong lensing features are visible.

Previous work

This cluster was discovered in the *ROSAT* All-Sky survey as a bright source 1RXS J041609.9–240358 (Voges et al., 1999). Postman et al. (2012) estimate its redshift from the *Chandra* X-ray spectrum as $z = 0.42 \pm 0.02$. Ebeling et al. (2014) provide spectroscopy for 65 galaxies in the field of MACS J0416.1–2403 and determine the cluster redshift as $z = 0.397$, the value we use in this work.

Sayers et al. (2013) analyse *Chandra* X-ray data for the cluster and find a mass of $M_{500c} = (9.1 \pm 2.0) \times 10^{14} h_{70}^{-1} M_\odot$, assuming a redshift of $z = 0.42$. They determine this value from the gas mass of $M_{g,500c} = (1.05 \pm 0.23) \times 10^{14} h_{70}^{-1} M_\odot$ with $f_{\mathrm{gas},500c} = 0.115$ in analogy to Mantz et al. (2010a).

Figure 5.20: *R-I* colour image of the candidate galaxy lens in the field of PLCKESZ G292.5+22.0. The cutout size is 0.5×0.5 arcmin^2, centred on $(\alpha, \delta) = (12^{\mathrm{h}}01^{\mathrm{m}}21.8^{\mathrm{s}}, -39°51'22'')$ (position B in Fig. 5.19).

The cluster is covered by the CLASH project (Postman et al., 2012) as part of the high magnification sample. Zitrin et al. (2013) find a highly elongated ($\approx 5:1$) critical area with extraordinarily high density of multiple images. The system has also been selected as an *HST* Frontier Field.

MACS J0416.1–2403 is not listed in the Planck Collaboration et al. (2014a) SZ catalogue and therefore below the 4.5σ detection significance limit in the Planck SZ map.

Weak lensing analysis

Our κ map of MACS J0416.1–2403 (see Fig. 5.21, central panel) shows a strong elongation of the matter density along the north-east to south-western direction, in line with the galaxy density and the strong lensing model of Zitrin et al. (2013). The distribution of galaxies near the cluster redshift in the overall field shows higher density in the south-western quadrant, consistent with the numerous small mass peaks detected in this region. Both observations are in line with the hypothesis of MACS J0416.1–2403 being located at the crossing point of two filaments running in a north-south and a north-east to south-west direction.

The centre of MACS J0416.1–2403 is ambiguous, with the two brightest galaxies differing in magnitude by only 0.02. Setting the centre of the system at the midpoint between the two brightest cluster galaxies as proposed by Zitrin et al. (2013) yields a best-fitting mass for the single halo analysis at $M_{200m} = (9.4^{+2.7}_{-2.5}) \times 10^{14} h_{70}^{-1} M_\odot$ ($M_{500c} = (5.5^{+1.5}_{-1.4}) \times 10^{14} h_{70}^{-1} M_\odot$), marginalizing over concentration. The observed shear profile and the confidence interval of the NFW fit are shown in Fig. 5.21 (bottom panel).

For comparison, we perform a single halo fit fixing the centre at the marginally brighter north eastern galaxy. This yields a consistent mass, yet the shear in the most central bin, which is excluded from the fit, at this position is significantly lower, indicating that the BCG is indeed slightly off-centred from the mass peak.

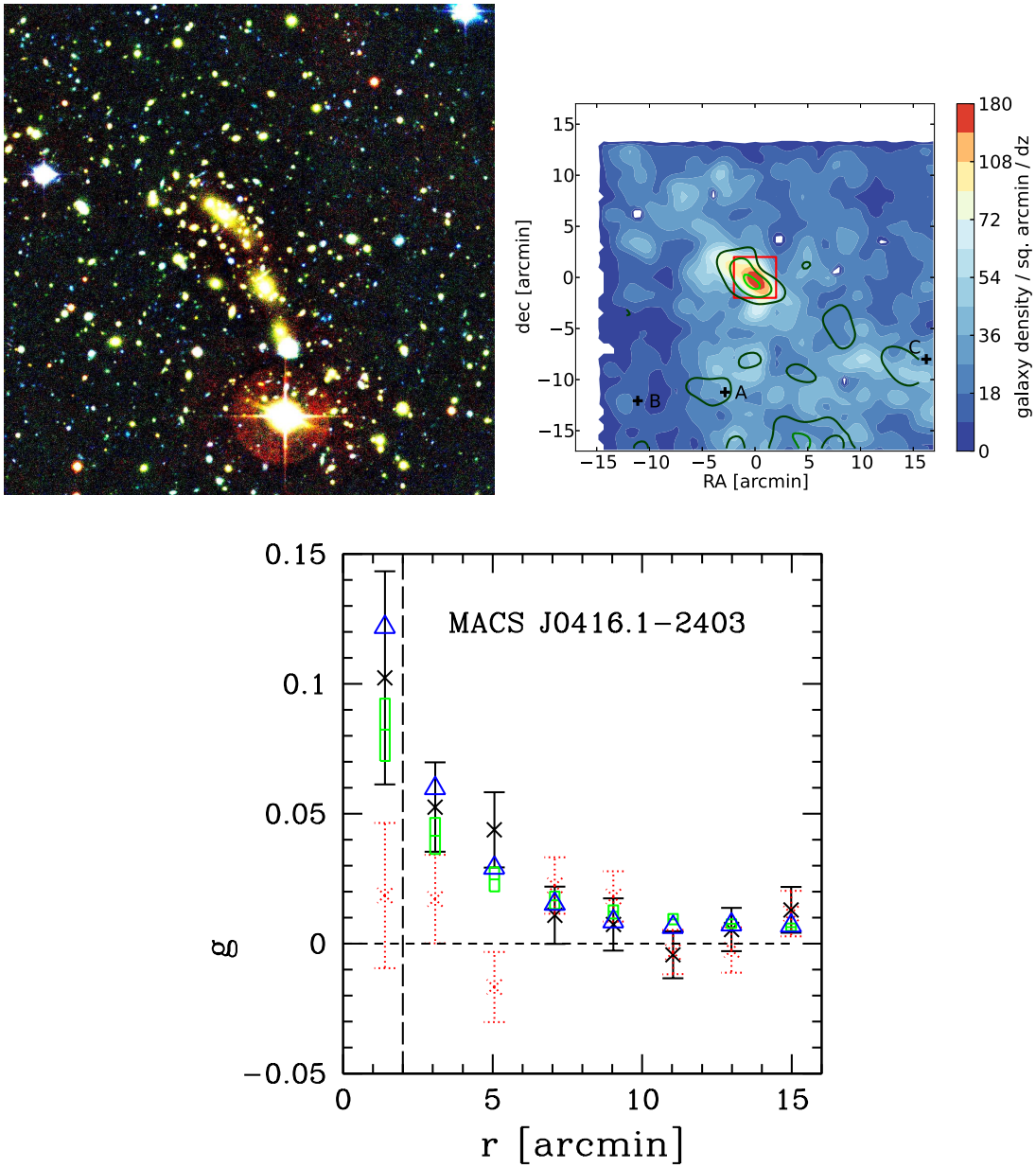

Figure 5.21: Colour image from *BRI* frames (top left panel), three-dimensional galaxy density and κ contours (top right panel) and shear profile (bottom panel) of MACS J0416.1–2403. The latter includes the prediction of tangential shear (blue triangles) from the SL+WL density profile of Zitrin et al. (2013, their Fig. 2). See Fig. 5.11 and Section 5.6.1 for details.

Subtraction of the maximum-likelihood profiles of neighbouring structures determined in a combined fit yields a slightly larger best-fitting mass of $M_{200m} = (9.8^{+2.8}_{-2.5}) \times 10^{14} h_{70}^{-1} M_\odot$ ($M_{500c} = (5.9^{+1.5}_{-1.5}) \times 10^{14} h_{70}^{-1} M_\odot$) *(updated)*.

Both of these estimates are below the X-ray measurement at $\approx 1.5\sigma$. This is less of a tension since it is to be expected that both X-ray estimate and spherical WL model fit are significantly influenced by the disturbed morphology of the system in the direction of the observed discrepancy and the X-ray analysis uses a slightly higher value for the cluster redshift.

Strong lensing

MACS J0416.1–2403 is a known prominent strong lensing system, with several of the known multiple images also visible from our data. Thanks to the availability of deeper *HST* and *Subaru* data from the CLASH survey, we can compare our shear measurement with the predicted shear from the Zitrin et al. (2013) projected density profile based on a combined weak and strong lensing analysis (blue triangles in Fig. 5.21, bottom panel). We find our shear measurements to be in good agreement with their model. Both our measurement and the Zitrin et al. (2013) model exceed the shear in the central region as predicted by the NFW fit (green). Since the latter is drawn with fixed concentration according to the Duffy et al. (2008) mass-concentration relation, this shows that the concentration of MACS J0416.1–2403 is indeed higher than average. Note that our mass measurement, however, is not based on the fixed concentration profile drawn here for illustration purposes, but rather marginalizes over concentration with a prior motivated from simulations (Bullock et al., 2001).

Non-Detection in Planck

Since MACS J0416.1–2403 is a large and highly magnifying gravitational lens, selected as such in the CLASH survey (Zitrin et al., 2013), the question is whether its non-detection in the Planck SZ catalogue is in line with expectations. We make a rough estimate of detection probability given the result of the WL analysis here.

MACS J0416.1–2403 is situated 44° away from the Galactic plane, in a region of expected average noise levels of the Planck SZ map. At the θ_{500c} corresponding to its best-fitting mass of $\theta_{500c} \approx 3$ arcmin, the Monte Carlo analysis of Planck Collaboration et al. (2014a, cf. their fig. 9) suggests 50% completeness at a Compton parameter of $Y_{500} \approx 6 \times 10^{-4}$ arcmin^2. This corresponds, in turn, to a mass of $M_{500c} \approx 7 \times 10^{14} h_{70}^{-1} M_\odot$, above the observed mass of the cluster. We therefore conclude there is no tension with either the Planck calibrations or our WL model, since both the SZ-detection and non-detection of MACS J0416.1–2403 are possible at the mass reconstructed from the shear. The non-detection of this relatively high-redshift system, however, is also made even more likely if there is a yet unaccounted for redshift dependence of the Planck SZ MOR (cf. Section 5.7.4).

5.6.8 SPT-CL J2248–4431

We refer the reader to the detailed WL analysis of the system by Gruen et al. (2013). Here, the system is only used as part of the combined analysis and our results are compared to the Planck results released after this study.

Comparison with SZ data

The de-biased significance for SPT at full depth is calculated as $\zeta = 32.8$, assuming the mass estimate of Williamson et al. (2011) and equation (5.22). Note that this is the de-biased significance at full SPT depth, while in fact Williamson et al. (2011) present the cluster based on less deep SPT observations (and consequently with lower measured significance).

Using the X-ray mass estimate of $M_{500c} = (12.6 \pm 0.2) \times 10^{14} h_{70}^{-1} M_\odot$ from Planck Collaboration et al. (2011b) as a fixed size prior and, alternatively, the self-consistency method, we determine the SZ mass estimate for the system at $M_{500c} = (14.5^{+0.7}_{-0.7}) \times 10^{14} h_{70}^{-1} M_\odot$ and $M_{500c} = (14.8^{+0.8}_{-0.8}) \times 10^{14} h_{70}^{-1} M_\odot$, respectively. We note that this result is $\approx 20\%$ higher than the previous estimate based on the early SZ catalogue in Gruen et al. (2013), due to the changed MOR which includes a hydrostatic bias of $(1 - b) = 0.8$. It is still consistent with the previous WL result. The substructure-subtracted WL result is lower than the SZ mass estimate by 1.5σ (1.8σ for the self-consistent method), consistent with the hypothesis that the substructure at $\theta = 3.5$ arcmin separation is blended with the main cluster in the Planck SZ signal or that the hydrostatic mass bias assumed in the Planck MOR is not correct in the case of this system.

Strong lensing

SPT-CL J2248–4431 is a prominent strong lensing system with several known arcs also visible in our data. Our lensing mass reconstruction has recently been compared with the strong lensing model of Monna et al. (2014), two independent CLASH re-analyses of the WFI data, which include magnification and strong lensing in addition to shear (Merten et al. 2014 and Umetsu et al. 2014) and a WL analysis of Dark Energy Survey science verification data (Melchior et al., 2014), in all cases with consistent mass estimates.

5.6.9 PSZ1 G168.02–59.95

Visual appearance

The central region of PSZ1 G168.02–59.95 is shown in Fig. 5.22, on a cutout size of 8×8 arcmin due to the smaller distance to the system. One can see the complex and disturbed structure of the bright central galaxy. The three-dimensional density is difficult to interpret due to the large masked area around a number of bright stars.

Previous work

PSZ1 G168.02–59.95 was first discovered by Abell (1958) and classified at the second-lowest of six richness classes.

Based on a magnitude-redshift relation, Quintana et al. (2000) give a redshift estimate of $z = 0.141$. The value adopted here is the spectroscopic $z = 0.1456$ from Mirkazemi et al. (2015), based on four cluster member galaxies.

The cluster is serendipitously discovered by the RASS as RXC J0214.6–0433 (Cruddace et al., 2002). Based on its X-ray luminosity and temperature in the *XMM* Cluster Survey, Viana et al. (2012) estimate the probability of detecting the system by its SZ signal in Planck to be 76 per cent. The system is also part of the CFHT X-ray cluster sample of Mirkazemi et al. (2015).

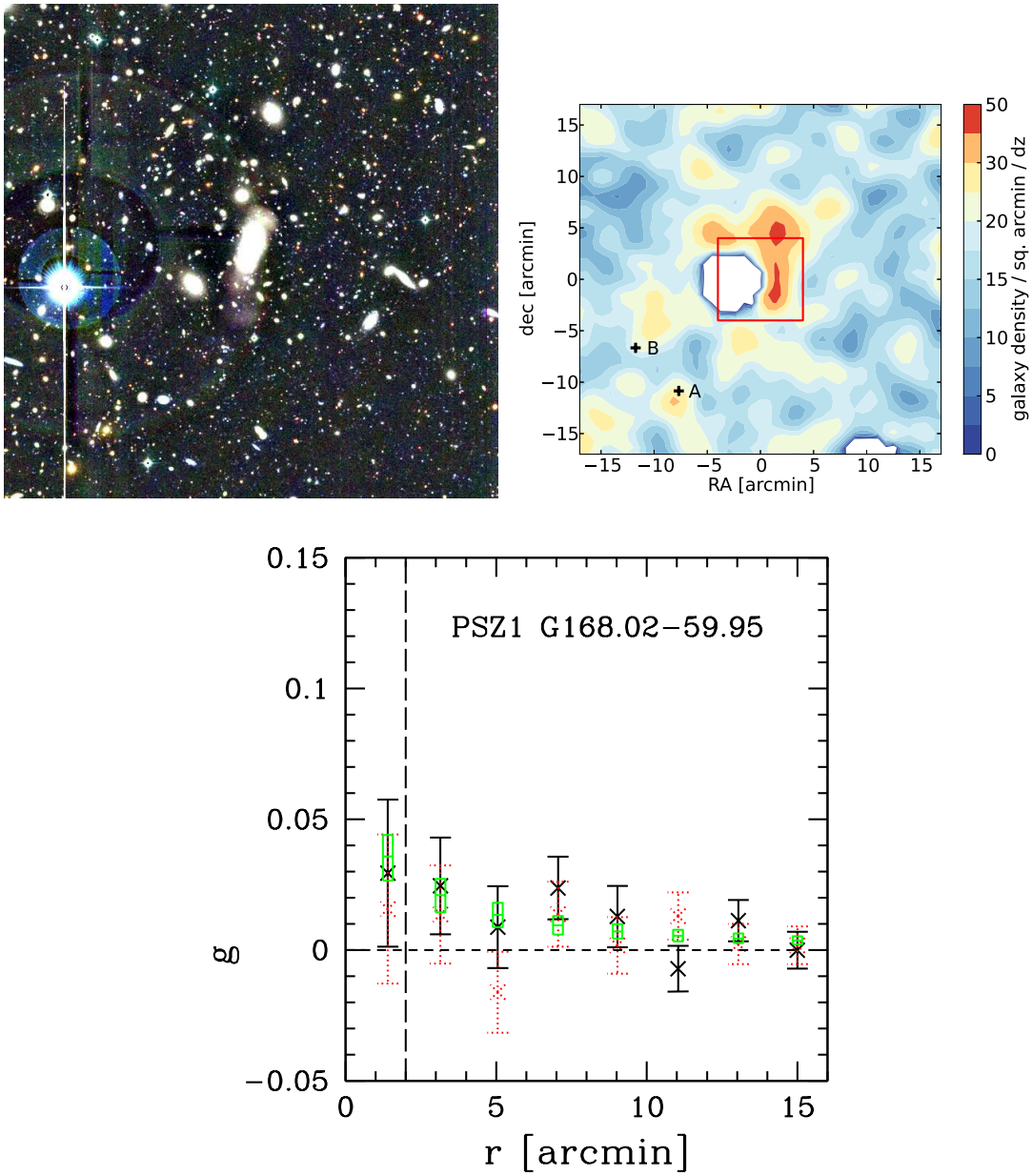

Figure 5.22: Colour image of 8×8 arcmin^2 central region from *gri* frames (top left panel), three-dimensional galaxy density smoothed with 1.5 arcmin radius Epanechnikov kernel (top right panel) and shear profile (bottom panel) of PSZ1 G168.02–59.95. See Fig. 5.11 and Section 5.6.1 for details.

The system is associated with the *ROSAT* bright X-ray source 1RXS J021439.0-433319 (Voges et al., 1999). We apply *ROSAT* band conversion factor, Galactic HI column density correction (Kalberla et al., 2005) and k-correction from tables 2-4 of Böhringer et al. (2004b). In this procedure, we assume an X-ray temperature $T_{\rm X} = 5$ keV, as justified by the relative independence of the conversion factors on $T_{\rm X}$ and the large intrinsic scatter of the $T_{\rm X} - L_{\rm X}$ relation (Pratt et al., 2009) that could be used for self-consistent calibration. The derived X-ray luminosity corresponds to a mass of $M_{500c} = (2.5 \pm 0.2) \times 10^{14} h_{70}^{-1} M_\odot$ according to the Reiprich & Böhringer (2002) $L_{\rm X} - M$ relation, which was calibrated using measurements under the assumption of HSE.

From the catalogued SZ likelihood of Planck Collaboration et al. (2014a) we calculate mass estimates using the X-ray θ_{500} as a fixed size and the self-consistency method as $M_{500c} = 4.6^{+0.6}_{-0.8} \times 10^{14} h_{70}^{-1} M_\odot$ and $5.0^{+0.9}_{-0.9} \times 10^{14} h_{70}^{-1} M_\odot$, respectively.

Tovmassian & Moiseev (1967) fail to detect radio emission from the system at 1410 MHz.

Weak lensing analysis

A single halo fit, fixing the centre at the BCG and marginalizing over concentration, yields $M_{200m} = (2.3^{+1.4}_{-1.1}) \times 10^{14} h_{70}^{-1} M_\odot$ ($M_{500c} = (1.2^{+0.7}_{-0.6}) \times 10^{14} h_{70}^{-1} M_\odot$). The observed shear profile and the confidence interval of the NFW fit are shown in Fig. 5.22 (bottom panel).

Subtraction of the maximum likelihood signal of neighbouring structures before re-fitting the central halo yields a consistent mass $M_{200m} = (2.5^{+1.5}_{-1.2}) \times 10^{14} h_{70}^{-1} M_\odot$ ($M_{500c} = (1.3^{+0.7}_{-0.6}) \times 10^{14} h_{70}^{-1} M_\odot$).

This result is marginally consistent with the X-ray mass estimate (1.5σ lower), yet significantly lower than the Planck SZ estimate at $\approx 3\sigma$.

Strong lensing

Consistent with the relatively low mass and redshift of the system, we find no evidence for strong lensing in PSZ1 G168.02–59.95.

5.6.10 PSZ1 G230.73+27.70

Visual appearance

Fig. 5.23 shows the central region of PSZ1 G230.73+27.70. A large number of cluster members is visible, although imaging is somewhat obstructed by a bright star in the south of the system. We note that in addition the central BCG, there are several additional diffuse elliptical galaxies of similar colour outside this cutout. Two of them (A and B) are included as halo centres in our multi-halo analysis of the system.

Previous work

In the Planck catalogue, PSZ1 G230.73+27.70 is associated with a system first described in the maxBCG catalog of clusters at a photometric redshift of $z = 0.2944$, although the Planck detection is centred on a galaxy with similar colour 4 arcmin away from the maxBCG centre.

Koester et al. (2007) give the $N_{r_{200}}$ richness of the maxBCG system as 60. Rykoff et al. (2012) calculate a richness $\lambda = 70.2 \pm 4.7$, to which corresponds a mass of $M_{200m} = (6.6 \pm 0.5) \times 10^{14} h_{70}^{-1} M_\odot$ with an intrinsic scatter of $\approx 30\%$.

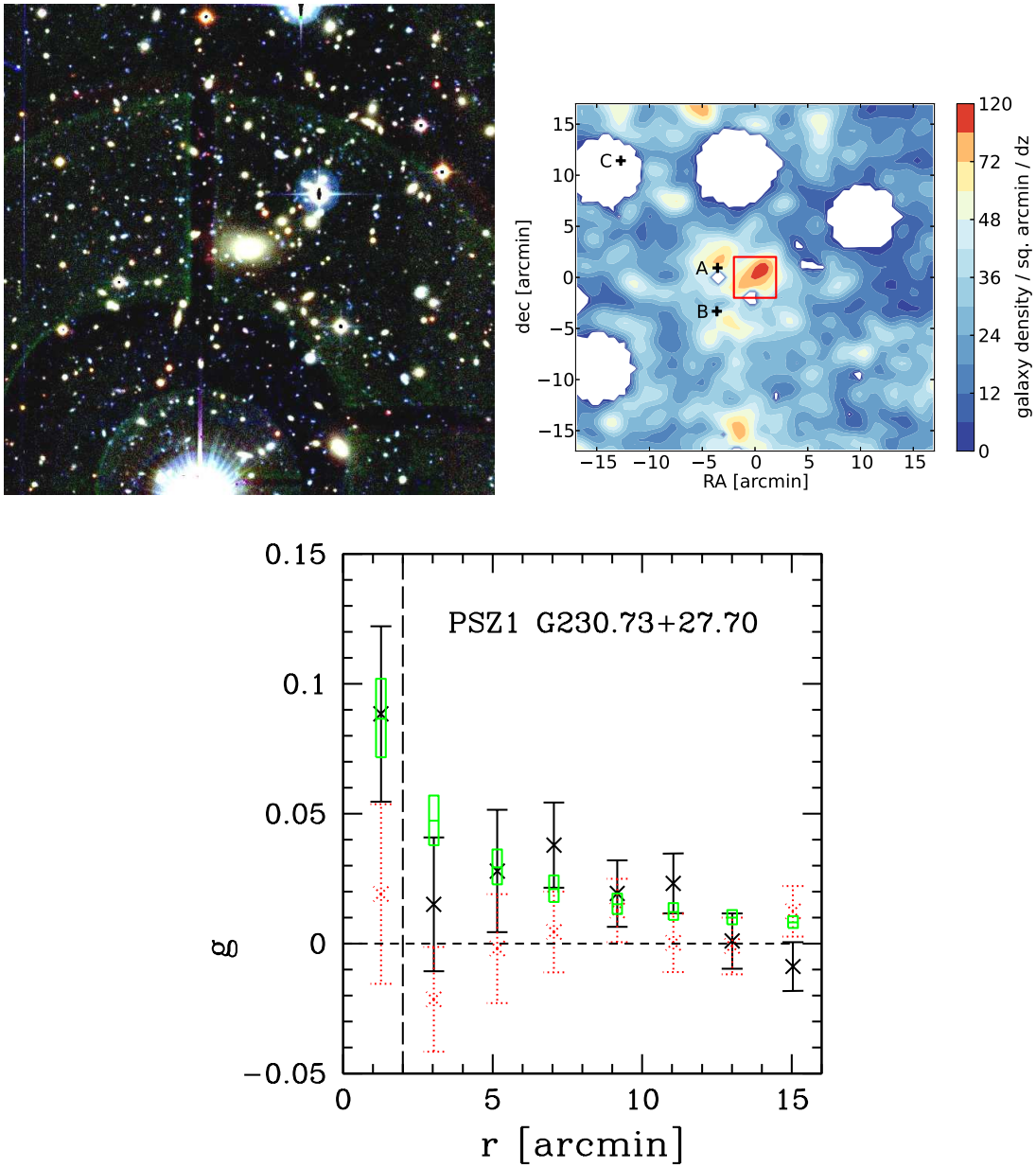

Figure 5.23: Colour image from *gri* frames (top left panel), three-dimensional galaxy density (top right panel) and shear profile (bottom panel) of PSZ1 G230.73+27.70. See Fig. 5.11 and Section 5.6.1 for details.

The system is associated with the *ROSAT* faint X-ray source 1RXS J090134.0-013900 (Voges et al., 2000). We apply *ROSAT* band conversion factor, Galactic HI column density correction (Kalberla et al., 2005) and k-correction from tables 2-4 of Böhringer et al. (2004b). In this procedure, we assume an X-ray temperature $T_{\rm X} = 5$ keV, as justified by the relative independence of the conversion factors on $T_{\rm X}$ and the large intrinsic scatter of the $T_{\rm X} - L_{\rm X}$ relation (Pratt et al., 2009) that could be used for self-consistent calibration. The derived X-ray luminosity corresponds to a mass of $M_{500c} = (3.6 \pm 0.8) \times 10^{14} h_{70}^{-1} M_\odot$ according to the Reiprich & Böhringer (2002) $L_{\rm X} - M$ relation, which was calibrated using measurements under the assumption of HSE.

From the catalogued SZ likelihood of Planck Collaboration et al. (2014a) we calculate mass estimates using the X-ray θ_{500} as a fixed size and the self-consistency method as $M_{500c} = 6.0^{+0.9}_{-1.0} \times 10^{14} h_{70}^{-1} M_\odot$ and $M_{500c} = 6.2^{+1.2}_{-1.3} \times 10^{14} h_{70}^{-1} M_\odot$, respectively.

Weak lensing analysis

A single halo fit, fixing the centre at the BCG and marginalizing over concentration, yields $M_{200m} = (10.0^{+3.9}_{-3.2}) \times 10^{14} h_{70}^{-1} M_\odot$ ($M_{500c} = (4.9^{+1.6}_{-1.5}) \times 10^{14} h_{70}^{-1} M_\odot$). The observed shear profile and the confidence interval of the NFW fit are shown in Fig. 5.23 (bottom panel).

Subtraction of the maximum-likelihood profiles of neighbouring structures yields a lower mass of $M_{200m} = (6.8^{+3.2}_{-2.6}) \times 10^{14} h_{70}^{-1} M_\odot$ ($M_{500c} = (3.5^{+1.5}_{-1.3}) \times 10^{14} h_{70}^{-1} M_\odot$).

Strong lensing

We find no evidence for strong lensing in the field of PSZ1 G230.73+27.70.

5.6.11 PSZ1 G099.84+58.45

Visual appearance

Fig. 5.24 shows the central region of PSZ1 G099.84+58.45. The giant arc west of the BCG can be seen along with a very large number of cluster member galaxies. The elongated pattern towards the north-eastern direction in the redshift density map (central panel) is identified visually, although only barely, as a diffuse filamentary structure of high-redshift galaxies.

Previous work

The system was first discovered as a strong lens by the CFHTLS Strong Lensing Legacy Survey (SL2S, Cabanac et al. 2007) as SL2S J141447+544703.

Cabanac et al. (2007) give the photometric redshift of the BCG as $z = 0.75$, while More et al. (2012) find, on the same data, $z = 0.63 \pm 0.02$. The photometric redshift for the central galaxy is $z = 0.71$ in our photometric redshift catalogue, from which we also calculate the outlier-clipped median photometric redshift of 32 visually selected cluster members at $z = 0.69$, which is the value we adopt in our analysis.

The system is associated with the *ROSAT* faint X-ray source 1RXS J141443.2+544652 (Voges et al., 2000), yet not resolved. We apply *ROSAT* band conversion factor, Galactic HI column density correction (Kalberla et al., 2005) and k-correction in extrapolation of tables 2-4 of Böhringer et al. (2004b). In this procedure, we assume an X-ray temperature $T_{\rm X} = 10$ keV, as justified by the relative independence of the conversion factors on $T_{\rm X}$ and

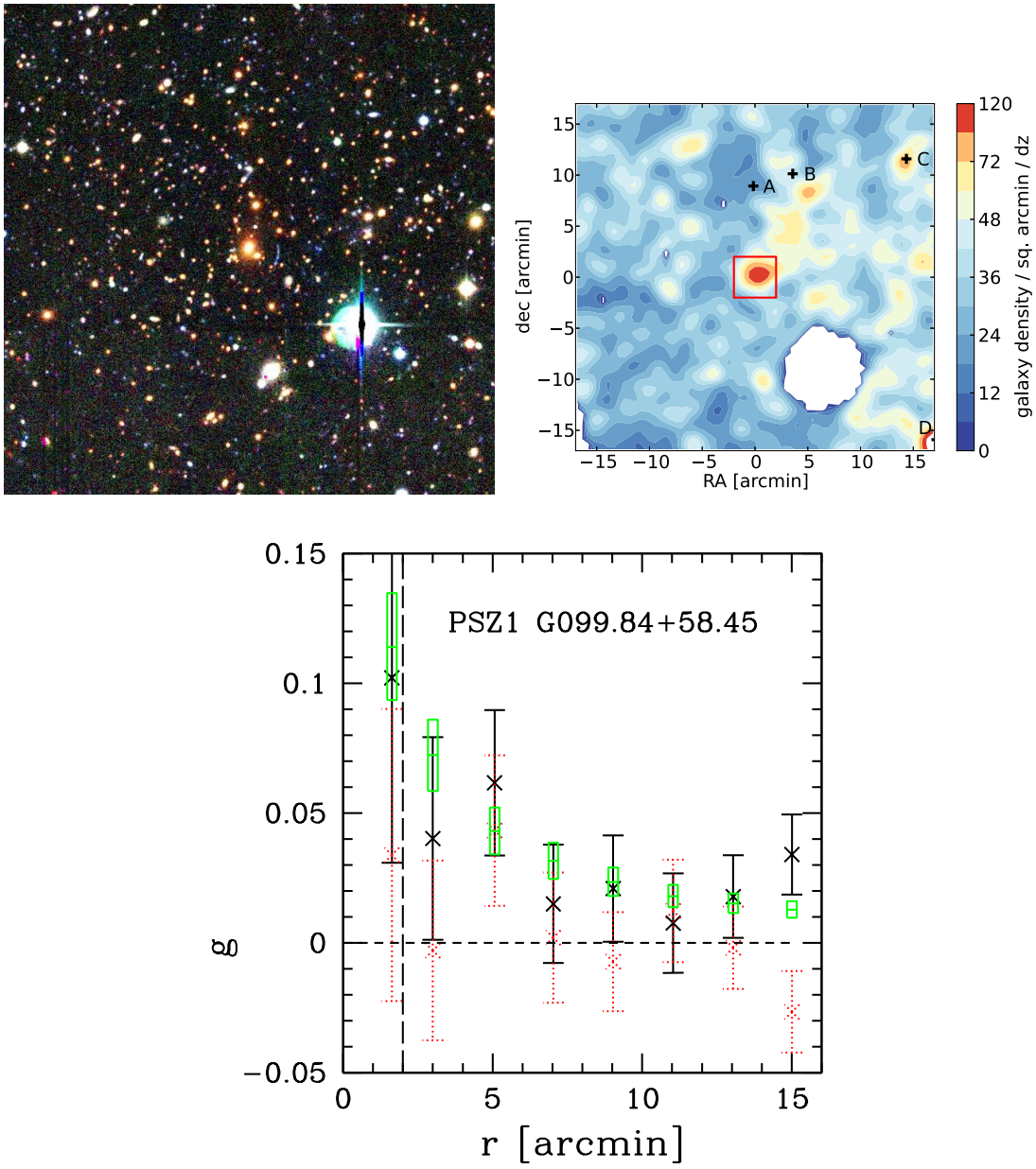

Figure 5.24: Colour image from *gri* frames (top left panel), three-dimensional galaxy density (top right panel) and shear profile (bottom panel) of PSZ1 G099.84+58.45. See Fig. 5.11 and Section 5.6.1 for details.

the large intrinsic scatter of the $T_{\rm X} - L_{\rm X}$ relation (Pratt et al., 2009) that could be used for self-consistent calibration. The derived X-ray luminosity corresponds to a mass of $M_{500c} = (12.5 \pm 2.0) \times 10^{14} h_{70}^{-1} M_\odot$ according to the Reiprich & Böhringer (2002) $L_{\rm X} - M$ relation, which was calibrated using measurements under the assumption of HSE.

From the catalogued SZ likelihood of Planck Collaboration et al. (2014a) we calculate mass estimates using the X-ray θ_{500} as a fixed size and the self-consistency method as $M_{500c} = 8.6^{+1.1}_{-1.2} \times 10^{14} h_{70}^{-1} M_\odot$ and $8.3^{+1.2}_{-1.3} \times 10^{14} h_{70}^{-1} M_\odot$, respectively.

Foëx et al. (2013) follow up the SL2S detections with WL analyses. Their singular isothermal sphere (SIS) fit to the object yields $\sigma_{\rm SIS} = 969^{+100}_{-130}$km s^{-1}, which we convert to (cf. Gruen et al. 2013, their equations 17 and 18) $M_{200m} = (7.1^{+2.5}_{-2.5}) \times 10^{14} h_{70}^{-1} M_\odot$ ($M_{500c} = 3.7^{+1.3}_{-1.3} \times 10^{14} h_{70}^{-1} M_\odot$).

A cluster identified by Yoon et al. (2008) at $(\alpha, \delta) = (14^{\rm h}13^{\rm m}26.3^{\rm s}, 54°45'22.0'')$ with spectroscopic redshift $z = 0.08278$ lies at ≈ 11.5 arcmin separation from PSZ1 G099.84+58.45. The centre of this system appears to be a galaxy brighter by 0.9 magnitudes than the one given by Yoon et al. (2008) and at a compatible spectroscopic redshift of $z = 0.0828$ at a separation of 1.6 arcmin with coordinates $(\alpha, \delta) = (14^{\rm h}13^{\rm m}27.3^{\rm s}, 54°43'46'')$. Due to the low redshift of the system, however, we do not use the position in our combined lensing analysis.

Weak lensing analysis

A single halo fit, fixing the centre at the BCG and marginalizing over concentration, yields $M_{200m} = (34.4^{+11.6}_{-10.2}) \times 10^{14} h_{70}^{-1} M_\odot$ ($M_{500c} = (18.1^{+5.8}_{-5.3}) \times 10^{14} h_{70}^{-1} M_\odot$). The observed shear profile and the confidence interval of the NFW fit are shown in Fig. 5.24 (bottom panel).

Subtraction of the maximum-likelihood profiles of neighbouring structures yields a mass of $M_{200m} = (38.3^{+13.5}_{-11.7}) \times 10^{14} h_{70}^{-1} M_\odot$ ($M_{500c} = (19.6^{+6.4}_{-5.8}) \times 10^{14} h_{70}^{-1} M_\odot$), marginally higher than the single-halo value. The high sensitivity of the reconstruction of the high redshift system on matter along the line of sight at lower redshift is due to the fact that the geometrical scaling factor of the lensing signal, $\frac{D_d D_{ds}}{D_s}$, causes a relative amplification of the foreground signal.

Despite being based on the same observational data and consistency with the strong lensing feature of the system (see following subsection), our results are in conflict with the SIS fit of Foëx et al. (2013) at $\approx 3\sigma$ significance (their $\sigma_{\rm SIS} = 969^{+100}_{-130}$km s^{-1} is significantly lower than our $\sigma_{\rm SIS} = 1540^{+162}_{-190}$km s^{-1} as fitted out to 10 arcmin).

Several effects can in principle contribute to an underestimation of the shear around rich, high redshift clusters. The method of determining β in Foëx et al. (2013) is based on the mean value calculated from the photometric redshift of all sources fainter than $m_{i'} = 21$ (except a colour-removed red sequence at the cluster redshift), and all these sources are used for calculating the shear profile. This is suboptimal for rich, high-redshift systems like PSZ1 G099.84+58.45, where most galaxies fainter than this limit are indeed foreground objects or (blue) cluster members. We have verified with the help of Foëx (private communication) that the difference between our photo-z based β estimated on their background sample and their method of determining β is indeed the primary cause of the discrepancy.

We note that the lensing analysis for this cluster includes data from a CFHT pointing (W3m0m0) with strongly ($> 10\%$) elliptical PSF along the ϵ_1 direction. Detailed analysis shows that for this particular field we measure significant non-zero mean ellipticity for galaxies along the same direction, particularly at low S/N, indicating an additive bias based on selection effects or insufficient correction for the PSF ellipticity. We verify that also in the CFHTLenS catalogues, S/N dependent non-zero ϵ_1 shear is present in this field. At a

highly elliptical PSF, such a bias due to source detection and the simplistic modelling of PSF ellipticity in KSB is not unexpected.

We choose to model the additive bias by the same functional form used for the multiplicative noise bias in Gruen et al. (2013, their equation 9) with $A = 0.005$, $B = 0.08$ and $C = 14$. We have verified that removing the pointing from our analysis or using it without this correction do not significantly alter our results.

Strong lensing

The system was originally discovered as a strong lens with a blue giant arc (Cabanac et al., 2007).

We note that for our best-fitting model with fiducial concentration, the arc redshift would have to be $z_s = 1.49$ to give rise to an Einstein radius at the observed arc radius $R_A = (14 \pm 1)$ arcsec (Cabanac et al., 2007). At the photometric redshift of the arc of $z_s \approx 2.0$, the same Einstein radius would be caused by a lens of $M_{200m} = 21.6 \times 10^{14} h_{70}^{-1} M_\odot$, 1.2σ below our best fit. While spectroscopic redshifts for lens and source would greatly enhance the constraining power of the strong lensing feature, this is still additional evidence for the correctness of our analysis.

5.6.12 PSZ1 G099.48+55.62

Visual appearance

The cluster image of PSZ1 G099.48+55.62 (cf. Fig. 5.25) is dominated by a BCG with bi-modal core and visibly disturbed wings.

Previous work

PSZ1 G099.48+55.62 was first discovered by Abell (1958) and classified at the third-lowest of six richness classes.

Struble & Rood (1999) quote a spectroscopic redshift of $z = 0.1051$, listing as the source the catalog of Lebedev & Lebedeva (1991), which is unavailable to the authors of this work.

The system is associated with the *ROSAT* bright X-ray source 1RXS J142830.5+565146 (Voges et al., 1999). We apply *ROSAT* band conversion factor, Galactic HI column density correction (Kalberla et al., 2005) and k-correction from tables 2-4 of Böhringer et al. (2004b). In this procedure, we assume an X-ray temperature $T_\mathrm{X} = 5$ keV, as justified by the relative independence of the conversion factors on T_X and the large intrinsic scatter of the $T_\mathrm{X} - L_\mathrm{X}$ relation (Pratt et al., 2009) that could be used for self-consistent calibration. The derived X-ray luminosity corresponds to a mass of $M_{500c} = (1.2 \pm 0.2) \times 10^{14} h_{70}^{-1} M_\odot$ according to the Reiprich & Böhringer (2002) $L_\mathrm{X} - M$ relation, which was calibrated using measurements under the assumption of HSE.

From the catalogued SZ likelihood of Planck Collaboration et al. (2014a) we calculate mass estimates using the X-ray θ_{500} as a fixed size and the self-consistency method as $M_{500c} = 3.2^{+0.4}_{-0.4} \times 10^{14} h_{70}^{-1} M_\odot$ and $3.8^{+0.5}_{-0.5} \times 10^{14} h_{70}^{-1} M_\odot$, respectively, noting that this value is significantly higher than the X-ray mass estimate.

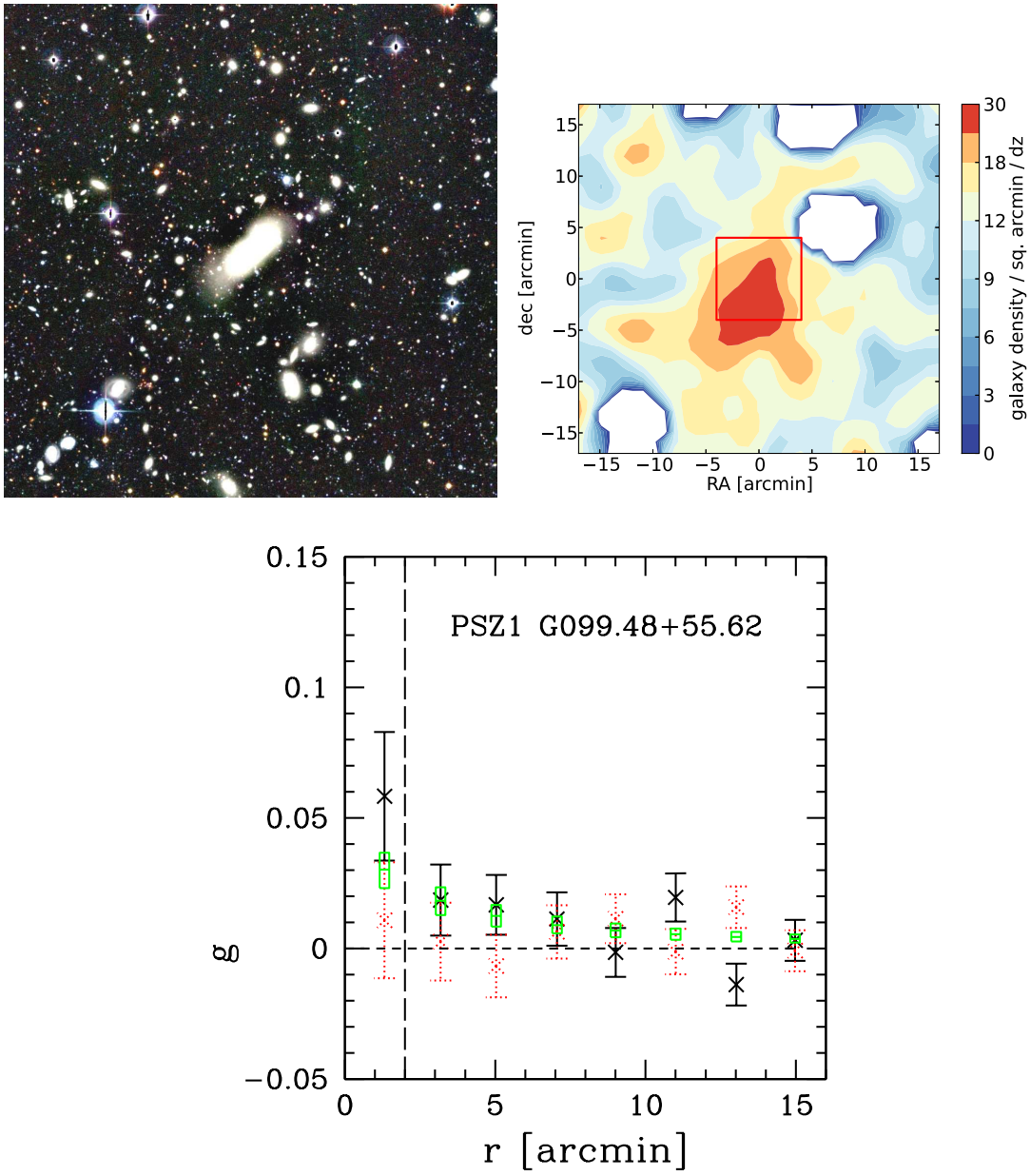

Figure 5.25: Colour image of 8×8 arcmin^2 central region from *gri* frames (top left panel), three-dimensional galaxy density smoothed with 2 arcmin radius Epanechnikov kernel (top right panel) and shear profile (bottom panel) of PSZ1 G099.48+55.62. See Fig. 5.11 and Section 5.6.1 for details.

Weak lensing analysis

A single halo fit, fixing the centre at the BCG and marginalizing over concentration, yields $M_{200m} = (1.9^{+1.2}_{-0.9}) \times 10^{14} h_{70}^{-1} M_\odot$ ($M_{500c} = (1.0^{+0.5}_{-0.4}) \times 10^{14} h_{70}^{-1} M_\odot$). The observed shear profile and the confidence interval of the NFW fit are shown in Fig. 5.25 (bottom panel).

We do not find additional structures in the field of view that would warrant a combined fit. The most prominent feature is a very diffuse concentration of high redshift galaxies towards the south-east of the cluster.

The WL measurement is consistent with our X-ray mass estimate. It is, however, below the Planck SZ value with 3σ significance.

Strong lensing

Consistent with the relatively low mass and redshift of the system, we find no evidence for strong lensing in PSZ1 G099.48+55.62.

5.7 Combined analysis

In the following, will combinedly analyse our WL mass estimates and compare them to the X-ray and SZ measurements. Table 5.4 gives an overview of the mass estimates used.

5.7.1 Comparison of X-ray and weak lensing mass estimates

We briefly compare the X-ray gas and total mass estimates for the WISCy sample with our WL analysis. Our full sample has the disadvantage that the X-ray mass estimation is far from homogeneous. However, the interesting question of a mean hydrostatic mass bias can still be addressed, since we have taken care to only use X-ray mass estimates calibrated under the assumption of HSE. For the subsample of eight clusters where X-ray gas mass estimates exist, we can make a more homogeneous analysis.

Fig. 5.26 shows a comparison of the two mass estimates. There is apparent good agreement between WL masses and X-ray based estimates. The most notable exception is the case of PLCKESZ G292.5+22.0, likely related to its complex structure (cf. Sec. 5.6.6).

We are interested in determining the intrinsic scatter, normalization and slope between X-ray mass estimate M^{X} and WL measurement M^{WL}. To this end, we assume a relation of the form

$$\frac{M^{\mathrm{WL}}_{500c}}{6 \times 10^{14} h_{70}^{-1} M_\odot} = 10^A \times \left(\frac{M^{\mathrm{X}}_{500c}}{6 \times 10^{14} h_{70}^{-1} M_\odot} \right)^B \tag{5.31}$$

with lognormal intrinsic scatter $\sigma_{\mathrm{int},\log_{10}}$. The pivot mass $M_p = 6 \times 10^{14} h_{70}^{-1} M_\odot$ is chosen such that errors in A and B are uncorrelated. Note that $A = 0$ and $B = 1$ is the case of agreement with hydrostatic calibration.

In order to determine confidence limits for the parameters, we calculate the likelihood

$$-2 \ln \mathcal{L}_i = \frac{\left[\log M_i^{\mathrm{WL}}/M_p - \log f(M_i^{\mathrm{X}})\right]^2}{\sigma^2_{i,\log M^{\mathrm{WL}}} + (B\sigma_{i,\log M^{\mathrm{X}}})^2 + \sigma^2_{\mathrm{int},\log_{10}}} + \ln \left[\sigma^2_{i,\log M^{\mathrm{WL}}} + (B\sigma_{i,\log M^{\mathrm{X}}})^2 + \sigma^2_{\mathrm{int},\log_{10}} \right] , \tag{5.32}$$

cluster	$M_{200m}^{\mathrm{WL,single}}$	$M_{500c}^{\mathrm{WL,single}}$	$M_{200m}^{\mathrm{WL,multi}}$	$M_{500c}^{\mathrm{WL,multi}}$	M_{500c}^{X}	$M_{\mathrm{gas},500c}^{\mathrm{X}}$	M_{200m}^{SPT}	$M_{500c}^{\mathrm{Planck}}$
SPT-CL J0509–5342	$8.4^{+3.4}_{-2.9}$	$4.7^{+1.9}_{-1.7}$	$6.6^{+3.1}_{-2.6}$	$3.8^{+1.7}_{-1.5}$	$5.6 \pm 0.6^{\mathrm{C}}$	0.56 ± 0.02	7.3 ± 1.5	-
SPT-CL J0551–5709	$11.7^{+5.1}_{-4.2}$	$6.6^{+2.6}_{-2.4}$	$11.7^{+5.1}_{-4.2}$	$6.6^{+2.6}_{-2.4}$	$3.4 \pm 0.4^{\mathrm{C}}$	0.51 ± 0.06	6.9 ± 1.5	-
SPT-CL J2332–5358	$14.5^{+4.0}_{-3.5}$	$7.5^{+1.8}_{-1.7}$	$15.3^{+4.2}_{-3.6}$	$7.9^{+1.8}_{-1.7}$	$6.7 \pm 0.5^{\mathrm{X}}$	0.76 ± 0.25	12.1 ± 1.4	-
SPT-CL J2355–5056	$8.0^{+3.7}_{-3.1}$	$4.1^{+1.7}_{-1.5}$	$3.8^{+2.4}_{-2.1}$	$2.1^{+1.4}_{-1.1}$	$3.8 \pm 0.4^{\mathrm{C}}$	0.39 ± 0.15	7.6 ± 1.0	-
PLCKESZ G287.0+32.9	$37.7^{+9.5}_{-7.6}$	$19.5^{+3.3}_{-3.2}$	$35.4^{+8.9}_{-7.1}$	$18.7^{+3.2}_{-3.1}$	$15.7 \pm 0.3^{\mathrm{X}}$	2.39 ± 0.30	-	$17.7^{+0.8}_{-0.9}$
PLCKESZ G292.5+22.0	$6.8^{+3.8}_{-3.0}$	$3.4^{+1.7}_{-1.4}$	$5.0^{+3.1}_{-2.5}$	$2.7^{+1.5}_{-1.3}$	$9.3 \pm 0.6^{\mathrm{X}}$	1.17 ± 0.04	-	$10.3^{+0.9}_{-1.0}$
MACS J0416.1–2403	$10.0^{+2.9}_{-2.6}$	$5.9^{+1.6}_{-1.5}$	$10.4^{+3.0}_{-2.6}$	$6.1^{+1.7}_{-1.5}$	$9.1 \pm 2.0^{\mathrm{C}}$	1.05 ± 0.23	-	-
SPT-CL J2248–4431	$31.1^{+6.3}_{-5.2}$	$13.8^{+2.8}_{-2.4}$	$24.7^{+6.3}_{-6.0}$	$9.9^{+2.6}_{-2.4}$	$12.6 \pm 0.2^{\mathrm{X}}$	1.89 ± 0.02	29.0 ± 3.7	$14.5^{+0.7}_{-0.7}$
PSZ1 G168.02–59.95	$2.3^{+1.4}_{-1.1}$	$1.2^{+0.7}_{-0.6}$	$2.5^{+1.5}_{-1.2}$	$1.3^{+0.7}_{-0.6}$	$2.5 \pm 0.2^{\mathrm{R}}$	-	-	$4.6^{+0.6}_{-0.8}$
PSZ1 G230.73+27.70	$10.0^{+3.9}_{-3.2}$	$4.9^{+1.6}_{-1.5}$	$6.8^{+3.2}_{-2.6}$	$3.5^{+1.5}_{-1.3}$	$3.6 \pm 0.8^{\mathrm{R}}$	-	-	$6.0^{+0.9}_{-1.0}$
PSZ1 G099.84+58.45	$34.4^{+11.6}_{-10.2}$	$18.1^{+5.8}_{-5.3}$	$38.3^{+13.5}_{-11.7}$	$19.6^{+6.4}_{-5.8}$	$12.5 \pm 2.0^{\mathrm{R}}$	-	-	$8.6^{+1.1}_{-1.2}$
PSZ1 G099.48+55.62	$1.9^{+1.2}_{-0.9}$	$1.0^{+0.5}_{-0.4}$	$1.9^{+1.2}_{-0.9}$	$1.0^{+0.5}_{-0.4}$	$1.2 \pm 0.2^{\mathrm{R}}$	-	-	$3.2^{+0.4}_{-0.4}$

Table 5.4: Summary of mass estimates for the WISCy sample. The columns give weak lensing (WL) results for single halo and multi halo reconstructions (cf. Sec. 5.4.5) in two definitions of spherical overdensity in units of $10^{14} h_{70}^{-1} M_{\odot}$. For Planck SZ, we use the estimates based on the X-ray size R_X (cf. Section 5.5.2). Details on the X-ray and SZ measurements can be found in the respective part of Section 5.6. Superscripts C (*Chandra*), X (*XMM-Newton*) and R (*ROSAT*) indicate the instrument used for the X-ray mass and gas mass estimates. Values for SPT-CL J2248–4431 are taken from Gruen et al. (2013) (WL, as in all other cases we use the mass estimate marginalized over the concentration parameter) and Planck Collaboration et al. (2011b) (X-ray).

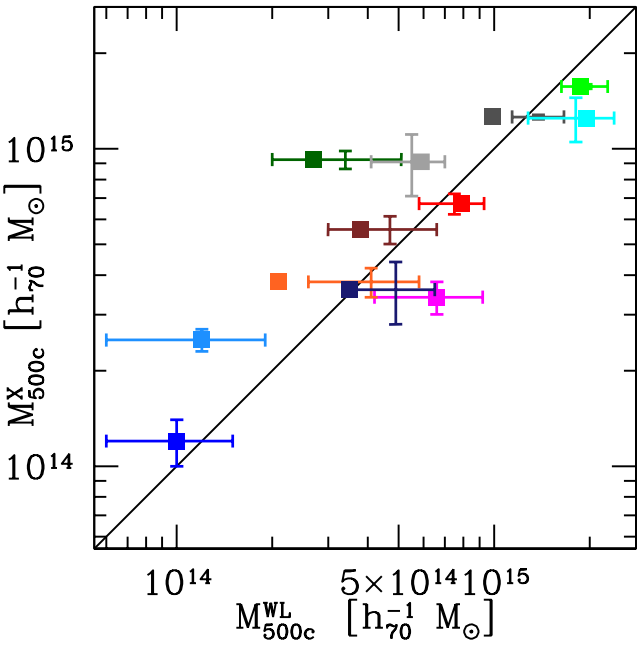

(a)

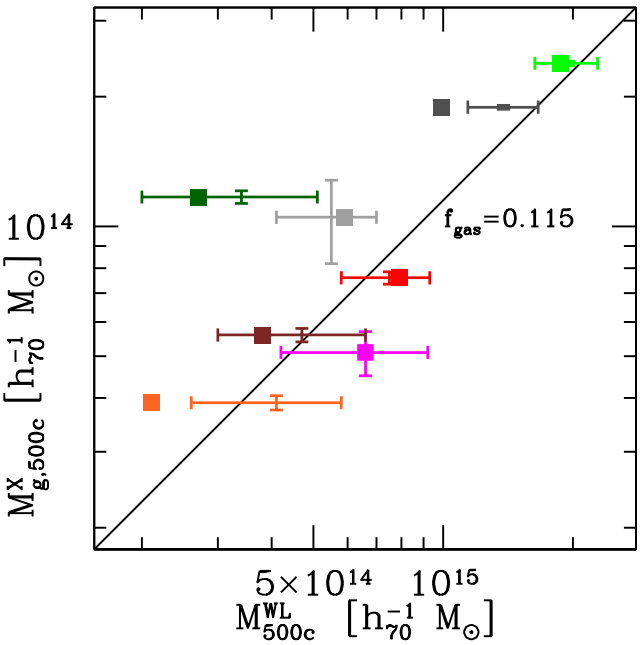

(b)

Figure 5.26: Comparison of X-ray mass estimates determined under the assumption of hydrostatic equilibrium (a) and X-ray gas masses (b) with our weak lensing result (see individual cluster analysis for details). Error bars indicate best-fitting value and confidence regions of single-halo fit. The solid symbols are best-fitting masses of the central halo in a combined fit to multiple structures in the field of view, to be interpreted with errors of similar size. Colour coding for the individual clusters is as in Fig. 5.27. Our measurements are consistent with no mean bias and no mass dependent bias of the HSE mass and a gas fraction $f_{\mathrm{gas},500c} = 0.115$.

where $f(M_i^{\rm X})$ is the relation of equation (5.31). In consideration of Gruen et al. (2011), we increase the WL uncertainties by 10% for all following analyses in order to account for intrinsic variations due to cluster substructure, orientation and projected structures.

For the WL masses based on a single-halo analysis, we get projected single-parameter confidence intervals of $A = 0.01^{+0.05}_{-0.05}$, $B = 1.06^{+0.18}_{-0.18}$ and $\sigma_{\rm int,log_{10}} = 0.00^{+0.07}_{-0.00}$. Using the estimates after subtraction of secondary haloes, we find $A = -0.03^{+0.06}_{-0.06}$, $B = 1.08^{+0.19}_{-0.18}$ and $\sigma_{\rm int,log_{10}} = 0.00^{+0.09}_{-0.00}$. This is consistent with no hydrostatic bias and regular scaling of X-ray observables with mass and marginally inconsistent with the assumption of a 20% negative bias of hydrostatic masses (as in the calibration of Planck Collaboration et al. 2014c).

The relation between gas mass and WL estimate of total mass is consistent with a gas fraction $f_{\rm gas,500c} = 0.128^{+0.029}_{-0.023}$, in line with the $f_{\rm gas,500c} = 0.115$ of Allen et al. (2008) and Mantz et al. (2010a). For the multi-halo estimates, the fit is much more uncertain but still consistent.

5.7.2 Comparison of SZ signal and mass

In the following, we will compare our WL measurements of cluster mass to SZ observables, namely the SPT significance and the Planck Compton parameter inside the θ_{500c} of the X-ray mass measurement. This is meant both as a test of the earlier calibrations of the MORs by Vanderlinde et al. (2010) and Planck Collaboration et al. (2014c) and an independent lensing-based determination of the MOR parameters.

In this, we need to account for uncertainties in both the WL mass measurement and the SZ signal, together with an intrinsic scatter. While some studies (e.g. Reiprich & Böhringer 2002; Foëx et al. 2013; Planck Collaboration et al. 2014c) have used line fitting techniques such as the one described in Akritas & Bershady (1996) in the past, this setting favours a Bayesian approach for unbiased estimation of the MOR parameters (cf. e.g. Kelly 2007). We therefore determine the parameters from the likelihood, in analogy to e.g. Hoekstra et al. (2012, their equations 7-9) and our equation (5.32), with lognormal uncertainties in all parameters,

$$\begin{aligned} -2\ln\mathcal{L}_i &= \frac{\left[\log f(M_i^{\rm WL}, z_i) - \log f_i\right]^2}{\left[\frac{{\rm d}\log f}{{\rm d}\log M}\sigma_{i,\log M^{\rm WL}}\right]^2 + \sigma^2_{i,\log f_i} + \sigma^2_{\rm int,log_{10}}} \\ &+ \ln\left[\left(\frac{{\rm d}\log f}{{\rm d}\log M}\sigma_{i,\log M^{\rm WL}}\right)^2 + \sigma^2_{i,\log f_i} + \sigma^2_{\rm int,log_{10}}\right] , \end{aligned} \tag{5.33}$$

where f_i is the SZ observable of cluster i with intrinsic scatter $\sigma_{\rm int,log_{10}}$, and $f(M, z)$ is the MOR.

Our key results are illustrated in Fig. 5.27, which we discuss subsequently. As for the X-ray comparison (see previous section) we increase the WL uncertainties by 10% for this procedure.

South Pole Telescope

For SPT, we assume the MOR of equation (5.22) (Vanderlinde et al., 2010). A direct comparison of WL estimate and SZ mass for the best-fitting parameters $A = 5.62$ and $B = 1.43$ (Vanderlinde et al., 2010) shows that while there is consistency within the errors, all our systems are measured with WL to be at a higher mass than predicted with the SZ MOR,

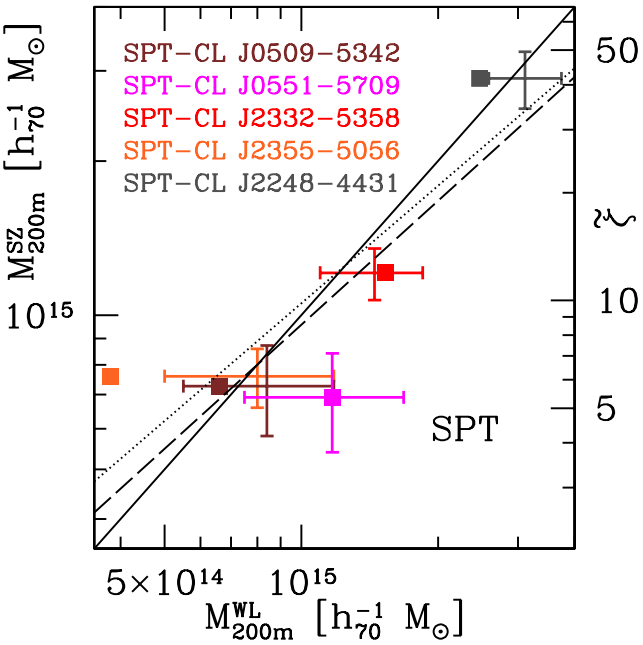

(a)

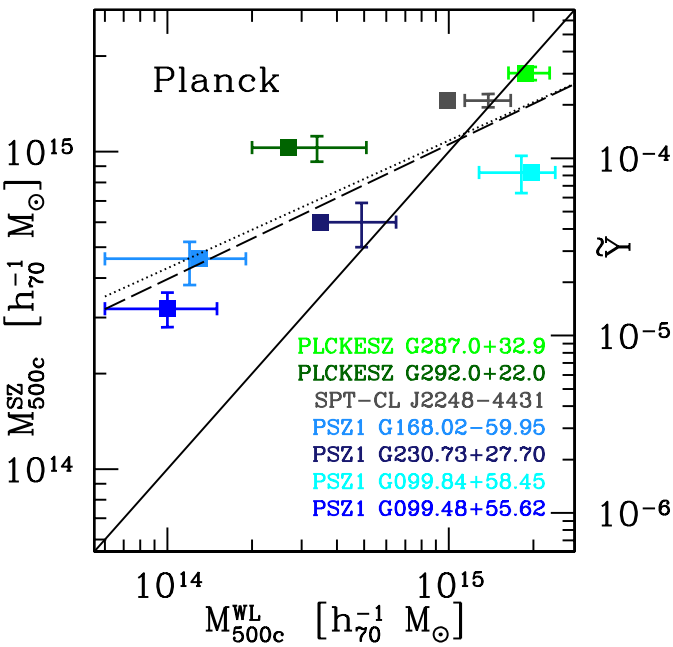

(b)

Figure 5.27: Comparison of SZ and weak lensing (WL) results for the WISCy clusters. Panel (a) shows SPT, panel (b) *Planck* clusters. The solid line indicates the mass-observable relations of the respective survey given by Vanderlinde et al. (2010) ($A = 5.62$, $B = 1.43$) and Planck Collaboration et al. (2014c) ($A = -4.19$, $B = 1.79$, $b = 0.2$, cf. equations 5.22 and 5.29). WL single halo fits and statistical uncertainties are given by the horizontal and vertical error bars. The solid symbols indicate best-fitting WL result after subtracting neighbouring structures, to be interpreted with errors of approximately the same size. Masses are compared to SPT significance ζ and Planck $Y^{R_X}_{500c}$ inside a sphere of the r_{500c} radius corresponding to the X-ray mass estimate, where we use shorthand notations $\tilde{\zeta} = \zeta[(1+z)/1.6]^{-C}$ and $\tilde{Y} = E(z)^{-2/3} D_A^2 Y^{R_X}_{500c} \mathrm{Mpc}^{-2}$. Dashed lines indicate the fit based on our single-halo WL analysis, and dotted lines the relation after subtracting the signal of neighbouring structures.

particularly at lower mass (cf. Fig. 5.27a). This effect is removed when modelling surrounding structures with WL separately (solid squares), which lowers the mass estimate for two systems considerably.

For the independent MOR determination (cf. equation 5.22), we fix $C = 1.4$ (Vanderlinde et al., 2010), since our SPT sample has little leverage on redshift dependence, and determine the remaining parameters A, B and the $\log_{10}$-normal intrinsic scatter $\sigma_{\mathrm{int},\log_{10}}$ from a combined likelihood.

We find parameters $A = 5.8^{+1.8}_{-1.8}$ and $B = 1.15^{+0.32}_{-0.22}$ from our single halo analysis (Fig. 5.27a, dashed line). These values are in agreement with the calibration of Vanderlinde et al. (2010) (solid line) at the 68% confidence level and we detect a scaling of SPT significance with mass at 3σ significance in the combined three-parametric likelihood. When we instead use the WL mass estimates made after subtraction of neighbouring structures, we find $A = 6.8^{+2.6}_{-2.0}$ and $B = 1.09^{+0.33}_{-0.47}$ (dotted line), also consistent with Vanderlinde et al. (2010). The shallower slope is mostly due to the unusually complex structure of SPT-CL J2355-5056, which results in a small mass of the central system in the multi-halo fit.

The intrinsic scatter is consistent with zero at 1σ confidence with best fits $\sigma_{\mathrm{int},\log_{10}} = 0$ and upper limits $\sigma_{\mathrm{int},\log_{10}} < 0.13$ (0.23) for the single-halo (the multiple halo) analysis, respectively. These values are consistent with previous results (Marrone et al., 2009, 2012; Hoekstra et al., 2012; Benson et al., 2013) and in agreement with predictions (e.g. Kay et al., 2012).

An analogous analysis using the MOR definition of Reichardt et al. (2013) and Benson et al. (2013) yields $A = 6.0^{+1.9}_{-1.8}$ and $B = 1.25^{+0.36}_{-0.28}$ at $\sigma_{\mathrm{int},\log_{10}} < 0.15$ for the single-halo and $A = 7.6^{+3.0}_{-2.6}$, $B = 1.02^{+0.62}_{-0.68}$ at $\sigma_{\mathrm{int},\log_{10}} = 0.15^{+0.18}_{-0.15}$ for the multi-halo modelling of neighbouring structures. In both cases, we fix the slope of the redshift dependence $C = 0.83$ (Reichardt et al., 2013; Benson et al., 2013). We find consistency with the MOR parameters of Reichardt et al. (2013) and Benson et al. (2013) within 68% confidence.

Planck

We perform a similar analysis for the Planck Y_{500c}, fitting for parameters A and B in equation (5.29) and the intrinsic scatter $\sigma_{\mathrm{int},\log_{10}}$. This returns $A + B\log_{10}(1-b) = -4.09^{+0.09}_{-0.08}$, $B = 0.76^{+0.20}_{-0.20}$ and $\sigma_{\mathrm{int},\log_{10}} = 0.14^{+0.12}_{-0.14}$.

The amplitude A is consistent with the value from Planck Collaboration et al. (2014c) when assuming no hydrostatic mass bias. Their baseline hydrostatic bias of $b = 0.2$ (corresponding to $A+B\log(1-b) = -4.36\pm0.02$ in Planck Collaboration et al. 2014c) is disfavoured from our data at $\approx 1.2\sigma$ significance in three-dimensional parameter space. Their combination of A, B, b, and $\sigma_{\mathrm{int},\log_{10}}$ is excluded at 3σ significance ($p < 0.0028$). This is due mostly to the shallower slope B in our measurement, with their value $B = 1.79$ excluded at 2.5σ significance in the three-dimensional parameter space. The discrepancy cannot be relieved by allowing a higher intrinsic scatter - even with the optimal $\sigma_{\mathrm{int},\log_{10}} = 0.38$ for the Planck A, b and B calibration, the latter is still excluded with high significance ($p < 0.004$) relative to our best fit. The maximum likelihood point with self-similar slope $B = 5/3$ (cf. e.g. Bonamente et al. 2008) is similarly unlikely in A-B-$\sigma_{\mathrm{int},\log_{10}}$ space ($p < 0.01$ for the best fit under the $B = 5/3$ constraint).

Our multi-halo analysis yields a consistent $A + B\log_{10}(1-b) = -4.06^{+0.10}_{-0.10}$, $B = 0.72^{+0.20}_{-0.19}$ and $\sigma_{\mathrm{int},\log_{10}} = 0.19^{+0.11}_{-0.12}$. It is inconsistent with the Planck Collaboration et al. (2014c) calibration with similar significance.

The cautionary remark has to be made that our disagreement with Planck Collaboration et al. (2014c) is based on a relatively small sample. The majority of the objects are at a comparatively low Planck SZ S/N ≤ 7, where the simple treatment of Malmquist bias likely does not capture selection biases completely. In addition, even one of the systems with higher significance, PLCKESZ G292.5+22.0 (see Section 5.6.6), is likely to be influenced strongly by neighbouring structures. It would therefore be of great benefit to increase the sample size, either with pointed lensing observations or a large area survey.

5.7.3 Hypothesis tests

For testing the dependence of deviations from the MOR on several cluster properties, we use Spearman rank correlation coefficients, which have been applied previously in comparable cluster studies (Lin et al., 2004; Foëx et al., 2012). After determining the unique ranking of a set of N entities by two properties A and B, the Spearman rank correlation coefficient ρ is defined as

$$\rho = 1 - \frac{6\sum_{i=1}^{N}(r_i^A - r_i^B)^2}{N(N^2-1)} \ , \tag{5.34}$$

where $r_i^A, r_i^B = 1, \ldots, N$ are the ranks of item i in the respective property. This definition ensures that the mean ρ for unrelated rankings is 0, while $\rho = 1$ ($\rho = -1$) corresponds to properties A and B which are a monotonically increasing (decreasing) function of each other. For the small sample size used in our work, the probability of random rankings to exceed some $|\rho|$ can be easily calculated by means of all permutations. In the following, we will always quote the probability of the null hypothesis p.

The Spearman rank coefficient between the $M^{\mathrm{SZ}}/M^{\mathrm{WL}}$ ratio and redshift for the five Planck clusters is $\rho = -0.93$, formally a 99% confidence ($p < 0.01$) for rejecting the null hypothesis (for both self-consistent and X-ray size prior SZ mass estimates). Indeed, the data suggest that for high redshift systems, our mass measurement with WL exceeds the expectations from the Planck SZ signal (and vice versa). We note that this is similar to testing for a connection between $M^{\mathrm{SZ}}/M^{\mathrm{WL}}$ and angular size (for which we also find $p < 0.01$), since θ_{500c} for our sample is ranked almost inversely as redshift (cf. Table 5.3). From a comparison of WL and X-ray mass estimates (cf. Fig 5.26), it appears that the highest redshift system PSZ1 G099.84+58.45 and the second-to-lowest redshift system PSZ1 G168.02–59.95 are outliers in the same direction, although not as strongly. This indicates that our particular sample might overestimate the effect. Yet also a comparison of $M^{\mathrm{SZ}}/M^{\mathrm{X}}$ rank with redshift yields evidence for an interdependence ($p < 0.01$). Interestingly, the likelihood analysis of Planck Collaboration et al. (2014c) also shows a redshift dependent tilt (cf. their fig. 7), where at redshifts $z > 0.5$ the majority of redshift-binned counts are below the predictions of any of the models, including their own best-fit to the SZ data.

For the five SPT clusters, the rank correlation of mass ratio with redshift is less significant ($\rho = 0.7$), consistent with no dependence at $p > 0.10$. We note that for this sample, the comparatively low dynamic range in redshift and mass make the ordering very noisy.

We combine mass ratios from *Planck* and SPT clusters into one by taking the arithmetic mean in the case of SPT-CL J2248–4431. Determining several Spearman rank coefficients, we find the following.

- Mass ratios are related to the ellipticity of the brightest cluster galaxy (BCG) with $\rho = 0.65$ (higher $M^{\mathrm{SZ}}/M^{\mathrm{WL}}$ with higher BCG ellipticity with confidence $p < 0.05$).

This is in line with the observation of Marrone et al. (2012), although we do not make a distinction here between relaxed and unrelaxed systems.

- Mass ratios are not found to be significantly related to the magnitude gap between the brightest and second-to-brightest cluster galaxy ($p > 0.68$). While the magnitude gap is a tracer of assembly history and has significant predictive power for richness at fixed mass (Hearin et al., 2013), we do not find evidence for any impact on SZ measurements.

5.7.4 Planck redshift dependence

As described in the previous sections, our data shows evidence for a redshift-dependent systematic offset of Planck Compton parameters from their values expected according to the WL measurement and the MOR (equation 5.29). In this section, we attempt to derive a modified MOR that includes a redshift dependent term.

We assume a MOR of the form

$$E(z)^{-2/3} \times \left(\frac{D_A^2 \times Y_{500c}}{\mathrm{Mpc}^2}\right) = 10^A \times \left(\frac{M_{500c}}{6 \times 10^{14} h_{70}^{-1} M_\odot}\right)^B \times \left(\frac{1+z}{1.31}\right)^C . \tag{5.35}$$

The normalization of the redshift term has been chosen such as to null the effect for the medium redshift clusters, for which our analysis above showed good agreement.

The projected 68% confidence interval in each of the parameters according to the likelihood of equation 5.33 is $A = -4.04^{+0.06}_{-0.08}$, $B = 1.08^{+0.25}_{-0.18}$ with an indication of a redshift dependence of $C = -3.8^{+2.0}_{-2.5}$. The same analysis with the multi-halo based estimates of mass yields a result that is consistent within the errors and in terms of its interpretation. Here we find 68% confidence intervals $A = -4.00^{+0.08}_{-0.08}$, $B = 1.13^{+0.25}_{-0.20}$, $C = -4.3^{+2.0}_{-2.7}$. In both cases, the combined (four-parametric) 68% confidence region allows $C = 0$.

If we assume a fixed slope $B = 1.79$ and intrinsic scatter $\sigma_{\mathrm{int,log_{10}}} = 0.07$ from Planck Collaboration et al. (2014c) and determine only the normalization A and the redshift slope C, we get $A = -4.12^{+0.12}_{-0.12}$, in marginal agreement with the Planck Collaboration et al. (2014c) parameters and a $b = 0.2$ hydrostatic bias, and a larger $C = -8.8^{+2.5}_{-2.8}$. The two parameter combined 68% confidence region still includes a wide range of values $C = -8.8^{+5.8}_{-6.0}$. For the multi-halo mass estimates, we find $A = -4.00^{+0.12}_{-0.14}$ and $C = -9.5^{+2.7}_{-2.5}$ (individual parameters) and $C = -9.5^{+6.0}_{-5.8}$ (combined).

Attempts to constrain C are made difficult by the fact that mass and redshift, and therefore B and C, are highly degenerate in the WISCy sample. The combined 68% confidence region of the four parameters allows for a redshift independent MOR with $C = 0$ at the expense of an even shallower mass slope B. In Fig. 5.28 we show the likelihood, based on single-halo mass estimates, in B-C space when fixing A and $\sigma_{\mathrm{int,log_{10}}}$ to their maximum likelihood values (cf. Section 5.7.2).

Finally, in the four-parametric likelihood of A, B, C and $\sigma_{\mathrm{int,log_{10}}}$, a self-similar slope $B = 5/3$ is consistent with the best fit, ($p < 0.42$) at the expense of a non-zero C.

We note that in the overlap of the sample of Hoekstra et al. (2012) with the Planck SZ catalogue, all except one system are at relatively low redshifts around $z \approx 0.2$. The only higher redshift system is MACS J0717.5+3745, a strong lens (Medezinski et al., 2013) at $z = 0.548$. For this cluster, the WL mass measurement by Hoekstra et al. (2012) is $2.5 \ldots 3\sigma$ above either of their fitted MORs, adding evidence to an unaccounted for redshift dependence of the MOR.

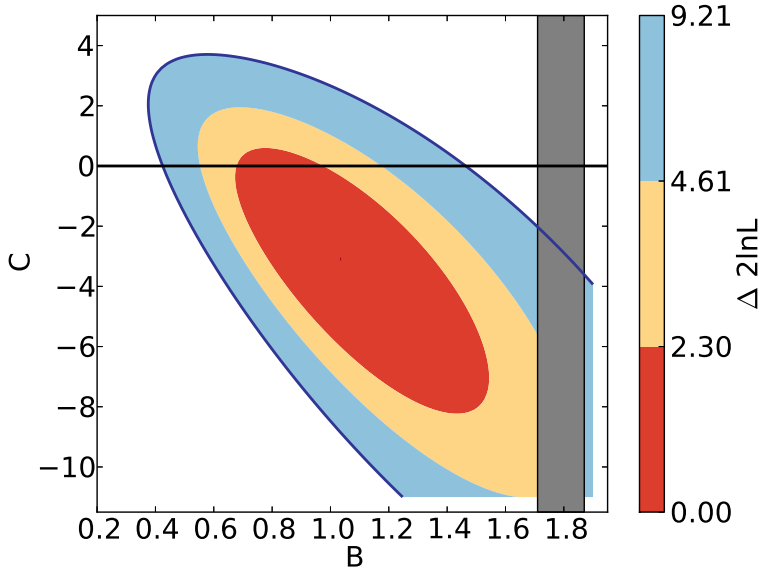

Figure 5.28: Likelihood of mass slope B versus redshift slope C when fixing amplitude and intrinsic scatter of Planck SZ MOR to their best-fitting values (cf. Section 5.7.2). The Planck Collaboration et al. (2014c) value of $B = 1.79 \pm 0.08$ (shaded grey region) is excluded with high significance unless in the case of a large redshift dependence. The physically expected $C = 0$ (black line) requires that the mass slope is significantly shallower.

We conclude by noting that the degeneracy between mass and redshift slope prohibits a conclusion on the origin of the MOR discrepancy from our WL measurement of masses alone.

Comparison with other SZ surveys

A problem with signal extraction or calibration of the Planck SZ would likely lead to differences with other SZ observations of the same clusters, and if the hypothesis of a redshift dependence should hold these differences should in turn be a function of redshift.

Hasselfield et al. (2013) compare SZ mass estimates of 11 clusters detected and published by both ACT and SPT with good agreement (cf. their fig. 21). Planck Collaboration et al. (2013b) have compared Planck and Arcminute Microkelvin Imager (AMI) measurements of 11 clusters, finding significant differences between the two even when assuming the same fixed pressure profile (PP) or a profile fitted to the individual objects based on X-ray observations. Neither of them make a redshift distinction in these analyses, however.

Following the recent releases of Planck (The Planck Collaboration et al. 2014a), ACT (Hasselfield et al., 2013) and SPT (Williamson et al., 2011; Reichardt et al., 2013) catalogues, we match objects detected both in Planck and either of the other catalogues. Rejecting systems with redshift differences $\Delta z > 0.03$ between the two respective catalogues and ones not successfully extracted with the Planck MMF3 algorithm, we find 13 matches with Hasselfield et al. (2013), 11 with Reichardt et al. (2013) and 19 with Williamson et al. (2011) (3 of which are also in Reichardt et al. 2013).

Fig. 5.29 shows the comparison of SZ based mass estimates for these 43 detections. For SPT and ACT, we use the published values of M_{500c}, while for Planck we apply the self-

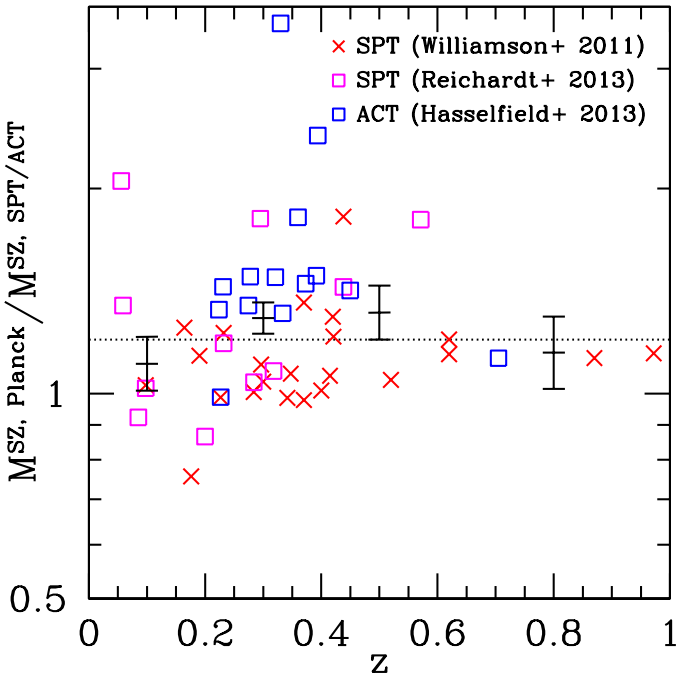

Figure 5.29: Comparison of Planck self-consistent mass estimates with ACT and SPT measurements (Williamson et al., 2011; Hasselfield et al., 2013; Reichardt et al., 2013). The dotted line indicates a 20% excess, the black error bars indicate log-mean values in redshift bins.

consistency technique (see Section 5.5.2) to estimate the mass. The deviation from mean agreement is significant with $\langle \log_{10} M^{\rm Planck}/M^{\rm ACT/SPT} \rangle = 0.10 \pm 0.02$. The binned geometric mean of the mass ratios is consistent with a 20% excess in the Planck estimates (corresponding to the hydrostatic bias factor applied there) with no significant indication for redshift dependence. For ACT, we have used the $M_{500c}^{\rm UPP}$ values based on the Arnaud et al. (2010) PP. Use of the alternative simulation and X-ray based Bode et al. (2012) MOR increases the ACT masses significantly, yet with no strong trend in redshift.

While this comparison therefore yields no evidence for a redshift dependence in the Planck catalogues that would support our WL based findings, the number of sometimes strong outliers indicates that the statistical uncertainties according to our interpretation of the Planck likelihoods might not be appropriate. A significantly larger uncertainty due to assumptions made during signal extraction, for instance, could reconcile the two strong outliers in our sample (PSZ1 G168.02–59.95 and PSZ1 G099.84+58.45) with the WL estimate and alleviate the tension with the assumption of redshift independence of the MOR.

5.7.5 Centring and shear

We briefly test the appropriateness of the NFW profile and our background selection scheme by comparing the tangential reduced shear measured in the innermost 2 arcmin around the cluster centre to the model prediction. The latter is derived from the confidence region in mass according to our shear profile fit (that only uses galaxies outside 2 arcmin radius) and assuming the Duffy et al. (2008) concentration-mass relation.

Deviations between model and data could be explained, for instance, by incorrect treat-

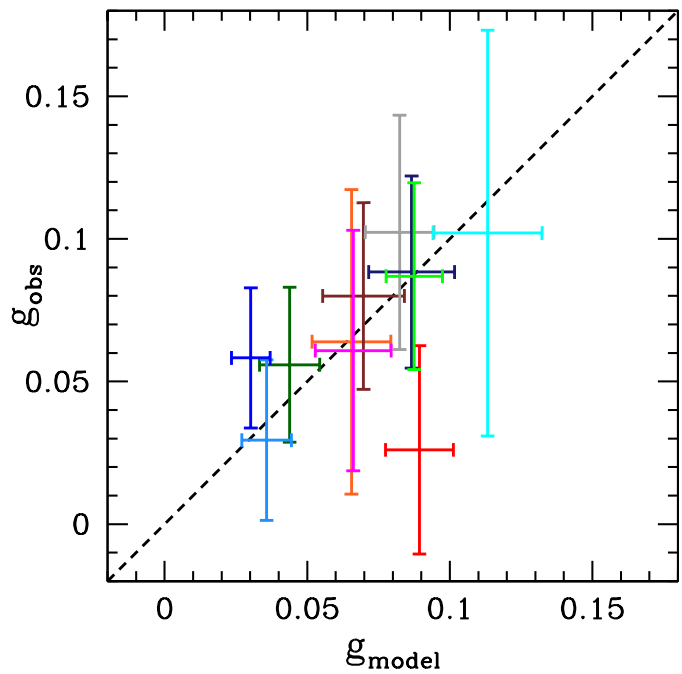

Figure 5.30: Central ($r \leq 2$ arcmin) reduced tangential shears as measured plotted against values according to NFW model fitted outside that region. The agreement between the two is consistent with the claim that the central slope of density profiles is as predicted by the model and our background selection is correct.

ment of the abundance of cluster members near the centre, offsets of the assumed from the true centre (for instance due to multimodality of the density profile), a deviation of the central mass profile slope from the NFW prediction or second-order shear bias (cf. Young et al., in preparation).

Fig. 5.30 shows the comparison of the model and measurement, which are consistent within the errors. The ratio of mean shears between model and data is 1.02 ± 0.10.

5.8 Conclusions

We have performed a weak lensing (WL) analysis of twelve clusters of galaxies selected by their Sunyaev-Zel'dovich (SZ) effect.

Among the methods for cluster WL measurements developed and used in the process are a magnitude-based background galaxy selection procedure, along with an account for contamination with cluster members and an optimised background cut (Section 5.3.1).

Several of the systems in our sample are very interesting in their own right, among them the *HST* Frontier Field clusters RXC J2248.7–4431 and MACS J0416.1–2403, but also SPT-CL J2355–5056 with its complex structures of neighbouring haloes and PLCKESZ G287.0+32.9 with a very large strong lensing cross-section as based on a large number of candidate strong lensing arcs.

The WL analysis of our cluster sample is consistent with zero mean bias in hydrostatic X-ray masses and no dependence of bias on mass. The gas fraction of our clusters is $f_{\mathrm{gas},500c} =$

$0.128^{+0.029}_{-0.023}$, in line with previous results and expectations.

Our main scientific goal, however, was the comparison of WL measurements with published SZ significances and Compton parameters according to mass-observable relations (MORs) for the SPT and *Planck* surveys.

We have found agreement with the SPT calibration, calibrated both from simulations (Vanderlinde et al., 2010; Reichardt et al., 2013) and a combined cosmology fit to X-ray observations and CMB (Benson et al., 2013), both with and without simultaneous modelling of surrounding projected structures.

In our combined sample, we have confirmed a trend of excess SZ mass estimate with respect to the WL measurement increasing with the projected ellipticity of the BCG, a proxy for projected halo elongation, as noticed before by Marrone et al. (2012).

Finally, our analysis of five Planck SZ-detected clusters shows significant disagreement with the Planck Collaboration et al. (2014c) SZ mass-observable relation as calibrated from X-ray observations. Multiple explanations appear possible, among them are as follows.

- A shallower mass slope of the MOR – we find a projected 68% confidence interval of $B = 0.76^{+0.20}_{-0.20}$, significantly shallower than the Planck Collaboration et al. (2014c) value of $B = 1.79$, which our data disfavours w.r.t. the best fit at 2.5σ significance in the three-dimensional parameter space. It appears difficult to find a physical reason for such a strong deviation from the self-similar $B = 5/3$. This is the case even more so as WL analyses of other SZ samples (including the WISCy SPT sample, Marrone et al. 2012 and Hoekstra et al. 2012) or X-ray samples (including WISCy) are compatible with the self-similar slope.

- An unaccounted for redshift dependence of the Compton parameter measurement – this could either be unphysical and related to the low resolution of the Planck beam compared to the angular size of moderate to high redshift clusters, or physical and related to a deviation of the pressure profiles of high redshift clusters from the locally determined Arnaud et al. (2010) profile. Speaking against the first hypothesis is the fact that *Planck* measurements and SZ observations of higher resolution agree without a strong trend in redshift (cf. Sec. 5.7.4).

- Noise bias – the simplified treatment of Malmquist bias (cf. equation 5.25) does not cover the full effect of biased object selection near the noise limit of the Planck SZ map. What speaks against this explanation is the fact that, in our sample, objects with relatively low SZ S/N ratio (all PSZ1 clusters) are found to be outliers in different directions.

- Sample variance – while these findings are of high formal significance, even given the small sample, one must be careful not to over-interpret the data. For instance, effects of blending with substructure (in the case of PLCKESZ G292.5+22.0) and halo orientation (in the cases of PSZ1 G099.48+55.62, PSZ1 G168.02–59.95 and PSZ1 G099.84+58.45, with large (small) BCG ellipticity at the lowest (highest) redshifts in our sample, respectively) could contribute to the deviations we observe. Blending might be a particularly severe problem in Planck due to the comparatively large beam size and is investigated in more detail in Kosyra et al. (in preparation). It would cause an effect different from intrinsic scatter, since blending can only *add* to the observed signal at fixed mass of the central halo.

The first two points especially are intrinsically hard to disentangle, since there is a strong correlation of mass and redshift in our sample and the Planck SZ catalogue in general. The most likely interpretation of our data, in light of Section 5.7.4, may be a moderate size/redshift dependent bias that would marginally reconcile our measurements with the self-similar B. Additional lensing measurements of SZ clusters, particularly at high redshift, would be of great value for testing the underlying assumptions on the pressure profile and the mass-observable relations themselves.

Acknowledgments

The authors thank Stefano Andreon, Bradford Benson, Lindsey Bleem, Gael Foëx, Eduardo Rozo, Mauro Sereno, Jochen Weller and Julia Young for helpful discussions.

This work was supported by SFB-Transregio 33 'The Dark Universe' by the Deutsche Forschungsgemeinschaft (DFG) and the DFG cluster of excellence 'Origin and Structure of the Universe'.

For the ESO Deep Public Survey data used in this work, observations have been carried out using the MPG/ESO 2.2m Telescope and the ESO New Technology Telescope (NTT) at the La Silla observatory under Program-ID No. 164.O-0561.

This work is based in part on observations obtained with MegaPrime/MegaCam, a joint project of CFHT and CEA/IRFU, at the Canada-France-Hawaii Telescope (CFHT) which is operated by the National Research Council (NRC) of Canada, the Institut National des Sciences de l'Univers of the Centre National de la Recherche Scientifique (CNRS) of France, and the University of Hawaii. This research used the facilities of the Canadian Astronomy Data Centre operated by the National Research Council of Canada with the support of the Canadian Space Agency. CFHTLenS data processing was made possible thanks to significant computing support from the NSERC Research Tools and Instruments grant program.

Part of this work has used spectroscopic data from SDSS-III. Funding for SDSS-III has been provided by the Alfred P. Sloan Foundation, the Participating Institutions, the National Science Foundation, and the U.S. Department of Energy Office of Science. The SDSS-III website is http://www.sdss3.org/.

SDSS-III is managed by the Astrophysical Research Consortium for the Participating Institutions of the SDSS-III Collaboration including the University of Arizona, the Brazilian Participation Group, Brookhaven National Laboratory, Carnegie Mellon University, University of Florida, the French Participation Group, the German Participation Group, Harvard University, the Instituto de Astrofisica de Canarias, the Michigan State/Notre Dame/JINA Participation Group, Johns Hopkins University, Lawrence Berkeley National Laboratory, Max Planck Institute for Astrophysics, Max Planck Institute for Extraterrestrial Physics, New Mexico State University, New York University, Ohio State University, Pennsylvania State University, University of Portsmouth, Princeton University, the Spanish Participation Group, University of Tokyo, University of Utah, Vanderbilt University, University of Virginia, University of Washington, and Yale University.

This research has made use of the SIMBAD data base, operated at CDS, Strasbourg, France.

Appendix A: Secondary components

The following table lists secondary clusters and groups in the cluster fields that were visually identified from colour images and redshift-sliced density maps or are listed in the SIMBAD database.

ID	R.A.	dec	r [’]	z	M_{200m}	external reference
SPT-CL J0509–5342						
A	05:09:11	-53:39:29	3.2	0.45^b	$2.4^{+2.6}_{-2.0}$	-[1]
B	05:07:50	-53:48:30	15.4	0.41^b	$0^{+2.3}_{-0.0}$	-
SPT-CL J0551–5709						
A	05:51:33	-57:14:21	5.7	0.09^c	$0^{+0.8}_{-0.0}$	ACO S 552 (Abell et al., 1989)
B	05:51:52	-57:18:15	9.8	0.59^b	$0^{+3.2}_{-0.0}$	-
SPT-CL J2332–5358						
A	23:32:36	-54:02:00	3.7	0.33^a	$0^{+1.0}_{-0}$	SCSO J233231.4–540135.8 (Menanteau et al., 2009)
B	23:33:32	-54:00:53	9.7	0.2^b	$0^{+0.8}_{-0.0}$	-
C	23:32:41	-54:08:20	10.0	0.71^b	$1.2^{+4.8}_{-1.2}$	-
D	23:30:31	-53:51:50	18.4	0.24^b	$5.0^{+2.9}_{-1.8}$	-
SPT-CL J2355–5056						
A	23:55:26	-50:53:26	4.0	0.3^b	$6.7^{+2.9}_{-2.1}$	-
B	23:55:10	-50:56:26	6.0	0.3^b	$1.2^{+1.7}_{-1.2}$	-
C	23:56:33	-50:57:12	7.4	0.24^b	$4.5^{+1.7}_{-1.7}$	-
D	23:55:38	-51:08:34	13.0	0.75^b	$24.3^{+6.9}_{-12.8}$	-
E	23:55:57	-51:10:15	14.8	0.11^b	$0.4^{+1.2}_{-0.4}$	APMCC 936 (Dalton et al., 1997)
F	23:54:20	-51:09:10	19.3	0.42^b	$2.2^{+4.5}_{-2.2}$	-
PLCKESZ G287.0+32.9						
A	11:50:57	-28:07:38	3.1	0.39^b	$0.8^{+2.4}_{-0.8}$	-
PLCKESZ G292.5+22.0						
A	12:01:11	-39:54:44	2.5	0.3^b	$0^{+2.9}_{-0.0}$	-
B	12:01:22	-39:51:22	3.3	0.3^b	$0^{+1.0}_{-0.0}$	-
C	12:01:17	-39:49:02	4.1	0.3^b	$0.9^{+2.7}_{-0.9}$	-
D	12:01:19	-39:46:20	6.6	0.3^b	$10.0^{+4.2}_{-4.4}$	-
E	12:01:35	-40:04:39	13.5	0.43^b	$7.0^{+4.0}_{-3.1}$	-
MACS J0416.1–2403						
A	04:16:22	-24:15:16	11.6	0.42^b	$3.9^{+2.0}_{-1.9}$	-
B	04:16:55	-24:16:04	16.4	0.23^b	$0^{+0.8}_{-0.0}$	-
C	04:14:58	-24:12:01	18.1	0.41^b	$0.6^{+1.4}_{-0.6}$	-
PSZ1 G168.02–59.95						
A	02:15:12	-04:44:51	13.3	0.2950^d	$3.0^{+1.2}_{-1.4}$	-
B	02:15:28	-04:40:41	13.5	0.3503^d	$1.8^{+1.4}_{-1.3}$	-
PSZ1 G230.73+27.70						
A	09:01:45	-01:38:22	3.7	0.2944^f	$0.0^{+1.3}_{-0.0}$	MaxBCG J135.43706–01.63946 (Koester et al., 2007)
B	09:01:45	-01:42:36	4.9	0.25^e	$2.9^{+2.3}_{-2.9}$	ZwCl 0859.2-0130 (Zwicky et al., 1961)
C	09:02:22	-01:27:32	17.1	0.2998^f	$0.0^{+1.6}_{-0.0}$	MaxBCG J135.59007–01.46456 (Koester et al., 2007)
PSZ1 G099.84+58.45						
A	14:14:48	54:55:59	8.9	0.2285^d	$0.9^{+1.3}_{-0.9}$	-
B	14:14:22	54:57:10	10.7	0.1581^d	$2.6^{+1.4}_{-1.4}$	-
C	14:13:07	54:58:36	18.4	0.77^e	$6.4^{+7.5}_{-5.7}$	-
D	14:12:49	54:31:04	23.4	0.69^e	$1.8^{+6.2}_{-1.8}$	-

Table 5.5: Sources for redshifts: (a) Menanteau et al. (2009), (b) red galaxy colour method of Section 5.4.5, (c) High et al. (2010), (d) spectroscopic redshift from SDSS, (e) photometric redshift (this work), (f) Koester et al. (2007). Additional notes: (1) this component is close to an extended X-ray source reported by Andersson et al. (2011). All masses are given in units of $10^{14} h_{70}^{-1} M_\odot$.

Chapter 6

Cosmic variance of the galaxy cluster weak lensing signal

Prologue

Lensing is a continuous struggle with noise. The rareness of their photons means that background galaxy images are noisy, hindering the measurement of their shapes. The intrinsic galaxy shapes and their limited number density, even in exceptionally deep and sharp data, mean that the weak shear around any single object can only ever be measured with moderate signal-to-noise ratio. The fact that photons are deflected by all structures along the line of sight implies that the shear signal of all but the most dominant clusters is potentially strongly affected by unrelated structures. These effects are sources of uncertainty when measuring the mass of a galaxy cluster with weak lensing. But that was not yet all.

Additional noise in cluster mass measurement is due to the variation of projected cluster density profiles at fixed mass and redshift, which is the subject of this project. With a semi-analytical model fitted to cluster profiles in N-body simulations, I find that this effect significantly influences weak lensing measurements of cluster mass. When not accounted for, the additional noise biases the constraints a weak lensing cluster survey can put on the parameters of a mass-observable relation and, consequently, cosmology. With an appropriate model for the profile variation, however, this can be prevented. The advantage of weak lensing, after all, is systematic accuracy, not statistical precision on individual objects.

This chapter is based on the paper Gruen, Seitz, Becker, Friedrich, & Mana (2015b), accepted for publication in MNRAS. The model ansatz, all theory codes for calculating components of the model, analysis and fitting code for determining model parameters, and the predictions in Section 6.5 were done by myself. Matthew R. Becker provided the lensing maps of simulated clusters used in this work. The convergence power spectrum used in Section 6.3.2 was calculated using a version of the NICAEA software modified by Oliver Friedrich. The cosmological and halo model codes were compared against the implementation of Annalisa Mana. All authors contributed to discussions and proofreading.

Copyright for the paper will be transferred to Oxford University Press for publication. Permission for non-commercial re-use of the material has been confirmed by the MNRAS editorial office.

Abstract

Intrinsic variations of the projected density profiles of clusters of galaxies at fixed mass are a source of uncertainty for cluster weak lensing. We present a semi-analytical model to account for this effect, based on a combination of variations in halo concentration, ellipticity and orientation, and the presence of correlated haloes. We calibrate the parameters of our model at the 10 per cent level to match the empirical cosmic variance of cluster profiles at $M_{200m} \approx 10^{14} \ldots 10^{15} h^{-1} M_\odot$, $z = 0.25 \ldots 0.5$ in a cosmological simulation. We show that weak lensing measurements of clusters significantly underestimate mass uncertainties if intrinsic profile variations are ignored, and that our model can be used to provide correct mass likelihoods. Effects on the achievable accuracy of weak lensing cluster mass measurements are particularly strong for the most massive clusters and deep observations (with ≈ 20 per cent uncertainty from cosmic variance alone at $M_{200m} \approx 10^{15} h^{-1} M_\odot$ and $z = 0.25$), but significant also under typical ground-based conditions. We show that neglecting intrinsic profile variations leads to biases in the mass-observable relation constrained with weak lensing, both for intrinsic scatter and overall scale (the latter at the 15 per cent level). These biases are in excess of the statistical errors of upcoming surveys and can be avoided if the cosmic variance of cluster profiles is accounted for.

6.1 Introduction

The largest objects ever formed depend most sensitively on small changes in the overall properties of the universe. It is for this reason that clusters of galaxies are a versatile probe of cosmology. The number density of clusters and its evolution with redshift is influenced by the expansion history, the density and level of inhomogeneity of matter in the universe and the growth of structures by means of gravitation. Both the parameters of a standard Λ cold dark matter (ΛCDM) model and deviations from primordial Gaussianity or General Relativity are therefore accessible to cluster cosmology (cf., e.g., Allen et al. 2004; Vikhlinin et al. 2009b; Rozo et al. 2010; Mantz et al. 2010b; Mana et al. 2013; Benson et al. 2013; Planck Collaboration et al. 2014c; Mantz et al. 2015 for individual analyses and Allen et al. 2011 for a recent review).

The building blocks of such analyses are (i) a cluster catalogue with well-defined selection function based on, e.g. optical, X-ray or Sunyaev & Zel'dovich (1972, hereafter SZ) properties, (ii) a prediction, based on theory or simulations, of how the number density of clusters at given mass and redshift depends on the cosmological parameters in question (e.g. Press & Schechter, 1974; Sheth & Tormen, 1999; Tinker et al., 2008) and (iii) a mass-observable relation (MOR) that connects the observable from (i) to the mass-based prediction from (ii) in terms of a likelihood. The latter must not only describe the mean relation of mass and observable but, because of the observable limited nature of any practical survey, also the intrinsic scatter in the observable at fixed mass (e.g. Lima & Hu, 2005).

With the advent of large cluster catalogues, our imperfect knowledge of the MOR remains the most important limiting factor of cluster cosmology. It is difficult to predict or simulate, to the level of accuracy required, all physical effects that influence the observables, particularly ones that are of baryonic nature. Thus, one needs to rely on an empirical calibration of the MOR.

The latter can in principle be done by means of self-calibration, i.e. by constraining both cosmology and MOR parameters from the cluster catalogue alone (Hu, 2003; Majumdar &

Mohr, 2004; Lima & Hu, 2005). However, this approach greatly reduces the cosmological power of cluster studies, especially when extensions to the most simple MOR and cosmological models are considered.

It is for this reason that weak lensing studies of clusters of galaxies are a particularly powerful complement to cluster cosmology. Being sensitive to all matter independent of its astrophysical state, lensing allows, in principle, an unbiased measurement of cluster mass. Several studies have used this approach to constrain MORs with lensing mass measurements of sets of individual clusters (e.g. Marrone et al., 2009, 2012; Hoekstra et al., 2012; von der Linden et al., 2014a; Gruen et al., 2014b; Mantz et al., 2015), with great prospects of further improving statistics with on-going and future large surveys.

For accurate constraints on the mean MOR and its intrinsic scatter to be derived, one needs to ensure that the mass likelihood from a lensing analysis includes all actual sources of uncertainty. For typical cluster lensing studies, the dominant uncertainty is observational, i.e. based on the limited number of intrinsically elliptical background galaxies. Since all structures between sources and observer cause a lensing signal, an additional, irreducible uncertainty results from the variance of the matter density along the line of sight (LOS; cf. e.g. Hoekstra, 2001, 2003). Most cluster lensing studies include either only the first or both of these effects when fitting the signature of a mass dependent density profile to observed data.

There is another source of uncertainty in weak lensing mass estimates, however, based on the fact that the projected density profiles of two clusters at the same virial mass can differ greatly. This could be described accurately only with detailed information about the shape and orientation of their central dark matter halo and the positions and masses of subhaloes and neighbouring structures. Due to its relatively low resolution, no weak lensing analysis is able to uncover all or even most of this information. However, the uncertainty of mass measurement will depend on the statistical properties of these variations. Previous work has either taken this source of noise into account with a low-parametric model for differences at fixed mass [most commonly only in terms of the concentration parameter, although see e.g. Marshall et al. (2002); AMI Consortium: Hurley-Walker et al. (2012) for a more complex Bayesian model], by means of an additional scatter in the relation between lensing-derived and true mass (e.g. Gruen et al., 2014b; Sereno & Ettori, 2014; Mantz et al., 2015), or neglected it entirely.

The goal of this work is to provide a model for the variations in projected density profiles of cluster of galaxies at fixed mass. We construct our model using analytical templates for the expected scatter due to variations in halo concentration, ellipticity and orientation, and its substructure and cosmic neighbourhood. We re-scale these templates to match the empirical variations of cluster profiles in a cosmological simulation, where both well-defined true masses and the lensing signal without any observational noise are known. We then use this semi-analytical covariance model to test and predict the accuracy of lensing measurements of cluster mass and MORs, and to assess the effect of neglecting intrinsic variations.

The structure of this paper is as follows. In Section 6.2, we briefly describe the simulations used. Section 6.3 defines the components of our model for the mean cluster profile and, in particular, its intrinsic covariance. In Section 6.4, we explain how the model is fitted to the simulated data. Effects of the intrinsic covariance on weak lensing cluster mass measurements and MOR studies are shown in Section 6.5, before we summarize in Section 6.6.

Conventions

Our calculations are presented in a flat *WMAP* 7 year cosmology (Komatsu et al., 2011) with $(\Omega_\mathrm{m}, \Omega_\mathrm{b}, \sigma_8, h, n) = (0.27, 0.044, 0.79, 0.7, 0.95)$, in consistency with the simulations used. The covariances can be readily re-scaled to different sets of cosmological parameters, up to a potential cosmology dependence of our model parameters. We explicitly write appropriate factors of $h = H_0/(100\ \mathrm{km\ s^{-1}\ Mpc^{-1}})$ where applicable. We denote the radii of spheres around the cluster centre with fixed overdensity as $r_{\Delta\mathrm{m}}$, where $\Delta = 200$ is the overdensity factor of the sphere with respect to the mean matter density ρ_m at the cluster redshift. The mass inside these spheres is labelled and defined correspondingly as $M_{\Delta\mathrm{m}} = \Delta \times \frac{4\pi}{3} r^3_{\Delta\mathrm{m}} \rho_\mathrm{m}$.

We use a linear matter power spectrum $P_\mathrm{lin}(k,z) = D^2(z) P_\mathrm{lin}(k,0)$ with the transfer function model including baryonic effects of Eisenstein & Hu (1998) and normalize to our value of σ_8. For the linear growth factor $D(z)$, normalized to $D(0) = 1$, we use the expression of Peacock & Dodds (1996). We define the corresponding linear matter two-point correlation as

$$\xi_\mathrm{lin}(r,z) = \frac{1}{2\pi^2} \int dk k^2 P_\mathrm{lin}(k,z) \frac{\sin(kr)}{kr} \ . \tag{6.1}$$

For the scaling of some of the cluster properties we will use the common definition of peak height

$$\nu = \delta_c / \sigma(M_{200m}, z) \ , \tag{6.2}$$

where $\delta_c = 1.686$ and

$$\sigma^2(M_{200m}, z) = D^2(z) \frac{1}{2\pi^2} \int dk\ k^2\ P_\mathrm{lin}(k,0) \left| w\left[k, \left(\frac{3M_{200m}}{4\pi\rho_{0,m}}\right)^{1/3}\right]\right|^2 , \tag{6.3}$$

with the Fourier transform of the top-hat window function of radius r, $w(k,r)$.

6.2 Simulations

We use the simulation labeled L1000W in Tinker et al. (2008). It consists of 1024^3 dark matter particles of mass $6.98 \times 10^{10} h^{-1} M_\odot$ in a box of comoving size 1 h^{-1} Gpc, simulated with the parallelized Adaptive Refinement Tree algorithm (Kravtsov et al., 1997; Gottloeber & Klypin, 2008) from redshift $z = 60$ to 0, at an effective spatial resolution of $30h^{-1}$ kpc. In a snapshot at redshift $z = 0.24533$ almost 15,000 haloes at $0.95 \times 10^{14} h^{-1} M_\odot \leq M_{200m} \leq 1.5 \times 10^{15} h^{-1} M_\odot$ are identified.

The same haloes are also used in Becker & Kravtsov (2011) and we employ the lensing maps computed in that work. For the selected haloes, the mass is integrated along the LOS and the lensing signal is determined on a grid of approximately 40 comoving kpc pixel^{-1} using the Born approximation as described in Becker & Kravtsov (2011, section 3). All matter within comoving $\pm 200\mathrm{Mpc}h^{-1}$ along the LOS and, transversely, in a square with comoving side length $20\mathrm{Mpc}h^{-1}$ centred on the cluster is included in the calculation. Background sources are assumed to be at a constant redshift $z_\mathrm{s} = 1$, where $\Sigma_\mathrm{crit} = 4.22 \times 10^{15} h M_\odot \mathrm{Mpc}^{-2}$. The density map inside a clustrocentric radius $\theta < 1$ arcmin is subject to resolution effects (Becker & Kravtsov, 2011, section 3), which is why we discard it from our analysis.

6.3 Model definition

In the following, we introduce our model for the covariance of projected cluster profiles. Its components, namely the model for the mean profile (Section 6.3.1) and the contributions to the covariance (Section 6.3.2), are described subsequently.

Consider the convergence profile of a given cluster with mass $M_{200m} =: M$ as

$$\boldsymbol{K} = \boldsymbol{\kappa}(M) + \boldsymbol{E} \ , \tag{6.4}$$

where $\boldsymbol{K}$ is the observed convergence profile and $\boldsymbol{\kappa}(M)$ is the mean convergence profile of clusters of fixed mass M. $\boldsymbol{E}$ is the residual between the two, which arises due to observational uncertainty and variations of the noiseless observable κ profile at fixed mass. These variations could be due to uncorrelated structures along the LOS or the projected cluster density profile itself. The latter *intrinsic* variations are the focus of this work.

The profiles are vectors measured in a system of radial bins, where bin $1 \leq i \leq n$ is defined as $\theta \in [\theta_{i,\mathrm{min}}, \theta_{i,\mathrm{max}}]$ without gaps, i.e. $\theta_{i,\mathrm{max}} = \theta_{i+1,\mathrm{min}}$.

Approximating the residuals $\boldsymbol{E}$ as a multivariate Gaussian with zero mean, one can write the likelihood for an observed $\boldsymbol{K}$ given a mass M as

$$\mathcal{L}(\boldsymbol{K}|M) = \frac{1}{\sqrt{(2\pi)^n \det[C(M)]}} \exp\left[-\frac{1}{2}\boldsymbol{E}^{\mathrm{T}} C^{-1}(M)\boldsymbol{E}\right] \ , \tag{6.5}$$

where we have introduced the covariance C of residuals $\boldsymbol{E}$. This $n \times n$ matrix is defined as

$$C_{ij} = \mathrm{Cov}(E_i, E_j) \ . \tag{6.6}$$

We make a semi-analytic ansatz for a parametric model of C as

$$C(M) = C^{\mathrm{obs}} + C^{\mathrm{LSS}} + c^{\mathrm{conc}}(\nu)C^{\mathrm{conc}}(M) + c^{\mathrm{corr}}(\nu)C^{\mathrm{corr}}(M) + c^{\mathrm{ell}}(\nu)C^{\mathrm{ell}}(M) \tag{6.7}$$

with contributions from observational uncertainty (i.e., shape noise in shear measurement and Poisson noise in magnification studies) C^{obs}, uncorrelated large-scale structure along the LOS C^{LSS}, scatter in halo concentration C^{conc}, correlated secondary haloes near the cluster C^{corr} and variations in halo ellipticity and orientation C^{ell}. The terms C^{obs} and C^{LSS} are independent of the cluster itself. In contrast to the common case where only these are considered, however, $C(M)$ inherits a mass dependence from the latter terms, which we will call *intrinsic* variations of the cluster profile. They are described in detail in Section 6.3.2. The empirical re-scaling factors $c^{\star}(\nu)$ of C^{corr}, C^{ell} and C^{conc} are determined by fitting the covariance model to the simulated haloes (see Section 6.4).

6.3.1 Mean profile

Several studies in the past have proposed functional forms for the three-dimensional density of dark matter haloes. Navarro, Frenk, & White (1997, hereafter NFW) found that haloes are well-fit by the two-parametric broken power-law profile

$$\rho_{\mathrm{NFW}}(r) = \frac{\rho_0}{(r/r_{\mathrm{s}})(1 + r/r_{\mathrm{s}})^2} \ , \tag{6.8}$$

with scale density ρ_0 and a scale radius r_{s} that can be expressed as a fraction of r_{200m} using the concentration $c_{200m} = r_{200m}/r_{\mathrm{s}}$.

Two additional effects need to be accounted for in a realistic description of halo density profiles. First, the enclosed mass of an NFW profile diverges logarithmically as $r \to \infty$. The density must therefore be truncated at large radii, for which a number of approaches have been proposed (e.g. Takada & Jain 2003; Hayashi & White 2008; Baltz, Marshall, & Oguri 2009, hereafter BMO). Secondly, the halo is embedded in an overdensity of correlated matter that contributes to the overall projected profile at all, and dominantly at large, radii. We closely follow the work of Oguri & Hamana (2011), who fit a superposition of a BMO profile with a linear two-halo term to simulated haloes, i.e.

$$\Sigma(M) = \kappa(M)\Sigma_{\rm crit} = \Sigma_{\rm 1h,BMO}(M) + \Sigma_{\rm 2h,lin}(M) \; . \tag{6.9}$$

We describe the one-halo (Section 6.3.1) and two-halo term (Section 6.3.1) in the following.

One-halo term

BMO define a truncated version of the NFW profile as

$$\rho_{\rm BMO}(r) = \rho_{\rm NFW}(r) \times \left(\frac{\tau_{200m}^2}{(r/r_{200m})^2 + \tau_{200m}^2} \right)^{\beta} \; , \tag{6.10}$$

where we use $\beta = 2$. Here we have introduced τ_{200m}, the multiple of r_{200m} around which the halo is smoothly truncated. The BMO profile can be analytically integrated to yield the projected profile $\Sigma_{\rm 1h,BMO}$, as well as the change in mass normalization due to missing density relative to the NFW profile (cf. BMO; Oguri & Hamana 2011 and the AMPLE code, `http://kipac.stanford.edu/collab/research/lensing/ample/ample.c`).

Besides mass, our one-halo term has two additional free parameters, the concentration c_{200m} and truncation radius τ_{200m}. We fix the former with the mass-concentration relation of Duffy et al. (2008). Oguri & Hamana (2011) note a weak dependence of $\tau_{\Delta_{\rm vir}{\rm m}}$ on mass. Our scaling relation of τ_{200m} is determined by fitting the mean κ profile of haloes in our simulation (cf. Section 6.2) in logarithmic bins of $\Delta \log_{10} M_{200m} = 0.05$ in the radial range of 3 to 15 arcmin using the full profile of equation (6.9), with τ as a free parameter. The uncertainties for our χ^2 minimization w.r.t. τ are derived from the ensemble variance of mean κ in the respective mass bin. We find that the relation is well described as a linear function of ν. Our fit in $\nu \in [2.2, 3.7]$ yields

$$\tau_{200m} = \begin{cases} 3.85 - 0.73\nu & \nu \leq 3.7 \\ 1.15 & \nu > 3.7 \end{cases} \; , \tag{6.11}$$

where we have assumed a constant value for τ_{200m} above the peak height range covered by our simulated haloes.

We note that the fact that more massive haloes are, on average, truncated at smaller multiples of their r_{200m} radii could be interpreted in terms of the steepening of the density slope with increasing mass accretion rate observed by Diemer & Kravtsov (2014).

Two-halo term

The two-halo surface mass density due to linear evolution around a cluster of mass M at redshift z can be written as (e.g. Oguri & Hamana 2011)

$$\Sigma_{\rm 2h,lin}(\theta) = b_{\rm h}(M,z)\, \rho_{c,0}\, \Omega_{\rm m}\, W(\theta,z)\, D_{\rm A}^{-2}(z) \; . \tag{6.12}$$

Here, $b_{\rm h}(M,z)$ is the linear bias of the cluster halo (which we calculate according to Tinker et al. 2010) and $D_{\rm A}(z)$ is the angular diameter distance to redshift z. We have defined the projected linear excess Lagrangian depth $W(\theta,z)$ as

$$\begin{aligned} W(\theta,z) &= [D_{\rm A}(z)\,(1+z)]^2 \int_{-\Delta\zeta}^{+\Delta\zeta} \xi_{\rm lin}\left(\sqrt{[D_{\rm A}(z)\,(1+z)\,\theta]^2+\zeta^2}, z\right) {\rm d}\zeta \\ &= \int \frac{l{\rm d}l}{2\pi}\, J_0(l\theta)\, P_{\rm lin}\left(\frac{l}{(1+z)D_{\rm A}(z)}, z\right) , \end{aligned} \tag{6.13}$$

where $\pm\Delta\zeta$ is the interval in comoving distance along the LOS integrated in our simulated projected density profiles. For large enough $\Delta\zeta$, almost all correlated matter is included in the integration and the latter equality holds. In equation (6.13), we have used the Bessel function of the first kind and order zero, J_0. W has units of comoving volume per solid angle and is readily interpreted as the excess in Lagrangian volume per solid angle that has moved to the projected vicinity of a structure with unit bias due to linear evolution.

The mass measurements of our haloes from the simulations contain all particles within r_{200m}. We therefore need to correct for contributions of two-halo matter $M_{\rm 2h}$ when defining the mass of the one-halo profile, which we do at first order as

$$M_{200m,1h} = M_{200m} - M_{\rm 2h}(r_{200m}, M_{200m}, z) \; . \tag{6.14}$$

Inside a sphere of radius r around the cluster centre, the mass of two-halo matter is

$$M_{\rm 2h}(r,M,z) = b_{\rm h}(M,z)\,\rho_{c,0}\,\Omega_{m,0}\,U(r,z) \; . \tag{6.15}$$

Here we have defined the linear excess Lagrangian volume inside a sphere of radius r as

$$U(r,z) = \int_0^{r(1+z)} {\rm d}r' \xi_{\rm lin}(r',z)\,4\pi r'^2 = D^2(z)\,U(r(1+z),0) \; . \tag{6.16}$$

Comparison to simulations

Figure 6.1 shows model and mean profiles of simulated haloes in two mass bins spanning most of the dynamic range of our halo catalogue (see Section 2.4 for details on the simulations). The model fits the data well at projected $r > 0.3 \times r_{200m}$, but moderately overestimates projected density at smaller radii, where an un-truncated NFW profile without two-halo contribution is a better fit. Potential reasons for the discrepancy include factual deviations of the simulated dark matter haloes from the NFW profile at small radii (cf. Becker & Kravtsov 2011, their Fig. 2, for an analysis based on the same cluster sample) and the simplified nature of our linear superposition of the collapsed halo profile with a linear two-halo term (cf. Hayashi & White 2008 for a different approach, in which the three-dimensional density is assumed to be piecewise equal to the NFW one-halo or a linear two-halo term, only). Since we only use the model for re-normalization of the ensemble mean profile to the mass of a given cluster (cf. Section 6.3.3), this is not problematic for our purposes.

6.3.2 Components of profile covariance

We have made the ansatz for the residual between a given, noise-free cluster κ profile $\boldsymbol{K}$ and the mean profile at its mass $\boldsymbol{\kappa}(M)$ as a sum of multivariate Gaussian vectors corresponding

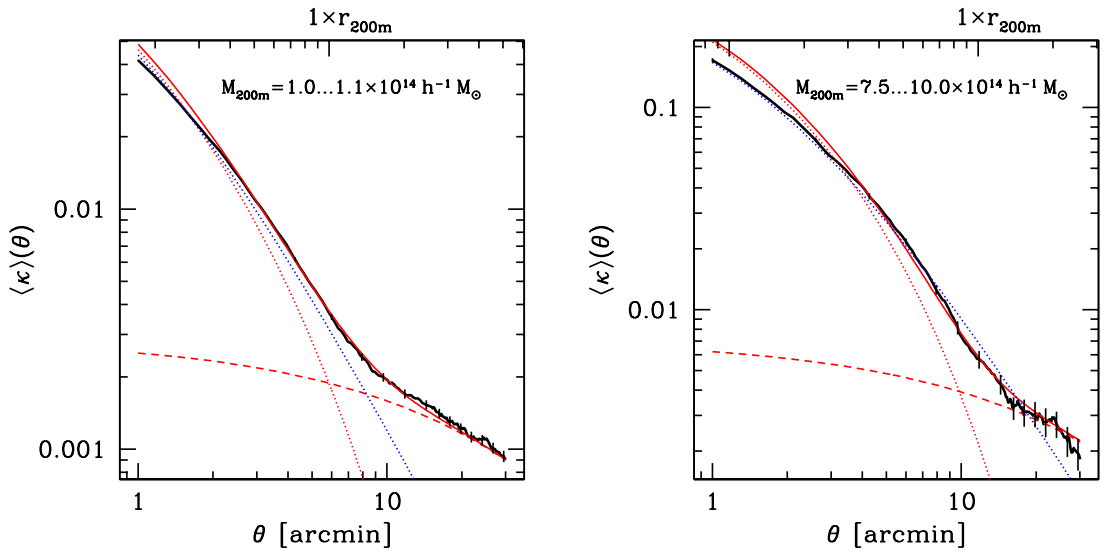

Figure 6.1: Mean convergence profiles of haloes at the low-mass (left) and high-mass (right) end of our sample, shown for haloes at the simulation redshift $z = 0.24533$ with corresponding angular (bottom axis) and r_{200m} (top axis) scales. Black lines show average profiles in the simulations, with error bars giving the uncertainty of the mean. Our model is shown as the red, solid line, composed of the BMO one-halo term (red, dotted) with truncation radius according to equation 6.11 and the two-halo term (red, dashed). The blue, dotted line shows un-truncated one-halo NFW profile for comparison.

to four distinct physical effects: uncorrelated large-scale structure along the LOS, variations in concentration, halo asphericity and orientation, and correlated haloes in the cluster substructure and neighbourhood (cf. equation 6.7). All of these effects have the potential to bias the lensing mass measurement or, equivalently, can be interpreted as a source of intrinsic covariance between the components of $\boldsymbol{K} - \boldsymbol{\kappa}(M)$ that causes additional intrinsic noise on a cluster-by-cluster basis. In this section, we provide analytic expressions for all four components of the intrinsic covariance.

Uncorrelated large-scale structure

For a given source population, random structures along the LOS introduce a covariance in convergence measured in angular bins, which can be written as (e.g. Schneider et al., 1998; Hoekstra, 2003; Umetsu et al., 2011)

$$C_{ij}^{\rm LSS} = \int \frac{l\mathrm{d}l}{2\pi}\, P_\kappa(l)\, \hat{J}_0(l\theta_i)\, \hat{J}_0(l\theta_j)\ . \tag{6.17}$$

Here, $\hat{J}_0(l\theta_i)$ is the area-weighted average of J_0 over annulus i. Using the identity (Abramowitz & Stegun 1965, their equation 9.1.30)

$$\left(\frac{1}{z}\frac{\mathrm{d}}{\mathrm{d}z}\right)^k [z^l J_l(z)] = z^{l-k} J_{l-k}(z)\ . \tag{6.18}$$

with $k = l = 1$ and integrating yields (cf. also Umetsu et al. 2011, their equation 16)

$$\hat{J}_0(l\theta_i) = \frac{1}{2dl\theta_i}\left\{(1+d)J_1\left[l(1+d)\theta_i\right] - (1-d)J_1\left[l(1-d)\theta_i\right]\right\}\ , \tag{6.19}$$

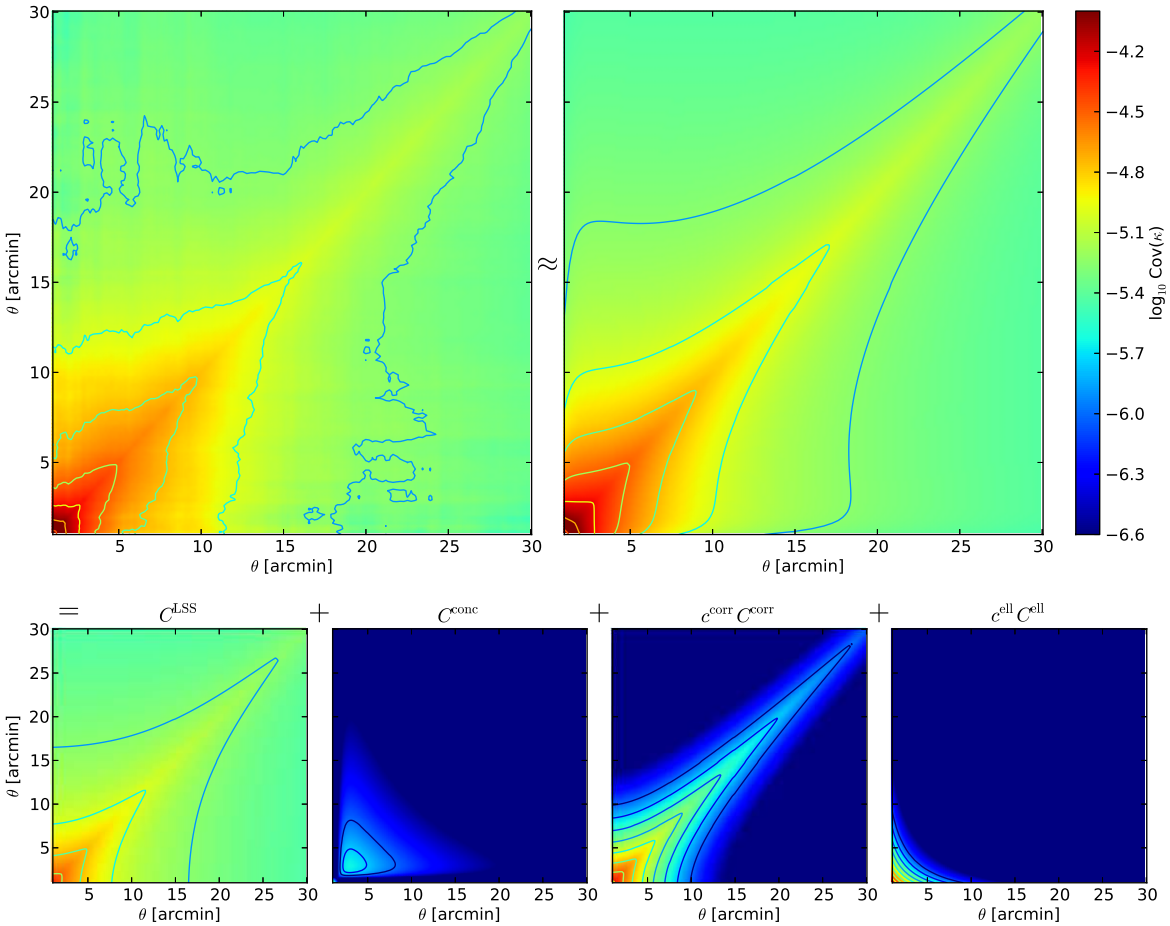

Figure 6.2: Illustration of our model for the profile covariance. Top-left panel shows the empirical intrinsic covariance of κ profiles between 1 and 30 arcmin of simulated clusters of mass $M_{200m} = 1.8 \ldots 2.2 \times 10^{14} M_\odot$. Our model prediction for the covariance is shown in the top-right panel. It is a linear combination of the components shown in the bottom panel. Even at this relatively low mass, uncorrelated large-scale structure (left in lower panel) is an insufficient description of the observed covariance, especially in the inner regions. We model the additional covariance as a linear combination of variation of the concentration parameter, the covariance of correlated haloes and halo ellipticity and orientation (remaining plots in lower panel). All panels use the same colour scale with contour lines spaced by $\Delta \log_{10} \mathrm{Cov}\kappa = 0.25$. At the mass plotted here, $c^{\mathrm{corr}} C^{\mathrm{corr}}$ is the dominant component of the intrinsic (co)variance on most scales, with significant contributions from $c^{\mathrm{ell}} C^{\mathrm{ell}}$ in the innermost region and subdominant concentration scatter. We note, however, that the relative importance of these three components changes as a function of mass (cf. Fig. 6.3).

where we have assumed an annulus of width $2d\theta_i$ from $(1-d)\theta_i$ to $(1+d)\theta_i$.

The convergence power spectrum P_κ in equation (6.17) is obtained from the matter power spectrum by means of the Limber (1954) approximation as

$$P_\kappa(l) = \frac{9H_0^2\Omega_\mathrm{m}^2}{4c^2}\int_{\chi_1}^{\chi_2} \mathrm{d}\chi \left(\frac{\chi_s-\chi}{\chi_s a(\chi)}\right)^2 P_\mathrm{nl}(l/\chi,\chi)\ , \tag{6.20}$$

where we have assumed a fixed comoving distance of the sources χ_s. For calculating C^LSS around our cluster haloes, we set the source redshift to a fixed $z_\mathrm{s}=1$ and limit the interval $[\chi_1,\chi_2]$ to the range of $\pm 200h^{-1}$ comoving Mpc included in the boxes around the cluster haloes (cf. Section 6.2). For the non-linear matter power spectrum P_nl we use the model of Smith et al. (2003) with the Eisenstein & Hu (1998) transfer function including baryonic effects. We perform the integral using a customized version of NICAEA (Kilbinger et al., 2009). The result is shown in the lower-left panel of Fig. 6.2.

Concentration

The covariance due to variations in concentration parameter at fixed mass is calculated as

$$C_{ij}^\mathrm{conc} = \int \mathrm{d}P(c)\kappa_i\kappa_j - \left[\int \mathrm{d}P(c)\kappa_i\right]\times\left[\int \mathrm{d}P(c)\kappa_j\right]\ , \tag{6.21}$$

where κ_i is taken to be the convergence of a halo of concentration c in annulus i. For the probability density $\mathrm{d}P(c)$, we assume a log-normal scatter of $\sigma_{\log_{10} c_{200m}} = 0.18$ (Bullock et al., 2001) about the mean concentration of Duffy et al. (2008). The result is shown in Fig. 6.2, lower second-to-left panel. As can be seen, it is subdominant at the radii considered here relative to other sources of intrinsic profile variation, at least for clusters of moderate mass, which illustrates the difficulty of measuring individual cluster concentrations with weak lensing.

Correlated large-scale structure

Clusters of galaxies are likely to form in overdense regions, where the abundance of additional (correlated) haloes is also higher than average. The mean effect of this on projected density is the two-halo term of equation (6.12). The stochastic variation of the number of correlated haloes around a cluster also contributes to the covariance of $\boldsymbol{\kappa}$.

We calculate the latter effect in a halo model, in analogy to Gruen et al. (2011, their Appendix A2). The idea is to split the set of all possible correlated haloes into subsets that are alike in the sense that they cause a similar shear signal, e.g. ones that are of similar mass and projected distance from the cluster. We then apply Poissonian statistics to the number of haloes that is actually present from each subset to get the covariance of the signal.

Let $\mathbb{H} = \{\boldsymbol{h}\}$ be the set of tuples $\boldsymbol{h}$ that completely characterize all possible correlated haloes, e.g. in terms of their coordinates and masses. Consider mutually exclusive and collectively exhaustive subsets $H_k \subset \mathbb{H}$ that are small enough such that $\forall H_k:\ \forall \boldsymbol{h}_a,\boldsymbol{h}_b \in H_k:$ $\Sigma^i(\boldsymbol{h}_a) \approx \Sigma^i(\boldsymbol{h}_b)$ is a good approximation for the surface mass density of such a halo averaged over annulus i. Then we can write the surface mass density of correlated haloes Σ^i_corr in annulus i as

$$\Sigma^i_\mathrm{corr} = \sum_k \lambda_k \Sigma^i(\boldsymbol{h}_k)\ . \tag{6.22}$$

The sum runs over all subsets k, of which $\boldsymbol{h}_k$ is an arbitrary element, respectively. The random variables $\lambda_k \geq 0$ describe the number of correlated haloes $\in H_k$ realized in a particular manifestation of a cluster.

The covariance of the linear combination of random variables in equation (6.22) is expressed as

$$C_{ij}^{\rm corr} \times \Sigma_{\rm crit}^2 = {\rm Cov}(\Sigma_{\rm corr}^i, \Sigma_{\rm corr}^j) = \sum_{k,l} {\rm Cov}(\lambda_k, \lambda_l)\, \Sigma^i(\boldsymbol{h}_k)\, \Sigma^j(\boldsymbol{h}_l)\ . \tag{6.23}$$

We make the assumption (discussed below) that the population random variables λ_k and λ_l of the haloes in sets H_k and H_l are Poisson distributed and mutually independent (${\rm Cov}(\lambda_k, \lambda_l) = \delta_{kl}\langle\lambda_k\rangle$). Then

$$C_{ij}^{\rm corr} \times \Sigma_{\rm crit}^2 = \sum_k \langle\lambda_k\rangle\, \Sigma^i(\boldsymbol{h}_k)\, \Sigma^j(\boldsymbol{h}_k) \approx \int_{\mathbb{H}} {\rm d}P_c(\boldsymbol{h}|\boldsymbol{h}_{\rm cl}) \Sigma^i(\boldsymbol{h}) \Sigma^j(\boldsymbol{h})\ . \tag{6.24}$$

For the latter equality we have defined a probability density ${\rm d}P_c(\boldsymbol{h}|\boldsymbol{h}_{\rm cl})$ of correlated haloes $\boldsymbol{h}$ around a cluster with properties $\boldsymbol{h}_{\rm cl}$ such that $\int_{H_k} {\rm d}P_c(\boldsymbol{h}|\boldsymbol{h}_{\rm cl}) = \langle\lambda_k\rangle$.

If we characterize secondary haloes only by their mass and projected angular distance from the cluster centre, i.e. $\boldsymbol{h} = (M, \theta)$, we can write

$${\rm d}P_c(\boldsymbol{h}|\boldsymbol{h}_{\rm cl}) = b(M_{\rm cl})\, b(M)\, \frac{{\rm d}N}{{\rm d}M{\rm d}V}\, W(\theta)\, 2\pi\theta\, {\rm d}\theta\, {\rm d}M\ , \tag{6.25}$$

all to be evaluated at the cluster redshift $z_{\rm cl}$. Here we have introduced the halo mass function $\frac{{\rm d}N}{{\rm d}M{\rm d}V}$ and used the projected linear excess Lagrangian depth W from equation (6.13), which assumes that pairs of haloes of masses $M_{\rm cl}$ and M cluster according to the linear matter two-point correlation and a mass dependent linear halo bias b as

$$\xi_{\rm hh}(M_{\rm cl}, M, z_{\rm cl} r) = b(M_{\rm cl}, z_{\rm cl})\, b(M, z_{\rm cl})\, \xi_{\rm lin}(r, z_{\rm cl})\ . \tag{6.26}$$

We perform the two-dimensional integral of equations 6.24 and 6.25, factoring out the cluster halo bias $b(M_{\rm cl}, z_{\rm cl})$ for later re-scaling of the covariance matrix to clusters of any mass. For the halo mass function and halo bias we use the models of Tinker et al. (2008, 2010). The haloes are modelled as BMO profiles (cf. Section 6.3.1) with concentration according to Duffy et al. (2008) and the truncation radius model of equation (6.11). We include contributions from haloes of mass $10^8 h^{-1} M_\odot \leq M_{200m} \leq 10^{15.5} h^{-1} M_\odot$.

Finally, we note that this approach neglects at least two additional effects: (i) a mutual (three-point) correlation of different correlated haloes is in fact expected, i.e. the presence of one massive, secondary halo makes the presence of tertiary haloes more likely and (ii) there is a correlation of halo shape and secondary haloes out to large distances, i.e. a filamentary structure. Both of these effects mean that the approach presented above yields merely a lower limit of the true covariance. We approximately compensate this by an empirical re-scaling of the covariance matrix with $c^{\rm corr}$. The resulting covariance matrix is shown in the lower second-to-right panel of Fig. 3.1.

Non-linearly correlated subhaloes

The model for correlated large-scale structure described above assumes a linear correlation of secondary haloes at all radii. A more realistic approach might be to make this assumption

only for haloes outside the virial radius and add a distinct population of subhaloes. We test this model as follows.

For the subhalo abundance inside the virial radius (Bryan & Norman, 1998, their equation 6) we use the subhalo mass function of Jiang & van den Bosch (2014). The surface density of haloes is distributed according to an NFW profile with concentration $c_{200m} = 3.9$, adapted from the measurement of $c_{200c} = 2.6$ by Budzynski et al. (2012) for Duffy et al. (2008) halo concentration, $M_{200m} = 2 \times 10^{14} h^{-1} M_\odot$ and the snapshot redshift. These assumptions yield $\mathrm{d}P_c$ for the subhalo case.

We assume a truncation of subhaloes at their r_{200m} radius, i.e. $\tau_{200m} = c_{200m}(M_{\mathrm{sub}})$, motivated by halo stripping. For the projected density profile of the individual subhalo, we ensure mass compensation by subtracting as much matter according to the mean subhalo density profile (equation 6.22) as is contained in the individual halo. Otherwise we apply the prescription of Section 6.3.2 to determine the subhalo shot noise covariance matrix C^{sub}. In this we are ignoring, as before for the linear correlation, both a potential dependence of the subhalo number density profile on the parent halo concentration and ellipticity (which might cause correlations between C^{sub} and the respective other components of the model) and mutual correlation of subhaloes.

The covariance for linearly correlated haloes in this model is calculated as in equation (6.24), yet using a virial sphere excised version of $W(\theta)$ to calculate $\mathrm{d}P_c(\boldsymbol{h}|\boldsymbol{h}_{\mathrm{cl}})$ in equation (6.25). Note that C^{corr} in this model explicitly depends on the halo mass rather than being a constant template that is re-scaled by the central halo bias.

We find that the predicted subhalo covariance is a significant contribution to the intrinsic covariance of the halo profile at the high mass end of our sample. The contribution is dominated by massive subhaloes that are sufficiently resolved by our simulations. When we fit a linear dependence of a re-scaling parameter $c^{\mathrm{sub}} = c_0^{\mathrm{sub}} + c_1^{\mathrm{sub}}(\nu - \nu_0^{\mathrm{sub}})$ together with $c_{0/1}^{\mathrm{corr}}$ and $c_{0/1}^{\mathrm{ell}}$ as described in Section 6.4 below, we find $c_0^{\mathrm{sub}} = 0.8 \pm 0.8$ and $c_1^{\mathrm{sub}} = -2 \pm 1.5$. Fixing $c_1^{\mathrm{sub}} = 0$ and $c_1^{\mathrm{corr}} = 0$ yields a best-fit $c_0^{\mathrm{sub}} = 0$. The contribution of subhaloes is particularly degenerate with the halo asphericity covariance C^{ell} (see Section 6.3.2). We conclude that a larger sample of massive haloes would be required to determine whether the addition of C^{sub} improves the model and therefore do not include it in the following analyses.

Halo asphericity

Dark matter haloes are known to be triaxial in general. The axis ratios and their orientation along the LOS can change the projected κ profile significantly. It is difficult, however, to model the effect in its full generality.

We therefore make the following simplified model for the covariance due to halo asphericity. In accordance with the dominant feature of halo shapes in nature, we assume them to have a prolate shape with minor-to-major axis ratio $0 < q = b/a = c/a \leq 1$. We define a coordinate system with ellipsoidal radius r_e such that

$$r_e^2 = \boldsymbol{x}^T \begin{pmatrix} q^{-2/3} & 0 & 0 \\ 0 & q^{-2/3} & 0 \\ 0 & 0 & q^{4/3} \end{pmatrix} \boldsymbol{x} \,, \tag{6.27}$$

where $\boldsymbol{x}^T = (x, y, z)$ is a Cartesian coordinate system centred on and aligned with z along the major axis of the halo. For the spherical coordinate system (R, θ, ϕ) with $\theta = 0$ along the

major axis,

$$r_e(R,\theta)/R = \sqrt{q^{-2/3}\sin^2\theta + q^{4/3}\cos^2\theta}\ . \tag{6.28}$$

We find the three-dimensional density of a prolate NFW halo by evaluating equation 6.8 at $r = r_e$. By virtue of the unit determinant, the volume of ellipsoidal shells is $V(r_e, r_e + \mathrm{d}r_e) = 4\pi r_e^2 \mathrm{d}r_e$. The usual normalization of ρ_0 therefore means that the density integrated out to an ellipsoidal radius $r_e = r_{200m}$ matches M_{200m}. However, we need to re-scale ρ_0 numerically for the mass inside a *sphere* of radius r_{200m} to match M_{200m} (cf. Jing & Suto 2002; Oguri et al. 2003; Corless & King 2007 for definitions based on ellipsoidal overdensity and Dietrich et al. 2014 for a spherical overdensity approach to ellipsoidal haloes).

Integration of ρ along the LOS yields the surface mass density for any combination of M_{200m}, c_{200m}, q and orientation angle α, where $\alpha = 0$ puts the major axis along the LOS. We take care to use an approximation to the analytical result for the integrated density inside the innermost region, $r/r_s < 10^{-3}$, where the diverging density leads to numerical instability. Here we can approximate $\theta \approx \alpha$ for most of the matter along the LOS to find the mean surface density inside a small projected radius $\delta v = \delta r/r_s$ as (cf. Bartelmann 1996; Wright & Brainerd 2000)

$$\begin{aligned}\langle\Sigma\rangle(<\delta v) &= \rho_0 r_s \times \left[(1-e^2)^{-1/3}\sin^2\alpha + (1-e^2)^{2/3}\cos^2\alpha\right]^{-1/2} \\ &\times \frac{4}{\delta v^2}\left[\frac{2}{\sqrt{1-\delta v^2}}\mathrm{arctanh}\left(\sqrt{\frac{1-\delta \mathrm{v}}{1+\delta \mathrm{v}}}\right) + \ln\left(\frac{\delta \mathrm{v}}{2}\right)\right]\ .\end{aligned} \tag{6.29}$$

The covariance matrix is integrated as

$$C_{ij}^{\mathrm{ell}} = \int \mathrm{d}P(q,\cos\alpha)\kappa_i\kappa_j - \left[\int \mathrm{d}P(q,\cos\alpha)\kappa_i\right] \times \left[\int \mathrm{d}P(q,\cos\alpha)\kappa_j\right]\ , \tag{6.30}$$

where κ_i is the mean surface density of a halo of axis ratio q and orientation angle α in annulus i. We assume isotropic orientation, i.e. a uniform distribution of $\cos\alpha \in [0,1]$, and a truncated Gaussian distribution of q

$$P(q) \propto \begin{cases} \mathcal{N}(\mu = 0.6, \sigma = 0.12), & 0.1 \le q \le 1 \\ 0, & q < 0.1 \vee q > 1 \end{cases}\ , \tag{6.31}$$

approximating the distribution of q for haloes of mass $\approx 10^{14} M_\odot$ as measured in simulations by Bett et al. (2007, cf. their Section 4.3). The resulting covariance matrix, re-scaled empirically by c^{conc}, is shown in the lower-right panel of Fig. 6.2. We see that the influence of halo ellipticity is limited to small radii compared to correlated and uncorrelated structures along the LOS, yet quite significant in that regime.

6.3.3 Covariance estimation

Given a model for $\boldsymbol{\kappa}(M_{200m})$ that we can subtract from the observed $\boldsymbol{K}$, any simulated cluster of mass M_{200m} yields an estimate for C as

$$\mathrm{Cov}(E_i, E_j) = \langle E_i E_j\rangle\ . \tag{6.32}$$

While this approach heavily relies on the accuracy of $\boldsymbol{\kappa}$, it is also possible to estimate the covariance matrix $C(M_{200m})$ from an ensemble of N simulated clusters of fixed mass M_{200m}

without assuming a model for the mean profile. This is done by applying the ensemble covariance estimator

$$\mathrm{Cov}(E_i, E_j) = \frac{N}{N-1}\langle \hat{E}_i \hat{E}_j \rangle \ , \tag{6.33}$$

where $\hat{\boldsymbol{E}}$ is the residual with respect to the ensemble mean profile. The variance of the estimator of equation (6.33) is larger than the one of equation (6.32) by a factor $N/(N-1)$. We decide to bin our clusters in mass in subsamples of $N = 24$, such that the loss of information due to not assuming a model for the true mean profile is negligible. However, especially at the massive end where the number of clusters in our simulations is small, this would introduce an additional variance of profiles due to the systematic change of mass within each subsample. We therefore define

$$\hat{E}_i^k = \sqrt{\frac{N}{N-1}} \left(K_i^k - N^{-1} \sum_{l=1}^{N} K_i^l \times \frac{\kappa_i^k}{\kappa_i^l} \right) , \tag{6.34}$$

where K_i^j and κ_i^j are the actual and model convergence of cluster j in radial bin i. Here, we have re-scaled each of the other cluster profiles to the expected value at the mass of cluster k by means of the model and amplified the deviations from the mean by $\sqrt{N/(N-1)}$ to correct for the bias of the maximum-likelihood ensemble variance, such that $\mathrm{Cov}(\hat{E}_i, \hat{E}_j) = \mathrm{Cov}(E_i, E_j)$.

6.4 Determination of covariance model parameters

The multivariate Gaussian of equation 6.5 corresponds to a log-likelihood

$$\begin{aligned} -2 \ln \mathcal{L} &= \ln \det C(M) \\ &+ [\boldsymbol{\kappa}(M) - \boldsymbol{K}]^{\mathrm{T}} C^{-1}(M) [\boldsymbol{\kappa}(M) - \boldsymbol{K}] \\ &+ \text{const} \ . \end{aligned} \tag{6.35}$$

This could be interpreted as a likelihood of mass or of the parameters of both the mean profile model $\boldsymbol{\kappa}(M)$ and the covariance model $C(M)$. For the latter, the first term on the right-hand side serves as a regularization that prevents run-off of the (co)variance estimate to infinity. In our case, as discussed above, we use a non-parametric profile model to replace $\boldsymbol{\kappa}(M) - \boldsymbol{K}$ by the $\hat{\boldsymbol{E}}$ of equation 6.34 and maximize the likelihood to constrain the parameters of the covariance model.

Equation 6.35 has the disadvantage that the precision matrix $C^{-1}(M)$ and $\det C(M)$ become numerically unstable due to the large conditional number and strong covariance between neighbouring radial bins. Related to this, the uncertainty of empirically estimated off-diagonal components of the covariance matrix is large (e.g. Taylor et al., 2013, their equation 18). We therefore decide to use equation 6.35, however with a diagonal model covariance matrix, i.e. one where all off-diagonal components are set to zero. We verify, using a toy model, that this yields an unbiased maximum-likelihood estimate of the covariance model parameters.

For the covariance model, we assume equation 6.7. The contribution of concentration becomes important only at large mass and small radii, and rather than (poorly) constraining it from the data we decide to adopt the Bullock et al. (2001) log-normal concentration scatter, i.e. we set $c^{\mathrm{conc}} = 1$.

As a baseline for $c^{\mathrm{corr}}(\nu)$ and $c^{\mathrm{ell}}(\nu)$ we use the mass-independent model

$$\begin{aligned} c^{\mathrm{corr}}(\nu) &= c^{\mathrm{corr}} = \text{const} \\ c^{\mathrm{ell}}(\nu) &= c^{\mathrm{ell}} = \text{const} \ . \end{aligned} \tag{6.36}$$

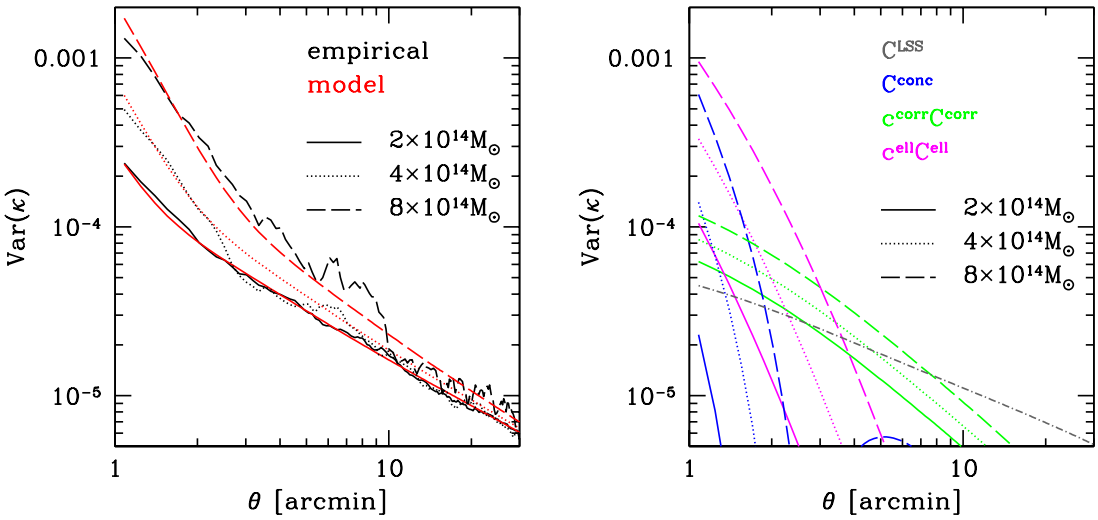

Figure 6.3: Empirical variance (black, left-hand panel) and variance model (red, left-hand panel) for clusters of mass $M_{200m} = 1.8 \ldots 2.2 \times 10^{14} h^{-1} M_\odot$ (solid lines), $M_{200m} = 3.5 \ldots 4.5 \times 10^{14} h^{-1} M_\odot$ (dotted) and $M_{200m} = 7 \ldots 9 \times 10^{14} h^{-1} M_\odot$ (dashed lines). Right-hand panel shows components of the model with $c^{\rm corr} = 5.0$ and $c^{\rm ell} = 3.7$ for all three cases (uncorrelated LSS inside the snapshot box shown as grey, dotted-dashed line).

As a test for mass dependence we also run our analysis with a model that allows for linear evolution in ν,

$$\begin{aligned} c^{\rm corr}(\nu) &= c_0^{\rm corr} + (\nu - \nu_0^{\rm corr}) c_1^{\rm corr} \\ c^{\rm ell}(\nu) &= c_0^{\rm ell} + (\nu - \nu_0^{\rm ell}) c_1^{\rm ell} \,, \end{aligned} \tag{6.37}$$

where we set the pivot points $\nu_0^{\rm corr} = 2.5$ and $\nu_0^{\rm ell} = 2.8$ to make errors on $c_0^\star$ and $c_1^\star$ approximately uncorrelated in the bootstrap runs.

6.4.1 Results

The best-fitting values for the parameters of equation (6.36) with errors estimated from bootstrapping are $c^{\rm corr} = 5.0 \pm 0.3$ and $c^{\rm ell} = 3.7 \pm 0.3$. Allowing for a linear dependence as in equation (6.37) these values are unchanged at best fit and we get no indication (but relatively poor constraints) for a ν dependence with $c_1^{\rm corr} = -0.04 \pm 0.88$ and $c_1^{\rm cell} = -0.05 \pm 0.79$. For the remainder of the analysis, we therefore adopt ν independent $c^{\rm corr} = 5.0$ and $c^{\rm ell} = 3.7$.

Figure 6.2 shows the full covariance model with these parameters for $M_{200m} = 2 \times 10^{14} h^{-1} M_\odot$. Figure 6.3 shows model and data variance for a range of masses. The model reproduces observed intrinsic variations well over a wide range of mass. We note, however, the large uncertainty in data variance due to our limited sample size.

6.4.2 Redshift dependence

In order to test for a potential redshift dependence of our model parameters, we repeat the analysis with a second snapshot at $z = 0.499$, using 788 haloes at $M_{200m} \geq 2 \times 10^{14} h^{-1} M_\odot$.

The best-fitting truncation radii are consistent with equation (6.11). We fit the parameters of equation (6.36) as in Section 6.4 and determine errors using bootstrapping. Empirical covariances are well reproduced by a model with $c^{\rm corr} = 4.2 \pm 1.1$ and $c^{\rm ell} = 3.8 \pm 0.9$. Due to the much smaller sample size and lower contrast of the haloes relative to LSS noise, the parameters are significantly less well constrained as in the $z = 0.245$ snapshot, however, consistent within the uncertainties.

We conclude that at the present level of statistical certainty the best-fit values of Section 6.4.1 can be used over the most relevant redshift range for cluster lensing of $z \approx 0.2 \ldots 0.5$.

6.5 Effect on weak lensing cluster surveys

In this section, we estimate the influence of intrinsic covariance of density profiles at fixed mass

- on mass measurements of individual clusters (Section 6.5.1)
- and on the determination of parameters of the mass-observable relation (MOR) in a lensing follow-up of a sample of clusters (Section 6.5.2).

In our analyses we fix the lens redshift to $z_{\rm l} = 0.24533$, the primary redshift of our simulated cluster profiles. We consider shear surveys of different depths, parametrized by the surface density $\mathfrak{n}$ of source galaxies, which we assume to lie at a fixed $z_{\rm s} = 1$. The three settings chosen roughly correspond to current large ground based surveys ($\mathfrak{n} = 10$ arcmin^{-2}), the best available ground-based data ($\mathfrak{n} = 50$ arcmin^{-2}) and space-based data ($\mathfrak{n} = 100$ arcmin^{-2}).

The full covariance of equation 6.7 contains, apart from uncorrelated and intrinsic variations of surface mass density, the measurement uncertainty of the survey $C^{\rm obs}$. For a shear survey, assume that we can measure the tangential gravitational shear $\boldsymbol{\gamma}$ in each annulus i with variance

$$\sigma^2_{\gamma,i} = \frac{\sigma^2_\epsilon}{\mathfrak{n} A_i} \,, \tag{6.38}$$

where $\sigma_\epsilon \approx 0.3$ is the shape noise (including intrinsic shape dispersion and measurement noise), $\mathfrak{n}$ is the background source density and A_i the area of annulus i. The n-dimensional covariance matrix of $\boldsymbol{\gamma}$ (ignoring intrinsic alignment and shear systematics) is diagonal with $C^{{\rm obs},\gamma}_{ii} = \sigma^2_{\gamma,i}$.

In the limit that annuli are thin, $\boldsymbol{\gamma}$ and $\boldsymbol{\kappa}$ are connected by a linear equation $\boldsymbol{\gamma} = G\boldsymbol{\kappa}$, where the $n \times n$ matrix G is defined such that

$$\gamma_i = \langle\kappa\rangle_{<i} - \kappa_i = \sum_{j=0}^{i-1} \kappa_j A_j / (\pi\theta^2_{i,\rm min}) - \kappa_i \,. \tag{6.39}$$

Our goal is to calculate the observational covariance $C^{\rm obs}$ of κ, which can be written as

$$C^{\rm obs} = G^{-1} C^{{\rm obs},\gamma} (G^{-1})^T \,. \tag{6.40}$$

The above derivation has omitted the technical step of breaking the mass-sheet degeneracy, which is necessary for G to be of full rank. To this end, we increase the dimensionality by 1 and let the newly introduced entry γ_{n+1} represent the convergence in the outermost radius, and the new κ_{n+1} be the mean convergence inside the innermost annulus. The measurement

error of γ_{n+1} is defined to be the LSS variance of κ on the outermost angular scale (this is essentially what happens in the common assumption of $\kappa = 0$ on large scales). The mean convergence inside the innermost annulus is connected to $\boldsymbol{\gamma}$ by the linear equation above. We later exclude the added component from our analysis again, i.e. we consider only the sub-matrix $i, j \in [1, n]$ (similar in effect to Mandelbaum et al. 2010).

We note that this ansatz for the observational covariance simplifies matters in at least two respects: (i) for any practical observation, shape noise will be a function of position, if only for the contamination with cluster member galaxies that is a function of distance from the centre (e.g. Medezinski et al., 2007; Sheldon et al., 2009; Melchior et al., 2014), and (ii) off-centring of the dark matter halo from the nominal centre of the analysis (e.g. Zitrin et al., 2012a). Both should be taken into account in actual measurements.

Apart from the *full model covariance* $C(M)$ of equation 6.7, we also define the *covariance without intrinsic variations*

$$C^{\mathrm{noint}} = C^{\mathrm{obs}} + C^{\mathrm{LSS}} \,. \tag{6.41}$$

For a model independent representation, we calculate the ensemble covariance of the re-scaled profiles (cf. equation 6.34) as $\hat{C}^{\mathrm{int}}(M)$. When calculating $\hat{C}^{\mathrm{int}}(M)$, we use 400 clusters that are nearest neighbours in a mass-ordered list of our simulated haloes to the target mass M and subtract the uncorrelated LSS covariance inside the simulation box. The *empirically estimated covariance* is

$$C^{\mathrm{emp}}(M) = C^{\mathrm{obs}} + C^{\mathrm{LSS}} + \hat{C}^{\mathrm{int}}(M) \,. \tag{6.42}$$

The following results are all derived assuming a set of logarithmic bins of 15 per cent width between 1 and 30 arcmin. We use the likelihood of equation (5.21), which optimally constrains mass when inserting the correct covariance matrix.

6.5.1 Mass confidence intervals

We determine the effect of intrinsic variations of the density profile on the validity of confidence intervals of weak lensing mass measurements. In this procedure, we assume the empirically estimated density profile covariance from our ensemble of simulated haloes to represent the true variability. We test for the effects of either taking into account intrinsic variations with the model proposed in this work or ignoring them. We design this test as follows.

At given mass M, we define and determine the full empirically estimated covariance $C^{\mathrm{emp}}(M)$ as described in equation (6.42). In a Monte Carlo simulation, we then generate profiles by adding a multivariate Gaussian random vector according to $C^{\mathrm{emp}}(M)$ to the model profile $\boldsymbol{\kappa}(M)$ (equation 6.9) of mass M.[1]

Consider one such realization $\boldsymbol{K}$. The likelihood in equation (5.21), now interpreted as a function of mass $\mathcal{L}(M'|\boldsymbol{K})$, can then be run over a range of model profiles $\boldsymbol{\kappa}(M')$ with different mass M'. For $C(M')$ and $C^{-1}(M')$ we use

- either the covariance without intrinsic variation C^{noint} of equation 6.41 (colour coded red in the following figures)

[1] As a test for the validity of considering only multivariate Gaussian variations over the mean profile, we perform another run where instead of a synthetic variation we use 100 nearest neighbours in mass around M, re-scale their profile to M using the model profiles of equation (6.9) and subtract their mean to generate 100 realistic random variations. We then add these (and multivariate Gaussian random vectors to simulate observational and uncorrelated LSS covariance) to the model profile at M and run the likelihood as described below. Results in this approach do not differ significantly from the synthetic multivariate Gaussian ones presented here.

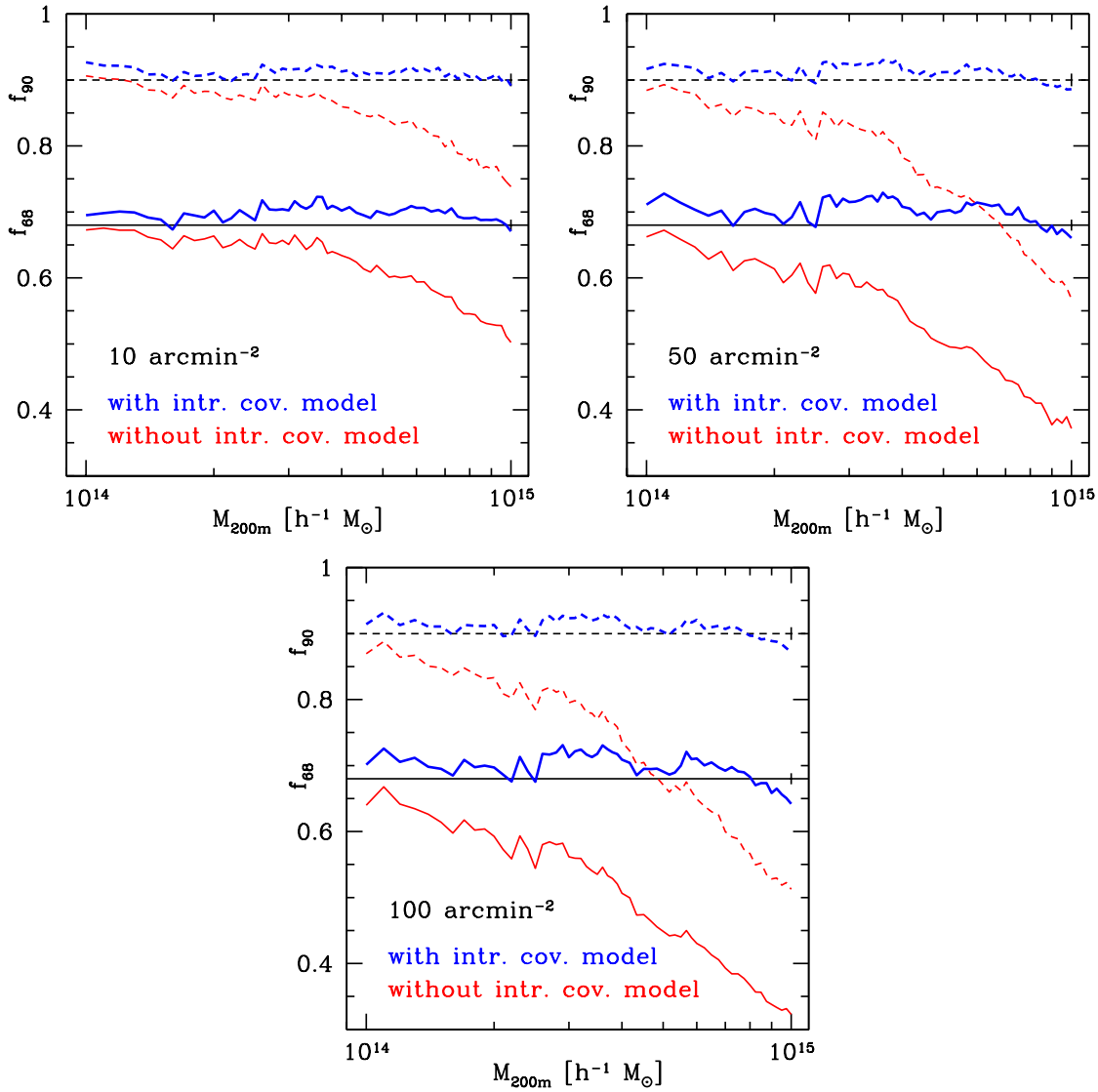

Figure 6.4: Fraction of weak lensing measurements of cluster mass where the true mass is inside the 68% (f_{68}, solid lines) and 90% (f_{90}, dashed lines) confidence interval (black lines at target levels for reference). In red, thin lines we show the common case where only measurement noise and uncorrelated LSS are considered for the covariance matrix (equation 6.41). Blue, thick lines show results that include our model for the intrinsic covariance (equation 6.7). Panels correspond to typical large ground based-surveys (top-left), best available ground based data (top-right) and space-based analyses (bottom). As data quality and cluster mass increase, intrinsic variations become a significant component of the uncertainty budget of weak lensing mass measurements and should not be ignored. All plots are for lenses at $z_l = 0.24533$.

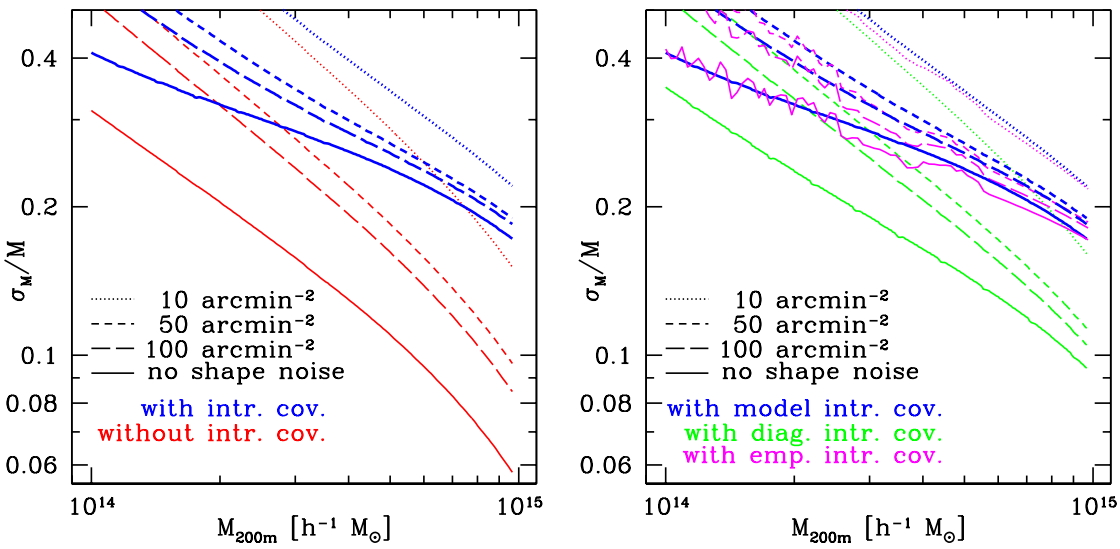

Figure 6.5: Left-hand panel: Relative uncertainty of weak lensing mass measurements from a Fisher analysis excluding (red) and including (blue, thick lines) intrinsic covariance according to our model. Not including intrinsic covariance leads to an underestimation of uncertainty, especially at high mass and large depth. Notably, the improvement of uncertainty for massive clusters going from typical (10 arcmin^{-2} background galaxies, dotted line) to noiseless measurements (solid line) is only modest when intrinsic variations are considered. Right-hand panel: Comparison of Fisher analysis made (i, blue, thick lines) with our model for intrinsic covariance, (ii, green) with our model, but setting off-diagonal elements of the covariance to zero, and (iii, magenta) with the empirically estimated intrinsic covariance. All results are for lenses at $z_l = 0.24533$.

- or the covariance of equation 6.7, including our parametric model for intrinsic variations (colour coded blue).

Note that the latter option requires to include the $\ln \det C$ term of the likelihood, since covariance is now a function of mass.

We determine 68% (and 90%) confidence intervals using mass limits where the likelihood is $2\Delta \ln \mathcal{L} = 1$ (and 2.7) worse than at best fit. We repeat the procedure for 10,000 realizations at every fixed mass and determine the empirical coverage, e.g. the fraction of cases in which the true mass lies inside these confidence intervals.

Results for three different survey depths are shown in Figure 6.4, where we now compare results of the two methods (red and blue lines) to the target levels of 68 and 90% (black lines). Increasingly with increasing mass, ignoring intrinsic variations leads to an underestimation of errors. Even for present surveys with relatively shallow depth, this manifests in $\approx 15\%$ excess outliers at the one and two sigma level for massive clusters at around $M_{200m} \approx 10^{15} h^{-1} M_\odot$. The effect is more severe in deeper data, where the relative importance of intrinsic over observational covariance increases.

Using our model covariance, confidence intervals are correctly estimated over a wide range of masses and even in deep data, with empirical coverage agreeing at the $\approx$ 3 per cent systematic level. The small number of systems above $M_{200m} > 10^{15} h^{-1} M_\odot$, however, limits the range of masses where we can evaluate the validity of our model. Note in this context that the scatter in the plots is due to the noise in $\hat{C}^{\rm int}(M)$, as estimated on a limited number

of clusters, rather than the number of realizations we run (the effect of the latter is indicated as the small vertical bar on the black lines).

Effect of intrinsic covariance on mass uncertainty

In the previous section, we found that the confidence interval based on a $\boldsymbol{\kappa}$ covariance matrix without contributions from intrinsic profile variation is significantly too narrow, especially for more massive clusters and larger depth of the data. Here, we perform a Fisher analysis to determine how well masses can be measured, a question particularly relevant for the design of lensing follow-up programmes.

For a mass dependent covariance matrix, the Fisher information for mass $\mathcal{F}$ reads (e.g. Vogeley & Szalay, 1996; Tegmark et al., 1997)

$$\mathcal{F}(M) = \left(\frac{\mathrm{d}\boldsymbol{\kappa}}{\mathrm{d}M}\right)^T C^{-1} \left(\frac{\mathrm{d}\boldsymbol{\kappa}}{\mathrm{d}M}\right) + \frac{1}{2}\mathrm{tr}\left[\left(C^{-1}\frac{\mathrm{d}C}{\mathrm{d}M}\right)^2\right] , \tag{6.43}$$

where $\boldsymbol{\kappa}$, C and their derivatives are taken to be evaluated at mass M.

We calculate the Fisher information for the model without intrinsic variations (equation 6.41) and our full model. In the first case, the second term of equation (6.43) drops because of the mass independence of the covariance. Including intrinsic variations, we also evaluate the second term, which however contributes to the Fisher information at most at the per cent level. The mass uncertainty σ_M is related to the Fisher information as $\sigma_M = \mathcal{F}^{-1/2}$.

The left-hand panel of Figure 6.5 shows relative uncertainties in mass σ_M/M due to a shear surveys of various depth. The increase in uncertainty due to intrinsic profile variation is substantial, even for shallow data with sufficiently massive clusters, but more strongly for deeper observations. Our results are consistent with the findings of Becker & Kravtsov (2011), who used the same simulations to derive uncertainties empirically rather than with a covariance model.

In the right-hand panel of Figure 6.5 we perform two additional tests.

- We compare the Fisher from our model (blue) to one generated with the empirically estimated covariance matrix (magenta lines). The derivatives of κ and covariance matrix w.r.t. mass in equation (6.43) are calculated from our covariance and mean profile model in both cases. We find agreement between the model and empirically estimated Fisher predictions within the scatter of the latter, i.e. at the ≈ 5 per cent level.

- We also estimate the mass uncertainty using only the intrinsic *variance*, i.e. setting the off-diagonal parts of our model covariance to zero (green lines). Note that this still includes off-diagonal covariance for the uncorrelated LSS and shape noise contributions. While the result depends somewhat on the binning scheme used, for the 15 per cent logarithmic bins we find that the variance-only version significantly underestimates mass uncertainty.

We conclude that the model, fitted to the intrinsic variance, reproduces the uncertainties. This is the case even though the latter are influenced significantly by off-diagonal contributions to the intrinsic covariance.

6.5.2 Mass-observable relations

We study the effect of intrinsic variations of projected cluster density profiles on weak lensing follow-up surveys used for determining parameters of a mass-observable relation. Consider an observable Y (which could be the Compton decrement, an X-ray mass proxy or an optical richness) with a power-law mass-observable relation that describes the fiducial value $Y_0(M)$ as a function of mass M,

$$\ln Y_0(M)/\hat{Y} = A + B \ln M/\hat{M} \ . \tag{6.44}$$

We have introduced here pivot values $\hat{Y}$ and $\hat{M}$ in addition to the power-law slope B and amplitude A.

The observed value of Y for any cluster shall include a log-normal intrinsic scatter $\sigma_{\rm int}$ and, for simplicity, also log-normally distributed measurement related uncertainty $\sigma_{\rm obs}$. The combined uncertainty $\sigma = \sqrt{\sigma_{\rm int}^2 + \sigma_{\rm obs}^2}$ leads to an observable

$$\ln Y(M) = \ln Y_0(M) + \mathcal{N}(\mu = 0, \sigma) \ . \tag{6.45}$$

Likelihood

Consider a single cluster with observed convergence profile $\boldsymbol{K}$ and measured observable Y. We maximize, as a function of MOR parameters, the likelihood

$$\begin{aligned} P(\boldsymbol{K}|Y, A, B, \sigma_{\rm int}) &= \int P(\boldsymbol{K}|M) P(M|Y, A, B, \sigma_{\rm int}) \, {\rm d}M \\ &\propto \int P(\boldsymbol{K}|M) P(Y|M, A, B, \sigma_{\rm int}) P(M) \, {\rm d}M \ . \end{aligned} \tag{6.46}$$

For $P(\boldsymbol{K}|M)$ we insert the expression of equation (6.5) with C equal to either our full model or the covariance without intrinsic variations. The term for the Y likelihood can be written as

$$P(Y|M, A, B, \sigma_{\rm int}) = \frac{\exp[-(\ln Y_0(M) - \ln Y)^2/(2\sigma^2)]}{\sqrt{2}\sigma} \, \Theta(Y - Y_{\rm lim}) P_{\rm det}^{-1}(M) \ . \tag{6.47}$$

Here we have used the Heaviside step function Θ to impose the observable limit $Y_{\rm lim}$ and re-normalized by the inverse of the detection probability

$$P_{\rm det}(M) = {\rm erfc}[(\ln Y_{\rm lim} - \ln Y_0(M))/(\sqrt{2}\sigma)]/2$$

to compensate for the removed part of the probability distribution (cf. Vikhlinin et al., 2009a, their equation A10) and correct for the (Malmquist) bias due to preferential selection of objects with positive contribution from scatter.

Finally, the normalized mass prior $P(M)$ can be written for an observable limited survey as

$$P(M) \propto \frac{{\rm d}n}{{\rm d}M}(M) P_{\rm det}(M) \left[\int {\rm d}M' \frac{{\rm d}n}{{\rm d}M}(M') P_{\rm det}(M') \right]^{-1} \tag{6.48}$$

to correct for (Eddington) bias due to the increase of abundance with decreasing mass. Note that $P(M)$ depends on the MOR by means of $P_{\rm det}$ and, by means of the halo mass function $\frac{{\rm d}n}{{\rm d}M}$, also on cosmology (for which we, however, assume fixed values in the simulations presented here).

Results

We simulate samples of clusters $1 \leq i \leq n$, where cluster i is characterized by its observable Y_i and an observed convergence profile $\boldsymbol{K}_i$.

For Y, we assume a MOR with $B = 5/3$ (the self-similar slope for Compton decrement $Y_{\rm SZ}$ and the X-ray equivalent $Y_{\rm X}$) and choose the pivots such that measurement errors on A and B are uncorrelated and $A = 0$. We assume an intrinsic scatter $\sigma_{\rm int} = 0.15$ and observational uncertainty of $\sigma_{\rm obs} = 0.05$.

The convergence profile $\boldsymbol{K}$ is simulated including a multivariate Gaussian deviation from equation (6.9), according to the full covariance (including uncorrelated LSS, measurement uncertainty of the survey and intrinsic variation as predicted from our model) of equation (6.7).

We take the sample to be observable limited, i.e. draw clusters with abundance proportional to the halo mass function, assign observables according to equations (6.44)-(6.45) and only accept objects where the observable exceeds the survey threshold, $Y > Y_{\rm lim}$. The threshold $Y_{\rm lim}$ is chosen as $Y_{\rm lim} = Y_0(M_{200m} = 4 \times 10^{14} h^{-1} M_\odot)$, comparable for instance to ongoing SZ surveys. The number of clusters drawn is taken to be representative of a volume of $V = 0.15 h^{-3}{\rm Gpc}^3$ (comoving, at $z = 0.24533$), which contains roughly 100 detections in our simulated survey.

Figure 6.6 shows the distribution of maximum likelihood estimates of the MOR parameters A, B and $\sigma_{\rm int}$, with contours enclosing 68 and 95 per cent of the 15,000 realizations, respectively. We find that the analysis using the full covariance (blue) reproduces the input MOR well. The feature near $\sigma_{\rm int} = 0$ is due to the hard prior $\sigma_{\rm int} > 0$, which pushes random realization with lower empirical scatter towards this limit. The analysis using the covariance without intrinsic variations (red) significantly overestimates intrinsic scatter. As an additional bias, the overall mass scale A (and, although less strongly, the slope B) are systematically underestimated. The move from a shallow (dotted) to deep (solid lines) surveys only moderately improves constraints and makes the bias due to using the covariance without intrinsic variations more apparent.

We note that the biases in A and B are due to a degeneracy between them and the intrinsic scatter. If the latter could be constrained externally with small uncertainty, e.g. by means of realistic simulations or by combining several observables with uncorrelated intrinsic scatter, the bias in the former would be mitigated even without a realistic model for the lensing covariance.

6.6 Conclusions

We have presented a model for the variation of projected density profiles of clusters of galaxies at fixed mass, constructed as a combination of the effects of variations of halo concentration, ellipticity and orientation, and correlated secondary structures.

The full covariance including our model for intrinsic variations faithfully reproduces confidence intervals in the weak lensing likelihood of cluster mass. We show that when intrinsic variations are ignored, uncertainties in lensing-derived mass are underestimated significantly (cf. Fig. 6.4).

Using the full covariance model we have made Fisher predictions for the accuracy of lensing measurements of cluster mass. We have shown that intrinsic variations take away some of the comparative advantage of studying a small sample of the most massive clusters with the deepest possible observations. For a massive cluster ($M_{200m} \approx 10^{15} h^{-1} M_\odot$ at $z = 0.25$) we

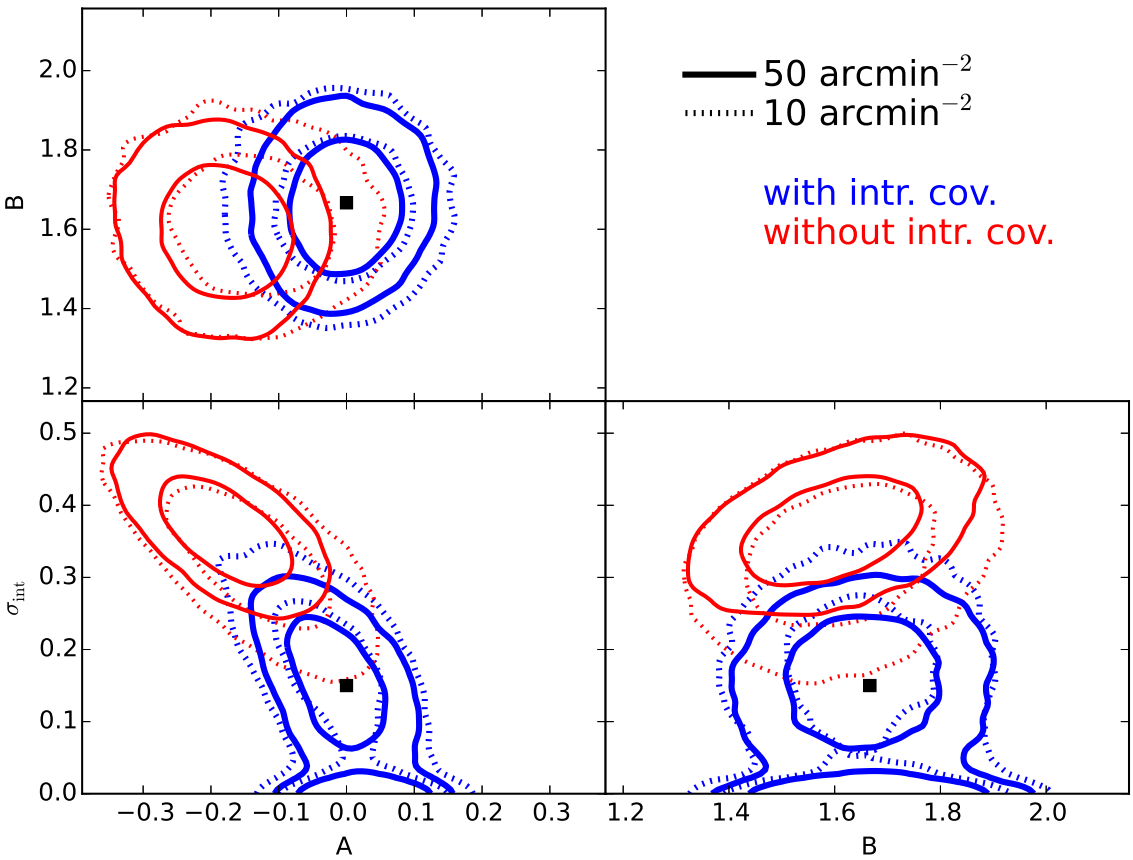

Figure 6.6: Distribution of maximum likelihood MOR parameters (true input indicated by black squares) estimated from a weak lensing follow-up of an observable limited sample. Input MOR is shown with black symbol. We show results for a shallow (dotted contours, $\mathfrak{n} = 10$ arcmin^{-2}) and deeper (solid contours, $\mathfrak{n} = 50$ arcmin^{-2}) lensing survey. Cluster profiles are simulated including intrinsic variation according to our model and the lensing likelihood for cluster mass is estimated including (blue, thick lines) and not including (red, thin lines) the intrinsic component of the covariance matrix in addition to shape noise and uncorrelated LSS. Inner and outer contours enclose 68 and 95 per cent of data points, respectively. Results are for lenses at $z_{\rm l} = 0.24533$.

find an irreducible relative uncertainty in lensing mass of ≈ 20 per cent due to intrinsic profile variations and uncorrelated LSS along the LOS, three times higher than the uncertainty from uncorrelated LSS alone. Our results agree with the analysis of Becker & Kravtsov (2011).

With simulations of mock surveys for constraining cluster MORs with lensing data, we have shown that intrinsic variations significantly bias the derived intrinsic scatter and amplitude if they are not accounted for in the lensing mass likelihood. For a follow-up of a sample of 100 clusters selected by $Y_{\rm SZ}$ above the fiducial value of the observable at $M_{200m} = 4 \times 10^{14} h^{-1} M_\odot$ at a redshift $z = 0.25$, the bias in the MOR amplitude is ≈ 15 per cent unless tight external constraints on the intrinsic scatter are available. Accounting for the cosmic variance of cluster lensing is therefore necessary for upcoming cluster surveys that target the calibration of MORs for cluster cosmology.

An implementation of the intrinsic profile covariance model described herein is available for download at `http://www.usm.uni-muenchen.de/people/dgruen/`.

Acknowledgements

We thank Gary Bernstein, Jörg Dietrich, Eduardo Rozo, Keiichi Umetsu and Peter Schneider for helpful discussions and Martin Kilbinger for support with the software NICAEA used in this work.

This work was supported by SFB-Transregio 33 'The Dark Universe' by the Deutsche Forschungsgemeinschaft (DFG) and the DFG cluster of excellence 'Origin and Structure of the Universe'.

Chapter 7

Summary

In this final chapter I summarize the results of the projects described in this thesis, with a focus on the main topic of weak lensing calibration for studies of clusters of galaxies. The human condition, as described by Eugene O'Neill, is characterized by our succeeding only to *push on to a greater failure*, and so I also give an outlook on related work I intend to pursue in the future.

7.1 Systematic improvements for lensing measurements

The next years are going to see a significant increase in the statistical power of weak lensing data sets, with the advent of surveys that feature an unprecedented combination of area and depth such as the Dark Energy Survey (DES, The Dark Energy Survey Collaboration 2005), the Hyper Suprime-Cam Survey (HSC, Miyazaki et al. 2012), the Kilo Degree Survey (KiDS, de Jong et al. 2013), the Large Synoptic Survey Telescope (LSST, Ivezic et al. 2008) or Euclid (Laureijs et al., 2011). With great statistical power, however, comes great systematic responsibility.

Two projects presented herein described data reduction techniques necessary for achieving this level of systematic accuracy. In Chapter 2 (Gruen et al., 2015a) I have described, and corrected, the mutual interaction of accumulating charges in CCD cameras. I have shown that the effect of this on galaxy shape measurements can cause per-cent level biases, above the statistical limits of upcoming weak lensing surveys. A correction based on charge-dependent linear shifts of effective pixel borders removes most of the effect, although the assumptions made in the modeling may have to be relaxed to meet the most demanding systematic requirements.

Chapter 3 (Gruen et al., 2014a) introduced an implementation of artifact filtering that is capable of detecting and masking artifact features in single frames by comparing them to the median stack. Apart from features with high per-pixel significance of surface brightness (such as cosmic rays or satellite trails), the spatial filtering method also allows to remove faint features such as reflections of bright star images. As an implementation in the common image co-addition software SWarp, it can be readily used in common data reduction pipelines.

Looking ahead, the combined efforts of the community in terms of systematic control of imaging data for lensing purposes are close to sufficient for the data to arrive imminently. Certainly, however, we will have to push further in the near future. In this context, I therefore

intend to work on three different issues:

- a continuation of work, done prior to this thesis, on bias-free shape measurement methods (Gruen et al., 2010). A fully Bayesian treatment appears to be the key to avoiding noise related biases (Bernstein & Armstrong, 2014) and can be achieved using either analytical or empirical methods.

- the accurate correction of instrumental effects that cause shape measurement biases in excess of the science requirements of future surveys such as LSST or Euclid, and

- an extension of the Bayesian method of estimating geometric scaling factors for weak gravitational lensing (Section 5.3.1). All of the various lensing probes are connected, in one way or another, to galaxies that are tracers of an underlying, correlated matter field. This causes an unavoidable position dependence of the source redshift prior. Taking the latter into account accurately will be necessary as the statistical uncertainty improves.

7.2 Lensing calibration of cluster MORs

Recent studies illustrate that calibration of mass-observable relations is the bottleneck to fully exploiting the cosmological power of clusters of galaxies (cf. Fig. 1.12 on p. 33). This will become even more apparent as the samples increase further in both size and spectral coverage, and the focus of studies shifts from constraints on the parameters of ΛCDM cosmology to less orthodox questions.

Chapter 5 (Gruen et al., 2014b) presented results on a weak lensing based mass calibration of hydrostatic X-ray masses and SZ observables of clusters selected from the South Pole Telescope and *Planck* SZ surveys.

From a comparison with X-ray mass estimates we find no indication for hydrostatic bias, with a 1σ upper limit of 15%. This is consistent with a number of comparable studies that find no or similarly small hydrostatic bias (cf. Zhang et al., 2010; Mahdavi et al., 2013; Israel et al., 2014), but in marginal disagreement with studies that find stronger hydrostatic X-ray biases of $\approx 30\%$ (cf. Mahdavi et al., 2008; Simet et al., 2015). Our slope for hydrostatic versus lensing mass is consistent with unity. The ratio of X-ray gas mass to weak lensing mass is consistent with gas fractions in the literature (Allen et al., 2008; Mantz et al., 2010a).

For the SZ calibration, we found agreement with the SPT MOR, regardless of method (Vanderlinde et al., 2010; Reichardt et al., 2013; Benson et al., 2013; Bocquet et al., 2015), in terms of both absolute scale and slope. Comparison of *Planck* signal and mass estimates, however, indicate a discrepancy that appears to correlate with redshift and mass: the SZ signal for distant and/or massive clusters is smaller than expected from the lensing mass estimate. A slope of *Planck* SZ versus mass that is shallower than self-similar, i.e. $Y \propto M^{\alpha}$ with $\alpha < 5/3$, has been found also by the recent study of von der Linden et al. (2014b). On the contrary, Hoekstra et al. (2015) find a mean bias but no significant deviation from the 5/3 slope.

It is clear, from these somewhat conflicting results, that the question of hydrostatic bias and *Planck* SZ calibration is not yet settled. For this reason, I plan to use the statistical power of upcoming DES lensing data to put tighter constraints on the *Planck* MOR. This is a particularly pressing problem for the cosmological return from what is the largest SZ cluster catalog to date. Thanks to the large number of *Planck* clusters overlapping DES (≈ 60 in

first-year data, about twice as many in the second season that has recently been completed), the data should allow to constrain an MOR well, ideally without added assumptions of self-similarity and perfect SZ data extraction.

The project described in Chapter 6 (Gruen et al., 2015b) is directly related to this. I have shown that intrinsic variations in cluster density profiles are a significant source of additional uncertainty for weak lensing mass estimates. A sufficiently realistic model of the cosmic variance is therefore key for lensing to yield unbiased MOR constraints (cf. Section 6.5.2). The model developed in Chapter 6 is capable of achieving this, yet constrained only at the ≈ 10 per-cent level. Other than an increase in volume for improved precision, future work might mitigate the limitations of mass and redshift range, of being based on dark matter only simulations, and of an untested potential cosmology dependence. Moreover, upcoming multi-probe cluster data sets, based e.g. on combined SZ, X-ray, optical and lensing data, require a full MOR model and covariance matrix of these probes at fixed mass. I plan to contribute to this in tightly coupled work with these data sets, hydrodynamic simulations, and theory.

7.3 Alternative structure probes

Cluster abundance is a powerful structure-based probe of cosmology, but it is not the only one. There are two others paths, connected to the contents of this thesis, that I would like to follow.

Thanks to the steepness and cosmology sensitivity of the mass function at the massive end (cf. Sec. 1.2.2) and the peculiarities of these systems, we have learned a lot about the Universe from a small number of rare objects (e.g. the Bullet cluster or several studies on massive and high-redshift systems in terms of extreme value statistics).

Chapter 4 described a detailed analysis of an exceptional cluster, RXC J2248.7–4431, both in terms of its mass density profile as measured with weak lensing and in terms of its cluster member population. With the selection of the system as a Hubble Frontier Field, the increased understanding of the cluster as a *gravitational telescope* is of even greater use.

One other potentially interesting system is PLCKESZ G287.0+32.9, identified as a candidate for being the largest known strong lens in Chapter 5. With multi-wavelength observations, spectroscopy and HST strong lensing follow-up, we could gain a better understanding of these most extreme environments and test our picture of structure formation in ΛCDM cosmology.

More interesting things might be left to find in a low density regime. Differences between dark energy and modified gravity explanations for cosmic expansion might be more easily differentiable in, e.g., filaments and voids, as theory and simulation based studies have started to explore (e.g. Clampitt et al., 2013). Weak lensing measurements of these structures, however, are notoriously difficult. The primary reason for this is their low density contrast that competes with the uncorrelated large-scale structure along the line of sight. In preliminary measurements in DES SV data I have explored, together with collaborators, the stacked lensing properties of underdensities in the projected galaxy field. These are well detectable in photometric surveys, yield a shear signal of high statistical significance, and also exhibit interesting cosmology dependence, that we intend to use in future work.

Bibliography

Abell, G. O. 1958: *The Distribution of Rich Clusters of Galaxies.*, ApJS, 3, 211

Abell, G. O., Corwin, Jr., H. G., & Olowin, R. P. 1989: *A catalog of rich clusters of galaxies*, ApJS, 70, 1

Abramowitz, M. & Stegun, I. 1965, Handbook of Mathematical Functions (Dover Publications)

Aguilar, M., Alberti, G., Alpat, B., Alvino, A., Ambrosi, G., Andeen, K., Anderhub, H., Arruda, L., Azzarello, P., Bachlechner, A., & et al. 2013: *First Result from the Alpha Magnetic Spectrometer on the International Space Station: Precision Measurement of the Positron Fraction in Primary Cosmic Rays of 0.5-350 GeV*, Physical Review Letters, 110, 141102

Ahn, C. P., Alexandroff, R., Allende Prieto, C., Anders, F., Anderson, S. F., Anderton, T., Andrews, B. H., Aubourg, É., Bailey, S., Bastien, F. A., & et al. 2014: *The Tenth Data Release of the Sloan Digital Sky Survey: First Spectroscopic Data from the SDSS-III Apache Point Observatory Galactic Evolution Experiment*, ApJS, 211, 17

Akritas, M. G. & Bershady, M. A. 1996: *Linear Regression for Astronomical Data with Measurement Errors and Intrinsic Scatter*, ApJ, 470, 706

Allen, S. W., Evrard, A. E., & Mantz, A. B. 2011: *Cosmological Parameters from Observations of Galaxy Clusters*, ARA&A, 49, 409

Allen, S. W., Rapetti, D. A., Schmidt, R. W., Ebeling, H., Morris, R. G., & Fabian, A. C. 2008: *Improved constraints on dark energy from Chandra X-ray observations of the largest relaxed galaxy clusters*, Mon. Not. Roy. Astron. Soc., 383, 879

Allen, S. W., Schmidt, R. W., Ebeling, H., Fabian, A. C., & van Speybroeck, L. 2004: *Constraints on dark energy from Chandra observations of the largest relaxed galaxy clusters*, Mon. Not. Roy. Astron. Soc., 353, 457

Allen, S. W., Schmidt, R. W., & Fabian, A. C. 2002: *Cosmological constraints from the X-ray gas mass fraction in relaxed lensing clusters observed with Chandra*, Mon. Not. Roy. Astron. Soc., 334, L11

Amara, A. & Réfrégier, A. 2008: *Systematic bias in cosmic shear: extending the Fisher matrix*, Mon. Not. Roy. Astron. Soc., 391, 228

AMI Consortium: Hurley-Walker, N., Bridle, S., Cypriano, E. S., Davies, M. L., Erben, T., Feroz, F., Franzen, T. M. O., Grainge, K., Hobson, M. P., Lasenby, A., Marshall, P. J., et al. 2012: *Bayesian analysis of weak gravitational lensing and Sunyaev-Zel'dovich data for six galaxy clusters*, Mon. Not. Roy. Astron. Soc., 419, 2921

Anderson, L., Aubourg, E., Bailey, S., Bizyaev, D., Blanton, M., Bolton, A. S., Brinkmann, J., Brownstein, J. R., Burden, A., Cuesta, A. J., da Costa, L. A. N., et al. 2012: *The clustering of galaxies in the SDSS-III Baryon Oscillation Spectroscopic Survey: baryon acoustic oscillations in the Data Release 9 spectroscopic galaxy sample*, Mon. Not. Roy. Astron. Soc., 427, 3435

Andersson, K., Benson, B. A., Ade, P. A. R., Aird, K. A., Armstrong, B., Bautz, M., Bleem, L. E., Brodwin, M., Carlstrom, J. E., Chang, C. L., Crawford, T. M., et al. 2011: *X-Ray Properties of the First Sunyaev-Zel'dovich Effect Selected Galaxy Cluster Sample from the South Pole Telescope*, ApJ, 738, 48

Angloher, G., Bauer, M., Bavykina, I., Bento, A., Bucci, C., Ciemniak, C., Deuter, G., von Feilitzsch, F., Hauff, D., Huff, P., Isaila, C., et al. 2012: *Results from 730 kg days of the CRESST-II Dark Matter search*, European Physical Journal C, 72, 1971

Annis, J., Soares-Santos, M., Strauss, M. A., Becker, A. C., Dodelson, S., Fan, X., Gunn, J. E., Hao, J., Ivezić, Ž., Jester, S., Jiang, L., et al. 2014: *The Sloan Digital Sky Survey Coadd: 275 deg^2 of Deep Sloan Digital Sky Survey Imaging on Stripe 82*, ApJ, 794, 120

Antilogus, P., Astier, P., Doherty, P., Guyonnet, A., & Regnault, N. 2014: *The brighter-fatter effect and pixel correlations in CCD sensors*, Journal of Instrumentation, 9, C3048

Applegate, D. E., von der Linden, A., Kelly, P. L., Allen, M. T., Allen, S. W., Burchat, P. R., Burke, D. L., Ebeling, H., Mantz, A., & Morris, R. G. 2014: *Weighing the Giants - III. Methods and measurements of accurate galaxy cluster weak-lensing masses*, Mon. Not. Roy. Astron. Soc., 439, 48

Arnaud, M., Pratt, G. W., Piffaretti, R., Böhringer, H., Croston, J. H., & Pointecouteau, E. 2010: *The universal galaxy cluster pressure profile from a representative sample of nearby systems (REXCESS) and the Y_{SZ} - M_{500} relation*, A&A, 517, A92

Avni, Y. 1976: *Energy spectra of X-ray clusters of galaxies*, ApJ, 210, 642

Baade, D., Meisenheimer, K., Iwert, O., Alonso, J., Augusteijn, T., Beletic, J., Bellemann, H., Benesch, W., Böhm, A., Böhnhardt, H., Brewer, J., et al. 1999: *The Wide Field Imager at the 2.2-m MPG/ESO telescope: first views with a 67-million-facette eye.*, The Messenger, 95, 15

Bagchi, J., Sirothia, S. K., Werner, N., Pandge, M. B., Kantharia, N. G., Ishwara-Chandra, C. H., Gopal-Krishna, Paul, S., & Joshi, S. 2011: *Discovery of the First Giant Double Radio Relic in a Galaxy Cluster Found in the Planck Sunyaev-Zel'dovich Cluster Survey: PLCK G287.0+32.9*, ApJ, 736, L8

Bahcall, N. A., Fan, X., & Cen, R. 1997: *Constraining Ω with Cluster Evolution*, ApJ, 485, L53

Baltz, E. A., Marshall, P., & Oguri, M. 2009: *Analytic models of plausible gravitational lens potentials*, J. Cosmol. Astropart. Phys., 1, 15

Bartelmann, M. 1996: *Arcs from a universal dark-matter halo profile*, A&A, 313, 697

Bartelmann, M. & Schneider, P. 2001: *Weak gravitational lensing*, Physics Reports, 340, 291

Battye, R. A. & Weller, J. 2003: *Constraining cosmological parameters using Sunyaev-Zel'dovich cluster surveys*, Phys. Rev. D, 68, 083506

Becker, M. R. & Kravtsov, A. V. 2011: *On the Accuracy of Weak-lensing Cluster Mass Reconstructions*, ApJ, 740, 25

Bender, R., Appenzeller, I., Böhm, A., Drory, N., Fricke, K. J., Gabasch, A., Heidt, J., Hopp, U., Jäger, K., Kümmel, M., Mehlert, D., et al. 2001: *The FORS Deep Field: Photometric Data and Photometric Redshifts*, in Deep Fields, ed. S. Cristiani, A. Renzini, & R. E. Williams, 96

Benson, B. A., de Haan, T., Dudley, J. P., Reichardt, C. L., Aird, K. A., Andersson, K., Armstrong, R., Ashby, M. L. N., Bautz, M., Bayliss, M., Bazin, G., et al. 2013: *Cosmological Constraints from Sunyaev-Zel'dovich-selected Clusters with X-Ray Observations in the First 178 deg^2 of the South Pole Telescope Survey*, ApJ, 763, 147

Bernstein, G. M. & Armstrong, R. 2014: *Bayesian lensing shear measurement*, Mon. Not. Roy. Astron. Soc., 438, 1880

Bernstein, G. M. & Jarvis, M. 2002: *Shapes and Shears, Stars and Smears: Optimal Measurements for Weak Lensing*, AJ, 123, 583

Bertin, E. 2006: *Automatic Astrometric and Photometric Calibration with SCAMP*, in Astronomical Society of the Pacific Conference Series, Vol. 351, Astronomical Data Analysis Software and Systems XV, ed. C. Gabriel, C. Arviset, D. Ponz, & S. Enrique, 112

Bertin, E. 2011: *Automated Morphometry with SExtractor and PSFEx*, in Astronomical Society of the Pacific Conference Series, Vol. 442, Astronomical Data Analysis Software and Systems XX, ed. I. N. Evans, A. Accomazzi, D. J. Mink, & A. H. Rots, 435

Bertin, E. & Arnouts, S. 1996: *SExtractor: Software for source extraction.*, A&AS, 117, 393

Bertin, E., Mellier, Y., Radovich, M., Missonnier, G., Didelon, P., & Morin, B. 2002: *The TERAPIX Pipeline*, in Astronomical Society of the Pacific Conference Series, Vol. 281, Astronomical Data Analysis Software and Systems XI, ed. D. A. Bohlender, D. Durand, & T. H. Handley, 228

Bett, P., Eke, V., Frenk, C. S., Jenkins, A., Helly, J., & Navarro, J. 2007: *The spin and shape of dark matter haloes in the Millennium simulation of a Λ cold dark matter universe*, Mon. Not. Roy. Astron. Soc., 376, 215

Bocquet, S., Saro, A., Mohr, J. J., Aird, K. A., Ashby, M. L. N., Bautz, M., Bayliss, M., Bazin, G., Benson, B. A., Bleem, L. E., Brodwin, M., et al. 2015: *Mass Calibration and Cosmological Analysis of the SPT-SZ Galaxy Cluster Sample Using Velocity Dispersion σ_v and X-Ray Y_X Measurements*, ApJ, 799, 214

Bode, P., Ostriker, J. P., Cen, R., & Trac, H. 2012: *Calibration of Nonthermal Pressure in Global Dark Matter Simulations of Clusters of Galaxies*, ArXiv e-prints, 1204.1762

Böhringer, H., Schuecker, P., Guzzo, L., Collins, C. A., Voges, W., Cruddace, R. G., Ortiz-Gil, A., Chincarini, G., De Grandi, S., Edge, A. C., MacGillivray, H. T., et al. 2004a: *The ROSAT-ESO Flux Limited X-ray (REFLEX) Galaxy cluster survey. V. The cluster catalogue*, A&A, 425, 367

Böhringer, H., Schuecker, P., Guzzo, L., Collins, C. A., Voges, W., Cruddace, R. G., Ortiz-Gil, A., Chincarini, G., De Grandi, S., Edge, A. C., MacGillivray, H. T., et al. 2004b: *The ROSAT-ESO Flux Limited X-ray (REFLEX) Galaxy cluster survey. V. The cluster catalogue*, A&A, 425, 367

Bonamente, M., Joy, M., LaRoque, S. J., Carlstrom, J. E., Nagai, D., & Marrone, D. P. 2008: *Scaling Relations from Sunyaev-Zel'dovich Effect and Chandra X-Ray Measurements of High-Redshift Galaxy Clusters*, ApJ, 675, 106

Bridle, S., Balan, S. T., Bethge, M., Gentile, M., Harmeling, S., Heymans, C., Hirsch, M., Hosseini, R., Jarvis, M., Kirk, D., Kitching, T., et al. 2010: *Results of the GREAT08 Challenge: an image analysis competition for cosmological lensing*, Mon. Not. Roy. Astron. Soc., 405, 2044

Brimioulle, F., Seitz, S., Lerchster, M., Bender, R., & Snigula, J. 2013: *Dark matter halo properties from galaxy-galaxy lensing*, Mon. Not. Roy. Astron. Soc., 432, 1046

Bryan, G. L. & Norman, M. L. 1998: *Statistical Properties of X-Ray Clusters: Analytic and Numerical Comparisons*, ApJ, 495, 80

Budzynski, J. M., Koposov, S. E., McCarthy, I. G., McGee, S. L., & Belokurov, V. 2012: *The radial distribution of galaxies in groups and clusters*, Mon. Not. Roy. Astron. Soc., 423, 104

Bullock, J. S., Kolatt, T. S., Sigad, Y., Somerville, R. S., Kravtsov, A. V., Klypin, A. A., Primack, J. R., & Dekel, A. 2001: *Profiles of dark haloes: evolution, scatter and environment*, Mon. Not. Roy. Astron. Soc., 321, 559

Butcher, H. & Oemler, Jr., A. 1978: *The evolution of galaxies in clusters. I - ISIT photometry of C1 0024+1654 and 3C 295*, ApJ, 219, 18

Cabanac, R. A., Alard, C., Dantel-Fort, M., Fort, B., Gavazzi, R., Gomez, P., Kneib, J. P., Le Fèvre, O., Mellier, Y., Pello, R., Soucail, G., et al. 2007: *The CFHTLS strong lensing legacy survey. I. Survey overview and T0002 release sample*, A&A, 461, 813

Calabretta, M. R., Valdes, F., Greisen, E. W., & Allen, S. L. 2004: *Representations of distortions in FITS world coordinate systems*, in Astronomical Society of the Pacific Conference Series, Vol. 314, Astronomical Data Analysis Software and Systems (ADASS) XIII, ed. F. Ochsenbein, M. G. Allen, & D. Egret, 551

Carlberg, R. G., Yee, H. K. C., Ellingson, E., Morris, S. L., Abraham, R., Gravel, P., Pritchet, C. J., Smecker-Hane, T., Hartwick, F. D. A., Hesser, J. E., Hutchings, J. B., et al. 1997: *The Average Mass Profile of Galaxy Clusters*, ApJ, 485, L13

Carlstrom, J. E., Ade, P. A. R., Aird, K. A., Benson, B. A., Bleem, L. E., Busetti, S., Chang, C. L., Chauvin, E., Cho, H.-M., Crawford, T. M., Crites, A. T., et al. 2011: *The 10 Meter South Pole Telescope*, PASP, 123, 568

Carlstrom, J. E., Holder, G. P., & Reese, E. D. 2002: *Cosmology with the Sunyaev-Zel'dovich Effect*, ARA&A, 40, 643

Clampitt, J., Cai, Y.-C., & Li, B. 2013: *Voids in modified gravity: excursion set predictions*, Mon. Not. Roy. Astron. Soc., 431, 749

Clowe, D., Markevitch, M., Bradač, M., Gonzalez, A. H., Chung, S. M., Massey, R., & Zaritsky, D. 2012: *On Dark Peaks and Missing Mass: A Weak-lensing Mass Reconstruction of the Merging Cluster System A520*, ApJ, 758, 128

Coles, P. & Lucchin, F. 2002, Cosmology (John Wiley & Sons)

Comis, B., de Petris, M., Conte, A., Lamagna, L., & de Gregori, S. 2011: *X-ray calibration of Sunyaev-Zel'dovich scaling relations with the ACCEPT catalogue of galaxy clusters observed by Chandra*, Mon. Not. Roy. Astron. Soc., 418, 1089

Corless, V. L. & King, L. J. 2007: *A statistical study of weak lensing by triaxial dark matter haloes: consequences for parameter estimation*, Mon. Not. Roy. Astron. Soc., 380, 149

Croton, D. J. 2013: *Damn You, Little h! (Or, Real-World Applications of the Hubble Constant Using Observed and Simulated Data)*, Proc. Astron. Soc. Aust., 30, 52

Cruddace, R., Voges, W., Böhringer, H., Collins, C. A., Romer, A. K., MacGillivray, H., Yentis, D., Schuecker, P., Ebeling, H., & De Grandi, S. 2002: *The ROSAT All-Sky Survey: a Catalog of Clusters of Galaxies in a Region of 1 steradian around the South Galactic Pole*, ApJS, 140, 239

Cunha, C. E., Lima, M., Oyaizu, H., Frieman, J., & Lin, H. 2009: *Estimating the redshift distribution of photometric galaxy samples - II. Applications and tests of a new method*, Mon. Not. Roy. Astron. Soc., 396, 2379

Cutri, R. M., Skrutskie, M. F., van Dyk, S., Beichman, C. A., Carpenter, J. M., Chester, T., Cambresy, L., Evans, T., Fowler, J., Gizis, J., Howard, E., et al. 2003, 2MASS All Sky Catalog of point sources. (NASA/IPAC Infrared Science Archive)

Dahlen, T., Mobasher, B., Somerville, R. S., Moustakas, L. A., Dickinson, M., Ferguson, H. C., & Giavalisco, M. 2005: *The Evolution of the Optical and Near-Infrared Galaxy Luminosity Functions and Luminosity Densities to $z \approx 2$*, ApJ, 631, 126

Dalton, G. B., Maddox, S. J., Sutherland, W. J., & Efstathiou, G. 1997: *The APM Galaxy Survey - V. Catalogues of galaxy clusters*, Mon. Not. Roy. Astron. Soc., 289, 263

de Grandi, S., Böhringer, H., Guzzo, L., Molendi, S., Chincarini, G., Collins, C., Cruddace, R., Neumann, D., Schindler, S., Schuecker, P., & Voges, W. 1999: *A Flux-limited Sample of Bright Clusters of Galaxies from the Southern Part of the ROSAT All-Sky Survey: The Catalog and LOG N-LOG S*, ApJ, 514, 148

de Jong, J. T. A., Kuijken, K., Applegate, D., Begeman, K., Belikov, A., Blake, C., Bout, J., Boxhoorn, D., Buddelmeijer, H., Buddendiek, A., Cacciato, M., et al. 2013: *The Kilo-Degree Survey*, The Messenger, 154, 44

DePoy, D. L., Abbott, T., Annis, J., Antonik, M., Barceló, M., Bernstein, R., Bigelow, B., Brooks, D., Buckley-Geer, E., Campa, J., Cardiel, L., et al. 2008: *The Dark Energy Camera (DECam)*, in SPIE, Vol. 7014

Derylo, G., Diehl, H. T., & Estrada, J. 2006: *0.250mm-thick CCD packaging for the Dark Energy Survey Camera array*, in SPIE, Vol. 6276, 8

Desai, S., Armstrong, R., Mohr, J. J., Semler, D. R., Liu, J., Bertin, E., Allam, S. S., Barkhouse, W. A., Bazin, G., Buckley-Geer, E. J., Cooper, M. C., et al. 2012: *The Blanco Cosmology Survey: Data Acquisition, Processing, Calibration, Quality Diagnostics, and Data Release*, ApJ, 757, 83

Diehl, H. T., Angstadt, R., Campa, J., Cease, H., Derylo, G., Emes, J. H., Estrada, J., Kubik, D., Flaugher, B. L., Holland, S. E., Jonas, M., et al. 2008: *Characterization of DECam focal plane detectors*, in SPIE, Vol. 7021, 7

Diehl, T. & For Dark Energy Survey Collaboration. 2012: *The Dark Energy Survey Camera (DECam)*, Physics Procedia, 37, 1332

Diemer, B. & Kravtsov, A. V. 2014: *Dependence of the Outer Density Profiles of Halos on Their Mass Accretion Rate*, ApJ, 789, 1

Dietrich, J. P., Böhnert, A., Lombardi, M., Hilbert, S., & Hartlap, J. 2012a: *The origin of peak-offsets in weak-lensing maps*, Mon. Not. Roy. Astron. Soc., 419, 3547

Dietrich, J. P., Werner, N., Clowe, D., Finoguenov, A., Kitching, T., Miller, L., & Simionescu, A. 2012b: *A filament of dark matter between two clusters of galaxies*, Nat, 487, 202

Dietrich, J. P., Zhang, Y., Song, J., Davis, C. P., McKay, T. A., Baruah, L., Becker, M., Benoist, C., Busha, M., da Costa, L. A. N., Hao, J., et al. 2014: *Orientation bias of optically selected galaxy clusters and its impact on stacked weak-lensing analyses*, Mon. Not. Roy. Astron. Soc., 443, 1713

Dodelson, S. 2004: *Cluster masses: Accounting for structure along the line of sight*, Phys. Rev. D, 70, 023008

Downing, M., Baade, D., Sinclaire, P., Deiries, S., & Christen, F. 2006: *CCD riddle: a) signal vs time: linear; b) signal vs variance: non-linear*, in SPIE, Vol. 6276, 9

Duffy, A. R., Schaye, J., Kay, S. T., & Dalla Vecchia, C. 2008: *Dark matter halo concentrations in the Wilkinson Microwave Anisotropy Probe year 5 cosmology*, Mon. Not. Roy. Astron. Soc., 390, L64

Dyson, F. W., Eddington, A. S., & Davidson, C. 1920: *A Determination of the Deflection of Light by the Sun's Gravitational Field, from Observations Made at the Total Eclipse of May 29, 1919*, Royal Society of London Philosophical Transactions Series A, 220, 291

Ebeling, H., Ma, C.-J., & Barrett, E. 2014: *Spectroscopic Redshifts of Galaxies within the Frontier Fields*, ApJS, 211, 21

Eddington, A. S. 1913: *On a formula for correcting statistics for the effects of a known error of observation*, Mon. Not. Roy. Astron. Soc., 73, 359

Einstein, A. 1915: *Die Feldgleichungen der Gravitation*, Sitzungsberichte der Königlich Preußischen Akademie der Wissenschaften, 844

Eisenstein, D. J. & Hu, W. 1998: *Baryonic Features in the Matter Transfer Function*, ApJ, 496, 605

Eisenstein, D. J., Zehavi, I., Hogg, D. W., Scoccimarro, R., Blanton, M. R., Nichol, R. C., Scranton, R., Seo, H.-J., Tegmark, M., Zheng, Z., Anderson, S. F., et al. 2005: *Detection of the Baryon Acoustic Peak in the Large-Scale Correlation Function of SDSS Luminous Red Galaxies*, ApJ, 633, 560

Erben, T., Hildebrandt, H., Miller, L., van Waerbeke, L., Heymans, C., Hoekstra, H., Kitching, T. D., Mellier, Y., Benjamin, J., Blake, C., Bonnett, C., et al. 2013: *CFHTLenS: the Canada-France-Hawaii Telescope Lensing Survey - imaging data and catalogue products*, Mon. Not. Roy. Astron. Soc., 433, 2545

Erben, T., Schirmer, M., Dietrich, J. P., Cordes, O., Haberzettl, L., Hetterscheidt, M., Hildebrandt, H., Schmithuesen, O., Schneider, P., Simon, P., Deul, E., et al. 2005: *GaBoDS: The Garching-Bonn Deep Survey. IV. Methods for the image reduction of multi-chip cameras demonstrated on data from the ESO Wide-Field Imager*, Astronomische Nachrichten, 326, 432

Erben, T., Van Waerbeke, L., Bertin, E., Mellier, Y., & Schneider, P. 2001: *How accurately can we measure weak gravitational shear?*, A&A, 366, 717

Erben, T., van Waerbeke, L., Mellier, Y., Schneider, P., Cuillandre, J.-C., Castander, F. J., & Dantel-Fort, M. 2000: *Mass-detection of a matter concentration projected near the cluster Abell 1942: Dark clump or high-redshift cluster?*, A&A, 355, 23

Estrada, J., Alvarez, R., Abbott, T., Annis, J., Bonati, M., Buckley-Geer, E., Campa, J., Cease, H., Chappa, S., DePoy, D., Derylo, G., et al. 2010: *Focal plane detectors for Dark Energy Camera (DECam)*, in SPIE, Vol. 7735, 1

Evrard, A. E., Bialek, J., Busha, M., White, M., Habib, S., Heitmann, K., Warren, M., Rasia, E., Tormen, G., Moscardini, L., Power, C., et al. 2008: *Virial Scaling of Massive Dark Matter Halos: Why Clusters Prefer a High Normalization Cosmology*, ApJ, 672, 122

Feller, W. 1945: *On the Normal Approximation to the Binomial Distribution*, Annals of Mathematical Statistics, 16, 4, 319

Flaugher, B. L., Abbott, T. M. C., Angstadt, R., Annis, J., Antonik, M. L., Bailey, J., Ballester, O., Bernstein, J. P., Bernstein, R. A., Bonati, M., Bremer, G., et al. 2012: *Status of the Dark Energy Survey Camera (DECam) project*, in SPIE, Vol. 8446, 11

Foëx, G., Motta, V., Limousin, M., Verdugo, T., More, A., Cabanac, R., Gavazzi, R., & Muñoz, R. P. 2013: *SARCS strong-lensing galaxy groups. I. Optical, weak lensing, and scaling laws*, A&A, 559, A105

Foëx, G., Soucail, G., Pointecouteau, E., Arnaud, M., Limousin, M., & Pratt, G. W. 2012: *The dark matter distribution in $z \approx 0.5$ clusters of galaxies. I. Determining scaling relations with weak lensing masses*, A&A, 546, A106

Friedmann, A. 1922: *Über die Krümmung des Raumes*, Zeitschrift für Physik, 10, 377

Friedmann, A. 1924: *Über die Möglichkeit einer Welt mit konstanter negativer Krümmung des Raumes*, Zeitschrift für Physik, 21, 326

Fruchter, A. S. & Hook, R. N. 2002: *Drizzle: A Method for the Linear Reconstruction of Undersampled Images*, PASP, 114, 144

Gavazzi, R. & Soucail, G. 2007: *Weak lensing survey of galaxy clusters in the CFHTLS Deep*, A&A, 462, 459

Gladders, M. D. & Yee, H. K. C. 2005: *The Red-Sequence Cluster Survey. I. The Survey and Cluster Catalogs for Patches RCS 0926+37 and RCS 1327+29*, ApJS, 157, 1

Gómez, P. L., Valkonen, L. E., Romer, A. K., Lloyd-Davies, E., Verdugo, T., Cantalupo, C. M., Daub, M. D., Goldstein, J. H., Kuo, C. L., Lange, A. E., Lueker, M., et al. 2012: *Optical and X-Ray Observations of the Merging Cluster AS1063*, AJ, 144, 79

Gössl, C. A., Bender, R., Fabricius, M., Hopp, U., Karasz, A., Kosyra, R., & Lang-Bardl, F. 2012: *Commissioning of the WWFI for the Wendelstein Fraunhofer Telescope*, in SPIE, Vol. 8446

Gössl, C. A. & Riffeser, A. 2002: *Image reduction pipeline for the detection of variable sources in highly crowded fields*, A&A, 381, 1095

Gottloeber, S. & Klypin, A. 2008: *The ART of Cosmological Simulations*, ArXiv e-prints, 0803.4343

Greisel, N., Seitz, S., Drory, N., Bender, R., Saglia, R. P., & Snigula, J. 2013: *Photometric Redshifts and Systematic Variations in the Spectral Energy Distributions of Luminous Red Galaxies from SDSS DR7*, ApJ, 768, 117

Greve, T. R., Vieira, J. D., Weiß, A., Aguirre, J. E., Aird, K. A., Ashby, M. L. N., Benson, B. A., Bleem, L. E., Bradford, C. M., Brodwin, M., Carlstrom, J. E., et al. 2012: *Submillimeter Observations of Millimeter Bright Galaxies Discovered by the South Pole Telescope*, ApJ, 756, 101

Groom, D. 2002: *Cosmic rays and other nonsense in astronomical CCD imagers*, Experimental Astronomy, 14, 45

Gruen, D., Bernstein, G. M., Jarvis, M., Rowe, B., Vikram, V., Plazas, A. A., & Seitz, S. 2015a: *Characterization and correction of charge-induced pixel shifts in DECam*, JInst submitted, ArXiv e-prints, 1501.02802

Gruen, D., Bernstein, G. M., Lam, T. Y., & Seitz, S. 2011: *Optimizing weak lensing mass estimates for cluster profile uncertainty*, Mon. Not. Roy. Astron. Soc., 416, 1392

Gruen, D., Brimioulle, F., Seitz, S., Lee, C.-H., Young, J., Koppenhoefer, J., Eichner, T., Riffeser, A., Vikram, V., Weidinger, T., & Zenteno, A. 2013: *Weak lensing analysis of RXC J2248.7–4431*, Mon. Not. Roy. Astron. Soc., 432, 1455

Gruen, D., Seitz, S., Becker, M. R., Friedrich, O., & Mana, A. 2015b: *Cosmic variance of the galaxy cluster weak lensing signal*, Mon. Not. Roy. Astron. Soc., accepted, ArXiv e-prints, 1501.01632

Gruen, D., Seitz, S., & Bernstein, G. M. 2014a: *Implementation of Robust Image Artifact Removal in SWarp through Clipped Mean Stacking*, PASP, 126, 158

Gruen, D., Seitz, S., Brimioulle, F., Kosyra, R., Koppenhoefer, J., Lee, C.-H., Bender, R., Riffeser, A., Eichner, T., Weidinger, T., & Bierschenk, M. 2014b: *Weak lensing analysis of SZ-selected clusters of galaxies from the SPT and Planck surveys*, Mon. Not. Roy. Astron. Soc., 442, 1507

Gruen, D., Seitz, S., Koppenhoefer, J., & Riffeser, A. 2010: *Bias-free Shear Estimation Using Artificial Neural Networks*, ApJ, 720, 639

Gunn, J. E., Carr, M., Rockosi, C., Sekiguchi, M., Berry, K., Elms, B., de Haas, E., Ivezić, Ž., Knapp, G., Lupton, R., Pauls, G., et al. 1998: *The Sloan Digital Sky Survey Photometric Camera*, AJ, 116, 3040

Guyonnet, A., Astier, P., Antilogus, P., Regnault, N., & Doherty, P. 2015: *Evidence for self-interaction of charge distribution in charge-coupled devices*, A&A, 575, A41

Guzzo, L., Schuecker, P., Böhringer, H., Collins, C. A., Ortiz-Gil, A., de Grandi, S., Edge, A. C., Neumann, D. M., Schindler, S., Altucci, C., & Shaver, P. A. 2009: *The REFLEX galaxy cluster survey. VIII. Spectroscopic observations and optical atlas*, A&A, 499, 357

Gwyn, S. D. J. 2008: *MegaPipe: The MegaCam Image Stacking Pipeline at the Canadian Astronomical Data Centre*, PASP, 120, 212

Haiman, Z., Mohr, J. J., & Holder, G. P. 2001: *Constraints on Cosmological Parameters from Future Galaxy Cluster Surveys*, ApJ, 553, 545

Hamilton, A. J. S. 2001: *Formulae for growth factors in expanding universes containing matter and a cosmological constant*, Mon. Not. Roy. Astron. Soc., 322, 419

Hasselfield, M., Hilton, M., Marriage, T. A., Addison, G. E., Barrientos, L. F., Battaglia, N., Battistelli, E. S., Bond, J. R., Crichton, D., Das, S., Devlin, M. J., et al. 2013: *The Atacama Cosmology Telescope: Sunyaev-Zel'dovich selected galaxy clusters at 148 GHz from three seasons of data*, J. Cosmol. Astropart. Phys., 7, 8

Hayashi, E. & White, S. D. M. 2008: *Understanding the halo-mass and galaxy-mass cross-correlation functions*, Mon. Not. Roy. Astron. Soc., 388, 2

Hearin, A. P., Zentner, A. R., Newman, J. A., & Berlind, A. A. 2013: *Mind the gap: tightening the mass-richness relation with magnitude gaps*, Mon. Not. Roy. Astron. Soc., 430, 1238

Heymans, C., Van Waerbeke, L., Bacon, D., Berge, J., Bernstein, G., Bertin, E., Bridle, S., Brown, M. L., Clowe, D., Dahle, H., Erben, T., et al. 2006: *The Shear Testing Programme - I. Weak lensing analysis of simulated ground-based observations*, Mon. Not. Roy. Astron. Soc., 368, 1323

Heymans, C., Van Waerbeke, L., Miller, L., Erben, T., Hildebrandt, H., Hoekstra, H., Kitching, T. D., Mellier, Y., Simon, P., Bonnett, C., Coupon, J., et al. 2012: *CFHTLenS: the Canada-France-Hawaii Telescope Lensing Survey*, Mon. Not. Roy. Astron. Soc., 427, 146

High, F. W., Hoekstra, H., Leethochawalit, N., de Haan, T., Abramson, L., Aird, K. A., Armstrong, R., Ashby, M. L. N., Bautz, M., Bayliss, M., Bazin, G., et al. 2012: *Weak-lensing Mass Measurements of Five Galaxy Clusters in the South Pole Telescope Survey Using Magellan/Megacam*, ApJ, 758, 68

High, F. W., Stalder, B., Song, J., Ade, P. A. R., Aird, K. A., Allam, S. S., Armstrong, R., Barkhouse, W. A., Benson, B. A., Bertin, E., Bhattacharya, S., et al. 2010: *Optical Redshift and Richness Estimates for Galaxy Clusters Selected with the Sunyaev-Zel'dovich Effect from 2008 South Pole Telescope Observations*, ApJ, 723, 1736

Hildebrandt, H., Erben, T., Dietrich, J. P., Cordes, O., Haberzettl, L., Hetterscheidt, M., Schirmer, M., Schmithuesen, O., Schneider, P., Simon, P., & Trachternach, C. 2006: *GaBoDS: The Garching-Bonn Deep Survey. V. Data release of the ESO Deep-Public-Survey*, A&A, 452, 1121

Hoekstra, H. 2001: *The effect of distant large scale structure on weak lensing mass estimates*, A&A, 370, 743

Hoekstra, H. 2003: *How well can we determine cluster mass profiles from weak lensing?*, Mon. Not. Roy. Astron. Soc., 339, 1155

Hoekstra, H., Donahue, M., Conselice, C. J., McNamara, B. R., & Voit, G. M. 2011a: *The Mass-L_x Relation for Moderate Luminosity X-ray Clusters*, ApJ, 726, 48

Hoekstra, H., Franx, M., Kuijken, K., & Squires, G. 1998: *Weak Lensing Analysis of CL 1358+62 Using Hubble Space Telescope Observations*, ApJ, 504, 636

Hoekstra, H., Hartlap, J., Hilbert, S., & van Uitert, E. 2011b: *Effects of distant large-scale structure on the precision of weak lensing mass measurements*, Mon. Not. Roy. Astron. Soc., 412, 2095

Hoekstra, H., Herbonnet, R., Muzzin, A., Babul, A., Mahdavi, A., Viola, M., & Cacciato, M. 2015: *The Canadian Cluster Comparison Project: detailed study of systematics and updated weak lensing masses*, ArXiv e-prints, 1502.01883

Hoekstra, H., Mahdavi, A., Babul, A., & Bildfell, C. 2012: *The Canadian Cluster Comparison Project: weak lensing masses and SZ scaling relations*, Mon. Not. Roy. Astron. Soc., 427, 1298

Hogg, D. W. 1999: *Distance measures in cosmology*, ArXiv e-prints, 9905116

Holder, G., Haiman, Z., & Mohr, J. J. 2001: *Constraints on Ω_m, Ω_Λ, and σ_8 from Galaxy Cluster Redshift Distributions*, ApJ, 560, L111

Holland, S. E., Bebek, C. J., Kolbe, W. F., & Lee, J. S. 2014: *Physics of fully depleted CCDs*, Journal of Instrumentation, 9, C3057

Holland, S. E., Dawson, K. S., Palaio, N. P., Saha, J., Roe, N. A., & Wang, G. 2007: *Fabrication of back-illuminated, fully depleted charge-coupled devices*, Nucl. Instrum. Methods Phys. Res., Sect. A, 579, 653

Holland, S. E., Groom, D. E., Palaio, N. P., Stover, R. J., & Mei, M. 2003: *Fully Depleted, Back-Illuminated Charge-Coupled Devices Fabricated on High-Resisitivity Silicon*, IEEE Trans. Elec. Dev., 50, 225

Holland, S. E., Kolbe, W. F., & Bebek, C. J. 2009: *Device Design for a 12.3-Megapixel, Fully Depleted, Back-Illuminated, High-Voltage Compatible Charge-Coupled Device*, IEEE Trans. Elec. Dev., 56, 2612

Hu, W. 2003: *Self-consistency and calibration of cluster number count surveys for dark energy*, Phys. Rev. D, 67, 081304

Hudelot, P., Goranova, Y., Mellier, Y., McCracken, H. J., Magnard, F., Monnerville, M., Smah, G., Cuillandre, J.-C., Withington, K., Regnault, N., Betoule, M., et al. 2012: *T0007: The Final CFHTLS Release*

Israel, H., Erben, T., Reiprich, T. H., Vikhlinin, A., Sarazin, C. L., & Schneider, P. 2012: *The 400d Galaxy Cluster Survey weak lensing programme. II. Weak lensing study of seven clusters with MMT/MegaCam*, A&A, 546, A79

Israel, H., Reiprich, T. H., Erben, T., Massey, R. J., Sarazin, C. L., Schneider, P., & Vikhlinin, A. 2014: *The 400d Galaxy Cluster Survey weak lensing programme. III. Evidence for consistent WL and X-ray masses at $z \approx 0.5$*, A&A, 564, A129

Ivezic, Z., Tyson, J. A., Abel, B., Acosta, E., Allsman, R., AlSayyad, Y., Anderson, S. F., Andrew, J., Angel, R., Angeli, G., Ansari, R., et al. 2008: *LSST: from Science Drivers to Reference Design and Anticipated Data Products*, ArXiv e-prints, 0805.2366

Janesick, J. R. 2001, Scientific charge-coupled devices (SPIE Press)

Jiang, F. & van den Bosch, F. C. 2014: *Statistics of Dark Matter Substructure: I. Model and Universal Fitting Functions*, ArXiv e-prints, 1403.6827

Jing, Y. P. & Suto, Y. 2002: *Triaxial Modeling of Halo Density Profiles with High-Resolution N-Body Simulations*, ApJ, 574, 538

Kacprzak, T., Zuntz, J., Rowe, B., Bridle, S., Refregier, A., Amara, A., Voigt, L., & Hirsch, M. 2012: *Measurement and calibration of noise bias in weak lensing galaxy shape estimation*, Mon. Not. Roy. Astron. Soc., 427, 2711

Kaiser, N. 2000: *A New Shear Estimator for Weak-Lensing Observations*, ApJ, 537, 555

Kaiser, N. & Squires, G. 1993: *Mapping the dark matter with weak gravitational lensing*, ApJ, 404, 441

Kaiser, N., Squires, G., & Broadhurst, T. 1995: *A Method for Weak Lensing Observations*, ApJ, 449, 460

Kalberla, P. M. W., Burton, W. B., Hartmann, D., Arnal, E. M., Bajaja, E., Morras, R., & Pöppel, W. G. L. 2005: *The Leiden/Argentine/Bonn (LAB) Survey of Galactic HI. Final data release of the combined LDS and IAR surveys with improved stray-radiation corrections*, A&A, 440, 775

Kay, S. T., Peel, M. W., Short, C. J., Thomas, P. A., Young, O. E., Battye, R. A., Liddle, A. R., & Pearce, F. R. 2012: *Sunyaev-Zel'dovich clusters in Millennium gas simulations*, Mon. Not. Roy. Astron. Soc., 422, 1999

Kelly, B. C. 2007: *Some Aspects of Measurement Error in Linear Regression of Astronomical Data*, ApJ, 665, 1489

Kilbinger, M. 2014: *Review article: Cosmology with cosmic shear observations*, ArXiv e-prints, 1411.0115

Kilbinger, M., Benabed, K., Guy, J., Astier, P., Tereno, I., Fu, L., Wraith, D., Coupon, J., Mellier, Y., Balland, C., Bouchet, F. R., et al. 2009: *Dark-energy constraints and correlations with systematics from CFHTLS weak lensing, SNLS supernovae Ia and WMAP5*, A&A, 497, 677

Kitching, T. D., Balan, S. T., Bridle, S., Cantale, N., Courbin, F., Eifler, T., Gentile, M., Gill, M. S. S., Harmeling, S., Heymans, C., Hirsch, M., et al. 2012: *Image analysis for cosmology: results from the GREAT10 Galaxy Challenge*, Mon. Not. Roy. Astron. Soc., 423, 3163

Kitching, T. D., Rowe, B., Gill, M., Heymans, C., Massey, R., Witherick, D., Courbin, F., Georgatzis, K., Gentile, M., Gruen, D., Kilbinger, M., et al. 2013: *Image Analysis for Cosmology: Results from the GREAT10 Star Challenge*, ApJS, 205, 12

Koester, B. P., McKay, T. A., Annis, J., Wechsler, R. H., Evrard, A., Bleem, L., Becker, M., Johnston, D., Sheldon, E., Nichol, R., Miller, C., et al. 2007: *A MaxBCG Catalog of 13,823 Galaxy Clusters from the Sloan Digital Sky Survey*, ApJ, 660, 239

Komatsu, E., Smith, K. M., Dunkley, J., Bennett, C. L., Gold, B., Hinshaw, G., Jarosik, N., Larson, D., Nolta, M. R., Page, L., Spergel, D. N., et al. 2011: *Seven-year Wilkinson Microwave Anisotropy Probe (WMAP) Observations: Cosmological Interpretation*, ApJS, 192, 18

Kosyra, R., Gössl, C., Hopp, U., Lang-Bardl, F., Riffeser, A., Bender, R., & Seitz, S. 2014: *The 64 Mpixel wide field imager for the Wendelstein 2m telescope: design and calibration*, Experimental Astronomy, 38, 213

Kravtsov, A. V., Klypin, A. A., & Khokhlov, A. M. 1997: *Adaptive Refinement Tree: A New High-Resolution N-Body Code for Cosmological Simulations*, ApJS, 111, 73

Kubik, D., Alvarez, R., Abbott, T., Annis, J., Bonati, M., Buckley-Geer, E., Campa, J., Cease, H., Chappa, S., DePoy, D., Derylo, G., et al. 2010: *Automated characterization of CCD detectors for DECam*, in SPIE, Vol. 7735, 5

Kuhlmann, S., Spinka, H., Bernstein, J. P., Beyer, K. A., Gades, L. M., Kasprzyk, T. E., Miceli, A., Spence, R. A., & Talaga, R. 2011: *Narrow-beam X-ray tests of CCD edge response*, Experimental Astronomy, 29, 135

Laureijs, R., Amiaux, J., Arduini, S., Auguères, J. ., Brinchmann, J., Cole, R., Cropper, M., Dabin, C., Duvet, L., Ealet, A., & et al. 2011: *Euclid Definition Study Report*, ArXiv e-prints, 1110.3193

Le Fèvre, O., Vettolani, G., Garilli, B., Tresse, L., Bottini, D., Le Brun, V., Maccagni, D., Picat, J. P., Scaramella, R., Scodeggio, M., Zanichelli, A., et al. 2005: *The VIMOS VLT deep survey. First epoch VVDS-deep survey: 11 564 spectra with 17.5* $\leq \mathrm{I_{AB}} \leq$ *24, and the redshift distribution over 0* $\leq$ z $\leq$ *5*, A&A, 439, 845

Lebedev, V. S. & Lebedeva, I. A. 1991: *The Complete List of Clusters of Galaxies with Measured Redshifts*, Astrofizicheskie Issledovaniia Izvestiya Spetsial'noj Astrofizicheskoj Observatorii, 31, 91

Lemaître, G. 1933: *L'Univers en expansion*, Annales de la Societe Scietifique de Bruxelles, 53, 51

Lima, M., Cunha, C. E., Oyaizu, H., Frieman, J., Lin, H., & Sheldon, E. S. 2008: *Estimating the redshift distribution of photometric galaxy samples*, Mon. Not. Roy. Astron. Soc., 390, 118

Lima, M. & Hu, W. 2005: *Self-calibration of cluster dark energy studies: Observable-mass distribution*, Phys. Rev. D, 72, 043006

Limber, D. N. 1954: *The Analysis of Counts of the Extragalactic Nebulae in Terms of a Fluctuating Density Field. II.*, ApJ, 119, 655

Lin, H., Dodelson, S., Seo, H.-J., Soares-Santos, M., Annis, J., Hao, J., Johnston, D., Kubo, J. M., Reis, R. R. R., & Simet, M. 2012: *The SDSS Co-add: Cosmic Shear Measurement*, ApJ, 761, 15

Lin, Y.-T., Mohr, J. J., & Stanford, S. A. 2004: *K-Band Properties of Galaxy Clusters and Groups: Luminosity Function, Radial Distribution, and Halo Occupation Number*, ApJ, 610, 745

Luppino, G. A. & Kaiser, N. 1997: *Detection of Weak Lensing by a Cluster of Galaxies at Z = 0.83*, ApJ, 475, 20

Mahdavi, A., Hoekstra, H., Babul, A., Bildfell, C., Jeltema, T., & Henry, J. P. 2013: *Joint Analysis of Cluster Observations. II. Chandra/XMM-Newton X-Ray and Weak Lensing Scaling Relations for a Sample of 50 Rich Clusters of Galaxies*, ApJ, 767, 116

Mahdavi, A., Hoekstra, H., Babul, A., & Henry, J. P. 2008: *Evidence for non-hydrostatic gas from the cluster X-ray to lensing mass ratio*, Mon. Not. Roy. Astron. Soc., 384, 1567

Majumdar, S. & Mohr, J. J. 2004: *Self-Calibration in Cluster Studies of Dark Energy: Combining the Cluster Redshift Distribution, the Power Spectrum, and Mass Measurements*, ApJ, 613, 41

Mana, A., Giannantonio, T., Weller, J., Hoyle, B., Hütsi, G., & Sartoris, B. 2013: *Combining clustering and abundances of galaxy clusters to test cosmology and primordial non-Gaussianity*, Mon. Not. Roy. Astron. Soc., 434, 684

Mandelbaum, R., Seljak, U., Baldauf, T., & Smith, R. E. 2010: *Precision cluster mass determination from weak lensing*, Mon. Not. Roy. Astron. Soc., 405, 2078

Mantz, A., Allen, S. W., Ebeling, H., Rapetti, D., & Drlica-Wagner, A. 2010a: *The observed growth of massive galaxy clusters - II. X-ray scaling relations*, Mon. Not. Roy. Astron. Soc., 406, 1773

Mantz, A., Allen, S. W., Rapetti, D., & Ebeling, H. 2010b: *The observed growth of massive galaxy clusters - I. Statistical methods and cosmological constraints*, Mon. Not. Roy. Astron. Soc., 406, 1759

Mantz, A. B., von der Linden, A., Allen, S. W., Applegate, D. E., Kelly, P. L., Morris, R. G., Rapetti, D. A., Schmidt, R. W., Adhikari, S., Allen, M. T., Burchat, P. R., et al. 2015: *Weighing the giants - IV. Cosmology and neutrino mass*, Mon. Not. Roy. Astron. Soc., 446, 2205

Marriage, T. A., Acquaviva, V., Ade, P. A. R., Aguirre, P., Amiri, M., Appel, J. W., Barrientos, L. F., Battistelli, E. S., Bond, J. R., Brown, B., Burger, B., et al. 2011: *The Atacama Cosmology Telescope: Sunyaev-Zel'dovich-Selected Galaxy Clusters at 148 GHz in the 2008 Survey*, ApJ, 737, 61

Marrone, D. P., Smith, G. P., Okabe, N., Bonamente, M., Carlstrom, J. E., Culverhouse, T. L., Gralla, M., Greer, C. H., Hasler, N., Hawkins, D., Hennessy, R., et al. 2012: *LoCuSS: The Sunyaev-Zel'dovich Effect and Weak-lensing Mass Scaling Relation*, ApJ, 754, 119

Marrone, D. P., Smith, G. P., Richard, J., Joy, M., Bonamente, M., Hasler, N., Hamilton-Morris, V., Kneib, J.-P., Culverhouse, T., Carlstrom, J. E., Greer, C., et al. 2009: *LoCuSS: A Comparison of Sunyaev-Zel'dovich Effect and Gravitational-Lensing Measurements of Galaxy Clusters*, ApJ, 701, L114

Marshall, P. J., Hobson, M. P., Gull, S. F., & Bridle, S. L. 2002: *Maximum-entropy weak lens reconstruction: improved methods and application to data*, Mon. Not. Roy. Astron. Soc., 335, 1037

Massey, R., Heymans, C., Bergé, J., Bernstein, G., Bridle, S., Clowe, D., Dahle, H., Ellis, R., Erben, T., Hetterscheidt, M., High, F. W., et al. 2007: *The Shear Testing Programme 2:*

Factors affecting high-precision weak-lensing analyses, Mon. Not. Roy. Astron. Soc., 376, 13

Maturi, M., Meneghetti, M., Bartelmann, M., Dolag, K., & Moscardini, L. 2005: *An optimal filter for the detection of galaxy clusters through weak lensing*, A&A, 442, 851

Maughan, B. J., Jones, C., Forman, W., & Van Speybroeck, L. 2008: *Images, Structural Properties, and Metal Abundances of Galaxy Clusters Observed with Chandra ACIS-I at* $0.1 < z < 1.3$, ApJS, 174, 117

McCracken, H. J., Milvang-Jensen, B., Dunlop, J., Franx, M., Fynbo, J. P. U., Le Fèvre, O., Holt, J., Caputi, K. I., Goranova, Y., Buitrago, F., Emerson, J. P., et al. 2012: *UltraVISTA: a new ultra-deep near-infrared survey in COSMOS*, A&A, 544, A156

McInnes, R. N., Menanteau, F., Heavens, A. F., Hughes, J. P., Jimenez, R., Massey, R., Simon, P., & Taylor, A. 2009: *First lensing measurements of SZ-detected clusters*, Mon. Not. Roy. Astron. Soc., 399, L84

Medezinski, E., Broadhurst, T., Umetsu, K., Coe, D., Benítez, N., Ford, H., Rephaeli, Y., Arimoto, N., & Kong, X. 2007: *Using Weak-Lensing Dilution to Improve Measurements of the Luminous and Dark Matter in A1689*, ApJ, 663, 717

Medezinski, E., Broadhurst, T., Umetsu, K., Oguri, M., Rephaeli, Y., & Benítez, N. 2010: *Detailed cluster mass and light profiles of A1703, A370 and RXJ1347–11 from deep Subaru imaging*, Mon. Not. Roy. Astron. Soc., 405, 257

Medezinski, E., Umetsu, K., Nonino, M., Merten, J., Zitrin, A., Broadhurst, T., Donahue, M., Sayers, J., Waizmann, J.-C., Koekemoer, A., Coe, D., et al. 2013: *CLASH: Complete Lensing Analysis of the Largest Cosmic Lens MACS J0717.5+3745 and Surrounding Structures*, ApJ, 777, 43

Melchior, P., Suchyta, E., Huff, E., Hirsch, M., Kacprzak, T., Rykoff, E., Gruen, D., Armstrong, R., Bacon, D., Bechtol, K., Bernstein, G. M., et al. 2014: *Mass and galaxy distributions of four massive galaxy clusters from Dark Energy Survey Science Verification data*, MNRAS accepted, ArXiv e-prints, 1405.4285

Melchior, P. & Viola, M. 2012: *Means of confusion: how pixel noise affects shear estimates for weak gravitational lensing*, Mon. Not. Roy. Astron. Soc., 424, 2757

Melin, J.-B., Bartlett, J. G., & Delabrouille, J. 2006: *Catalog extraction in SZ cluster surveys: a matched filter approach*, A&A, 459, 341

Menanteau, F., González, J., Juin, J.-B., Marriage, T. A., Reese, E. D., Acquaviva, V., Aguirre, P., Appel, J. W., Baker, A. J., Barrientos, L. F., Battistelli, E. S., et al. 2010a: *The Atacama Cosmology Telescope: Physical Properties and Purity of a Galaxy Cluster Sample Selected via the Sunyaev-Zel'dovich Effect*, ApJ, 723, 1523

Menanteau, F., Hughes, J. P., Barrientos, L. F., Deshpande, A. J., Hilton, M., Infante, L., Jimenez, R., Kosowsky, A., Moodley, K., Spergel, D., & Verde, L. 2010b: *Southern Cosmology Survey. II. Massive Optically Selected Clusters from 70 Square Degrees of the Sunyaev-Zel'dovich Effect Common Survey Area*, ApJS, 191, 340

Menanteau, F., Hughes, J. P., Jimenez, R., Hernandez-Monteagudo, C., Verde, L., Kosowsky, A., Moodley, K., Infante, L., & Roche, N. 2009: *Southern Cosmology Survey. I. Optical Cluster Detections and Predictions for the Southern Common-Area Millimeter-Wave Experiments*, ApJ, 698, 1221

Merten, J., Meneghetti, M., Postman, M., Umetsu, K., Zitrin, A., Medezinski, E., Nonino, M., Koekemoer, A., Melchior, P., Gruen, D., Moustakas, L. A., et al. 2014: *CLASH: The Concentration-Mass Relation of Galaxy Clusters*, ArXiv e-prints, 1404.1376

Meyers, J. E. & Burchat, P. R. 2014: *Impact of Atmospheric Chromatic Effects on Weak Lensing Measurements*, ArXiv e-prints, 1409.6273

Miller, L., Heymans, C., Kitching, T. D., van Waerbeke, L., Erben, T., Hildebrandt, H., Hoekstra, H., Mellier, Y., Rowe, B. T. P., Coupon, J., Dietrich, J. P., et al. 2013: *Bayesian galaxy shape measurement for weak lensing surveys - III. Application to the Canada-France-Hawaii Telescope Lensing Survey*, Mon. Not. Roy. Astron. Soc., 429, 2858

Mirkazemi, M., Finoguenov, A., Pereira, M. J., Tanaka, M., Lerchster, M., Brimioulle, F., Egami, E., Kettula, K., Erfanianfar, G., McCracken, H. J., Mellier, Y., et al. 2015: *Brightest X-Ray Clusters of Galaxies in the CFHTLS Wide Fields: Catalog and Optical Mass Estimator*, ApJ, 799, 60

Miyazaki, S., Hamana, T., Ellis, R. S., Kashikawa, N., Massey, R. J., Taylor, J., & Refregier, A. 2007: *A Subaru Weak-Lensing Survey. I. Cluster Candidates and Spectroscopic Verification*, ApJ, 669, 714

Miyazaki, S., Komiyama, Y., Nakaya, H., Kamata, Y., Doi, Y., Hamana, T., Karoji, H., Furusawa, H., Kawanomoto, S., Morokuma, T., Ishizuka, Y., et al. 2012: *Hyper Suprime-Cam*, in SPIE, Vol. 8446

Mo, H., van den Bosch, F., & White, S. 2010, Galaxy Formation and Evolution (Cambridge University Press)

Mohr, J. J., Adams, D., Barkhouse, W., Beldica, C., Bertin, E., Cai, Y. D., da Costa, L. A. N., Darnell, J. A., Daues, G. E., Jarvis, M., Gower, M., et al. 2008: *The Dark Energy Survey data management system*, in SPIE, Vol. 7016

Mohr, J. J., Armstrong, R., Bertin, E., Daues, G., Desai, S., Gower, M., Gruendl, R., Hanlon, W., Kuropatkin, N., Lin, H., Marriner, J., et al. 2012: *The Dark Energy Survey data processing and calibration system*, in SPIE, Vol. 8451

Monna, A., Seitz, S., Greisel, N., Eichner, T., Drory, N., Postman, M., Zitrin, A., Coe, D., Halkola, A., Suyu, S. H., Grillo, C., et al. 2014: *CLASH: $z \approx 6$ young galaxy candidate quintuply lensed by the frontier field cluster RXC J2248.7–4431*, Mon. Not. Roy. Astron. Soc., 438, 1417

More, A., Cabanac, R., More, S., Alard, C., Limousin, M., Kneib, J.-P., Gavazzi, R., & Motta, V. 2012: *The CFHTLS-Strong Lensing Legacy Survey (SL2S): Investigating the Group-scale Lenses with the SARCS Sample*, ApJ, 749, 38

Mroczkowski, T. 2011: *A New Approach to Obtaining Cluster Mass from Sunyaev-Zel'dovich Effect Observations*, ApJ, 728, L35

Mukhanov, V. F. & Chibisov, G. V. 1981: *Quantum fluctuations and a nonsingular universe*, Soviet Journal of Experimental and Theoretical Physics Letters, 33, 532

Nagai, D., Vikhlinin, A., & Kravtsov, A. V. 2007: *Testing X-Ray Measurements of Galaxy Clusters with Cosmological Simulations*, ApJ, 655, 98

Nakajima, R., Bernstein, G. M., Fadely, R., Keeton, C. R., & Schrabback, T. 2009: *Improved Constraints on the Gravitational Lens Q0957+561. I. Weak Lensing*, ApJ, 697, 1793

Navarro, J. F., Frenk, C. S., & White, S. D. M. 1996: *The Structure of Cold Dark Matter Halos*, ApJ, 462, 563

Navarro, J. F., Frenk, C. S., & White, S. D. M. 1997: *A Universal Density Profile from Hierarchical Clustering*, ApJ, 490, 493

Newman, A. B., Treu, T., Ellis, R. S., Sand, D. J., Nipoti, C., Richard, J., & Jullo, E. 2013: *The Density Profiles of Massive, Relaxed Galaxy Clusters. I. The Total Density Over Three Decades in Radius*, ApJ, 765, 24

Niemi, S.-M., Cropper, M., Szafraniec, M., & Kitching, T. 2014: *Measuring a Charge-Coupled Device Point Spread Function: Euclid Visible Instrument CCD273-84 PSF Performance*, Experimental Astronomy accepted, ArXiv e-prints, 1412.5382

Oemler, Jr., A. 1974: *The Systematic Properties of Clusters of Galaxies. Photometry of 15 Clusters*, ApJ, 194, 1

Oguri, M. & Blandford, R. D. 2009: *What is the largest Einstein radius in the universe?*, Mon. Not. Roy. Astron. Soc., 392, 930

Oguri, M. & Hamana, T. 2011: *Detailed cluster lensing profiles at large radii and the impact on cluster weak lensing studies*, Mon. Not. Roy. Astron. Soc., 414, 1851

Oguri, M., Lee, J., & Suto, Y. 2003: *Arc Statistics in Triaxial Dark Matter Halos: Testing the Collisionless Cold Dark Matter Paradigm*, ApJ, 599, 7

Okabe, N., Bourdin, H., Mazzotta, P., & Maurogordato, S. 2011: *Subaru Weak-lensing Study of A2163: Bimodal Mass Structure*, ApJ, 741, 116

Okabe, N., Smith, G. P., Umetsu, K., Takada, M., & Futamase, T. 2013: *LoCuSS: The Mass Density Profile of Massive Galaxy Clusters at $z = 0.2$*, ApJ, 769, L35

Okabe, N., Zhang, Y., Finoguenov, A., Takada, M., Smith, G. P., Umetsu, K., & Futamase, T. 2010: *LoCuSS: Calibrating Mass-observable Scaling Relations for Cluster Cosmology with Subaru Weak-lensing Observations*, ApJ, 721, 875

Olsen, L. F., Miralles, J.-M., da Costa, L., Benoist, C., Vandame, B., Rengelink, R., Rité, C., Scodeggio, M., Slijkhuis, R., Wicenec, A., & Zaggia, S. 2006a: *ESO imaging survey: infrared observations of CDF-S and HDF-S*, A&A, 452, 119

Olsen, L. F., Miralles, J.-M., da Costa, L., Madejsky, R., Jørgensen, H. E., Mignano, A., Arnouts, S., Benoist, C., Dietrich, J. P., Slijkhuis, R., & Zaggia, S. 2006b: *ESO imaging survey: infrared deep public survey*, A&A, 456, 881

Peacock, J. A. & Dodds, S. J. 1996: *Non-linear evolution of cosmological power spectra*, Mon. Not. R. Astron. Soc., 280, L19

Peebles, P. J. E. 1993, Principles of Physical Cosmology (Princeton University Press)

Perlmutter, S., Aldering, G., Goldhaber, G., Knop, R. A., Nugent, P., Castro, P. G., Deustua, S., Fabbro, S., Goobar, A., Groom, D. E., Hook, I. M., et al. 1999: *Measurements of* Ω *and* Λ *from 42 High-Redshift Supernovae*, ApJ, 517, 565

Pickles, A. J. 1998: *A Stellar Spectral Flux Library: 1150-25000 Å*, PASP, 110, 863

Piffaretti, R., Arnaud, M., Pratt, G. W., Pointecouteau, E., & Melin, J.-B. 2011: *The MCXC: a meta-catalogue of x-ray detected clusters of galaxies*, A&A, 534, A109

Piffaretti, R. & Valdarnini, R. 2008: *Total mass biases in X-ray galaxy clusters*, A&A, 491, 71

Plagge, T., Benson, B. A., Ade, P. A. R., Aird, K. A., Bleem, L. E., Carlstrom, J. E., Chang, C. L., Cho, H.-M., Crawford, T. M., Crites, A. T., de Haan, T., et al. 2010: *Sunyaev-Zel'dovich Cluster Profiles Measured with the South Pole Telescope*, ApJ, 716, 1118

Planck Collaboration, Ade, P. A. R., Aghanim, N., Armitage-Caplan, C., Arnaud, M., Ashdown, M., Atrio-Barandela, F., Aumont, J., Aussel, H., Baccigalupi, C., & et al. 2014a: *Planck 2013 results. XXIX. The Planck catalogue of Sunyaev-Zeldovich sources*, A&A, 571, A29

Planck Collaboration, Ade, P. A. R., Aghanim, N., Armitage-Caplan, C., Arnaud, M., Ashdown, M., Atrio-Barandela, F., Aumont, J., Baccigalupi, C., Banday, A. J., & et al. 2014b: *Planck 2013 results. XVI. Cosmological parameters*, A&A, 571, A16

Planck Collaboration, Ade, P. A. R., Aghanim, N., Armitage-Caplan, C., Arnaud, M., Ashdown, M., Atrio-Barandela, F., Aumont, J., Baccigalupi, C., Banday, A. J., & et al. 2014c: *Planck 2013 results. XX. Cosmology from Sunyaev-Zeldovich cluster counts*, A&A, 571, A20

Planck Collaboration, Ade, P. A. R., Aghanim, N., Arnaud, M., Arroja, F., Ashdown, M., Aumont, J., Baccigalupi, C., Ballardini, M., Banday, A. J., & et al. 2015a: *Planck 2015 results. XVII. Constraints on primordial non-Gaussianity*, ArXiv e-prints

Planck Collaboration, Ade, P. A. R., Aghanim, N., Arnaud, M., Ashdown, M., Atrio-Barandela, F., Aumont, J., Baccigalupi, C., Balbi, A., Banday, A. J., Barreiro, R. B., et al. 2013a: *Planck intermediate results. III. The relation between galaxy cluster mass and Sunyaev-Zeldovich signal*, A&A, 550, A129

Planck Collaboration, Ade, P. A. R., Aghanim, N., Arnaud, M., Ashdown, M., Aumont, J., Baccigalupi, C., Balbi, A., Banday, A. J., Barreiro, R. B., & et al. 2011a: *Planck early results. VIII. The all-sky early Sunyaev-Zeldovich cluster sample*, A&A, 536, A8

Planck Collaboration, Ade, P. A. R., Aghanim, N., Arnaud, M., Ashdown, M., Aumont, J., Baccigalupi, C., Balbi, A., Banday, A. J., Barreiro, R. B., & et al. 2011b: *Planck early results. XI. Calibration of the local galaxy cluster Sunyaev-Zeldovich scaling relations*, A&A, 536, A11

Planck Collaboration, Ade, P. A. R., Aghanim, N., Arnaud, M., Ashdown, M., Aumont, J., Baccigalupi, C., Banday, A. J., Barreiro, R. B., Bartlett, J. G., & et al. 2015b: *Planck 2015 results. XXIV. Cosmology from Sunyaev-Zeldovich cluster counts*, ArXiv e-prints

Planck Collaboration, Aghanim, N., Arnaud, M., Ashdown, M., Atrio-Barandela, F., Aumont, J., Baccigalupi, C., Balbi, A., Banday, A. J., Barreiro, R. B., Bartlett, J. G., et al. 2012: *Planck intermediate results. I. Further validation of new Planck clusters with XMM-Newton*, A&A, 543, A102

Planck Collaboration, Aghanim, N., Arnaud, M., Ashdown, M., Aumont, J., Baccigalupi, C., Balbi, A., Banday, A. J., Barreiro, R. B., Bartelmann, M., & et al. 2011c: *Planck early results. IX. XMM-Newton follow-up for validation of Planck cluster candidates*, A&A, 536, A9

Planck Collaboration, AMI Collaboration, Ade, P. A. R., Aghanim, N., Arnaud, M., Ashdown, M., Aumont, J., Baccigalupi, C., Balbi, A., Banday, A. J., & et al. 2013b: *Planck intermediate results. II. Comparison of Sunyaev-Zeldovich measurements from Planck and from the Arcminute Microkelvin Imager for 11 galaxy clusters*, A&A, 550, A128

Plazas, A. A. & Bernstein, G. M. 2012: *Atmospheric dispersion effects in weak lensing measurements*, ArXiv e-prints

Plazas, A. A., Bernstein, G. M., & Sheldon, E. S. 2014: *On-Sky Measurements of the Transverse Electric Fields' Effects in the Dark Energy Camera CCDs*, PASP, 126, 750

Poincaré, H. 1905, Science and Hypothesis (Walter Scott)

Poli, F., Giallongo, E., Menci, N., D'Odorico, S., & Fontana, A. 1999: *The Evolution of the Galaxy Sizes in the New Technology Telescope Deep Field: A Comparison with Cold Dark Matter Models*, ApJ, 527, 662

Postman, M., Coe, D., Benítez, N., Bradley, L., Broadhurst, T., Donahue, M., Ford, H., Graur, O., Graves, G., Jouvel, S., Koekemoer, A., et al. 2012: *The Cluster Lensing and Supernova Survey with Hubble: An Overview*, ApJS, 199, 25

Pratt, G. W., Croston, J. H., Arnaud, M., & Böhringer, H. 2009: *Galaxy cluster X-ray luminosity scaling relations from a representative local sample (REXCESS)*, A&A, 498, 361

Press, W. H. & Schechter, P. 1974: *Formation of Galaxies and Clusters of Galaxies by Self-Similar Gravitational Condensation*, ApJ, 187, 425

Quintana, H., Infante, L., Fouque, P., Carrasco, E. R., Cuevas, H., Hertling, G., & Nuñez, I. 2000: *Photometry of the Central Regions in a Complete Sample of High Bautz-Morgan-Type Abell Clusters. I. Observations and Data Calibration*, ApJS, 126, 1

Ragozzine, B., Clowe, D., Markevitch, M., Gonzalez, A. H., & Bradač, M. 2012: *Weak-lensing Results for the Merging Cluster A1758*, ApJ, 744, 94

Rasmussen, A., Antilogus, P., Astier, P., Claver, C., Doherty, P., Dubois-Felsmann, G., Gilmore, K., Kahn, S., Kotov, I., Lupton, R., O'Connor, P., et al. 2014: *A framework for modeling the detailed optical response of thick, multiple segment, large format sensors for precision astronomy applications*, in SPIE, Vol. 9150, 17

Redlich, M., Bartelmann, M., Waizmann, J.-C., & Fedeli, C. 2012: *The strongest gravitational lenses. I. The statistical impact of cluster mergers*, A&A, 547, A66

Refregier, A., Kacprzak, T., Amara, A., Bridle, S., & Rowe, B. 2012: *Noise bias in weak lensing shape measurements*, Mon. Not. Roy. Astron. Soc., 425, 1951

Reichardt, C. L., Stalder, B., Bleem, L. E., Montroy, T. E., Aird, K. A., Andersson, K., Armstrong, R., Ashby, M. L. N., Bautz, M., Bayliss, M., Bazin, G., et al. 2013: *Galaxy Clusters Discovered via the Sunyaev-Zel'dovich Effect in the First 720 Square Degrees of the South Pole Telescope Survey*, ApJ, 763, 127

Reiprich, T. H. & Böhringer, H. 2002: *The Mass Function of an X-Ray Flux-limited Sample of Galaxy Clusters*, ApJ, 567, 716

Reyes, R., Mandelbaum, R., Hirata, C., Bahcall, N., & Seljak, U. 2008: *Improved optical mass tracer for galaxy clusters calibrated using weak lensing measurements*, Mon. Not. Roy. Astron. Soc., 390, 1157

Rhoads, J. E. 2000: *Cosmic-Ray Rejection by Linear Filtering of Single Images*, PASP, 112, 703

Riess, A. G., Filippenko, A. V., Challis, P., Clocchiatti, A., Diercks, A., Garnavich, P. M., Gilliland, R. L., Hogan, C. J., Jha, S., Kirshner, R. P., Leibundgut, B., et al. 1998: *Observational Evidence from Supernovae for an Accelerating Universe and a Cosmological Constant*, AJ, 116, 1009

Robertson, H. P. 1935: *Kinematics and World-Structure*, ApJ, 82, 284

Romano, A., Fu, L., Giordano, F., Maoli, R., Martini, P., Radovich, M., Scaramella, R., Antonuccio-Delogu, V., Donnarumma, A., Ettori, S., Kuijken, K., et al. 2010: *Abell 611. I. Weak lensing analysis with LBC*, A&A, 514, A88

Rosati, P., Borgani, S., & Norman, C. 2002: *The Evolution of X-ray Clusters of Galaxies*, ARA&A, 40, 539

Rowe, B. 2010: *Improving PSF modelling for weak gravitational lensing using new methods in model selection*, Mon. Not. Roy. Astron. Soc., 404, 350

Rowe, B., Jarvis, M., Mandelbaum, R., Bernstein, G. M., Bosch, J., Simet, M., Meyers, J. E., Kacprzak, T., Nakajima, R., Zuntz, J., Miyatake, H., et al. 2014: *GalSim: The modular galaxy image simulation toolkit*, Astronomy & Computing accepted, ArXiv e-prints, 1407.7676

Rozo, E., Wechsler, R. H., Rykoff, E. S., Annis, J. T., Becker, M. R., Evrard, A. E., Frieman, J. A., Hansen, S. M., Hao, J., Johnston, D. E., Koester, B. P., et al. 2010: *Cosmological Constraints from the Sloan Digital Sky Survey maxBCG Cluster Catalog*, ApJ, 708, 645

Rubin, V. C., Ford, W. K. J., & . Thonnard, N. 1980: *Rotational properties of 21 SC galaxies with a large range of luminosities and radii, from NGC 4605 /R = 4kpc/ to UGC 2885 /R = 122 kpc/*, ApJ, 238, 471

Rykoff, E. S., Koester, B. P., Rozo, E., Annis, J., Evrard, A. E., Hansen, S. M., Hao, J., Johnston, D. E., McKay, T. A., & Wechsler, R. H. 2012: *Robust Optical Richness Estimation with Reduced Scatter*, ApJ, 746, 178

Rykoff, E. S., Rozo, E., Busha, M. T., Cunha, C. E., Finoguenov, A., Evrard, A., Hao, J., Koester, B. P., Leauthaud, A., Nord, B., Pierre, M., et al. 2014: *redMaPPer. I. Algorithm and SDSS DR8 Catalog*, ApJ, 785, 104

Sahlen, M., Viana, P. T. P., Liddle, A. R., Romer, A. K., Davidson, M., Hosmer, M., Lloyd-Davies, E., Sabirli, K., Collins, C. A., Freeman, P. E., Hilton, M., et al. 2009: *The XMM Cluster Survey: forecasting cosmological and cluster scaling-relation parameter constraints*, Mon. Not. Roy. Astron. Soc., 397, 577

Salzberg, S., Chandar, R., Ford, H., Murthy, S. K., & White, R. 1995: *Decision trees for automated identification of cosmic-ray hits in Hubble Space Telescope images*, PASP, 107, 279

Sayers, J., Czakon, N. G., Mantz, A., Golwala, S. R., Ameglio, S., Downes, T. P., Koch, P. M., Lin, K.-Y., Maughan, B. J., Molnar, S. M., Moustakas, L., et al. 2013: *Sunyaev-Zel'dovich-measured Pressure Profiles from the Bolocam X-Ray/SZ Galaxy Cluster Sample*, ApJ, 768, 177

Schechter, P. 1976: *An analytic expression for the luminosity function for galaxies.*, ApJ, 203, 297

Schirmer, M., Erben, T., Hetterscheidt, M., & Schneider, P. 2007: *GaBoDS: the Garching-Bonn Deep Survey. IX. A sample of 158 shear-selected mass concentration candidates*, A&A, 462, 875

Schirmer, M., Erben, T., Schneider, P., Wolf, C., & Meisenheimer, K. 2004: *GaBoDS: The Garching-Bonn Deep Survey. II. Confirmation of EIS cluster candidates by weak gravitational lensing*, A&A, 420, 75

Schlafly, E. F. & Finkbeiner, D. P. 2011: *Measuring Reddening with Sloan Digital Sky Survey Stellar Spectra and Recalibrating SFD*, ApJ, 737, 103

Schlegel, D. J., Finkbeiner, D. P., & Davis, M. 1998: *Maps of Dust Infrared Emission for Use in Estimation of Reddening and Cosmic Microwave Background Radiation Foregrounds*, ApJ, 500, 525

Schneider, P. 1996: *Detection of (dark) matter concentrations via weak gravitational lensing*, Mon. Not. Roy. Astron. Soc., 283, 837

Schneider, P. 2005: *Weak Gravitational Lensing*, ArXiv e-prints, 0509252

Schneider, P., King, L., & Erben, T. 2000: *Cluster mass profiles from weak lensing: constraints from shear and magnification information*, A&A, 353, 41

Schneider, P. & Seitz, C. 1995: *Steps towards nonlinear cluster inversion through gravitational distortions. 1: Basic considerations and circular clusters*, A&A, 294, 411

Schneider, P., van Waerbeke, L., Jain, B., & Kruse, G. 1998: *A new measure for cosmic shear*, Mon. Not. Roy. Astron. Soc., 296, 873

Schrabback, T., Erben, T., Simon, P., Miralles, J.-M., Schneider, P., Heymans, C., Eifler, T., Fosbury, R. A. E., Freudling, W., Hetterscheidt, M., Hildebrandt, H., et al. 2007: *Cosmic shear analysis of archival HST/ACS data. I. Comparison of early ACS pure parallel data to the HST/GEMS survey*, A&A, 468, 823

Schrabback, T., Hartlap, J., Joachimi, B., Kilbinger, M., Simon, P., Benabed, K., Bradač, M., Eifler, T., Erben, T., Fassnacht, C. D., High, F. W., et al. 2010: *Evidence of the accelerated expansion of the Universe from weak lensing tomography with COSMOS*, A&A, 516, A63

Seitz, C. & Schneider, P. 1995: *Steps towards nonlinear cluster inversion through gravitational distortions II. Generalization of the Kaiser and Squires method.*, A&A, 297, 287

Seitz, C. & Schneider, P. 1997: *Steps towards nonlinear cluster inversion through gravitational distortions. III. Including a redshift distribution of the sources.*, A&A, 318, 687

Seitz, S. & Schneider, P. 1996: *Cluster lens reconstruction using only observed local data: an improved finite-field inversion technique.*, A&A, 305, 383

Seitz, S., Schneider, P., & Ehlers, J. 1994: *Light propagation in arbitrary spacetimes and the gravitational lens approximation*, Classical and Quantum Gravity, 11, 2345

Semler, D. R., Šuhada, R., Aird, K. A., Ashby, M. L. N., Bautz, M., Bayliss, M., Bazin, G., Bocquet, S., Benson, B. A., Bleem, L. E., Brodwin, M., et al. 2012: *High-redshift Cool-core Galaxy Clusters Detected via the Sunyaev-Zel'dovich Effect in the South Pole Telescope Survey*, ApJ, 761, 183

Sereno, M. & Ettori, S. 2014: *Comparing Masses in Literature (CoMaLit) - I. Bias and scatter in weak lensing and X-ray mass estimates of clusters*, ArXiv e-prints, 1407.7868

Sheldon, E. S., Johnston, D. E., Scranton, R., Koester, B. P., McKay, T. A., Oyaizu, H., Cunha, C., Lima, M., Lin, H., Frieman, J. A., Wechsler, R. H., et al. 2009: *Cross-correlation Weak Lensing of SDSS Galaxy Clusters. I. Measurements*, ApJ, 703, 2217

Sheth, R. K. & Tormen, G. 1999: *Large-scale bias and the peak background split*, Mon. Not. Roy. Astron. Soc., 308, 119

Shi, X. & Komatsu, E. 2014: *Analytical model for non-thermal pressure in galaxy clusters*, Mon. Not. Roy. Astron. Soc., 442, 521

Sifón, C., Menanteau, F., Hasselfield, M., Marriage, T. A., Hughes, J. P., Barrientos, L. F., González, J., Infante, L., Addison, G. E., Baker, A. J., Battaglia, N., et al. 2013: *The Atacama Cosmology Telescope: Dynamical Masses and Scaling Relations for a Sample of Massive Sunyaev-Zel'dovich Effect Selected Galaxy Clusters*, ApJ, 772, 25

Simet, M., Battaglia, N., Mandelbaum, R., & Seljak, U. 2015: *Weak lensing calibration of mass bias in the RBC X-ray galaxy cluster catalog*, ArXiv e-prints, 1502.01024

Smith, R. E., Peacock, J. A., Jenkins, A., White, S. D. M., Frenk, C. S., Pearce, F. R., Thomas, P. A., Efstathiou, G., & Couchman, H. M. P. 2003: *Stable clustering, the halo model and non-linear cosmological power spectra*, Mon. Not. Roy. Astron. Soc., 341, 1311

Song, J., Zenteno, A., Stalder, B., Desai, S., Bleem, L. E., Aird, K. A., Armstrong, R., Ashby, M. L. N., Bayliss, M., Bazin, G., Benson, B. A., et al. 2012: *Redshifts, Sample Purity, and BCG Positions for the Galaxy Cluster Catalog from the First 720 Square Degrees of the South Pole Telescope Survey*, ApJ, 761, 22

Spinelli, P. F., Seitz, S., Lerchster, M., Brimioulle, F., & Finoguenov, A. 2012: *Weak-lensing mass estimates of galaxy groups and the line-of-sight contamination*, Mon. Not. Roy. Astron. Soc., 420, 1384

Staniszewski, Z., Ade, P. A. R., Aird, K. A., Benson, B. A., Bleem, L. E., Carlstrom, J. E., Chang, C. L., Cho, H.-M., Crawford, T. M., Crites, A. T., de Haan, T., et al. 2009: *Galaxy Clusters Discovered with a Sunyaev-Zel'dovich Effect Survey*, ApJ, 701, 32

Struble, M. F. & Rood, H. J. 1999: *A Compilation of Redshifts and Velocity Dispersions for ACO Clusters*, ApJS, 125, 35

Sunyaev, R. A. & Zel'dovich, Y. B. 1972: *The Observations of Relic Radiation as a Test of the Nature of X-Ray Radiation from the Clusters of Galaxies*, Comments on Astrophysics and Space Physics, 4, 173

Takada, M. & Jain, B. 2003: *The three-point correlation function in cosmology*, Mon. Not. Roy. Astron. Soc., 340, 580

Taylor, A., Joachimi, B., & Kitching, T. 2013: *Putting the precision in precision cosmology: How accurate should your data covariance matrix be?*, Mon. Not. Roy. Astron. Soc., 432, 1928

Tegmark, M., Taylor, A. N., & Heavens, A. F. 1997: *Karhunen-Loève Eigenvalue Problems in Cosmology: How Should We Tackle Large Data Sets?*, ApJ, 480, 22

The Dark Energy Survey Collaboration. 2005: *The Dark Energy Survey*, ArXiv e-prints, 0510346

Tinker, J., Kravtsov, A. V., Klypin, A., Abazajian, K., Warren, M., Yepes, G., Gottlöber, S., & Holz, D. E. 2008: *Toward a Halo Mass Function for Precision Cosmology: The Limits of Universality*, ApJ, 688, 709

Tinker, J. L., Robertson, B. E., Kravtsov, A. V., Klypin, A., Warren, M. S., Yepes, G., & Gottlöber, S. 2010: *The Large-scale Bias of Dark Matter Halos: Numerical Calibration and Model Tests*, ApJ, 724, 878

Tovmassian, H. M. & Moiseev, I. G. 1967: *Radio emission from clusters of galaxies*, Australian Journal of Physics, 20, 715

Umetsu, K., Broadhurst, T., Zitrin, A., Medezinski, E., Coe, D., & Postman, M. 2011: *A Precise Cluster Mass Profile Averaged from the Highest-quality Lensing Data*, ApJ, 738, 41

Umetsu, K., Medezinski, E., Nonino, M., Merten, J., Postman, M., Meneghetti, M., Donahue, M., Czakon, N., Molino, A., Seitz, S., Gruen, D., et al. 2014: *CLASH: Weak-lensing Shear-and-magnification Analysis of 20 Galaxy Clusters*, ApJ, 795, 163

Šuhada, R., Song, J., Böhringer, H., Benson, B. A., Mohr, J., Fassbender, R., Finoguenov, A., Pierini, D., Pratt, G. W., Andersson, K., Armstrong, R., et al. 2010: *XMM-Newton detection of two clusters of galaxies with strong SPT Sunyaev-Zel'dovich effect signatures*, A&A, 514, L3

Valentijn, E. A., McFarland, J. P., Snigula, J., Begeman, K. G., Boxhoorn, D. R., Rengelink, R., Helmich, E., Heraudeau, P., Kleijn, G. V., Vermeij, R., Vriend, W.-J., et al. 2007: *Astro-WISE: Chaining to the Universe*, in Astronomical Society of the Pacific Conference Series, Vol. 376, Astronomical Data Analysis Software and Systems XVI, ed. R. A. Shaw, F. Hill, & D. J. Bell, 491

van Dokkum, P. G. 2001: *Cosmic-Ray Rejection by Laplacian Edge Detection*, PASP, 113, 1420

Vandame, B. 2001: *Fast Hough Transform for Robust Detection of Satellite Tracks*, in Mining the Sky, ed. A. J. Banday, S. Zaroubi, & M. Bartelmann, 595

Vanderlinde, K., Crawford, T. M., de Haan, T., Dudley, J. P., Shaw, L., Ade, P. A. R., Aird, K. A., Benson, B. A., Bleem, L. E., Brodwin, M., Carlstrom, J. E., et al. 2010: *Galaxy Clusters Selected with the Sunyaev-Zel'dovich Effect from 2008 South Pole Telescope Observations*, ApJ, 722, 1180

Viana, P. T. P., da Silva, A., Ramos, E. P. R. G., Liddle, A. R., Lloyd-Davies, E. J., Romer, A. K., Kay, S. T., Collins, C. A., Hilton, M., Hosmer, M., Hoyle, B., et al. 2012: *The XMM Cluster Survey: predicted overlap with the Planck Cluster Catalogue*, Mon. Not. Roy. Astron. Soc., 422, 1007

Vikhlinin, A., Burenin, R. A., Ebeling, H., Forman, W. R., Hornstrup, A., Jones, C., Kravtsov, A. V., Murray, S. S., Nagai, D., Quintana, H., & Voevodkin, A. 2009a: *Chandra Cluster Cosmology Project. II. Samples and X-Ray Data Reduction*, ApJ, 692, 1033

Vikhlinin, A., Kravtsov, A. V., Burenin, R. A., Ebeling, H., Forman, W. R., Hornstrup, A., Jones, C., Murray, S. S., Nagai, D., Quintana, H., & Voevodkin, A. 2009b: *Chandra Cluster Cosmology Project III: Cosmological Parameter Constraints*, ApJ, 692, 1060

Vogeley, M. S. & Szalay, A. S. 1996: *Eigenmode Analysis of Galaxy Redshift Surveys. I. Theory and Methods*, ApJ, 465, 34

Voges, W., Aschenbach, B., Boller, T., Bräuninger, H., Briel, U., Burkert, W., Dennerl, K., Englhauser, J., Gruber, R., Haberl, F., Hartner, G., et al. 1999: *The ROSAT all-sky survey bright source catalogue*, A&A, 349, 389

Voges, W., Aschenbach, B., Boller, T., Brauninger, H., Briel, U., Burkert, W., Dennerl, K., Englhauser, J., Gruber, R., Haberl, F., Hartner, G., et al. 2000: *ROSAT all-sky survey faint source catalogue.*, IAU Circ., 7432, 1

von der Linden, A., Allen, M. T., Applegate, D. E., Kelly, P. L., Allen, S. W., Ebeling, H., Burchat, P. R., Burke, D. L., Donovan, D., Morris, R. G., Blandford, R., et al. 2014a: *Weighing the Giants - I. Weak-lensing masses for 51 massive galaxy clusters: project overview, data analysis methods and cluster images*, Mon. Not. Roy. Astron. Soc., 439, 2

von der Linden, A., Mantz, A., Allen, S. W., Applegate, D. E., Kelly, P. L., Morris, R. G., Wright, A., Allen, M. T., Burchat, P. R., Burke, D. L., Donovan, D., et al. 2014b: *Robust weak-lensing mass calibration of Planck galaxy clusters*, Mon. Not. Roy. Astron. Soc., 443, 1973

von Soldner, J. G. 1804: *Ueber die Ablenkung eines Lichtstrals von seiner geradlinigen Bewegung, durch die Attraktion eines Weltkörpers, an welchem er nahe vorbei geht*, in Astronomisches Jahrbuch für das Jahr 1804, ed. J. E. Bode (Berlin: G. A. Lange)

Waizmann, J.-C., Redlich, M., & Bartelmann, M. 2012: *The strongest gravitational lenses. II. Is the large Einstein radius of MACS J0717.5+3745 in conflict with ΛCDM?*, A&A, 547, A67

Walker, A. G. 1937: *On Milne's Theory of World-Structure*, Proceedings of the London Mathematical Society, s2-42, 90

Wang, L. & Steinhardt, P. J. 1998: *Cluster Abundance Constraints for Cosmological Models with a Time-varying, Spatially Inhomogeneous Energy Component with Negative Pressure*, ApJ, 508, 483

Warren, S. J., Hambly, N. C., Dye, S., Almaini, O., Cross, N. J. G., Edge, A. C., Foucaud, S., Hewett, P. C., Hodgkin, S. T., Irwin, M. J., Jameson, R. F., et al. 2007: *The United Kingdom Infrared Telescope Infrared Deep Sky Survey First Data Release*, Mon. Not. Roy. Astron. Soc., 375, 213

Weller, J. & Albrecht, A. 2002: *Future supernovae observations as a probe of dark energy*, Phys. Rev. D, 65, 103512

Weller, J., Battye, R. A., & Kneissl, R. 2002: *Constraining Dark Energy with Sunyaev-Zel'dovich Cluster Surveys*, Physical Review Letters, 88, 231301

Wen, Z. L., Han, J. L., & Liu, F. S. 2010: *Mass function of rich galaxy clusters and its constraint on* σ_8, Mon. Not. Roy. Astron. Soc., 407, 533

Williamson, R., Benson, B. A., High, F. W., Vanderlinde, K., Ade, P. A. R., Aird, K. A., Andersson, K., Armstrong, R., Ashby, M. L. N., Bautz, M., Bazin, G., et al. 2011: *A Sunyaev-Zel'dovich-selected Sample of the Most Massive Galaxy Clusters in the 2500 deg*^{2} *South Pole Telescope Survey*, ApJ, 738, 139

Wittgenstein, L. 1922, Tractatus Logico-Philosophicus (Routledge & Kegan Paul)

Wright, C. O. & Brainerd, T. G. 2000: *Gravitational Lensing by NFW Halos*, ApJ, 534, 34

Yoon, J. H., Schawinski, K., Sheen, Y.-K., Ree, C. H., & Yi, S. K. 2008: *A Spectrophotometric Search for Galaxy Clusters in SDSS*, ApJS, 176, 414

Zenteno, A., Song, J., Desai, S., Armstrong, R., Mohr, J. J., Ngeow, C.-C., Barkhouse, W. A., Allam, S. S., Andersson, K., Bazin, G., Benson, B. A., et al. 2011: *A Multiband Study of the Galaxy Populations of the First Four Sunyaev-Zel'dovich Effect Selected Galaxy Clusters*, ApJ, 734, 3

Zhang, Y.-Y., Okabe, N., Finoguenov, A., Smith, G. P., Piffaretti, R., Valdarnini, R., Babul, A., Evrard, A. E., Mazzotta, P., Sanderson, A. J. R., & Marrone, D. P. 2010: *LoCuSS: A Comparison of Cluster Mass Measurements from XMM-Newton and Subaru – Testing Deviation from Hydrostatic Equilibrium and Non-thermal Pressure Support*, ApJ, 711, 1033

Zitrin, A., Bartelmann, M., Umetsu, K., Oguri, M., & Broadhurst, T. 2012a: *Miscentring in galaxy clusters: dark matter to brightest cluster galaxy offsets in 10 000 Sloan Digital Sky Survey clusters*, Mon. Not. Roy. Astron. Soc., 426, 2944

Zitrin, A., Meneghetti, M., Umetsu, K., Broadhurst, T., Bartelmann, M., Bouwens, R., Bradley, L., Carrasco, M., Coe, D., Ford, H., Kelson, D., et al. 2013: *CLASH: The Enhanced Lensing Efficiency of the Highly Elongated Merging Cluster MACS J0416.1–2403*, ApJ, 762, L30

Zitrin, A., Rephaeli, Y., Sadeh, S., Medezinski, E., Umetsu, K., Sayers, J., Nonino, M., Morandi, A., Molino, A., Czakon, N., & Golwala, S. R. 2012b: *Cluster-cluster lensing and the case of Abell 383*, Mon. Not. Roy. Astron. Soc., 420, 1621

Zuntz, J., Kacprzak, T., Voigt, L., Hirsch, M., Rowe, B., & Bridle, S. 2013: *IM3SHAPE: a maximum likelihood galaxy shear measurement code for cosmic gravitational lensing*, Mon. Not. Roy. Astron. Soc., 434, 1604

Zwicky, F. 1933: *Die Rotverschiebung von extragalaktischen Nebeln*, Helvetica Physica Acta, 6, 110

Zwicky, F. 1937: *Nebulae as Gravitational Lenses*, Physical Review, 51, 290

Zwicky, F., Herzog, E., Wild, P., Karpowicz, M., & Kowal, C. T. 1961, Catalogue of galaxies and of clusters of galaxies, Vol. I (California Institute of Technology)

Curriculum Vitæ

Name:	Daniel Grün
Citizenship:	German

Education

- **2011–2015, Ph.D. in Physics**
  University Observatory Munich, Faculty of Physics, Ludwig-Maximilians-Universität
  and International Max Planck Research School (IMPRS) on Astrophysics
  Munich, Germany
- **2010–2011, Master's thesis**
  Department of Physics and Astronomy, University of Pennsylvania
  Philadelphia, Pennsylvania, USA
- **2009–2011, M.Sc. in Physics**
  Faculty of Physics, Ludwig-Maximilians-Universität
  Munich, Germany
- **2006–2009, B.Sc. in Physics**
  Faculty of Physics, Ludwig-Maximilians-Universität
  Munich, Germany
- **2006, Abitur**
  Lessing-Gymnasium, Winnenden, Germany

Publications

Publications (first author)

Gruen, D.; Bernstein, G. M.; Jarvis, M.; Rowe, B.; Vikram, V.; Plazas, A. A.; Seitz, S.: *Characterization and correction of charge-induced pixel shifts in DECam*, JINST submitted, arXiv:1501.02802

Gruen, D.; Seitz, S.; Becker, M.; Friedrich, O.; Mana, A.: *Cosmic variance of the galaxy cluster weak lensing signal*, MNRAS accepted, arXiv:1501.01632

Gruen, D.; Seitz, S.; Kosyra, R.; Brimioulle, F.; Koppenhoefer, J.; Lee, C.-H.; Bender, R.; Riffeser, A.; Eichner, T.; Weidinger, T.; Bierschenk, M.: *Weak lensing analysis of SZ-selected clusters of galaxies from the SPT and Planck surveys*, 2014, MNRAS, 442, 2, 1507

Gruen, D.; Seitz, S.; Bernstein, G. M.: *Implementation of robust image artifact removal in SWarp through clipped mean stacking*, 2014, PASP, 126, 936, 158

Gruen, D.; Brimioulle, F.; Seitz, S.; Lee, C.-H.; Young, J.; Koppenhoefer, J.; Eichner, T.; Riffeser, A.; Vikram, V.; Weidinger, T.; Zenteno, A.: *Weak lensing analysis of RXC J2248.7-4431*, 2013, MNRAS, 432, 2, 1455

Gruen, D.; Bernstein, G. M.; Lam, T. Y.; Seitz, S.: *Optimizing weak lensing mass estimates for cluster profile uncertainty*, 2011, MNRAS, 416, 2, 1392

Gruen, D.; Seitz, S.; Koppenhoefer, J.; Riffeser, A.: *Bias-free shear estimation using artificial neural networks*, 2010, ApJ, 720, 1, 639

Publications (co-author)

Drlica-Wagner, A.; ... **Gruen, D.**; et al.: *Search for Gamma-Ray Emission from DES Dwarf Spheroidal Galaxy Candidates with Fermi-LAT Data*, ApJL submitted, arXiv:1503.02632

Publications (co-author)

(continued)

Bechtol, K.; ... **Gruen, D.**; et al.: *Eight New Milky Way Companions Discovered in First-Year Dark Energy Survey Data*, ApJ submitted, arXiv:1503.02584

Balbinot, E.; ... **Gruen, D.**; et al.: *The LMC geometry and outer stellar populations from early DES data*, MNRAS accepted, arXiv:1502.05050

Papadopoulos, A.; ... **Gruen, D.**; et al.: *DES13S2cmm: The First Superluminous Supernova from the Dark Energy Survey*, MNRAS accepted, arXiv:1501.07232

Kosyra, R.; **Gruen, D.**; Seitz, S.; Mana, A.; Rozo, E.; Rykoff, E.; Sanchez, A.; Bender, R.: *Environment-based selection effects of Planck clusters*, MNRAS submitted, arXiv:1501.02840

Chang, C.; ... **Gruen, D.**; et al.: *Modelling the Transfer Function for the Dark Energy Survey*, ApJ submitted, arXiv:1411.0032

Diehl, H. T.; ... **Gruen, D.**; et al.: *The Dark Energy Survey and operations: Year 1*, 2014, SPIE, 9149

Melchior, P.; Suchyta, E.; Huff, E.; Hirsch, M.; Kacprzak, T.; Rykoff, E.; **Gruen, D.**; et al.: *Mass and galaxy distributions of four massive galaxy clusters from Dark Energy Survey Science Verification data*, MNRAS submitted, arXiv:1405.4285

Merten, J.; Meneghetti, M.; Postman, M.; Umetsu, K.; Zitrin, A.; Medezinski, E.; Nonino, M.; Koekemoer, A.; Melchior, P.; **Gruen, D.**; et al.: *CLASH: The Concentration-Mass Relation of Galaxy Clusters*, ApJ submitted, arXiv:1404.1376

Umetsu, K.; ... **Gruen, D.**; et al.: *CLASH: Weak-Lensing Shear-and-Magnification Analysis of 20 Galaxy Clusters*, 2014, ApJ, 795, 163

Bernstein, G. M.; **Gruen, D.**: *Resampling images in Fourier domain*, 2014, PASP, 126, 937, 287

Kitching, T. D.; Rowe, B.; Gill, M.; Heymans, C.; Massey, R.; Witherick, D.; Courbin, F.; Georgatzis, K.; Gentile, M.; **Gruen, D.**; et al.: *Image Analysis for Cosmology: Results from the GREAT10 Star Challenge*, 2013, ApJS, 205, 2, 12, 11

Abbott, T.; ... **Gruen, D.**; et al.: *First SN Discoveries from the Dark Energy Survey*, 2012, ATEL, 4668

Acknowledgements

This work has benefitted from financial support, infrastructure, and opportunities for scientific exchange provided by SFB-Transregio 33 'The Dark Universe' by the Deutsche Forschungsgemeinschaft (DFG), the DFG cluster of excellence 'Origin and Structure of the Universe' and the Dark Energy Survey Collaboration.

On a personal note, I would like to close by expressing my gratitude to the people who were and are a part of this story.

I thank Dr. Stella Seitz for her supervision, all the way from a project during my undergraduate studies until today. Her experience and help, her encouragement, positive spirit, and her trust in me have been the basis for this thesis. I am grateful to her and to Prof. Dr. Ralf Bender for their continued support.

I am indebted to my collaborators and co-authors for their ideas, contributions, and the numerous helpful discussions we have had. I especially thank Prof. Dr. Gary Bernstein for his mentorship and support that has been a great source of motivation to me since the days of my Master's thesis.

At the University Observatory, I enjoyed the friendly and helpful spirit I experienced. For this I thank all friends and colleagues there, particularly Dr. Thomas Eichner, Dr. Natascha Greisel, Mihael Kodric, Dr. Johannes Koppenhöfer, Dr. Chien-Hsiu Lee, Dr. Anna Monna, Markus Michael Rau, Dr. Arno Riffeser, and Dr. Julia Young.

I am grateful to have met Dr. Fabrice Brimioulle, Oliver Friedrich, Ralf Kosyra, and Dr. Annalisa Mana. Thank you for the enthusiasm – sometimes the frustration – and always the friendship that we could share. Likewise, I thank all my friends for their moral and sometimes culinary support, among them Vincenz Dölle, Dr. Michele Fontanini, Matthias Mader, Dr. Andrés A. Plazas, Fabian Stöhr, Ludwig Straub, Dr. Vinu Vikram, and Philipp Wullstein.

I thank my mother and father, my Oma Scherlinger and Opa Jo, and all my family, for guiding me along their part of this way. It is from you that I have learnt to think, to speak, to be curious, and to believe in myself. I will remain grateful for that as long as I shall do.

Finally, I would like to thank Renata, the love of my life, for being there through all these years of good and, occasionally, bad times. I believe that our story, if that may ever be done, must be told as one. The next chapter is yet unwritten, and I am excited to find out with you what it will be.